Doctoral theses at NTNU, 2022:144

Olav Galteland

Nanothermodynamics and Molecular Simulations of Fluids in Porous Media

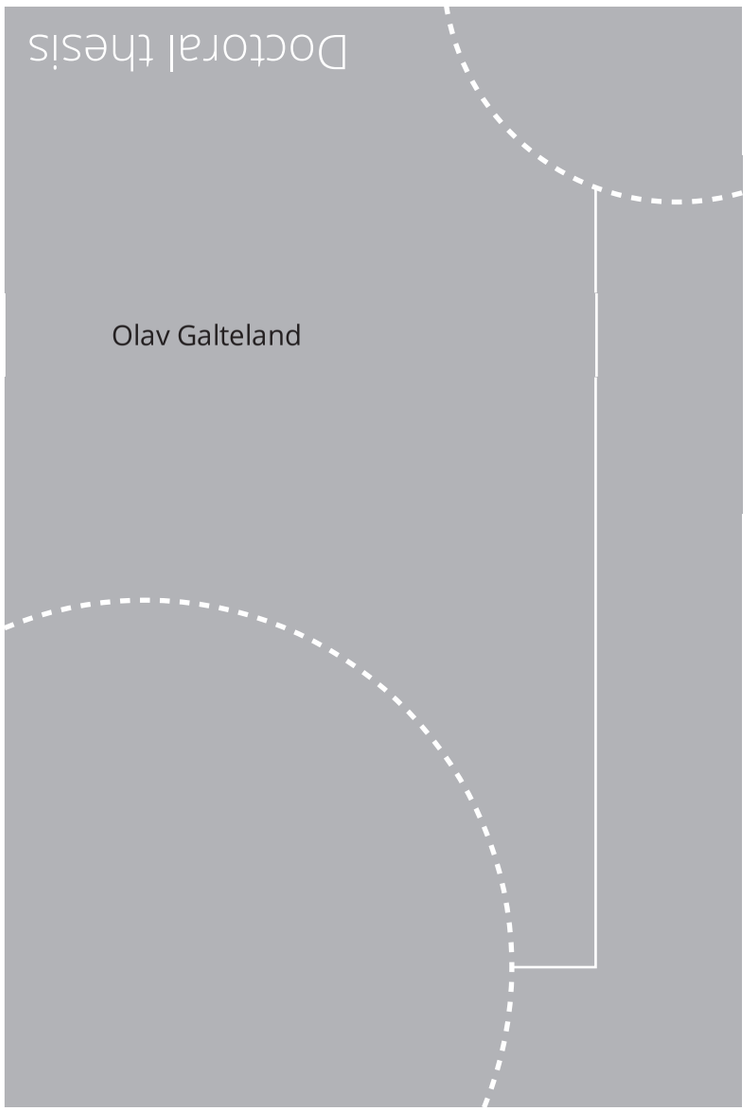

ISBN 978-82-326-6654-6 (printed ver.)
ISBN 978-82-326-6620-1 (electronic ver.)
ISSN 1503-8181 (printed ver.)
ISSN 2703-8084 (electronic ver.)

NTNU
Norwegian University of
Science and Technology

NTNU
Norwegian University of
Science and Technology
Thesis for the degree of
Philosophiae Doctor
Faculty of Natural Sciences
Department of Chemistry

Doctoral theses at NTNU, 2022:144

NTNU

NTNU
Norwegian University of
Science and Technology

Olav Galteland

Nanothermodynamics and Molecular Simulations of Fluids in Porous Media

Thesis for the degree of Philosophiae Doctor

Trondheim, May 2022

Norwegian University of Science and Technology
Faculty of Natural Sciences
Department of Chemistry

NTNU
Norwegian University of Science and Technology

Thesis for the degree of Philosophiae Doctor

Faculty of Natural Sciences
Department of Chemistry

ISBN 978-82-326-6654-6 (printed ver.)
ISBN 978-82-326-6620-1 (electronic ver.)
ISSN 1503-8181 (printed ver.)
ISSN 2703-8084 (electronic ver.)

Doctoral theses at NTNU, 2022:144

PRINTED IN NORWAY
NO - 1598

NORDIC SWAN ECOLABEL
Printed matter
2041 0731

Printed by Skipnes Kommunikasjon AS

Summary

The thermodynamic and transport properties of fluids confined to porous media are in this thesis investigated with nanothermodynamics, non-equilibrium thermodynamics, and molecular simulations. This thesis has two parts, where the first part gives an introduction to porous media, thermodynamics, and molecular simulations. The thermodynamics used and developed in this work are described in detail, with extra focus on the theory of nanothermodynamics. The molecular simulations used in this work are described, and the calculation of the local pressure tensor is described in detail. The second part of this thesis consists of nine scientific articles. Six of them are published in peer-reviewed journals, while three have been submitted and are available as preprints. The articles are enumerated from I to IX and are sorted by their published date, or submission date for those that have not been published yet.

Articles I and II apply non-equilibrium thermodynamics to describe the non-isothermal transport of a two-phase fluid in a representative elementary volume (REV) of a porous medium. The thermodynamic variables of the REV are defined, and the entropy production and flux-force equations are derived. The thermodynamic variables of the REV are constructed from additive contributions, namely from the bulks phases, surfaces, and three-phase contact lines. There are three driving forces present, the thermal force, a chemical force, and a pressure force. These articles set the stage for subsequent computational investigations of transport in porous media.

In article III, we investigate a single-phase fluid in a face-centered cubic (fcc) of solid particles. The fcc lattice is nanoporous, and we find that we need to introduce the integral pressure. The integral pressure is a concept from nanothermodynamics and is different from the differential pressure for small systems, which is the normal pressure. We realized with this work, that to calculate the

driving force in non-equilibrium conditions, namely the pressure gradient, we first needed to compose a procedure to calculate the pressure of a porous medium. This article initiated our interest in using nanothermodynamics to describe fluids in nanoporous media.

In the next articles IV, V, VI, VIII, we calculated the thermodynamic properties of fluids in nanoporous media using nanothermodynamics. The thermodynamic properties we calculated were for example the integral pressure, surface tension, entropy, and disjoining pressure. We investigated slit pores (IV, V, VI), pipes (VI), and fcc lattices (VIII). In articles IV, VI, and VIII we investigated a single-phase fluid, while in article V we investigated a liquid-vapor equilibrium in a slit pore. These articles gave us confidence that we understood and could describe such systems. For the slit pore, we related the mechanical pressure tensor to the thermodynamic integral pressure, normal pressure, and surface tension.

In article VII, we investigated a transition from a bulk fluid to a close-packing fluid in a slit pore when controlling either the height of the slit pore or the normal pressure. The system can be seen as a primitive model for deformable porous media when controlling the pressure because the pore volume was free to fluctuate. When controlling the height on the other hand the porous medium was completely non-deformable. To transform from the height-controlled free energy to pressure-controlled free energy we found for certain conditions that one must use the Legendre-Fenchel transform, and not the usual Legendre transform [1, 2]. This article was inspired by the stretching of short polymers, which shows a similar behavior [3].

In article IX, we applied what we learned in the previous works and calculated the transport coefficients of a single-phase fluid in a fcc lattice of solid spheres. We assumed that the integral pressure is constant when the system is in equilibrium and used this to calculate the integral pressure in a bulk fluid in equilibrium with the porous media. From this, we constructed an equation of state which relates the fluid density of the porous medium, temperature, and porosity to the integral pressure. The gradient in integral pressure is the driving force for fluid flow. Together with the mass flux and shear viscosity, we calculated the hydraulic conductivity and permeability of the system.

In addition to the articles listed above, I have published an article on the interactions between prolate ellipsoidal nanoparticles adsorbed at liquid-vapor interfaces [4]. This article is based on my master's thesis [5] and is not included here. In this article, we investigated interactions between prolate ellipsoidal nanoparticles adsorbed to liquid-vapor interfaces. Here the interaction between fluid and

solid is central, which is also the case for fluids in porous media.

During my time as a PhD candidate, I have primarily used the open-source software LAMMPS for molecular simulations [6]. I have contributed to LAMMPS by implementing two modules. These modules have been essential in this work, and hopefully, they will also be useful for others.

List of articles

I. Signe Kjelstrup, Dick Bedeaux, Alex Hansen, Bjørn Hafskjold, **Olav Galteland**
Non-isothermal Transport of Multi-Phase Fluids in Porous Media. The Entropy Production
Frontiers in Physics, 6, 126. (2018)
DOI: 10.3389/fphy.2018.00126

II. Signe Kjelstrup, Dick Bedeaux, Alex Hansen, Bjørn Hafskjold, **Olav Galteland**
Non-isothermal Transport of Multi-Phase Fluids in Porous Media. Constitutive Equations
Frontiers in Physics, 6, 150. (2019)
DOI: 10.3389/fphy.2018.00150

III. **Olav Galteland**, Dick Bedeaux, Bjørn Hafskjold, and Signe Kjelstrup.
Pressures Inside a Nano-Porous Medium. The Case of a Single Phase Fluid
Frontiers in Physics, 7, 60. (2019)
DOI: 10.3389/fphy.2019.00060

IV. Mate Erdős, **Olav Galteland**, Dick Bedeaux, Signe Kjelstrup, Othonas A. Moultos, Thijs J. H. Vlugt
Gibbs Ensemble Monte Carlo Simulation of Fluids in Confinement: Relation Between the Differential and Integral Pressures
Nanomaterials, 10(2), 293. (2020)
DOI: 10.3390/nano10020293

V. Michael T. Rauter, **Olav Galteland**, Mate Erdős, Othonas A. Moultos, Thijs J. H. Vlugt, Sondre K. Schnell, Dick Bedeaux, Signe Kjelstrup.
Two-Phase Equilibrium Conditions in Nanopores
Nanomaterials, 10(4), 608. (2020)
DOI: 10.3390/nano10040608

VI. **Olav Galteland**, Dick Bedeaux, Signe Kjelstrup
Nanothermodynamic Description and Molecular Simulation of a Single-Phase Fluid in a Slit Pore
Nanomaterials, 11(1), 165. (2021)
DOI: 10.3390/nano11010165

VII. **Olav Galteland**, Eivind Bering, Kim Kristiansen, Dick Bedeaux, Signe Kjelstrup
Legendre-Fenchel Transforms Capture Layering Transitions in Porous Media
Submitted (2021)
DOI: 10.48550/arXiv:2111.15253

VIII. **Olav Galteland**, Michael T. Rauter, Kevin K. Varughese, Dick Bedeaux, Signe Kjelstrup
Defining the Pressures of a Fluid in a Nanoporous, Heterogeneous Medium
Submitted (2022)
DOI: 10.48550/arXiv:2201.13060

IX. **Olav Galteland**, Michael T. Rauter, Mina S. Bratvold, Thuat T. Trinh, Dick Bedeaux, Signe Kjelstrup
Local Thermodynamic Description of Isothermal Single-Phase Flow in Porous Media
Submitted (2022)
DOI: 10.48550/arXiv:2203.02334

Other contributions

I have co-authored the following article during my time as a PhD candidate. This article is based on my MSc thesis, and is not included in the PhD thesis.

> **Olav Galteland**, Fernando Bresme, Bjørn Hafskjold
> *Solvent-Mediated Forces Between Ellipsoidal Nanoparticles Adsorbed at Liquid–Vapor Interfaces*
> Langmuir, 36(48), 14530-14538. (2020)
> DOI: 10.1021/acs.langmuir.0c02243

I have also contributed to the Large-scale Atomic/Molecular Massively Parallel Simulator (LAMMPS) by implementing calculations of the local pressure tensor in Cartesian and spherical coordinates, and additions to the local cylindrical pressure tensor. More details can be found in section 3.6.1 and 3.6.2. The code is available in the `develop` branch in the LAMMPS GitHub repository[1].

[1] See `https://github.com/lammps/lammps/pull/3165`

Acknowledgements

First of all, I would like to thank my supervisor, Signe Kjelstrup, and my co-supervisors, Dick Bedeaux and Bjørn Hafskjold. You are very knowledgeable, and you have been very encouraging and supportive. You have dedicated a lot of time for me and my projects, and I am very thankful for all your help. During the past four and a half years we have become a great team. I am very grateful and honored to have been your student.

I would also like to thank all my co-authors. I have enjoyed our scientific discussions and you have taught me a lot. I would also like to thank PoreLab and all my coworkers there. In particular, I would like to thank Marie-Laure Olivier for facilitating a very positive working environment. Thanks to Thijs J.H. Vlugt and TU Delft for hosting my research stay at TU Delft.

The simulations were performed on resources provided by UNINETT Sigma2 - the National Infrastructure for High-Performance Computing and Data Storage in Norway with project numbers NN9229K and NN8022K. I thank the Research Council of Norway for its Centres of Excellence funding scheme, project number 262644, PoreLab.

I am forever grateful for all the love and support from my wife and son, Lilja and Jørgen.

Contents

Chapter 1

Introduction

A porous medium is a material that contains space, which can be occupied by fluids. Examples of porous media include water and petroleum reservoirs, zeolites, membranes, blood vessels, and cement. This long list of examples hints at the challenge posed by studying fluids in porous media; there is a vast range of different types of porous media. Figure 1.1 shows two examples of porous media, a porous membrane electrode assembly found in a fuel cell and a metal-organic framework (MOF). The systems considered in this thesis are systems with two or three phases, where one of the phases always is the solid material that makes up the porous structure and the other(s) are fluid phases.

Many new green technologies use different porous media, and precise descriptions of transport in these are consequently very important. This can be used to find the optimal design of fuel cells [7, 8], understand how to store captured carbon dioxide [9–14], how to produce clean water and electricity from waste heat [15–19], or how to describe transport in lithium-ion battery electrodes and separators [20–22].

The mechanisms of transport in porous media have varying impacts on the vast range of sizes and shapes of the pores. The size of the pores can vary from nanometer size and up, and the shapes can vary from simple shapes like pipes and slit pores to complex geometries found in zeolites or sandstone. The proportion of surface energy to the total energy increases with decreasing size. This is a consequence of the square-cubed law, namely that the surface area scales with the square of the system size, while the volume scales with the cube of the system size. For porous media, the surface energies are significant. In addition, the chemistry and mechanical properties of the porous medium must also be considered. The

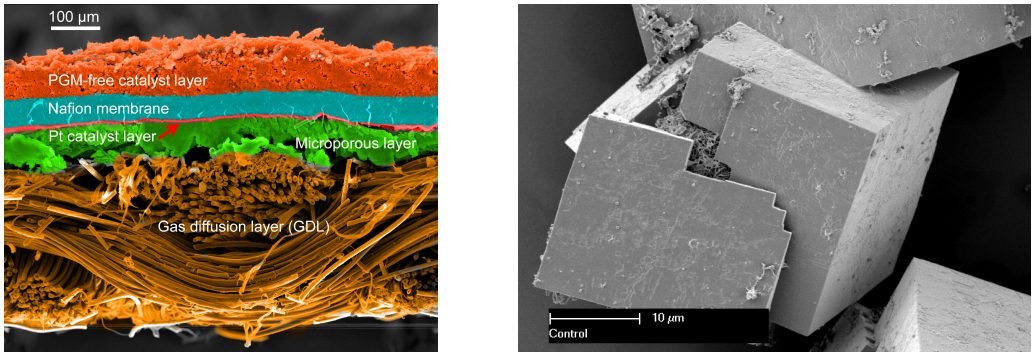

(a) **(b)**

Figure 1.1: **(a)** Scanning electron micrograph of a membrane electrode assembly cross section in a proton-exhange fuel cell. Reproduced from Yin *et al.* [23][1]. **(b)** Scanning electron micrograph of a crystal of metal-organic framework. The porous structure is much smaller than the resolution of the image and can not be seen. Reproduced from CSIRO[2].

ambition of the field is to have a detailed description of transport in porous media with a minimal amount of complexity. Typical variables to describe transport in porous media are saturation, porosity, tortuosity, pore connectivity, contact angle, and surface-to-volume ratios. Which of these variables are necessary? This thesis contributes to answers to these questions.

In this work, the thermodynamic properties of fluids in porous media are described with nanothermodynamics. Thermodynamics is a field of science that describes physical properties which are central in transport in porous media, for example, pressure and temperature. Classical thermodynamics describes systems in the thermodynamic limit, where the number of atoms and molecules approaches a very large number. However, fluids in porous media are not necessarily within the thermodynamic limit. To tackle this issue, we have for the first time utilized nanothermodynamics to describe fluids in porous media [24]. The transport properties are then described with non-equilibrium thermodynamics. Non-equilibrium thermodynamics extends classical thermodynamics to describe the transport of systems out of equilibrium [25–28]. The combination of nanothermodynamics and non-equilibrium thermodynamics to describe transport in porous media is novel, and I consider this to be a promising direction to obtain general and precise descriptions.

[1]Reproduced from Yin *et al.* [23] under the CC BY-SA 4.0 license.
[2]Reproduced from CSIRO under the CC BY 3.0 license.

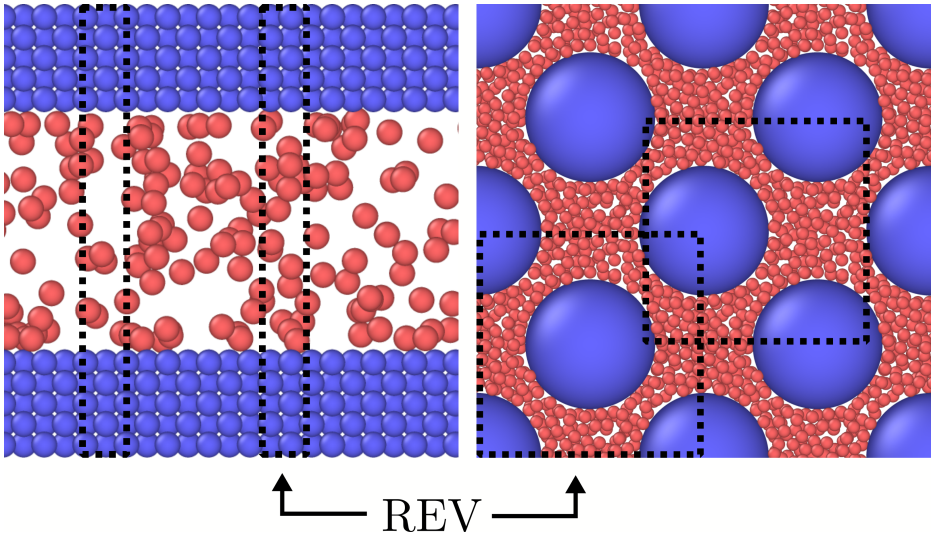

Figure 1.2: A single-phase fluid in a slit pore (left) and a face-centered cubic (fcc) lattice of solid spheres (right). The blue spheres represent solid and the red spheres represent fluid particles. The dotted black lines indicate the size of the representative elementary volume (REV), which gives a continuous description in which fluxes and forces can be determined.

Upscaled descriptions of transport in porous media are a prominent strategy to reduce the complexity. In general terms, this entails taking the complex details of a system and defining a combination with less complexity. The goal is to reduce the complexity while keeping the necessary detail for the purpose. For example, we can take molecular details such as atom positions, velocities, and forces, and combine them into properties such as pressure, mass flux, and temperature. One common procedure in porous media research is to define a representative elementary volume (REV). In this work, we define the REV to be a volume that is large enough, but not larger, to be statistically representative of the system. From a statistical mechanical point of view, the REV includes all available microstates of the system. Two REVs are illustrated in figure 1.2, the REVs of a single-phase fluid in a slit pore and a face-centered cubic (fcc) lattice of solid spheres. The REV gives a continuous description of the porous media, which in turn gives an integration path to calculate transport coefficients from local fluxes and forces. In this work, we specify a thermodynamic procedure to construct the REV which is general for all porous media. We derive the Gibbs equation for the REV, and in turn derive the entropy production and flux-force equations for the REV. This

gives a thermodynamic theory of coupled transport on the Darcy scale and gives a thermodynamic basis for Darcy's law. This definition of the REV differs from other definitions, such as the definition by Nordahl and Ringrose [29], which uses a constant permeability as a criterion for the REV size. We follow a similar procedure of volume integrals by Whitaker [30], as we use additive variables to define the REV. In further analysis, however, we deviate from Whitaker.

To investigate the assumptions and relations in the theory described in chapter 2 in this thesis, we apply molecular simulations as computational techniques. Molecular simulations are alternatives to time-consuming and costly laboratory and field experiments. They do not eliminate the need for experiments but are useful supplements. Molecular simulations simulate individual atoms or molecules, from which thermodynamic properties can be determined. To simulate transport in porous media we employ non-equilibrium molecular dynamics [31]. The molecular simulations are described in detail in chapter 3. More common in porous media research is the use of computational techniques such as pore-network models [32–35] and lattice Boltzmann simulations [36, 37]. However, using molecular simulations we can obtain thermodynamic variables such as pressure, temperature, and chemical potential directly from the molecular variables. This is not the case for pore-network models or lattice Boltzmann simulations. On the other hand, molecular simulations are computationally expensive, and the systems studied will inherently be much smaller than what pore-network models or lattice Boltzmann simulations can handle. All in all, molecular simulations are well suited for tackling the research questions in this PhD thesis.

Pressure has been of special interest in this work. Using nanothermodynamics, we define integral and differential pressures as well as surface tensions. With molecular simulations, we calculate the mechanical pressure tensor. There is no consensus on how these properties are related [38–40], and in fact, the local mechanical pressure tensor is ambiguous [41]. It was shown by Schofield and Henderson that the pressure due to a pair-wise particle interaction can be distributed along any curve connecting the pair [42]. In articles V and VI, we related the mechanical pressure tensor to the integral pressure, differential pressure, and surface tension by volume averages. These relations gave self-consistent relations between the properties. Other relations may also be possible. In articles VIII and IX, we used an equation of state approach, where the integral pressure was calculated in a bulk fluid. The integral pressure of a representative elementary volume (REV) in equilibrium with the bulk fluid was assumed to be constant. In this way, we were able to construct an equation of state for the integral pressure as a function

of the temperature, fluid mass density, and porosity of the REV. This is a new procedure, which I believe is general and can be applied to complex geometries and multiphase fluids.

The field of porous media research started with Henry Darcy in the 19th century. In 1856 he published a book with the English translation `The Public Fountains of the City of Dijon` [43], in which a section of the appendix described a collection of experiments of water flow in sand columns, and subsequently the discovery of what is now known as Darcy's law. Darcy's law describes the volume flux of a single-phase fluid in a porous medium with an applied pressure difference, in its later generalized form it is given as

$$q = -\frac{k\Delta p}{\eta L}, \tag{1.1}$$

where k is the permeability of the porous medium, η is the shear viscosity, Δp is the pressure difference across the medium, and L is the length of the porous medium. Darcy's law is similar to Fourier's law of heat conduction and Fick's law of diffusion. Later, it was shown that the Navier-Stokes equation reduces to Darcy's law by assuming laminar flow. Non-equilibrium thermodynamics also yields a similar equation when the volume flux and pressure gradient are the only flux-force terms. Darcy's law has been successfully applied in many engineering applications, maybe most notably in the petroleum industry. The law has been empirically extended to include two-phase flow, to model for example water and oil transport in petroleum reservoirs. However, for describing coupled transport in for example porous separators [44] we need more precise descriptions.

Darcy's equation describes transport on what is known as the Darcy scale. The REV is on the Darcy scale. For a single-phase fluid in a slit pore or a pipe, the REV spans the width of the pore [45–47], while for a single-phase fluid in a fcc lattice of solid spheres, the smallest REV is a unit cell [48–50]. This is illustrated in figure 1.2. The REV gives a continuous path in which fluxes and forces can be described. If we imagine displacing each solid particle in the fcc lattice a tiny amount or if we allow the width of the slit pore to vary along its surface, the REV increases to accommodate the variation. In addition, for multi-phase flow, the size of the REV must also increase. The REV is constructed of additive thermodynamic variables of the individual phases, surfaces, and contact lines of the REV. For example, the internal energy of the REV is a sum of the internal energy of the phases, surfaces, and lines.

In the next chapters, the thermodynamic theory and molecular simulations used in this work are described. In chapter 2, the thermodynamic theory is

described with an extra emphasis on nanothermodynamics. In chapter 3, the molecular simulations are described with a special focus on the calculation of the mechanical pressure tensor in Cartesian and spherical coordinates.

Chapter 2

Thermodynamics

The properties of fluids depend on temperature and pressure, but also the size and shape of the fluids. Fluids in porous media can have a vast range of different sizes and shapes. In this work, we use thermodynamics to get a systematic description of fluids in porous media. Thermodynamics is a field of science that describes how physical properties such as energy, chemical potentials, pressure, and temperature are related. In section 2.1, the mathematical background of thermodynamics is emphasized, as this becomes important when thermodynamic relations are applied to nanosized systems in section 2.3. Section 2.2 introduces the connection between thermodynamics and statistical mechanics, and transport in porous media is described with non-equilibrium thermodynamics in section 2.4.

2.1 Introduction to thermodynamics

The first law of thermodynamics states that the total energy of an isolated system is conserved [51]. The classical statement of this is that an infinitesimal change in internal energy $\mathrm{d}U$ of a system is the sum of the infinitesimal heat δQ and work δW supplied to the system,

$$\mathrm{d}U = \delta Q + \delta W. \tag{2.1}$$

Internal energy is the energy contained in the system, such as thermal energy and particle interactions.

2.1.1 Exact and inexact differentials

The symbols $\mathrm{d}f$ and δf represent infinitesimal changes in the function f. The difference between the two is that $\mathrm{d}f$ represents the exact differential of f, while δf represents the inexact differential. Heat and work are path functions which means that they depend on the path taken, and can not be written as exact differentials. The internal energy is a state function which means that it only depends on the state it is in and not the path that it has taken to get there, and it can be written as an exact differential. The exact differential is also be called the total differential. In this chapter, the terms exact and inexact differentials will be used, but note that we have used the terms total differential instead of exact differential in some of the articles in this thesis.

The exact differential of the function $f = f(x, y)$ is

$$\mathrm{d}f(x,y) = \left(\frac{\partial f}{\partial x}\right)_y \mathrm{d}x + \left(\frac{\partial f}{\partial y}\right)_x \mathrm{d}y \tag{2.2}$$

where x and y are independent variables. The subscripts of the partial derivatives indicate the variables that are held constant when differentiating. In this example, it is obvious which variables are kept constant during differentiation. In section 2.1.3 I introduce transformations of control variables, which underlines that this notation is important in thermodynamics.

Exact and inexact differentials

The differential of a function $f = f(x_1, x_2, \ldots, x_n)$ is exact when it can be written as

$$\mathrm{d}f(x_1, x_2, \ldots, x_n) = \sum_{i=1}^{n} \left(\frac{\partial f}{\partial x_i}\right)_{x_{j\neq i}} \mathrm{d}x_i. \tag{2.3}$$

If it can not, the differential $\delta f(x_1, x_2, \ldots, x_n)$ is inexact.

When a function can be written as an exact differential, the order of differentiation does not matter. This implies

$$\left(\frac{\partial}{\partial y}\left(\frac{\partial f}{\partial x}\right)_y\right)_x = \left(\frac{\partial}{\partial x}\left(\frac{\partial f}{\partial y}\right)_x\right)_y, \tag{2.4}$$

which is known as Maxwell relations. From this, relations between thermodynamic variables can be obtained, which is a great advantage of describing systems in terms of thermodynamics.

Heat and work are path functions, but if we assume reversible processes they can be expressed in terms of state functions. Work can for example be pressure-volume work where the system does work on the environment by expanding its volume. In that case, the infinitesimal reversible work applied to the system is

$$\delta W = -p\mathrm{d}V, \tag{2.5}$$

where p is the pressure and $\mathrm{d}V$ is the exact differential of the volume. Work can also be the work of stretching a surface or line. In the ideal case of reversible processes, the infinitesimal heat is

$$\delta Q = T\mathrm{d}S, \tag{2.6}$$

where T is the temperature and $\mathrm{d}S$ is the exact differential of the entropy. By introducing this into equation 2.1 we obtain the exact differential of the internal energy

$$\mathrm{d}U(S,V) = T\mathrm{d}S - p\mathrm{d}V. \tag{2.7}$$

Since this is the exact differential of the internal energy, temperature and pressure must be

$$T = \left(\frac{\partial U}{\partial S}\right)_V \quad \text{and} \quad p = -\left(\frac{\partial U}{\partial V}\right)_S, \tag{2.8}$$

respectively. We will from now on consider these as the definitions of temperature and pressure. Temperature and entropy are conjugate variables, and so are pressure and volume. We have the following Maxwell relation,

$$\left(\frac{\partial T}{\partial V}\right)_S = -\left(\frac{\partial p}{\partial S}\right)_V. \tag{2.9}$$

Temperature and pressure are intensive variables, while entropy and volume are extensive variables. Extensive variables double in size when the system doubles in size, while intensive variables do not depend on the system size. Extensive variables are Euler homogeneous functions of the first order, while intensive variables are Euler homogeneous functions of the zeroth-order.

2.1.2 Euler's theorem of homogeneous functions

An Euler homogeneous function increases by a factor λ^k when the arguments are multiplied by a factor λ,

$$f(\lambda x, \lambda y) = \lambda^k f(x,y) \tag{2.10}$$

where f is Euler homogeneous of order k. For example, the function $f = 2x+3y$ is Euler homogeneous of the first order, while the function $f = 2x^2+5y$ is not Euler homogeneous. By differentiating with respect to λ on both sides, reorganizing, and letting $\lambda = 1$, we obtain

$$kf(x,y) = \left(\frac{\partial f}{\partial x}\right)_y x + \left(\frac{\partial f}{\partial y}\right)_x y. \tag{2.11}$$

The functions $(\partial f/\partial x)_y$ and $(\partial f/\partial y)_x$ are homogeneous of degree $k-1$. This is known as Euler's theorem of homogeneous functions.

Euler's theorem of homogeneous functions

Let $f = f(x_1, x_2, \ldots, x_n)$ be a homogeneous function of order k such that

$$f(\lambda x_1, \lambda x_2, \ldots, \lambda x_n) = \lambda^k f(x_1, x_2, \ldots, x_n), \tag{2.12}$$

then

$$kf(x_1, x_2, \ldots, x_n) = \sum_{i=1}^{n} \left(\frac{\partial f}{\partial x_i}\right)_{x_{j\neq i}} x_i. \tag{2.13}$$

The internal energy is a function of only extensive variables and is consequently an Euler homogeneous of the first order. It can for example be a function of entropy, volume, and the number of particles of each component i. Since it is an Euler homogeneous function of the first order, we can in that case write

$$U(S,V,\boldsymbol{N}) = \left(\frac{\partial U}{\partial S}\right)_{V,\boldsymbol{N}} S + \left(\frac{\partial U}{\partial V}\right)_{S,\boldsymbol{N}} V + \sum_{i=1}^{C} \left(\frac{\partial U}{\partial N_i}\right)_{S,V,N_{j\neq i}} N_i, \tag{2.14}$$

where $\boldsymbol{N} = [N_1, N_2, \ldots, N_C]$ is a vector with the number of particles of C components.

The conjugate variable to the number of particles of component i is the chemical potential of component i. The temperature, pressure, and chemical potential are defined as

$$T := \left(\frac{\partial U}{\partial S}\right)_{V,\boldsymbol{N}}, \quad p := -\left(\frac{\partial U}{\partial V}\right)_{S,\boldsymbol{N}}, \quad \mu_i := \left(\frac{\partial U}{\partial N_i}\right)_{S,V,N_{j\neq i}}. \tag{2.15}$$

In the definition of the chemical potential, the number of particles of all other components $j \neq i$ is kept constant together with the entropy and volume. The symbol $:=$ indicates that the left-hand side is equal to the right-hand side by

definition. The chemical potential can be considered to be the energy required to add one more particle to the system while keeping the mentioned variables constant.

If you take the exact differential of both sides of equation 2.14 and apply the chain rule, you will get

$$\mathrm{d}U(S,V,\boldsymbol{N}) = T\mathrm{d}S + S\mathrm{d}T - p\mathrm{d}V - V\mathrm{d}p + \boldsymbol{\mu}\cdot\mathrm{d}\boldsymbol{N} + \boldsymbol{N}\cdot\mathrm{d}\boldsymbol{\mu}. \tag{2.16}$$

Where $\boldsymbol{\mu} = [\mu_1, \mu_2, \ldots, \mu_C]$ is the vector with the chemical potentials of each component and $\boldsymbol{\mu}\cdot\mathrm{d}\boldsymbol{N}$ denotes the inner product of the chemical potentials and number of particles. This equation of the exact differential of the internal energy does not agree with the definition in equation 2.3. However, Euler's homogeneous function theorem states that a function of T, p, and μ must be of the zeroth-order when the conjugate variables S, V, and N are of the first order. This means that

$$S\mathrm{d}T - V\mathrm{d}p + \boldsymbol{N}\cdot\mathrm{d}\boldsymbol{\mu} = 0. \tag{2.17}$$

This equation is known as the Gibbs-Duhem equation. The exact differential of the internal energy stated in equation 2.16 reduces to

$$\mathrm{d}U(S,V,\boldsymbol{N}) = T\mathrm{d}S - p\mathrm{d}V + \boldsymbol{\mu}\cdot\mathrm{d}\boldsymbol{N}. \tag{2.18}$$

This equation comes from requiring that the internal energy is a state function and that it is an Euler homogeneous function of the first order with the control variables $S, V, \boldsymbol{N}$.

A necessary assumption when using thermodynamic relations is that the internal energy is an Euler homogeneous function of the first order. One way to think of it is to ask oneself if the control variables completely describe the system. Is this the complete set of independent control variables? If the system for example has surfaces or lines, and the surface area or line length is not included as a control variable the internal energy will not be Euler homogeneous of the first order. For example, a function $f(x,y) = \pi x + \sqrt{2}y + ez$ is not Euler homogeneous of the first order with the given variables, while the function $f(x,y,z) = \pi x + \sqrt{2}y + ez$ is. One may always include surface areas, line lengths, points, and so on. Fluids in porous media can be complex, and there might be unknown extensive variables that the internal energy is a function of which makes it problematic to describe with classical thermodynamics. However, nanothermodynamics as described in section 2.3, can describe fluids in porous media in a very general and original manner.

2.1.3 Free energy transforms

Gibbs and Helmholtz introduced the concept of free energy, which is the energy available to do work in a given environment [51]. The free energies are state functions, but they are not Euler homogeneous. The environment decides which variables are controlled. For example, imagine a sealed container that allows energy, but not masses, to be transferred from the environment. In this case, the sensible control variables are temperature, volume, and the number of particles. In statistical mechanics, a set of control variables is characterized as an ensemble, and this particular set of control variables is called the canonical ensemble. In article VII, we investigate the free energy transforms of a single-phase fluid in a slit pore.

The Helmholtz energy is the free energy in an environment where the temperature, volume, and number of particles are controlled. The Helmholtz energy is by definition [51, 52]

$$A(T, V, \boldsymbol{N}) := U(S, V, \boldsymbol{N}) - TS. \tag{2.19}$$

This is a Legendre transform of the internal energy. Similarly, the enthalpy is defined as

$$H(S, p, \boldsymbol{N}) := U(S, V, \boldsymbol{N}) + pV, \tag{2.20}$$

and the Gibbs energy is defined as the Legendre transforms of the enthalpy,

$$G(T, p, \boldsymbol{N}) := H(S, p, \boldsymbol{N}) - TS. \tag{2.21}$$

The grand potential, with the temperature, volume, and chemical potential as control variables, can be defined as

$$\Omega(T, V, \boldsymbol{\mu}) := A(T, V, \boldsymbol{N}) - \boldsymbol{\mu} \cdot \boldsymbol{N}. \tag{2.22}$$

Legendre transform

The Legendre transform of a differentiable convex function $f = f(t)$ is

$$F(s) = f(t) - st. \tag{2.23}$$

The Legendre-Fenchel transform is sometimes called the Legendre transform, however, in this work, we will keep the distinction between the two transforms. The

Legendre-Fenchel transform is defined in section 2.2. The Legendre-Fenchel transform applies to differentiable non-convex functions, while the Legendre transform applies to differentiable convex functions. For convex functions, the Legendre-Fenchel transform reduces to the Legendre transform. A convex function has a non-negative second derivative everywhere. In article VII, we investigate a system where the Helmholtz energy is non-convex. In that case, the Legendre transform does not apply. In section 2.3, we shall see that nanothermodynamics defines the free energies differently.

2.2 Statistical mechanics

In statistical mechanics, statistical methods are applied to collections of particles to describe for example fluids and solids. This is done by expressing the particles and their interactions with a Hamiltonian and calculating the partition function. The Hamiltonian describes the energy of the possible states, and the partition function describes the statistics of each possible state in a given ensemble. Thermodynamic variables can be derived from the partition functions.

The Hamiltonian is a function of the generalized momenta $\boldsymbol{p}_i$ and positions $\boldsymbol{r}_i$ of particle i. The Hamiltonian of a system of N particles interacting with a pair-wise interaction potential $u(\boldsymbol{r}_i, \boldsymbol{r}_j)$ is

$$\mathcal{H}(\boldsymbol{p}_1, \ldots, \boldsymbol{p}_N, \boldsymbol{r}_1, \ldots, \boldsymbol{r}_N) = \sum_{i=1}^{N} \frac{\boldsymbol{p}_i \cdot \boldsymbol{p}_i}{2m_i} + \sum_{i=1}^{N} \sum_{j>i}^{N} u(\boldsymbol{r}_i, \boldsymbol{r}_j), \tag{2.24}$$

where m_i is the mass of particle i and the last two sums indicate a sum over all particle pairs of i and j. The Hamiltonian depends on the momenta and position of all N particles. The pair-wise interaction potential will be simplified in section 3.3 to only depend on the distance between particle i and j, $r_{ij} = |\boldsymbol{r}_j - \boldsymbol{r}_i|$. This implies that the pair-wise interaction is rotational spherical symmetric, and does not depend on the relative orientations of the particles. Other forms of the Hamiltonian are possible, for example with more complex interact potentials or with external forces.

In the microcanonical ensemble, the internal energy U, volume V, and the number of particles N are constant. The internal energy is simply equal to the Hamiltonian. In the canonical ensemble, where the temperature, volume, and the number of particles are constant, the internal energy is free to fluctuate. The

canonical partition function is the integral of the Boltzmann factor

$$Z = \frac{1}{h^{3N} N!} \int_{-\infty}^{\infty} \cdots \int_{-\infty}^{\infty} \exp(-\beta \mathcal{H}) \mathrm{d}\boldsymbol{p}_1 \ldots \mathrm{d}\boldsymbol{p}_N \mathrm{d}\boldsymbol{r}_1 \ldots \mathrm{d}\boldsymbol{r}_N. \tag{2.25}$$

The integrals are of all momenta and positions from minus infinity to plus infinity. There are $6N$ integrals, one per dimension and particle for the momenta and positions. This integral can only be solved analytically for very simple cases. The factor $N!$ in the denominator is because the particles are indistinguishable, and the factor h^{3N} comes from the requirement that the quantum mechanical partition function approaches the classical partition function given here. The thermodynamic beta is $\beta = (k_\mathrm{B} T)^{-1}$, k_B is Boltzmann's constant, and h is Planck's constant. The exponential $\exp(-\beta \mathcal{H})$ is known as the Boltzmann factor and is proportional to the probability for a system to be in the given state. The internal energy in the canonical ensemble is the ensemble average of the Hamiltonian

$$\begin{aligned} U &= \frac{1}{Z} \frac{1}{h^{3N} N!} \int_{-\infty}^{\infty} \cdots \int_{-\infty}^{\infty} \mathcal{H} \exp(-\beta \mathcal{H}) \mathrm{d}\boldsymbol{p}_1 \ldots \mathrm{d}\boldsymbol{p}_N \mathrm{d}\boldsymbol{r}_1 \ldots \mathrm{d}\boldsymbol{r}_N = \langle \mathcal{H} \rangle \\ &= -\frac{\partial \ln Z}{\partial \beta}. \end{aligned} \tag{2.26}$$

which can be simplified to the derivative of the logarithm of the canonical partition function with respect to the thermodynamic beta. The ensemble average is denoted with angle brackets $\langle \ldots \rangle$. From the definition of the Helmholtz energy from thermodynamics, one can show that the Helmholtz energy is related to the canonical partition function

$$A = -k_\mathrm{B} T \ln Z. \tag{2.27}$$

2.2.1 Ensemble transformations

The isothermal-isobaric partition function can be obtained from a Laplace transform of the canonical partition function

$$\Delta = \int_0^{\infty} Z \exp(-\beta p V) \mathrm{d}V, \tag{2.28}$$

where the Gibbs energy is

$$G = -k_\mathrm{B} T \ln \Delta. \tag{2.29}$$

Correspondingly, the grand canonical partition function can also be obtained from a Laplace transform of the canonical partition function. However, in this case with the chemical potential and number of particles as variables,

$$\Xi = \int_0^{\infty} Z \exp(-\beta \mu N) \mathrm{d}N, \tag{2.30}$$

where the grand potential is

$$\Omega = -k_{\mathrm{B}}T \ln \Xi. \tag{2.31}$$

The identification of the Gibbs energy and grand potential comes from thermodynamics.

Laplace transform

The Laplace transform of a function $f = f(t)$ is

$$F(s) = \int_0^\infty f(t) \exp(-st) \mathrm{d}t. \tag{2.32}$$

By introducing the Gibbs energy and Helmholtz energy into the Laplace transform of the canonical partition function to the isothermal-isobaric partition function we obtain

$$\exp(-\beta G) = \int_0^\infty \exp(-\beta(A + pV)) \mathrm{d}V. \tag{2.33}$$

If the variance of the pressure in the canonical ensemble is sufficiently small we can use the saddlepoint approximation, and the expression can be simplified to [2,3,53]

$$G = \min(A + pV). \tag{2.34}$$

This is known as the Legendre-Fenchel transform [1]. If the Helmholtz energy is convex, this reduces to the familiar Legendre transform $G = A + pV$. Similar transformations can be done for the enthalpy and grand potential, and other free energies.

Legendre-Fenchel transform

The Legendre-Fenchel transform of a differentiable function $f = f(t)$ is

$$F(s) = \max_s [f(t) - ft] \tag{2.35}$$

In article VII we investigate the free energy transform of a single-phase fluid in a slit pore with controlled width to controlled normal pressure. We show that the transformation must be done with the Legendre-Fenchel transform, and not the Legendre transform when the system is sufficiently small. This is because the Helmholtz energy is non-convex. Bering *et al.* have shown that the free energy of

a short polymer stretched is non-convex when stretched with controlled length [3]. Similarly, aggregating nanoparticles in solution have non-convex free energy as a function of nanoparticle separation [4, 54, 55]. In these cases, one must therefore apply the Legendre-Fenchel transform to obtain the transformed free energy.

Statistical mechanics can undoubtedly describe nanosized systems in a way that classical thermodynamics can not, as statistical mechanics starts with particle momenta and interactions with the Hamiltonian. This requires complete information about the Hamiltonian. However, statistical mechanics does not give the framework of thermodynamics and is therefore not sufficient. In the next section, we shall see that nanothermodynamics can give the thermodynamic framework of nanosized systems in an original and general manner.

2.3 Nanothermodynamics

Nanothermodynamics [24] is also known as thermodynamics of small systems, and was developed by Terrell Hill (1917-2014). The book `Thermodynamics of small systems. Part I` by Hill was published in 1963 [56], in the following year he published part II. In the early 2000s he published several papers on the topic [57–60]. Hill set to solve the issue that the internal energy is not necessarily Euler homogeneous of the first order for small systems. This problem was solved by instead of describing one small system, he described a large ensemble of non-interacting small systems. The single system is small, but the ensemble is large.

Hill imagined the large ensemble of small systems to be for example a dilute solution of colloids, such that each colloid is a small system. Each small system has internal energy, entropy, volume, and a number of particles of each component. By introducing the ensemble of small systems the number of small systems and the subdivision potential is introduced as a new set of conjugate variables. Figure 2.1 illustrates the process of changing the number of small systems. The energy required to add one more small system to the ensemble of systems, while keeping the total internal energy, entropy, volume, and the number of particles of each component, is the subdivision potential. In this section, I describe the nanothermodynamic procedure in general and afterward apply it to fluids in porous media.

2.3.1 The nanothermodynamic procedure

The internal energy of the ensemble of small systems is a function of the total entropy S_t, total volume V_t, the total number of particles of each component i

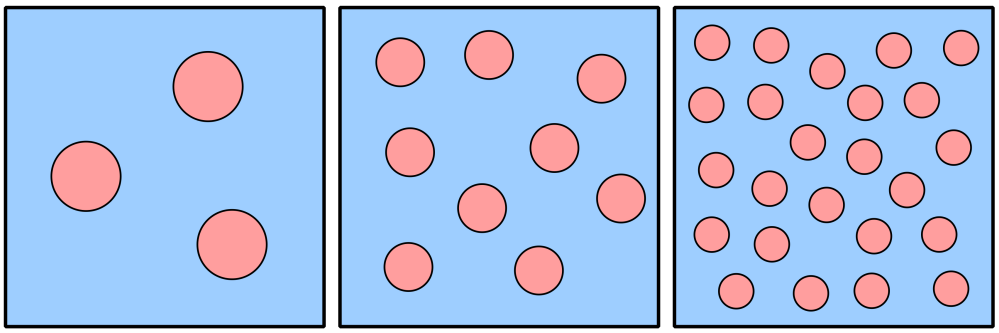

Figure 2.1: Illustration of an ensemble of spherical colloids, where each colloid (red circle) is considered a small system. The number of small systems increases from left to right, while keeping the total entropy S_t, total volume V_t, and the total number of particles of each component $N_{t,i}$ constant.

$N_{t,i}$, and the number of small systems $\mathcal{N}$,

$$U_t = U_t(S_t, V_t, \boldsymbol{N}_t, \mathcal{N}). \tag{2.36}$$

The exact differential of the total internal energy of an ensemble of small systems is

$$\begin{aligned} \mathrm{d}U_t(S_t, V_t, \boldsymbol{N}_t, \mathcal{N}) = &\left(\frac{\partial U_t}{\partial S_t}\right)_{V_t, \boldsymbol{N_t}, \mathcal{N}} \mathrm{d}S_t + \left(\frac{\partial U_t}{\partial V_t}\right)_{S_t, \boldsymbol{N_t}, \mathcal{N}} \mathrm{d}V_t \\ &+ \sum_{i=1}^{C} \left(\frac{\partial U_t}{\partial \boldsymbol{N_t}}\right)_{S_t, V_t, N_{t,j\neq i}, \mathcal{N}} \mathrm{d}\boldsymbol{N_t} + \left(\frac{\partial U_t}{\partial \mathcal{N}}\right)_{S_t, V_t, \boldsymbol{N_t}} \mathrm{d}\mathcal{N}, \end{aligned} \tag{2.37}$$

where the subscript t denotes that it is the total internal energy, entropy, volume, and the number of particles of the ensemble of small systems. The temperature, pressure, and chemical potential are defined similarly as in Gibbs thermodynamics,

$$\begin{aligned} T &:= \left(\frac{\partial U_t}{\partial S_t}\right)_{V_t, \boldsymbol{N_t}, \mathcal{N}}, \\ p &:= -\left(\frac{\partial U_t}{\partial V_t}\right)_{S_t, \boldsymbol{N_t}, \mathcal{N}}, \\ \mu_i &:= \left(\frac{\partial U_t}{\partial \boldsymbol{N_t}}\right)_{S_t, V_t, N_{t,j\neq i}, \mathcal{N}}. \end{aligned} \tag{2.38}$$

The subscripts indicate which variables are kept constant during differentiation. With the introduction of the number of small systems $\mathcal{N}$, the subdivision potential ε is introduced as a new conjugate variable. It is defined as

$$\varepsilon := \left(\frac{\partial U_t}{\partial \mathcal{N}}\right)_{S_t, V_t, \boldsymbol{N_t}}. \tag{2.39}$$

This is the energy required to add one more small system to the ensemble of systems while keeping the total entropy, volume, and the number of particles constant. This is a general type of work, which can include the work of stretching or bending a surface. The advantage of this description of work is that it describes all types of work, without explicitly defining variables such as lines, points, curvatures, and so on. The internal energy is an Euler homogeneous function of the first order, which means that we can write it as

$$U_t(S_t, V_t, \boldsymbol{N}_t, \mathcal{N}) = TS_t - pV_t + \boldsymbol{\mu} \cdot \boldsymbol{N}_t + \varepsilon \mathcal{N}. \tag{2.40}$$

So far I have described the total internal energy of an ensemble of small systems, however, we usually want to describe a single small system in a specific ensemble. As an example to clarify the procedure, I will describe a single-phase and single-component system in the canonical ensemble. The procedure is as follows.

1. Choose additive variables that describe the ensemble of small systems and the desired control variables for the single small system. The control variables must be represented in terms of the additive variables. In this example we choose the additive variables S_t, V_t, N_t, and $\mathcal{N}$ and control variables $T, V = V_t/\mathcal{N}$, and $N = N_t/\mathcal{N}$.

2. Replace the total additive variable with the average additive variable for the variables that are not transformed and introduce them to the exact differential of the total internal energy. In this example, we wish to transform the free energy to be a function of the temperature in place of the entropy. We introduce the average additive variables of the other variables $V_t = V\mathcal{N}$ and $N_t = N\mathcal{N}$ into the exact differential of the total internal energy

$$\mathrm{d}U_t = T\mathrm{d}S_t - p\mathcal{N}\mathrm{d}V + \mu\mathcal{N}\mathrm{d}N + (\varepsilon - pV + \mu N)\mathrm{d}\mathcal{N}. \tag{2.41}$$

   The terms in the parentheses in the last term defines the replica energy of the ensemble,

$$X(T, V, N) := \varepsilon - pV + \mu N. \tag{2.42}$$

   In this example, we can identify the replica energy as the Helmholtz energy.

3. Introduce the average additive properties and divide the total internal energy by the number of small systems. From this, we obtain the internal energy of a single small system. In this example, we have $U_t = U\mathcal{N}$ and $S_t = S\mathcal{N}$ in addition to the previously stated averages. From this, we obtain the average internal energy of one small system,

$$\begin{aligned} U = \frac{U_t}{\mathcal{N}} &= \frac{1}{\mathcal{N}}\left(TS_t - pV_t + \mu N_t + \varepsilon\mathcal{N}\right) \\ &= TS - pV + \mu N + \varepsilon \\ &= TS + X(T, V, N). \end{aligned} \tag{2.43}$$

   This is a Legendre transform of the internal energy to the replica energy, see equation 2.23.

4. Introduce the remaining average additive properties into the exact differential of the total internal energy in equation 2.41 and collect terms,

$$\mathcal{N}\mathrm{d}U = T\mathcal{N}\mathrm{d}S - p\mathcal{N}\mathrm{d}V + \mu\mathcal{N}\mathrm{d}N + (X + TS - U)\mathrm{d}\mathcal{N} \tag{2.44}$$

   In the previous step, we found the terms in the parentheses in the last term to be zero. By dividing this equation with the number of small systems we obtain the exact differential of the internal energy of one small system,

$$\mathrm{d}U(S, V, N) = T\mathrm{d}S - p\mathrm{d}V + \mu\mathrm{d}N. \tag{2.45}$$

   The internal energy of the single system is not necessarily Euler homogeneous of the first order, it is only the total internal energy of the ensemble that is Euler homogeneous of the first order.

5. Finally, we find the exact differential of the replica energy

$$\mathrm{d}X(T, V, N) = -S\mathrm{d}T - p\mathrm{d}V + \mu\mathrm{d}N. \tag{2.46}$$

   With this equation, we can obtain relations between the thermodynamic properties of a small system. The difference between the replica energy and the free energy is that the replica energy is defined in terms of the subdivision potential and its additive properties and not the Legendre transform.

2.3.2 Subdivision potential

We started with the set of additive variables $S_t, V_t, \boldsymbol{N}_t, \mathcal{N}$ in equation 2.37, but other choices of additive variables are also possible. Changing the set of additive

variables changes the definitions of the conjugate variables. For example, with the set of variables $S_t, V_t, a_t, \boldsymbol{N}_t, \mathcal{N}$, where a_t is the total surface area, the subdivision potential is defined as

$$\varepsilon := \left(\frac{\partial U_t}{\partial \mathcal{N}}\right)_{S_t, V_t, a_t, \boldsymbol{N_t}}. \tag{2.47}$$

This may seem like an insignificant difference from the previous definition of the subdivision potential in equation 2.39. However, this can be understood as extracting the work of stretching a surface from the term $\varepsilon \mathrm{d}\mathcal{N}$ and placing it into the new term $\gamma \mathrm{d}a_t$, where

$$\gamma := \left(\frac{\partial U_t}{\partial a_t}\right)_{S_t, V_t, \boldsymbol{N_t}, \mathcal{N}} \tag{2.48}$$

is the surface tension. Another way to view it is that the term $\varepsilon \mathrm{d}\mathcal{N}$ collects any work that can be done on the system which is not described by the other control variables. The definition of the subdivision potential changes accordingly. In this way, the total internal energy is Euler homogeneous of the first order. For simple systems where the other control variables completely describe the system the subdivision potential is zero. In this work, we have observed that for systems encountered in the field of porous media research the subdivision potential will be an important part of the description.

2.3.3 Integral pressure

For the control variables T, V, and μ the system is in the grand canonical ensemble. By following the nanothermodynamic procedure described above with S_t, V_t, N_t, and $\mathcal{N}$ as an additive variable, we obtain the replica energy

$$X(T, V, \mu) = \varepsilon - pV. \tag{2.49}$$

This is equal to the grand potential. The exact differential of the replica energy is

$$\mathrm{d}X(T, V, \mu) = -S\mathrm{d}T - p\mathrm{d}V - N\mathrm{d}\mu. \tag{2.50}$$

Hill defined a new pressure, namely the integral pressure, as the replica energy divided by volume,

$$\hat{p} := -\frac{X}{V} = p - \frac{\varepsilon}{V}. \tag{2.51}$$

The integral pressure $\hat{p}$ is different from the differential pressure p for non-zero subdivision potentials. The name integral and differential pressure was coined by

Hill and reflects the fact that they are integral and differential properties. The differential pressure is related to the integral pressure by

$$p = -\left(\frac{\partial X}{\partial V}\right)_{T,\mu} = \hat{p} + V\left(\frac{\partial \hat{p}}{\partial V}\right)_{T,\mu}. \tag{2.52}$$

From this equation, we conclude that the differential and integral pressures are equal when the integral pressure does not depend on the volume. This must also imply that the subdivision potential is zero. A system is large when the differential and integral pressures are equal.

For porous media, there can be multiple bulks, surfaces, and contact lines. The grand potential is additive, meaning that we can attribute energy contributions from each bulk phase, each surface, and each line. This can consequently also be done for the integral pressure. In general, the integral pressure is

$$\hat{p} = \frac{1}{V}\left(\sum_{\alpha=1}^{m} p_\alpha V_\alpha - \sum_{\alpha=1}^{m}\sum_{\beta>\alpha}^{m} \gamma_{\alpha\beta} a_{\alpha\beta} - \sum_{\alpha=1}^{m}\sum_{\beta>\alpha}^{m}\sum_{\delta>\beta}^{m} \tau_{\alpha\beta\delta} L_{\alpha\beta\delta} - \varepsilon\right), \tag{2.53}$$

where m are the number of phases, and$\tau_{\alpha\beta\delta}$ and $L_{\alpha\beta\delta}$ are the line tension and line length of the three-phase line between the α-, β-, and δ-phases, respectively. In general, the line energy is very small compared to the bulk and surface energy and can be neglected [54]. We incorporate the subdivision potential into the pressures and surface tensions,

$$\hat{p} = \frac{1}{V}\left(\sum_{\alpha=1}^{m} \hat{p}_\alpha V_\alpha - \sum_{\alpha=1}^{m}\sum_{\beta>\alpha}^{m} \hat{\gamma}_{\alpha\beta} a_{\alpha\beta}\right), \tag{2.54}$$

where the integral pressure of phase α is $\hat{p}_\alpha$ and the integral surface tension of the $\alpha\beta$-surface is $\hat{\gamma}_{\alpha\beta}$. For small systems, the integral pressures and surface tensions differ from the differential properties. For a two-phase fluid of a wetting fluid w and non-wetting fluid nw in a porous medium, the integral pressure is

$$\begin{aligned}\hat{p} =& \hat{p}_w \phi S_w + \hat{p}_{nw}\phi(1 - S_w) + \hat{p}_s(1-\phi) \\ &- \hat{\gamma}_{w,nw}\frac{a_{w,nw}}{V} - \hat{\gamma}_{w,s}\frac{a_{w,s}}{V} - \hat{\gamma}_{nw,s}\frac{a_{nw,s}}{V},\end{aligned} \tag{2.55}$$

where the line tensions are neglected. The porosity is the fraction of pore volume to the total volume, defined as $\phi := (V_w + V_{nw})/V$. The wetting saturation is defined as the fraction of volume of wetting fluid to the pore volume, defined as $S_w := V_w/(V_w + V_{nw})$.

2.3.4 Single-phase fluid in an open slit pore

The slit pore with a single-phase and -component fluid is a simple porous medium. It has two parallel stiff walls separated by a distance h, and the volume of a slit pore is $V = ah/2$, where a is the surface area. The representative elementary volume (REV) of this system is a volume that spans the height h of the slit pore. This system was investigated in articles V, VI, and VII. In this subsection, I emphasize the impact of the various choices for additive variables.

A valid choice of additive variables for this system are S_t, V_t, N_t, and $\mathcal{N}$, but other choices are also valid. An open thermodynamic system can exchange particles and energy with the environment, which means that the energy and number of particles can fluctuate. The control variables are then T, V, and μ. The exact differential of the total internal energy is

$$\mathrm{d}U_t(S_t, V_t, N_t, \mathcal{N}) = T\mathrm{d}S_t - p\mathrm{d}V_t + \mu\mathrm{d}N_t + \varepsilon\mathrm{d}\mathcal{N}. \tag{2.56}$$

The temperature, pressure, chemical potential, and subdivision potential are defined as

$$T := \left(\frac{\partial U_t}{\partial S_t}\right)_{V_t,N_t,\mathcal{N}}, \qquad p := -\left(\frac{\partial U_t}{\partial V_t}\right)_{S_t,N_t,\mathcal{N}}, \tag{2.57}$$

$$\mu := \left(\frac{\partial U_t}{\partial N_t}\right)_{S_t,V_t,\mathcal{N}}, \qquad \varepsilon := \left(\frac{\partial U_t}{\partial \mathcal{N}}\right)_{S_t,V_t,N_t}. \tag{2.58}$$

To obtain the desired control variables, we must transform the entropy to temperature and the number of particles to chemical potential. We do this by introducing the total volume $V_t = V\mathcal{N}$,

$$\mathrm{d}U_t(S_t, V_t, N_t, \mathcal{N}) = T\mathrm{d}S_t - p\mathcal{N}\mathrm{d}V + \mu\mathrm{d}N_t + (\varepsilon - pV)\mathrm{d}\mathcal{N}. \tag{2.59}$$

We define the last term as the replica energy,

$$X := \varepsilon - pV. \tag{2.60}$$

The internal energy is

$$U = TS + \mu N + X \tag{2.61}$$

and the exact differential of the internal energy is

$$\mathrm{d}U(S, V, N) = T\mathrm{d}S - p\mathrm{d}V + \mu\mathrm{d}N. \tag{2.62}$$

The exact differential of the replica energy is then

$$\mathrm{d}X(T, V, \mu) = -S\mathrm{d}T - p\mathrm{d}V - N\mathrm{d}\mu. \tag{2.63}$$

Since this is an exact differential, we can identify the entropy, pressure, and number of particles as

$$S = -\left(\frac{\partial X}{\partial T}\right)_{V,\mu}, \quad p = -\left(\frac{\partial X}{\partial V}\right)_{T,\mu}, \quad N = -\left(\frac{\partial X}{\partial \mu}\right)_{T,V}. \tag{2.64}$$

From this, we can investigate the subdivision potential by introducing the definition of the pressure into the replica energy, and obtain

$$\varepsilon = X - V\left(\frac{\partial X}{\partial V}\right)_{T,\mu}. \tag{2.65}$$

The volume of a slit pore can change in two ways, either by changing the distance between the plates h or the size of the plates a.

$$\varepsilon = X - h\left(\frac{\partial X}{\partial h}\right)_{T,\mu,a} - a\left(\frac{\partial X}{\partial a}\right)_{T,\mu,h}. \tag{2.66}$$

By introducing the definition of the integral pressure $\hat{p} := -X/V$ we obtain

$$\varepsilon = \hat{p}V + hV\left(\frac{\partial \hat{p}}{\partial h}\right)_{T,\mu,a} + aV\left(\frac{\partial \hat{p}}{\partial a}\right)_{T,\mu,h}. \tag{2.67}$$

In article VI, we show that for large heights h the pressure is constant and as a consequence, the subdivision potential with this definition is also constant. For small heights, the pressure oscillates as a function of the height with a period equal to the diameter of the fluid particle size. This is known as the disjoining or solvation pressure [61,62]. With this definition, the subdivision potential must be non-zero when the disjoining pressure is non-zero.

Surface area as a variable

We made an arbitrary choice for the additive variables. If we add the total surface area a_t to the set of additive variables, the control variables are T, V, a, and μ. We can do this because for a slit pore we can vary the volume while keeping the surface area constant, and vice versa. The additive variables are independent. The subdivision potential for this set of additive variables is defined as

$$\varepsilon := \left(\frac{\partial U_t}{\partial \mathcal{N}}\right)_{S_t,V_t,a_t,N_t}. \tag{2.68}$$

The total volume and the total surface area are kept constant during differentiation. In the previous definition, only the volume was kept constant during differentiation. The replica energy is defined as

$$X := \varepsilon - pV + \gamma a, \tag{2.69}$$

and the exact differential of the replica energy is

$$\mathrm{d}X(T,V,a,\mu) = -S\mathrm{d}T - p\mathrm{d}V + \gamma\mathrm{d}a - N\mathrm{d}\mu \tag{2.70}$$

where we can identify the pressure and surface tension as

$$p = -\left(\frac{\partial X}{\partial V}\right)_{T,a,\mu} \quad \text{and} \quad \gamma = \left(\frac{\partial X}{\partial a}\right)_{T,V,\mu}. \tag{2.71}$$

To get information about the subdivision potential we introduce the pressure and surface tension into the replica energy and reorganize

$$\varepsilon = X - V\left(\frac{\partial X}{\partial V}\right)_{T,a,\mu} - a\left(\frac{\partial X}{\partial a}\right)_{T,V,\mu}. \tag{2.72}$$

The only way to change the volume while keeping both the surface area and shape constant is to change the height h. To change the surface area while keeping the volume constant, the slit pore must be deformed in two steps. First, the surface area is deformed at a constant height, then the height is deformed at a constant surface area, while the total change in volume is zero. We rewrite the partial derivatives in terms of the height and surface area and obtain

$$\varepsilon = X - a\left(\frac{\partial X}{\partial a}\right)_{T,h,\mu}, \tag{2.73}$$

where the derivatives in terms of the height have been canceled. By defining the integral pressure $\hat{p} := -X/V$ and introducing this, we find

$$\varepsilon = aV\left(\frac{\partial \hat{p}}{\partial a}\right)_{T,\mu,h}. \tag{2.74}$$

Since the height derivative term has been canceled, this entails that the subdivision potential does not depend on the height. The subdivision is zero for any height, given that the surface area is large.

Height as a variable

If we substitute the volume with the height in the set of additive variables, such that the additive variables are S_t, h_t, a_t, N_t, and $\mathcal{N}$, and the control variables are T, h, a, and μ we have yet another definition of the subdivision potential,

$$\varepsilon := \left(\frac{\partial U_t}{\partial \mathcal{N}}\right)_{S_t,h_t,a_t,N_t}. \tag{2.75}$$

With this definition, the total height is kept constant instead of the total volume. The definition of replica energy is the same

$$X := \varepsilon - pV + \gamma a, \tag{2.76}$$

while the exact differential of the replica energy is

$$\mathrm{d}X(T, V, a, \mu) = -S\mathrm{d}T - \frac{pa}{2}\mathrm{d}h + \gamma \mathrm{d}a - N\mathrm{d}\mu. \tag{2.77}$$

We can identify the pressure and surface tension as

$$p = -\frac{2}{a}\left(\frac{\partial X}{\partial h}\right)_{T,a,\mu} \quad \text{and} \quad \gamma = \left(\frac{\partial X}{\partial a}\right)_{T,h,\mu}. \tag{2.78}$$

By introducing these definitions and the integral pressure $\hat{p} := -X/V$ to the replica energy and reorganizing, we obtain

$$\varepsilon = \hat{p}V + hV\left(\frac{\partial \hat{p}}{\partial h}\right)_{T,\mu,a} + aV\left(\frac{\partial \hat{p}}{\partial a}\right)_{T,\mu,h}. \tag{2.79}$$

This gives the same relation as the control variable set T, V, and μ.

There are many valid choices for the additive variables and it is indeed a choice. However, some choices are better than others, sets that give minimal description are preferable. In the latter example, the additive variables S_t, V_t, a_t, N_t, and $\mathcal{N}$ define the subdivision potential such that the system is only small when the surface area is small. For this reason, this set of additive variables is preferred and was the one used in article VI. The definition of the conjugate variables depends on the set of additive variables, the subdivision potentials between the sets of variables can't be compared. In general, we are interested in quantifying the subdivision potential, as this will give a measure of the smallness of the system.

Another reason to not choose height as a variable is because the definition of the surface tension will be very uncommon. This can be seen by introducing the integral pressure into the surface tension,

$$\gamma(T, h, a, \mu) = -\frac{\hat{p}h}{2} - V\left(\frac{\partial \hat{p}}{\partial a}\right)_{T,\mu,h}. \tag{2.80}$$

For large heights h, the integral pressure approaches the differential pressure, but from the first part of this equation, it is clear that the surface tension decreases with a slope equal to $\hat{p}/2$ as the height increases. This is very counterintuitive, as one would expect the surface tension to approach a constant for increasing heights. This set of control variables should therefore be avoided. With the volume and

surface area as control variables, the definition of the surface tension gives the equation

$$\gamma(T,V,a,\mu) = -\frac{h^2}{2}\left(\frac{\partial\hat{p}}{\partial h}\right)_{T,\mu,a} - V\left(\frac{\partial\hat{p}}{\partial a}\right)_{T,\mu,a}. \tag{2.81}$$

This is the usual form of surface tension. The only difference is that in the equation 2.80, the height is kept constant in the definition of the surface tension, while in equation 2.81 the volume is kept constant.

Similar procedures can be done to determine the subdivision potential for pipes, where the volume, surface area, radius, or length are sensible control variable choices to describe the geometry. Maximum two of these can be chosen at a time. By doing the same procedure as for the slit pore, we find that volume and surface area are the control variables that give the minimal description of the subdivision potential. For this reason, we have chosen volume and surface area instead of other geometrical variables.

For a spherical geometry, there is only one degree of freedom, namely the radius. In this case, one must choose either the volume, surface area, or radius as a control variable. Strøm and co-authors have investigated nanothermodynamic descriptions of adsorptions on spherical surfaces using the volume as a control variable [63], and surface area as a control variable [64].

2.4 Non-equilibrium thermodynamics

Non-equilibrium thermodynamics extends thermodynamics to describe systems out of equilibrium, which has been used to describe transport in porous media in the articles in this thesis. Lars Onsager (1903-1976) is considered to be the founder of the field with his papers from 1931 [25,26]. de Groot and Mazur have written a thorough description of non-equilibrium thermodynamics [27], and Kjelstrup and Bedeaux have extended this with a description for heterogeneous media [65]. In non-equilibrium thermodynamics, the entropy production and flux-force relations of a system are derived. This can be used to model coupled transport processes in porous media.

To obtain a complete non-equilibrium description, we need the balance equations for the entropy and other relevant additive properties. This can for example be the mass, charge, and internal energy balance equations. Depending on which forces are present in a system, different balance equations are relevant. In this thesis, only the balance equations for entropy, mass, and internal energy are nec-

essary. The entropy balance equation is,

$$\frac{\partial}{\partial t}s(x,t) = -\frac{\partial J_s}{\partial x} + \sigma, \tag{2.82}$$

where $s(x,t) = S/V$ is the entropy density of the volume element, J_s is the entropy flux, and σ is the entropy production. The entropy production has SI units J/m^{3}sK and is the entropy produced in the volume element. This is caused by the system being out of equilibrium and as the second law of thermodynamics states, $\sigma \geq 0$.

In the case when the entropy, S, volume, V, and mass, M_i of each component i are the set of additive variables, the exact differential of the entropy density is the local form of Gibb's equation,

$$\mathrm{d}s = \frac{1}{T}\mathrm{d}u - \frac{1}{T}\sum_{i=1}^{C}\mu_i \mathrm{d}\rho_i. \tag{2.83}$$

Where $u = U/V$ is the internal energy density, $\rho_i = M_i/V$ is the mass density of component i, and C is the number of components. By using this equation, we assume the system to be in local equilibrium. There is evidence for the assumption of local equilibrium to hold for chemical reactions in temperature gradients [66], in two-phase systems [67, 68], and even in shock waves [69, 70]. However, it is far unknown if local equilibrium holds for the REV. By introducing the Gibbs equation to the entropy balance we obtain

$$\frac{\partial}{\partial t}s(x,t) = \frac{1}{T}\frac{\partial u}{\partial t} - \frac{1}{T}\sum_{i=1}^{C}\mu_i\frac{\partial \rho_i}{\partial t}. \tag{2.84}$$

For non-reacting neutral components, the internal energy and mass balances are

$$\frac{\partial}{\partial t}u(x,t) = -\frac{\partial J_u}{\partial x} \quad \text{and} \quad \frac{\partial}{\partial t}\rho_i(x,t) = -\frac{\partial J_i}{\partial x}. \tag{2.85}$$

where J_u is the internal energy flux and J_i is the ith mass flux. We use these equations to obtain the entropy flux and entropy production. This is done by introducing the energy and mass balance into the entropy balance equation,

$$\frac{\partial}{\partial t}s(x,t) = -\frac{\partial}{\partial x}\left[\frac{1}{T}\left(J_u - \sum_{i=1}^{C}\mu_i J_i\right)\right] + J_u\frac{\partial}{\partial x}\left(\frac{1}{T}\right) - \sum_{i=1}^{C}\frac{\partial}{\partial x}J_i\left(\frac{\mu_i}{T}\right). \tag{2.86}$$

Where the product rule on the form $gf' = (fg)' - fg'$ has been used. In this equation, we can identify the entropy flux as

$$J_s(x,t) = \frac{1}{T}\left(J_u - \sum_{i=1}^{C}\mu_i J_i\right) \tag{2.87}$$

and the entropy production as

$$\sigma(x,t) = J_u \frac{\partial}{\partial x}\left(\frac{1}{T}\right) - \sum_{i=1}^{C} J_i \frac{\partial}{\partial x}\left(\frac{\mu_i}{T}\right) \tag{2.88}$$

Other variables and effects may also come into the Gibbs equation and balance equations.

In general, the second law of thermodynamics is a sum of the flux-force products

$$\sigma = \sum_{i=1}^{n} J_i X_i \geq 0, \tag{2.89}$$

where J_i are independent fluxes, X_i are the conjugate forces, and n is the number of flux-force conjugate pairs. The flux-force conjugate pair can be for example the internal energy flux J_u and gradient of the inverse temperature $\partial T^{-1}/\partial x$. So far, the only assumption has been local equilibrium. The next assumption needed is a relation between the fluxes and forces. A common assumption is that the fluxes J_i are linear combinations of all forces X_j,

$$J_i = \sum_{j=1}^{n} L_{ij} X_j, \tag{2.90}$$

where L_{ij} are the transport coefficients for transport, which must be obtained from experiments or simulations. Onsager proved that the coefficient matrix is symmetric $L_{ij} = L_{ji}$ [25,26]. In 1968 he was awarded the Nobel Prize in Chemistry for this discovery. In articles I and II, we use this to derive the entropy production and flux-force equations of a non-isothermal two-phase fluid in a REV. In article IX, we use the equations from articles I and II to simulate single-phase flow in porous medium and to calculate the permeability.

Chapter 3

Molecular simulations

Molecular simulations have been the tools to investigate assumptions in the thermodynamic theories of fluids in porous media. Molecular dynamics (MD) and Monte Carlo (MC) simulations are computational techniques to simulate individual atoms, molecules, or collections of atoms. They are particle-based, where each particle has a mass and position. In MD the particle also has a velocity. The particles interact with an interaction potential that depends on the particle positions. The particles in molecular simulations can make up complex structures such as proteins [71, 72], DNA [73, 74], viruses [75–77], and much more. However, molecular simulations are computationally expensive techniques, meaning that the timescale and system size are limited. The most advanced simulations can simulate 10^{12} particles for 0.6 ns [78]. Molecular simulations are suitable to investigate a wide range of questions such as CO_2 sequestration in metal-organic frameworks [9, 13, 14] or water transport in carbon nanotubes [79]. It has a close relationship to thermodynamics and is well suited to investigate thermodynamic relations.

3.1 Molecular dynamics

In molecular dynamics, the particle positions and velocities are iteratively updated based on the total force acting on each particle. Symbols in bold represent vectors. Particle i is iteratively assigned a new position $\boldsymbol{r}_i$ and velocity $\boldsymbol{v}_i$ based on the total force $\boldsymbol{f}_i$ acting on the particle and its mass m_i. This is done by numerically integrating Newton's second law [80, 81]. Symbols in bold are vectors. The force

acting on particle i due to all other particles j is

$$\boldsymbol{f}_i(\boldsymbol{r}_i) = -\sum_{\substack{j=1 \\ j\neq i}}^{N} \boldsymbol{f}_{ij}(\boldsymbol{r}_{ij}), \tag{3.1}$$

where the sum is over all other particles j and $\boldsymbol{f}_{ij}(\boldsymbol{r}_{ij})$ is the force acting on particle i due to particle j, and $\boldsymbol{r}_{ij} = \boldsymbol{r}_j - \boldsymbol{r}_i$ is the vector from particle i to j. The pair-wise force is obtained from the pair-wise interaction potential,

$$\boldsymbol{f}_{ij}(\boldsymbol{r}_{ij}) = -\frac{\partial u(r_{ij})}{\partial \boldsymbol{r}_{ij}}. \tag{3.2}$$

The pair-wise interaction $u(r_{ij})$ is in this case rotational spherical symmetric; it only depends on the distance $r_{ij} = |\boldsymbol{r}_{ij}|$ and not the relative orientations of the particle pair. The pair-wise interaction $u(r_{ij})$ determines the nature of the particles. This can model for example Coulomb interactions, bond, and torsional angles, Pauli repulsion, and more. In this work, we have used variations of the Lennard-Jones potential [82] which models Pauli repulsion due to overlapping electron orbitals and London dispersion forces.

The first step of an MD program is to initialize the particle positions and velocities. The particle positions can for example be initialized by being placed in a regular lattice. The velocities are typically initialized by assigning a velocity to a particle from a Maxwell-Boltzmann distribution.

The velocity Verlet algorithm has been used in this work to numerically integrate Newton's second law [83]. This algorithm is a further development of Verlet integration [84], which is named after and applied to MD by the french physicist Loup Verlet (1931-2019). The cumulative errors in position and velocity from the velocity Verlet algorithm are $\mathcal{O}(\Delta t^2)$. The positions, accelerations, and velocities of particle i at timestep $t + \Delta t$ is calculated as follow

1. Calculate positions

$$\boldsymbol{r}_i(t + \Delta t) = \boldsymbol{r}_i(t) + \boldsymbol{v}_i(t)\Delta t + \frac{1}{2}\boldsymbol{a}_i\Delta t^2. \tag{3.3}$$

2. Calculate accelerations

$$\boldsymbol{a}_i(t + \Delta t) = -\frac{1}{m_i}\sum_{\substack{j=1 \\ j\neq i}}^{N} \frac{\partial}{\partial \boldsymbol{r}_i} u_{ij}(\boldsymbol{r}_i(t + \Delta t)). \tag{3.4}$$

3. Calculate velocities

$$\boldsymbol{v}_i(t + \Delta t) = \boldsymbol{v}_i(t) + \frac{1}{2}(\boldsymbol{a}_i(t) + \boldsymbol{a}_i(t + \Delta t))\Delta t. \tag{3.5}$$

3.2 Monte Carlo

Monte Carlo methods are a class of computational algorithms to obtain numerical averages by random sampling. The name refers to the randomness in the casinos of Monte Carlo. Monte Carlo has been used in statistical physics to calculate ensemble averages of thermodynamic properties. The statistical mechanical background has been described in more detail in section 2.2. The ensemble average of a property A can be approximated with

$$\langle A \rangle \approx \frac{1}{n} \sum_{k=1}^{n} A_k(\boldsymbol{r}_1, \ldots, \boldsymbol{r}_N) \tag{3.6}$$

where n is the number of configurations, $A_k(\boldsymbol{r}_1, \ldots, \boldsymbol{r}_N)$ is value of a A with the particle configuration $\boldsymbol{r}_1, \ldots, \boldsymbol{r}_N$ [85]. To ensure that the configurations are drawn from the correct probability distribution. An initial configuration is generated. This can for example be a face-centered lattice of particles, and this configuration is denoted $\mathtt{o}$ (old). A trial move is then made to make a new configuration $\mathtt{n}$ (new) from the old configuration. This trial move can be for example displacing a random particle with a small random displacement Δr. This move is accepted with a probability

$$\mathrm{acc}(\mathtt{o} \to \mathtt{n}) = \exp(-\beta(\mathcal{U}(\mathtt{n}) - \mathcal{U}(\mathtt{o}))). \tag{3.7}$$

This move is accepted if a uniformly random number between 0 and 1 is less than $\mathrm{acc}(\mathtt{o} \to \mathtt{n})$, and rejected it otherwise. Trial moves are iteratively applied to the configurations until a large number of configurations are generated. From this, the ensemble average can be calculated.

3.3 Force fields

The force field, also called the interaction potential, describes the interaction between particles in molecular simulations, and as a consequence the nature of the particles. The force field can model Coulombic interactions, Pauli exclusion forces, London dispersion forces, covalent bonds, and more. In this work, we have used three variations of the Lennard-Jones (LJ) potential. We have used the truncated and shifted Lennard-Jones (LJTS), the Lennard-Jones/spline (LJ/s), and the Weeks-Chandler-Anderson (WCA) interaction potentials. The LJ potential is [82]

$$u^{\mathrm{LJ}}(r) = 4\epsilon \left[\left(\frac{\sigma}{r}\right)^{12} - \left(\frac{\sigma}{r}\right)^{6} \right], \tag{3.8}$$

where ϵ and σ characterize the interaction strength and particle size, respectively. The minimum of the interaction potential is ϵ and σ is the pair-wise separation distance r where the interaction strength is zero. The Lennard-Jones potentials are short-ranged, where the r^{-12} term models the Pauli repulsion of overlapping electron orbitals, while the r^{-6} models London dispersion forces. The truncated and shifted Lennard-Jones potential is truncated such that the potential is zero above a cut-off $r_c = 2.5\sigma$, and is shifted such that the potential is continuous,

$$u^{\mathrm{LJTS}}(r) \begin{cases} u^{\mathrm{LJ}}(r) - u^{\mathrm{LJ}}(r_c) & r \leq r_c \\ 0 & r > r_c. \end{cases} \tag{3.9}$$

The Lennard-Jones/spline fits a third-degree polynomial from the inflection point r_s of the LJ potential to the cut-off r_c

$$u^{\mathrm{LJ/s}}(r) = \begin{cases} u^{\mathrm{LJ}}(r) & \text{if } r \leq r_s, \\ a(r - r_c)^2 + b(r - r_c)^3 & \text{if } r_s < r \leq r_c, \\ 0 & \text{else.} \end{cases} \tag{3.10}$$

The parameters are fitted such that the potential, force, and the derivative of the force are continuous at the inflection point r_s. The parameters are $r_s = (26/7)^{(1/6)}\sigma$, $a = -24192/3211(\epsilon/r_s^2)$, $b = -387072/61009(\epsilon/r_s^3)$ and $r_c = (67/48)r_s$. Hafskjold *et.al.* [86] and Kristiansen [87] describe details on the properties of the Lennard-Jones/spline potential.

The Weeks-Chandler-Anderson interaction potential is

$$u^{\mathrm{WCA}}(r) = \begin{cases} u^{\mathrm{LJ}}(r) - u^{\mathrm{LJ}}(2^{1/6}) & r \leq 2^{1/6} \\ 0 & r > 2^{1/6}. \end{cases} \tag{3.11}$$

The WCA potential is only repulsive since the Lennard-Jones potential is at the minimum at $r = 2^{1/6}$.

We have used Lennard-Jones reduced units in this work to work with numbers close to unity. For example, the particle diameter is reduced units is equal to σ instead of $10^{-12}\,\mathrm{m}$. Units are reduced with the particle diameter σ, potential energy minimum ϵ, particle mass m, and the Boltzmann constant k_{B}. A full list of reduced units is shown in table 3.1. To obtain SI units values for σ and ϵ fitted to a specific material can be inserted.

Table 3.1: Properties are reduced with Lennard-Jones variables σ and ϵ, and the mass m and Boltzmann constant k_B.

Property	Symbol	Reduced form
Energy	E^*	E/ϵ
Length	L^*	L/σ
Temperature	T^*	Tk_B/ϵ
Time	t^*	$t\sqrt{\epsilon/(m\sigma^2)}$
Force	f^*	$f\sigma/\epsilon$
Density	n^*	$n\sigma^3$
Entropy	S^*	S/k_B
Pressure	p^*	$p\sigma^3/\epsilon$

3.4 Boundary conditions

To simulate a large system while minimizing computational cost, we used periodic boundary conditions. A particle close to the boundary interacts with periodic images of particles on the other side of the simulation box, and if a particle crosses the boundary, it is moved to the other end of the simulation box.

In articles IV, V, VI, and VII, we have used flat or cylindrical walls as boundary conditions, with two different implementations. In articles IV and VI, the walls were implemented as external fields with the Weeks-Chandler-Anderson and Lennard-Jones/spline potentials, as described section 3.3, and in articles V and VII, the walls were implemented by placing particles in a fcc lattice. In the first case, the wall is completely smooth, while in the second case the walls have a surface roughness. The slip conditions are not specified directly but depend on the nature of the particle-wall interaction. For an external wall potential, there will be full-slip flow (plug flow), since there is no resistance for the fluid to flow, while for a particle wall there will be partial- or no-slip flow [79, 88–90].

3.5 Ensembles

The control variables describe the connection between the system and the environment, as described in chapter 2. In molecular simulations, the environment is often imagined, and not part of the simulation. In the canonical ensemble (N, V, T), the temperature T is controlled while the internal energy U and entropy s are free to fluctuate. To control the temperature we need to use a thermostat algorithm.

Common thermostat algorithms include Langevin, Nosé-Hoover, and Berendsen. In this work, we have used a Nosé-Hoover [91, 92] style thermostat by Shinoda *et al.* [93].

In the grand canonical ensemble (μ, V, T) the chemical potential μ is controlled and the number of particles is free to fluctuate. To control the chemical potential we have used grand canonical Monte Carlo. This is done by adding or removing particles to the simulation box [80]. A particle is inserted at a random position in the simulation box with a probability

$$\mathrm{acc}(N \to N+1) = \frac{V}{\Lambda^3(N+1)} \exp[\beta(\mu - \mathcal{U}(N+1) + \mathcal{U}(N)]. \tag{3.12}$$

A random particle is removed from the simulation box with a probability

$$\mathrm{acc}(N \to N-1) = \frac{\Lambda^3(N+1)}{V} \exp[-\beta(\mu + \mathcal{U}(N-1) - \mathcal{U}(N)]. \tag{3.13}$$

Where $\Lambda = \sqrt{h^2/(2\pi m k_\mathrm{B} T)}$ is the de Broglie thermal wavelength, h is the Planck constant, $\mathcal{U}$ is the total potential energy and $\beta = 1/(k_\mathrm{B}T)$.

In article VII the isothermal-isobaric ensemble (N, p, T) was simulated, where the normal pressure p was controlled in a slit pore. This was done by applying a controlled force on the walls of the slit pore.

3.6 The mechanical pressure tensor

The pressures of heterogeneous systems have been of special interest in this work. The pressures of a fluid in a slit pore were investigated in articles IV, V, VI, VII, in a cylindrical pore in articles IV, and a REV of a porous medium in articles I, II, III, VIII, IX. The thermodynamic pressures are usually equated to components of the mechanical pressure tensor, however, it is debated how and if this should be done [38–40].

For homogeneous media, there is only one thermodynamic pressure, and the mechanical pressure tensor is isotropic, *i.e.* the diagonal components are equal. The thermodynamic pressure of a bulk fluid is equal to the mean of the diagonal components of the mechanical pressure tensor. In Cartesian coordinates it is,

$$p = \frac{1}{3}\langle \mathrm{Tr}(\mathbb{P})\rangle = \frac{1}{3}\langle P_{xx} + P_{yy} + P_{zz}\rangle. \tag{3.14}$$

To avoid confusion, the thermodynamic pressure is denoted with a lower case p, the mechanical pressure tensor with blackboard bold $\mathbb{P}$, and the mechanical

pressure tensor components with upper case $P_{\alpha\beta}$ with subscripts indicating the component. Where $P_{\alpha\beta} = \mathbb{P} \cdot (\boldsymbol{e}_\alpha^T \times \boldsymbol{e}_\beta)$, where $\boldsymbol{e}_\alpha$ and $\boldsymbol{e}_\beta$ are the unit vectors in the α- and β-directions, respectively. The Cartesian mechanical pressure tensor components are

$$\mathbb{P} = \begin{bmatrix} P_{xx} & P_{xy} & P_{xz} \\ P_{yx} & P_{yy} & P_{yz} \\ P_{zx} & P_{zy} & P_{zz} \end{bmatrix}. \tag{3.15}$$

The mechanical pressure tensor is symmetric, meaning that $P_{\alpha\beta} = P_{\beta\alpha}$. The α and β can also indicate the same direction, *i.e.* the components P_{xx}, P_{yy}, and P_{zz} are also included in the general term $P_{\alpha\beta}$.

The diagonal components are commonly assigned to thermodynamic pressures or tensions. For example in a slit pore of width h, as described in article V and VI, we equate the integral pressure to the average of the tangential pressure component, the differential pressure to the normal pressure tensor component, and the surface tension to the excess,

$$\hat{p} = \frac{1}{h}\int_0^h P_T(x)\mathrm{d}x, \quad p_\perp = P_N, \quad \text{and} \quad \gamma = \int_{x_a}^{x_b} (P_N - P_T(x))\mathrm{d}x. \tag{3.16}$$

The slit pore walls are here in the yz-plane, such that $P_T = \frac{1}{2}(P_{yy} + P_{zz})$ and $P_N = P_{xx}$. The off-diagonal components can for example be used to calculate the shear viscosity [94–96], as we did in article IX.

The method of calculating the mechanical pressure tensor used in most molecular simulations was first derived by Irving and Kirkwood in 1950. The mechanical pressure tensor can be written as a sum of a kinetic and a virial contribution [41],

$$P_{\alpha\beta} = P_{\alpha\beta}^k + P_{\alpha\beta}^v. \tag{3.17}$$

The kinetic contribution in a volume V is

$$P_{\alpha\beta}^k = \frac{1}{V}\sum_{i=1}^{N} m_i(v_{i,\alpha} - \langle v_\alpha \rangle)(v_{i,\beta} - \langle v_\beta \rangle) \tag{3.18}$$

where N is the number of particles in the volume V. This volume can be a subvolume of the total volume. The mass of particle i is m_i and $v_{i,\alpha} = \boldsymbol{v}_i \cdot \boldsymbol{e}_\alpha$ is the velocity of particle i in the α-direction. In Cartesian coordinates the velocity vector is

$$\boldsymbol{v}_i = \begin{bmatrix} v_{i,x} & v_{i,y} & v_{i,y} \end{bmatrix}. \tag{3.19}$$

The streaming velocity in the α-direction is

$$\langle v_\alpha \rangle = \frac{1}{N} \sum_{i=1}^{N} v_{i,\alpha}. \tag{3.20}$$

The mean of the diagonal components of the kinetic contribution reduces to the ideal gas law when the streaming velocity is zero, $\langle P_{\alpha\alpha} \rangle = \rho k_\mathrm{B} T$. The virial contribution to the mechanical pressure tensor in a volume V is

$$P^v_{\alpha\beta} = \sum_{i=1}^{N_t} \sum_{j>i}^{N_t} P^v_{ij,\alpha\beta}. \tag{3.21}$$

Here the sums are over all particles N_t regardless of whether they are in the volume V or not, and $P^v_{ij,\alpha\beta}$ is the virial,

$$P^v_{ij,\alpha\beta} = -\frac{f_{ij,\alpha}}{V} \int_{C_{ij} \in V} \mathrm{d}l_\beta. \tag{3.22}$$

The force acting on particle i due to particle j in the α-direction is $f_{ij,\alpha} = \boldsymbol{f}_{ij} \cdot \boldsymbol{e}_\alpha$. The curve C_{ij} can be any continuous curve that starts at the center of particle i and ends at the center of particle j. The line integral is the β-component of the curve C_{ij} that is inside the volume V. This implies that particle pairs where both particles are outside the volume can contribute to the pressure of that volume, as long as the curve C_{ij} is contained in the volume.

Schofield and Henderson showed that since any continuous curve C_{ij} from the center of particle i to the center of particle j is allowed, the mechanical pressure tensor is ambiguous [42]. Figure 3.1 shows two common choices for the curve C_{ij} in Cartesian and spherical coordinates, namely the Irving-Kirkwood and the Harasima curves. The dotted lines indicate the subvolume boundaries, the black solid line indicates a phase boundary, and the colored solid lines indicate two possible choices for the curve C_{ij}. The Irving-Kirkwood curve is the line from the center of particle i to the center of particle j. The Harasima curve is made up of three continuous curves [97]. First the line normal to the phase boundary from the center of particle i to the phase boundary, second the curve along the phase boundary, and third the line normal to the phase boundary from the phase boundary to the center of particle j. The two choices for C_{ij} contribute differently to the subvolumes, but the total contribution is the same. Harasima [97] and Schofield and Henderson [42] showed that for a sufficiently large volume, the choice of the curve does not matter. If both particle i and j are inside the volume, then

$$P^v_{ij,\alpha\beta} = -\frac{f_{ij,\alpha} r_{ij,\beta}}{V} \tag{3.23}$$

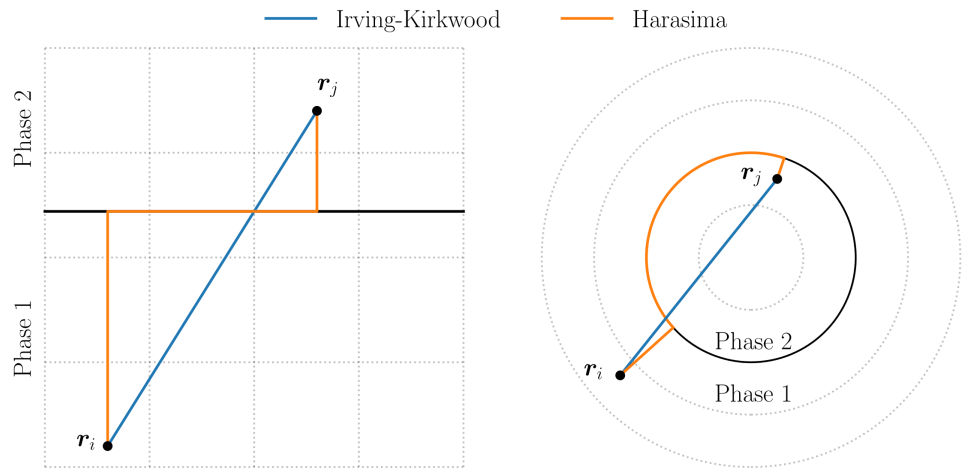

Figure 3.1: The Irving-Kirkwood and Harasima curves for calculating the virial contribution to the mechanical pressure tensor in Cartesian coordinates (left) and spherical coordinates (right).

for both the Irving-Kirkwood and the Harasima curves. Where $r_{ij,\beta} = \boldsymbol{r}_{ij} \cdot \boldsymbol{e}_\beta$ is the distance between particle i and j in the β-direction.

The mechanical pressure tensor calculation can be controlled by checking if they obey conservation of momentum at mechanical equilibrium,

$$\nabla \cdot \mathbb{P} = 0, \tag{3.24}$$

where ∇ is the differential operator. In Cartesian coordinates it is

$$\nabla = \left[\frac{\partial}{\partial x}, \quad \frac{\partial}{\partial y}, \quad \frac{\partial}{\partial z}\right]. \tag{3.25}$$

Ikeshoji and Hafskjold have shown that the mechanical pressure tensor calculated with the Irving-Kirkwood and the Harasima curves obey conservation of momentum at mechanical equilibrium in Cartesian coordinates [98]. In spherical coordinates, the mechanical pressure tensor calculated with the Irving-Kirkwood curve obeys conservation of momentum at mechanical equilibrium, while the Harasima curve does not [98]. Blokhuis and Bedeaux have also shown that the Harasima curve gives incorrect expressions for the Tolman length for spherical surfaces [99]. In this work, we have used the Irving-Kirkwood curve for all calculations of the mechanical pressure tensor.

3.6.1 Cartesian coordinates

In this subsection, the mechanical pressure tensor of a volume $V = \Delta x \Delta y \Delta z$ with the Irving-Kirkwood curve in Cartesian coordinates is described in detail. First, we define two points $\boldsymbol{a}$ and $\boldsymbol{b}$. If particle i is in the volume, then $\boldsymbol{a} = \boldsymbol{r}_i$, and if particle j is in the volume then $\boldsymbol{b} = \boldsymbol{r}_j$. If particle i is outside the volume $\boldsymbol{a}$ is the point where the curve C_{ij} enters the volume. If particle j is outside the volume $\boldsymbol{b}$ is the point where the curve exits C_{ij} the volume.

The virial contribution to the mechanical pressure tensor due to the ij particle pair with the Irving-Kirkwood curve is then

$$P^v_{ij,\alpha\beta} = -\frac{f_{ij,\alpha}(b_\beta - a_\beta)}{V}, \tag{3.26}$$

where $(b_\beta - a_\beta)$ is the length of the β-component of the curve C_{ij} that is contained in the volume. If both particles are in the volume $(b_\beta - a_\beta) = r_{ij,\beta}$, meaning that equation 3.26 reduces to equation 3.23. Figure 3.2 shows an example where particles i and j are outside the volume, but the curve C_{ij} passes through the volume. To be clear, the full tensor of the contribution due to the ij particle pair is

$$\mathbb{P}^v_{ij} = -\frac{1}{V}\begin{bmatrix} f_{ij,x}(b_x - a_x) & f_{ij,x}(b_y - a_y) & f_{ij,x}(b_z - a_z) \\ f_{ij,y}(b_x - a_x) & f_{ij,y}(b_y - a_y) & f_{ij,y}(b_z - a_z) \\ f_{ij,z}(b_x - a_x) & f_{ij,z}(b_y - a_y) & f_{ij,z}(b_z - a_z) \end{bmatrix}. \tag{3.27}$$

For flat phase boundaries in the yz-plane, the yy- and zz-components of the mechanical pressure tensor are equal. The tensor can be rewritten as a normal component $P_N = P_{xx}$ and a tangential component $P_T = (P_{yy} + P_{zz})/2$. Conservation of momentum at mechanical equilibrium states that

$$\frac{\partial P_N}{\partial x} = 0 \quad \text{and} \quad \frac{\partial P_T}{\partial y} = \frac{\partial P_T}{\partial z} = 0. \tag{3.28}$$

This means that the normal component is constant through a flat surface and that the tangential component is constant along a flat surface. We have used this fact to control the calculation of the Cartesian mechanical pressure tensor. The surface tension of a flat surface in the yz-plane can be calculated as

$$\gamma = \int_{x_a}^{x_b} (P_N - P_T) \mathrm{d}x, \tag{3.29}$$

where x_a and x_b are positioned far away from the surface on either side of it.

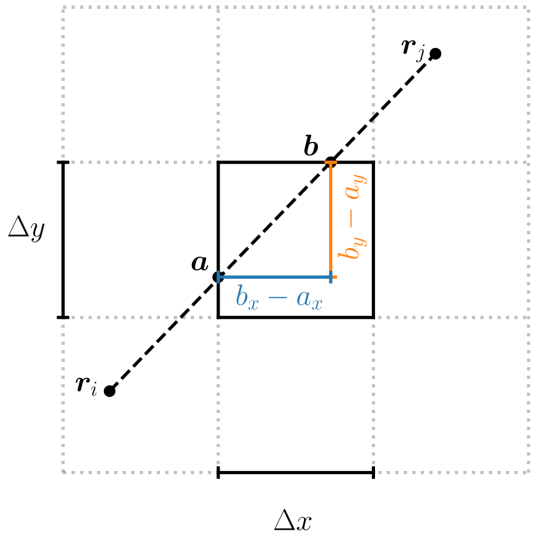

Figure 3.2: A projection of a simulation where particles i and j are outside the subvolume $V = \Delta x \Delta y \Delta z$, but the Irving-Kirkwood curve (black dashed line) is partly inside. The points $\boldsymbol{a}$ and $\boldsymbol{b}$ are the entry and exit points of the curve in the volume. The contribution to the mechanical pressure tensor is calculated from the distances $b_x - a_x$, $b_y - a_y$, and $b_z - a_z$ (not shown), see equation 3.27.

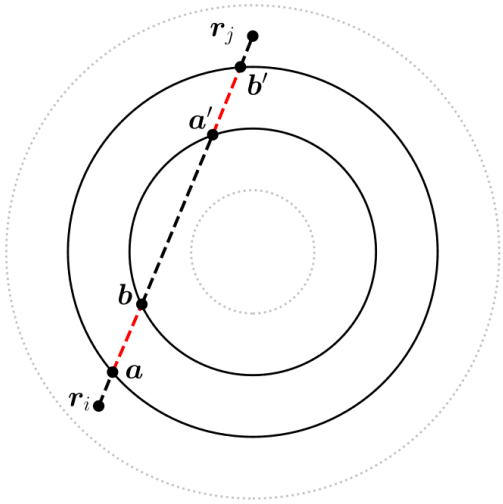

Figure 3.3: A projection of a spherical shell volume where both particle i and j are outside. Since the Irving-Kirkwood contour passes through the volume the interaction contributes to the pressure. The red dashed lines illustrate the segments of the contour that contributes, while the black dashed lines illustrate the segments that do not contribute to the spherical shell. There are two entry and two exit points, (a, b) and (a', b').

3.6.2 Spherical coordinates

In this subsection, the calculation of the mechanical pressure tensor in spherical coordinates with the Irving-Kirkwood curve is described in detail. A spherical shell of radius R and thickness ΔR is considered. In spherical coordinates the mechanical pressure tensor is

$$\mathbb{P} = \begin{bmatrix} P_{rr} & P_{r\theta} & P_{r\phi} \\ P_{\theta r} & P_{\theta\theta} & P_{\theta\phi} \\ P_{\phi r} & P_{\phi\theta} & P_{\phi\phi} \end{bmatrix}, \tag{3.30}$$

where r is the radial direction, $\theta \in [0, \pi]$ is the polar angle, and $\phi \in [0, 2\pi]$ is the azimuthal angle.

A point on the Irving-Kirkwood curve can be described as

$$\boldsymbol{l}(\lambda) = \boldsymbol{r}_i + \lambda \boldsymbol{r}_{ij}, \quad \text{where} \quad 0 \leq \lambda \leq 1, \tag{3.31}$$

where $\boldsymbol{r}_i$ is the position of particle i, $\boldsymbol{r}_{ij} = \boldsymbol{r}_j - \boldsymbol{r}_i$ is the vector from particle i to j, and $\boldsymbol{r}_i$ and $\boldsymbol{r}_j$ are vectors from the origin of the spherical coordinate system.

The length of the vector $\boldsymbol{l}(\lambda)$ is

$$l(\lambda) = |\boldsymbol{l}(\lambda)| = \sqrt{r_i^2 + 2\lambda(\boldsymbol{r}_i \cdot \boldsymbol{r}_{ij}) + \lambda^2 r_{ij}^2}, \tag{3.32}$$

where $r_i = |\boldsymbol{r}_i|$ and $r_{ij} = |\boldsymbol{r}_{ij}|$. We define two points $\boldsymbol{a}$ and $\boldsymbol{b}$ on the curve C_{ij}. These points are the entry and exit points of the Irving-Kirkwood curve if particle i and j are outside the volume. An Irving-Kirkwood curve can have up to two entry and exit points, see figure 3.3, but each pair of entry and exit points will be handled separately.

The entry and exit points can be described as

$$\boldsymbol{a} = \boldsymbol{r}_i + \lambda_a \boldsymbol{r}_{ij} \quad \text{and} \quad \boldsymbol{b} = \boldsymbol{r}_i + \lambda_b \boldsymbol{r}_{ij}, \tag{3.33}$$

where $0 \leq \lambda_a \leq 1$ and $0 \leq \lambda_b \leq 1$. If particle i and j are outside the subvolume, then $\boldsymbol{a}$ and $\boldsymbol{b}$ are the entry and exits points of the curve C_{ij}. If they are inside the subvolume, then $\boldsymbol{a} = \boldsymbol{r}_i$ and $\boldsymbol{b} = \boldsymbol{r}_j$. The virial contribution to the mechanical pressure tensor due to the ij particle pair with the Irving-Kirkwood curve is then

$$P^v_{ij,\alpha\beta} = -\frac{1}{V}\int_{\lambda_a}^{\lambda_b} (\boldsymbol{e}_\alpha \cdot \boldsymbol{f}_{ij})(\boldsymbol{e}_\beta \cdot \boldsymbol{r}_{ij}) \mathrm{d}\lambda = \frac{f_{ij}}{r_{ij}V}\int_{\lambda_a}^{\lambda_b} (\boldsymbol{e}_\alpha \cdot \boldsymbol{r}_{ij})(\boldsymbol{e}_\beta \cdot \boldsymbol{r}_{ij}) \mathrm{d}\lambda \tag{3.34}$$

where $\boldsymbol{e}_\alpha$ is the unit vector in the α direction, which is a function of λ. In the second equality we have used that the force vector is parallel to the distance vector, such that we can insert $\boldsymbol{f}_{ij} = -f_{ij}(\boldsymbol{r}_{ij}/r_{ij})$, where $f_{ij} = |\boldsymbol{f}_{ij}|$. The force and the distance vectors do not depend on λ.

The unit vectors are

$$\begin{aligned}
\boldsymbol{e}_r &= \frac{\boldsymbol{l}(\lambda)}{l(\lambda)} \\
\boldsymbol{e}_\theta &= \frac{1}{l\sqrt{l_x^2 + l_y^2}} \begin{bmatrix} l_x l_z & l_y l_z & -(l_x^2 + l_y^2) \end{bmatrix}, \quad \text{and} \\
\boldsymbol{e}_\phi &= \frac{1}{\sqrt{l_x^2 + l_y^2}} \begin{bmatrix} -l_y & l_x & 0 \end{bmatrix}.
\end{aligned} \tag{3.35}$$

The rr-component of the spherical mechanical pressure tensor is

$$\begin{aligned}
P^v_{ij,rr} &= \frac{f_{ij}}{r_{ij}V}\int_{\lambda_a}^{\lambda_b} \frac{\lambda^2 r_{ij}^4 + 2\lambda r_{ij}^2(\boldsymbol{r}_i \cdot \boldsymbol{r}_{ij}) + (\boldsymbol{r}_i \cdot \boldsymbol{r}_{ij})^2}{\lambda^2 r_{ij}^2 + 2\lambda(\boldsymbol{r}_i \cdot \boldsymbol{r}_{ij}) + r_i^2} \mathrm{d}\lambda \\
&= \frac{f_{ij}}{V}\left(r_{ij}(\lambda_b - \lambda_a) + F(\lambda_b) - F(\lambda_a)\right).
\end{aligned} \tag{3.36}$$

The function $F(\lambda)$ is

$$F(\lambda) = -l_0 \arctan\left(\frac{\lambda r_{ij}^2 + (\boldsymbol{r}_i \cdot \boldsymbol{r}_{ij})}{r_{ij} l_0}\right), \quad \text{where} \quad l_0 = \sqrt{r_i^2 - \frac{(\boldsymbol{r}_i \cdot \boldsymbol{r}_{ij})^2}{r_{ij}^2}}. \quad (3.37)$$

The $\phi\phi$-component is

$$\begin{aligned} P^v_{ij,\phi\phi} &= \frac{f_{ij}}{r_{ij} V} \int_{\lambda_a}^{\lambda_b} \frac{(r_{i,x} r_{ij,y} - r_{i,y} r_{ij,x})^2}{\lambda^2 r_{ij,xy}^2 + 2\lambda(\boldsymbol{r}_{i,xy} \cdot \boldsymbol{r}_{ij,xy}) + r_{i,xy}^2} \mathrm{d}\lambda \\ &= \frac{f_{ij}}{r_{ij} V} \frac{(r_{i,x} r_{ij,y} - r_{i,y} r_{ij,x})^2}{r_{ij,xy} l_{xy,0}} \left(G(\lambda_b) - G(\lambda_a)\right) \end{aligned}, \quad (3.38)$$

where $\boldsymbol{r}_{i,xy} = [r_{i,x}, r_{i,y}, 0]$ and $\boldsymbol{r}_{ij,xy} = [r_{ij,x}, r_{ij,y}, 0]$ are projects of $\boldsymbol{r}_i$ and $\boldsymbol{r}_{ij}$ on the xy-plane, respectively. The function $G(\lambda)$ is

$$G(\lambda) = \arctan\left(\frac{r_{ij,xy}^2 + (\boldsymbol{r}_{i,xy} \cdot \boldsymbol{r}_{ij,xy})^2}{r_{ij,xy} l_{xy,0}}\right), \quad (3.39)$$

where

$$l_{xy,0} = \sqrt{r_{i,xy}^2 - \frac{(\boldsymbol{r}_{i,xy} \cdot \boldsymbol{r}_{ij,xy})^2}{r_{ij,xy}^2}}. \quad (3.40)$$

For spherical radially symmetric systems, the $\theta\theta$- and $\phi\phi$-components of the mechanical pressure tensor are equal. The tensor can be rewritten with the normal component $P_N = P_{rr}$ and tangential component $P_T = (P_{\phi\phi} + P_{\theta\theta})/2$. Conservation of momentum at mechanical equilibrium states that

$$P_T(r) = P_N(r) + \frac{r}{2} \frac{\partial P_N(r)}{\partial r}. \quad (3.41)$$

This relation can be used to check if the normal and tangential components are consistent.

3.7 Non-equilibrium molecular dynamics

In article IX, we used non-equilibrium molecular dynamics to study the mass flux and pressure gradient relationship. To generate the flux and force, we used the reflecting particle method (RPM) [100]. It was applied to the x-boundary of the simulation box to induce a pressure gradient. The RPM allowed particles to cross the periodic x-boundary from right to left with a probability $1-q$, and to be reflected with a probability $q \in [0, 1]$. A value $q = 0$ entailed that no fluid particles were reflected, while a value $q = 1$ entailed that all fluid particles were reflected

when attempting to cross the x-boundary from right to left. The fluid particles were never reflected when crossing the x-boundary from left to right. The pressure gradient was controlled by varying the probability q. This is a boundary-driven non-equilibrium molecular dynamics method to induce a pressure gradient that has minimal disturbance on the fluid particles away from the boundary [31]. An alternative would be to apply a constant force to all particles in the simulation [79], which is a bulk-driven method.

Chapter 4

Conclusions

The main goal of this work has been to contribute to the development of an upscaled thermodynamic theory of transport in porous media. The theory we have proposed is upscaled in the sense that it describes the thermodynamic state of the representative elementary volume (REV) as a whole, rather than the state of the individual phases, surfaces, lines, and points. The REV was here defined as a volume large enough to be statistically representative of the thermodynamic properties of the system. In articles I and II, we derived the Gibbs equation of the REV, which was used to derive the entropy production and flux-force equations for isothermal two-phase flow in porous media. This gave a thermodynamic basis for Darcy's law but also allowed for coupled transport in porous media. More importantly, we believe this upscaling procedure is general and can be applied to all transport phenomena in porous media.

The first step to investigate the proposed theory was to construct the REV for a simple system in equilibrium and determine the thermodynamic properties of the REV. Article III investigated a single-phase fluid in a porous structure made up of solid particles in a face-centered cubic (fcc) lattice with molecular dynamics simulations. With the assumption that the pressure of the REV is constant everywhere, we find that we must introduce the integral pressure to give a coherent relationship between the fluid and solid pressures. The integral pressure was first described by Hill, in what is now known as nanothermodynamics. This work was the first step in calculating the REV pressure of a porous medium, and w concluded that the REV of this system was the size of a unit cell.

In articles IV, V, and VI, we further investigated the integral pressure in different geometries. In article IV, we investigated the integral pressure in both

a cylindrical and a slit pore, and we investigated the relationship between the differential and integral pressures in these geometries. In article V, we investigated a liquid-vapor interface in a slit pore. We find that by relating the fluid pressure to the average normal mechanical pressure tensor component, the integral pressure is equal to the average tangential mechanical pressure tensor component. In equilibrium, this relation is shown to be constant across the liquid-vapor interface. The fluid pressure is not constant for contact angles $\theta \neq 90°$, since the difference in liquid and vapor pressure is given by Young-Laplace's equation. We find that as a consequence of Young-Laplace's and Young's equation the integral pressure is constant. We conclude that the integral pressure gradient is the driving force for fluid flow, and not for example the fluid pressure gradients. In article VI, we give a pedagogical and in-depth nanothermodynamic description of a single-phase fluid in a slit pore. The difference between the integral pressure and the differential pressure is the subdivision potential. In this work, we conclude that the subdivision potential is zero for a single-phase fluid in a slit pore when the surface area is sufficiently large, regardless of how close the parallel walls are.

Article VII considers again a single-phase fluid in a slit pore, however, now the Helmholtz and Gibbs energies are compared. We investigated the system when either the height or when the normal pressure was controlled. We find that since the Helmholtz energy is non-convex for sufficiently small pores, one can not use the Legendre transform to transform the Gibbs energy but need to use the Legendre-Fenchel transform.

Article VIII lays the equilibrium foundation for non-equilibrium studies in article IX. In article VIII, a procedure to calculate an equation of state for the REV of a single-phase fluid in a fcc lattice of solid spheres was developed. This was done with the assumption that the integral pressure is constant everywhere in equilibrium. Since the integral pressure is equal to the differential pressure in the bulk phase, we can determine the integral pressure of the REV. In this way, we have an equation of state that relates the temperature, fluid density, and porosity of the REV to the integral pressure. This procedure is used in article IX in non-equilibrium conditions to calculate the transport coefficient. One conclusion from this work is that the integral pressure of the REV for this particular system is equal to the differential pressure, because of the symmetry of the fcc lattice.

This work has laid a theoretical foundation for studying coupled transport processes in porous media, and we have developed a procedure to obtain the thermodynamic properties of the REV. So far, we have only applied this to simple systems with a single driving force. In the future, I hope this can be used to study

coupled transport of heat, mass, and charge in porous media with multiple fluid phases.

One crucial assumption of non-equilibrium thermodynamics is the assumption of local equilibrium. It is unknown if this assumption holds for the REV. There are competing interests for the size of the REV since the REV must be large enough to represent the system, but also small enough for the assumption of local equilibrium to hold. There is evidence for local equilibrium to hold for heterogeneous media, such as liquid-vapor interfaces. Related to this, it is not determined what the subdivision potential of a generalized REV is. In article IX, we conclude that the integral pressure is equal to the differential pressure for the given geometry on the REV scale. Since the REV by definition is large, it is reasonable to assume the integral pressure of the REV always to be equal to the differential pressure of the REV. This has yet to be investigated. However, we emphasize that this is not the case for the individual phases. For example, the integral solid pressure is not necessarily equal to the differential solid pressure.

Article I

Signe Kjelstrup, Dick Bedeaux, Alex Hansen, Bjørn Hafskjold, **Olav Galteland**

Non-isothermal Transport of Multi-Phase Fluids in Porous Media. The Entropy Production

Frontiers in Physics, 6, 126. (2018)
DOI: 10.3389/fphy.2018.00126

Article I

Article I

frontiers in Physics

ORIGINAL RESEARCH
published: 08 November 2018
doi: 10.3389/fphy.2018.00126

Non-isothermal Transport of Multi-phase Fluids in Porous Media. The Entropy Production

Signe Kjelstrup[1]*, *Dick Bedeaux*[1], *Alex Hansen*[2], *Bjørn Hafskjold*[1] and *Olav Galteland*[1]

[1] PoreLab, Department of Chemistry, Norwegian University of Science and Technology, Trondheim, Norway, [2] PoreLab, Department of Physics, Norwegian University of Science and Technology, Trondheim, Norway

We derive the entropy production for transport of multi-phase fluids in a non-deformable, porous medium exposed to differences in pressure, temperature, and chemical potentials. Thermodynamic extensive variables on the macro-scale are obtained by integrating over a representative elementary volume (REV). Contributions come from porous media specific properties, phase volumes, surface areas, and contact lines. Curvature effects are neglected. Using Euler homogeneity of the first order, we obtain the Gibbs equation for the REV. From this we define the intensive variables, the temperature, pressure, and chemical potentials, and, using the balance equations, we derive the entropy production for the REV. The entropy production defines sets of independent conjugate thermodynamic fluxes and forces in the standard way. The transport of two-phase flow of immiscible components is used to give a first illustration of the equations.

Keywords: porous media, energy dissipation, two-phase flow, excess surface- and line-energies, pore-scale, representative elementary volume, macro-scale, non-equilibrium thermodynamics

OPEN ACCESS

Edited by:
Antonio F. Miguel,
Universidade de Évora, Portugal

Reviewed by:
Francisco J. Valdes-Parada,
Universidad Autónoma Metropolitana, Mexico
A. Murat,
University of Ontario Institute of Technology, Canada

***Correspondence:**
Signe Kjelstrup
signe.kjelstrup@ntnu.no

Specialty section:
This article was submitted to Interdisciplinary Physics, a section of the journal Frontiers in Physics

Received: *05 September 2018*
Accepted: *16 October 2018*
Published: *08 November 2018*

Citation:
Kjelstrup S, Bedeaux D, Hansen A, Hafskjold B and Galteland O (2018) Non-isothermal Transport of Multi-phase Fluids in Porous Media. The Entropy Production. Front. Phys. 6:126. doi: 10.3389/fphy.2018.00126

1. INTRODUCTION

The aim of this article is to develop the basis for a macro-scale description of multi-phase flow in porous media in terms of non-equilibrium thermodynamics. The system consists of several fluid phases in a medium of constant porosity. The aim is to describe the transport of these on the scale of measurements; i.e., on the macro-scale, using properties defined on this scale, which represent the underlying structure on the micro-scale. The effort is not new; it was pioneered more than 30 years ago [1–4], and we shall build heavily on these results, in particular those of Hassanizadeh and Gray [2, 3] and Gray and Miller [5].

The aim is also still the original one; to obtain a systematic description, which can avoid arbitrariness and capture the essential properties of multi-component multi-phase flow-systems. Not only bulk energies need be taken into account to achieve this for porous media. Also excess surface- and line-energies must be considered, see e.g., [6]. But, unlike what has been done before, we shall seek to reduce drastically the number of variables needed for the description, allowing us still to make use of the systematic theory of non-equilibrium thermodynamics. While the entropy production in the porous medium so far has been written as a combination of contributions from each phase, interface and contact line, we shall write the property for a more limited set of macro-scale variables. In this sense, we deviate widely from the Thermodynamically Constrained Averaging Theory [5]. Nevertheless, we will be able to describe experiments and connect variables within the classical scheme of non-equilibrium thermodynamics. The reduction of variables is possible as long as the system is Euler homogeneous of the first kind.

The theory of non-equilibrium thermodynamics was set up by Onsager [7, 8] and further developed for *homogeneous* systems during the middle of the last century [9]. It was the favored thermodynamic basis of Hassanizadeh and Gray for their description of porous media. These authors [2, 3] discussed also other approaches, e.g., the theory of mixtures in macroscopic continuum mechanics, cf. [1, 4]. Gray and Miller [5] argued that it is the simplest of the many approaches in non-equilibrium thermodynamics.

The theory of classical non-equilibrium thermodynamics has been extended to deal with a particular case of flow in heterogeneous systems, namely transport along [10] and perpendicular [11] to layered interfaces. A derivation of the entropy production for heterogeneous systems *on the macro-scale* has not been given, however, even if one can find several uses of this property [6]. Transport in porous media takes place, not only under pressure gradients. Temperature gradients will frequently follow from transport of mass, for instance in heterogeneous catalysis [12], in polymer electrolyte fuel cells, in batteries [11, 13], or in capillaries in frozen soils during frost heave [14]. The number of this type of phenomena is enormous. We have chosen to consider first the vectorial driving forces related to changes in pressure, chemical composition, and temperature, staying away for the time being from deformations, chemical reactions, or forces leading to stress [15]. The multi-phase flow problem is thus in focus.

The development of a general thermodynamic basis for multi-phase flow started by introduction of thermodynamic properties for each component in each phase, interface, and three-phase contact line [2, 3]. A representative volume element (REV) was introduced, consisting of bulk phases, interfaces, and three-phase contact lines. Balance equations were formulated for each phase in the REV, and the total REV entropy production was the sum of the separate contributions from each phase.

Hansen et al. [16] recognized recently that the motion of fluids at the coarse-grained level could be described by extensive variables. The properties of Euler homogeneous functions could then be used to create relations between the flow rates at this level of description. This work, however, did not address the coarse-graining problem itself. We shall take advantage of Euler homogeneity also here and use it in the coarse-graining process described above.

Like Gray et al. [2, 3, 5], we use the entropy production as the governing property. But rather than dealing with the total entropy production as a sum of several parts, we shall seek to define the total entropy production directly from a basis set of a few coarse-grained variables. This will be done here for the REV, see [17] for a preliminary version. Once the entropy production has been formulated, we shall set up the independent constitutive equations. This will be done in subsequent work, see the preliminary version [18]. There we highlight the consequences of the model, and show that new experimental relations can be found. We shall find that the description is able to add insight in already published experimental results and design new experiments.

The overall aim is thus to contribute toward solving the scaling problem; i.e., how a macro-level description can be obtained consistent with the micro-level one, by defining transport equations on the macro-level. The aim of the present work, seen in this context, is to present the basis for a description of central transport phenomena, namely those due to thermal, chemical, mechanical, and gravitational forces. We shall propose a systematic, course-grained procedure that will be simple in practical use.

2. SYSTEM

Consider a heterogeneous system as illustrated by the (white) box in **Figure 1**. The system is a porous medium of fixed porosity filled with several immiscible fluids. There is net transport in one direction only, the x-direction. On the scale of measurement, the system is without structure. By zooming in, we see the pore scale. A collection of pores with two fluids is schematically shown in **Figure 2**.

A temperature, pressure, and/or chemical potential difference is applied between the inlet and the outlet, and these differences can be measured. The pressure difference Δp between the outlet and the inlet was defined for steady state conditions by Tallakstad et al. [19], as the time average of the fluctuating difference $\Delta p(t)$:

$$\Delta p = \frac{1}{t_\mathrm{e} - t_\mathrm{b}} \int_{t_\mathrm{b}}^{t_\mathrm{e}} \Delta p(t) dt. \tag{1}$$

Here t is the time. Subscript "b" denotes beginning and "e" denotes the end of the measurement. We adopt similar definitions for ΔT and $\Delta \mu_i$. It is possible, through application of separate inlet channels, to control the flow into and out of the system and find the flow of each component, to define the flow situation in **Figure 1**. In the presence of two immiscible phases, it is only possible to define the pressure difference between the inlet and the outlet for the phases, Δp^w and Δp^n, if there is continuity in the respective phases.

We will repeatedly use two-phase flow of single components as an example, where w indicates the most wetting and n the least wetting phase. We refer to them simply as the wetting and the non-wetting phase. In most of the paper we consider a multi-phase fluid. In the system pictured in **Figure 2**, there is flow within the REV in the direction of the pore. This is not necessarily the direction given by the overall pressure gradient. The flow on the macro-scale, however, is always in the direction of the pressure gradient. Net flow in other directions are zero due to isolation of the system in these directions. By flow on the macro-scale, we mean flow in the direction of the overall pressure gradient along the x-coordinate in **Figure 1**. The value of this average flow is of interest.

The representative volume element, REV, is constructed from a collection of pores like those contained in the red square in **Figure 2**. In **Figure 1**, three REVs are indicated (magenta structured squares). In a homogeneous system, statistical mechanical distributions of molecular properties lead to the macroscopic properties of a volume element. In a heterogeneous system like here, the statistical distributions are over the states within the REV. The collection of pores in the REV, cf. **Figure 2**, should be of a size that is large enough to provide meaningful

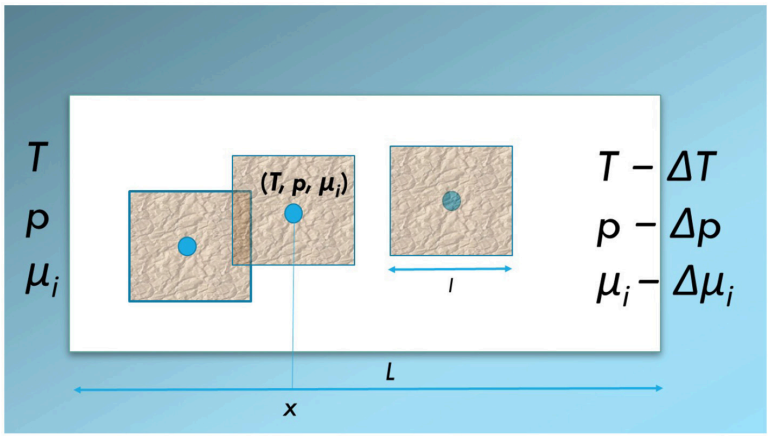

FIGURE 1 | Schematic illustration of a heterogeneous system (white box, length L) exposed to a difference in temperature, ΔT, pressure, Δp, or chemical potential $\Delta\mu_i$. The system is isolated in the $y, z-$directions. Net flows take place in the $x-$direction. Three representative elementary volumes, REVs (magenta squares, length l) are indicated. The REVs may overlap. Each is represented by a set of variables (p, T, μ_i) which defines a state (blue dot). Such states can be defined anywhere on the x-axis.

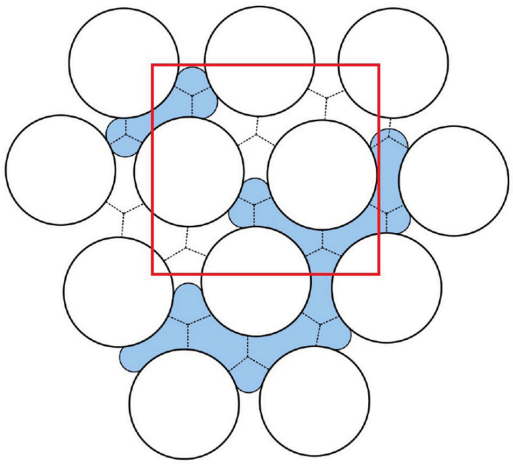

FIGURE 2 | A schematic collection of pores filled with two immiscible liquids. In order to compute the system properties, we define a REV. A REV is indicated in the figure by the red square. Courtesy of M. Vassvik.

values for the extensive variables, and therefore well defined intensive variables (see below, Equations 19 and 20), cf. section 3.2 below. Thermodynamic relations can be written for each REV.

State variables characterize the REV. They are represented by the (blue) dots in **Figure 1**. The size of the REV depends on its composition and other conditions. Typically, the extension of a REV, l, is large compared to the pore size of the medium, and small compared to the full system length L. This construction of a REV is similar to the procedure followed in smoothed particle hydrodynamics [20], cf. the discussion at the end of the work.

The REVs so constructed, can be used to make a path of states, over which we can integrate across the system. Each REV in the series of states, is characterized by variables T, p, μ_i, as indicated by the blue dots in **Figure 1**. Vice versa, each point in a porous medium can be seen as a center in a REV. The states are difficult to access directly, but can be accessed via systems in equilibrium with the states, as is normal in thermodynamics. This is discussed at the end of the work. We proceed to define the REV-variables.

3. PROPERTIES OF THE REV

3.1. Porosity and Saturation

Consider a solid matrix of constant porosity ϕ. We are dealing with a class of systems that are homogeneous in the sense that the typical pore diameter and pore surface area, on the average, are the same everywhere. There are m phases in the system. The pores are filled with a mixture of $m-1$ fluid phases; the solid matrix is phase number m. Properties will depend on the time, but this will not be indicated explicitly in the equations.

In a simple case, the phases are immiscible single components. The chemical constituents are then synonymous with a phase, and the number of phases is the number of components. The state of the REV can be characterized by the volumes of the fluid phases $V^{\alpha,\mathrm{REV}}, \alpha = 1, .., m-1$ and of the solid medium $V^{m,\mathrm{REV}}$. The total volume of the pores is

$$V^{p,\mathrm{REV}} \equiv \sum_{\alpha=1}^{m-1} V^{\alpha,\mathrm{REV}}. \tag{2}$$

while the volume of the REV is

$$V^{\mathrm{REV}} \equiv V^{m,\mathrm{REV}} + V^{p,\mathrm{REV}} + \sum_{\alpha>\beta>\delta=1}^{m} V^{\alpha\beta\delta,\mathrm{REV}}. \quad (3)$$

Superscript REV is used to indicate a property of the REV. The last term is the sum of the excess volumes of the three-phase contact lines. While the excess volume of the surfaces is zero by definition, this is not the case for the three-phase contact lines. The reason is that the dividing surfaces may cross each other at three lines which have a slightly different location. The corresponding excess volume is in general very small, and will from now on be neglected. This gives the simpler expression

$$V^{\mathrm{REV}} \equiv V^{m,\mathrm{REV}} + V^{p,\mathrm{REV}}. \quad (4)$$

All these volumes can be measured.

The porosity, ϕ, and the saturation, $\hat{S}$, are given by

$$\phi \equiv \frac{V^{p,\mathrm{REV}}}{V^{\mathrm{REV}}} \quad \text{and} \quad \hat{S}^{\alpha} \equiv \frac{V^{\alpha,\mathrm{REV}}}{V^{p,\mathrm{REV}}} = \frac{V^{\alpha,\mathrm{REV}}}{\phi V^{\mathrm{REV}}}. \quad (5)$$

The porosity and the saturation are intensive variables. They do not depend on the size of the REV. They have therefore no superscript. It follows from these definitions that

$$\sum_{\alpha=1}^{m-1} \hat{S}^{\alpha} = 1 \quad \text{and} \quad V^{m,\mathrm{REV}} = (1-\phi)\, V^{\mathrm{REV}} \quad (6)$$

In addition to the volumes of the different bulk phases (they are fluids or solids) $m \geq \alpha \geq 1$, there are interfacial areas, Ω, between each two phases in the REV: $\Omega^{\alpha\beta,\mathrm{REV}}$, $m \geq \alpha > \beta \geq 1$. The total surface area of the pores is measurable. It can be split between various contributions

$$\Omega^{p,\mathrm{REV}} = \sum_{\alpha=1}^{m-1} \Omega^{m\alpha,\mathrm{REV}} \quad (7)$$

When the surface is not completely wetted, we can estimate the surface area between the solid m and the fluid phase α, from the total pore area available and the saturation of the component.

$$\Omega^{m\alpha,\mathrm{REV}} = \hat{S}^{\alpha}\Omega^{p,\mathrm{REV}} \quad (8)$$

This estimate is not correct for strongly wetting components or dispersions. In those cases, films can form at the walls, and $\Omega^{m\alpha,\mathrm{REV}}$ is not proportional to $\hat{S}^{\alpha}$. In the class of systems we consider, all fluids touch the wall, and there are no films of one fluid between the wall and another fluid.

3.2. Thermodynamic Properties of the REV

We proceed to define the thermodynamic properties of the REV within the volume V^{REV} described above. In addition to the volume, there are other additive variables. They are the masses, the energy, and the entropy. We label the components (the chemical constituents) using italic subscripts. There are in total n components distributed over the phases, surfaces, and contact lines. The mass of component i, M_i^{REV}, in the REV is the sum of bulk masses, $M_i^{\alpha,\mathrm{REV}}$, $m \geq \alpha \geq 1$, the excess interfacial masses, $M_i^{\alpha\beta,\mathrm{REV}}$, $m \geq \alpha > \beta \geq 1$, and the excess line masses, $M_i^{\alpha\beta\delta,\mathrm{REV}}$, $m \geq \alpha > \beta > \delta \geq 1$.

$$M_i^{\mathrm{REV}} = \sum_{\alpha=1}^{m} M_i^{\alpha,\mathrm{REV}} + \sum_{\alpha>\beta=1}^{m} M_i^{\alpha\beta,\mathrm{REV}} + \sum_{\alpha>\beta>\delta=1}^{m} M_i^{\alpha\beta\delta,\mathrm{REV}} \quad (9)$$

There is some freedom in how we allocate the mass to the various phases and interfaces [11, 21]. We are e.g., free to choose a dividing surface such that one $M_i^{\alpha\beta,\mathrm{REV}}$ equals zero. A zero excess mass will simplify the description, but will introduce a reference. The dividing surface with zero $M_i^{\alpha\beta,\mathrm{REV}}$ is the equimolar surface of component i. The total mass of a component in the REV is, however, *independent* of the location of the dividing surfaces. From the masses, we compute the various mass densities

$$\rho_i \equiv \frac{M_i^{\mathrm{REV}}}{V^{\mathrm{REV}}}, \quad \rho_i^{\alpha} \equiv \frac{M_i^{\alpha,\mathrm{REV}}}{V^{\alpha,\mathrm{REV}}},$$
$$\rho_i^{\alpha\beta} \equiv \frac{M_i^{\alpha\beta,\mathrm{REV}}}{\Omega^{\alpha\beta,\mathrm{REV}}}, \quad \rho_i^{\alpha\beta\delta} \equiv \frac{M_i^{\alpha\beta\delta,\mathrm{REV}}}{\Lambda^{\alpha\beta\delta,\mathrm{REV}}} \quad (10)$$

where ρ_i and ρ_i^{α} have dimension kg.m^{-3}, $\rho_i^{\alpha\beta}$ has dimension kg.m^{-2} and $\rho_i^{\alpha\beta\delta}$ has dimension kg.m^{-1}.

All densities are for the REV. If we increase the size of the REV, by for instance doubling its size, V^{REV}, M_i^{REV} and other extensive variables will all double. They will double, by doubling all contributions to these quantities. But this is not the case for the density ρ_i or the other densities. They remain the same, independent of the size of the REV. This is true also for the densities of the bulk phases, surfaces, and contact lines. Superscript REV is therefore not used for the densities.

Within one REV there are natural fluctuations in the densities. But the densities make it possible to give a description on the macro-scale independent of the precise size of the REV. The densities will thus be used in the balance equations on the macro-scale. The density ρ_i^{α} may vary somewhat in V^{α}. We can then find M_i^{α} as the integral of ρ_i^{α} over V^{α}. Equation (10) then gives the volume-averaged densities.

The internal energy of the REV, U^{REV}, is the sum of bulk internal energies, $U^{\alpha,\mathrm{REV}}$, $m \geq \alpha \geq 1$, the excess interfacial internal energies, $U^{\alpha\beta,\mathrm{REV}}$, $m \geq \alpha > \beta \geq 1$, and the excess line internal energies, $U^{\alpha\beta\delta,\mathrm{REV}}$, $m \geq \alpha > \beta > \delta \geq 1$:

$$U^{\mathrm{REV}} = \sum_{\alpha=1}^{m} U^{\alpha,\mathrm{REV}} + \sum_{\alpha>\beta=1}^{m} U^{\alpha\beta,\mathrm{REV}} + \sum_{\alpha>\beta>\delta=1}^{m} U^{\alpha\beta\delta,\mathrm{REV}} \quad (11)$$

The summation is taken over all phases, interfaces, and contact lines (if non-negligible). We shall see in a subsequent paper how these contributions may give specific contributions to the driving force. The internal energy densities are defined by

$$u \equiv \frac{U^{\mathrm{REV}}}{V^{\mathrm{REV}}}, \quad u^{\alpha} \equiv \frac{U^{\alpha,\mathrm{REV}}}{V^{\alpha,\mathrm{REV}}},$$

$$u^{\alpha\beta} \equiv \frac{U^{\alpha\beta,\mathrm{REV}}}{\Omega^{\alpha\beta,\mathrm{REV}}},\ u^{\alpha\beta\delta} \equiv \frac{U^{\alpha\beta\delta,\mathrm{REV}}}{\Lambda^{\alpha\beta\delta,\mathrm{REV}}} \tag{12}$$

Their dimensions are J.m^{-3} (u, u^{α}), J.m^{-2} $(u^{\alpha\beta})$, and J.m^{-1} $(u^{\alpha\beta\delta})$, respectively.

The entropy in the REV, S^{REV}, is the sum of the bulk entropies, $S^{\alpha,\mathrm{REV}}$, $m \geq \alpha \geq 1$, the excess entropies, $S^{\alpha\beta,\mathrm{REV}}$, $m \geq \alpha > \beta \geq 1$, the excess line entropies, $S^{\alpha\beta\delta,\mathrm{REV}}$, $m \geq \alpha > \beta > \delta \geq 1$, and a configurational contribution, $S^{\mathrm{REV}}_{\mathrm{conf}}$, from the geometrical distribution of the fluid phases within the pores:

$$S^{\mathrm{REV}} = \sum_{\alpha=1}^{m} S^{\alpha,\mathrm{REV}} + \sum_{\alpha>\beta=1}^{m} S^{\alpha\beta,\mathrm{REV}} + \sum_{\alpha>\beta>\delta=1}^{m} S^{\alpha\beta\delta,\mathrm{REV}} + S^{\mathrm{REV}}_{\mathrm{conf}} \tag{13}$$

The entropy densities are defined by

$$s \equiv \frac{S^{\mathrm{REV}}}{V^{\mathrm{REV}}},\ s^{\alpha} \equiv \frac{S^{\alpha,\mathrm{REV}}}{V^{\alpha,\mathrm{REV}}},\ s^{\alpha\beta} \equiv \frac{S^{\alpha\beta,\mathrm{REV}}}{\Omega^{\alpha\beta,\mathrm{REV}}},$$
$$s^{\alpha\beta\delta} \equiv \frac{S^{\alpha\beta\delta,\mathrm{REV}}}{\Lambda^{\alpha\beta\delta,\mathrm{REV}}},\ s_{\mathrm{conf}} \equiv \frac{S^{\mathrm{REV}}_{\mathrm{conf}}}{V^{\mathrm{REV}}} \tag{14}$$

and have the dimensions J.K^{-1}.m^{-3} $(s, s^{\alpha}, s_{\mathrm{conf}})$, J.K^{-1}.m^{-2} $(s^{\alpha\beta})$, and J.K^{-1}.m^{-1} $(s^{\alpha\beta\delta})$, respectively. To explain the configurational contribution in more detail; consider the example of stationary two-phase flow in a single tube of varying diameter described by Sinha et al. [22]. The tube contains one bubble of one fluid in the other. The bubble touches the wall; it can not form a film between the tube wall and the other fluid. The probability per unit of length of the tube to find the center of mass of the bubble at position x_b, was $\Pi(x_b)$ [22]. Knowing this probability distribution, we can compute the entropy of an ensemble of single tubes (in this case a very long tube composed of the single ones). It is equal to

$$S^{\mathrm{REV}}_{\mathrm{conf}} = k_{\mathrm{B}} \int_0^{\ell} \Pi(x_b) \ln \ell \Pi(x_b) dx_b \tag{15}$$

For a network of pores it is more appropriate to give the probability distribution for the fluid-fluid interfaces. This has not yet been done explicitly.

For the volume, Equations (2) and (4) apply when the contact lines give a negligible contribution. The dividing surfaces have by definition no excess volume. For all the other extensive thermodynamic variables, like the enthalpy, Helmholtz energy, Gibbs energy, and the grand potential, relations similar to Equations (11) and (13) apply. We shall later show how this affects the driving forces [18].

To summarize this section; we have defined a basis set of variables for a class of systems, where these variables are additive in the manner shown. From the set of REV-variables we obtain the densities, u, s, or ρ_i to describe the heterogeneous system on the macro-scale. A series of REVs of this type, is needed for integration across the system, see section 5.

3.3. REV Size Considerations

As an illustration of the REV construction, consider the internal energy of two isothermal, immiscible and incompressible fluids (water and decane) flowing in a Hele-Shaw type cell composed of silicone glass beads. The relevant properties of the fluids can be found in **Table 1** The porous medium is a hexagonal network of 3,600 links, as illustrated in **Figure 3**. The network is periodic in the longitudinal and the transverse directions and a pressure difference of 1.8×10^4 Pa drives the flow in the longitudinal direction. The overall saturation of water is 0.4. The network flows were simulated using the method of Aker et al. [23], see [24] for details.

TABLE 1 | Fluid properties used to compute the candidate REV internal energy, for a network containing water (n) and decane (w) within silica glass beads (p) at atmospheric pressure and 293 K.

Parameter	Value	Unit	References
η^w	9.2×10^{-4}	Pa.s	[25]
η^n	1.0×10^{-3}	Pa.s	[25]
γ^{wp}	2.4×10^{-2}	N.m^{-1}	[26]
γ^{np}	7.3×10^{-2}	N.m^{-1}	[26]
γ^{wn}	5.2×10^{-2}	N.m^{-1}	[27]
$-u^w$	2.8×10^8	J.m^{-3}	[25]
$-u^n$	3.4×10^8	J.m^{-3}	[25]

The internal energy of the REV is, according to section 3.2, a sum over the two fluid bulk contributions and three interface contributions,

$$U^{\mathrm{REV}} = U^{m,\mathrm{REV}} + \sum_{i\in\{w,n\}} \left\{U^{i,\mathrm{REV}}\right\} + U^{wn,\mathrm{REV}} + U^{np,\mathrm{REV}} + U^{wp,\mathrm{REV}} \tag{16}$$

$$= U^{m,\mathrm{REV}} + V^{p,\mathrm{REV}} \sum_{i\in\{w,n\}} \left\{\hat{S}^i u^i\right\} + u^{wn}\Omega^{wn,\mathrm{REV}} + u^{np}\Omega^{np,\mathrm{REV}} + u^{wp}\Omega^{wp,\mathrm{REV}}. \tag{17}$$

where, u^i is the internal energy density of phase i and u^{ij} is the excess internal energy per interfacial area between phase i and phase j. We assume u^i and u^{ij} to be constant. For simplicity, u^{ij} is approximated by interfacial tension, denoted γ^{ij}. The internal energy of the porous matrix is constant in this example and is therefore set to zero.

Candidate REVs are of different sizes, see **Table 2**. The 5.4 × 6 mm (green), and 10.4 × 12 mm (blue) candidate REVs are shown in **Figure 3**. For all candidate REVs, U^{REV} is calculated according to Equation (17) at each time step. Since the measured saturations and interfacial areas are fluctuating in time, so is the internal energy. A time-step weighted histogram of the internal energy presents the probability distribution.

The probability distributions of U^{REV} are shown in **Figure 4** for the 5.2 × 6 mm (green) and 10.4 × 12 mm (blue) candidate REVs. In both plots, the vertical lines represent the internal energy the REV would have if it were occupied by one of the fluids alone. We denote the difference in internal energy between these two single-phase states by ΔU^{REV}.

The mean value of the U^{REV} for all candidate REVs are given in **Table 2**, along with mean density $u = U^{\mathrm{REV}}/V^{\mathrm{REV}}$ and the standard deviation of U^{REV} divided by ΔU^{REV}. The latter

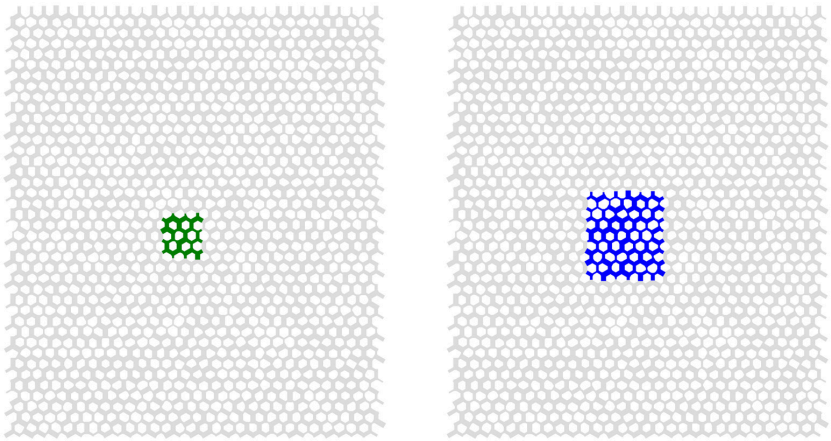

FIGURE 3 | Illustration of the link network and two of the candidate REVs under consideration. The left candidate REV (green) is 5.2 × 6 mm and the right candidate REV (blue) is 10.4 × 12 mm.

TABLE 2 | Mean values of U^{REV} and u for candidate REVs of different sizes, along with the standard deviation of U^{REV} divided by ΔU^{REV}. The latter quantity represents a measure of the relative size of the fluctuations in U^{REV}.

Candidate REV Size	**Mean $\left(U^{\mathrm{REV}}\right)$ /J**	**$\pm\left(U^{\mathrm{REV}}\right)$ $/\Delta U^{\mathrm{REV}}$**	**Mean (u) / 10^7 J m^{-3}**
5.2 × 6.0 mm	−2.82	0.069	−6.04
7.8 × 9.0 mm	−5.46	0.047	−5.19
10.4 × 12.0 mm	−9.60	0.037	−5.13
13.0 × 15.0 mm	−15.4	0.028	−5.25
15.6 × 18.0 mm	−22.2	0.024	−5.27
18.3 × 21.0 mm	−29.9	0.021	−5.22
20.8 × 24.0mm	−39.1	0.017	−5.23

quantity is a measure of the relative size of the fluctuations in U^{REV}. Due to the additivity of U^{REV}, the mean values of U^{REV} increases roughly proportional to the candidate REV size. But this happens only after the REV has reached a minimum size, here 7.8 × 9.0 mm. For the larger candidate REVs, the mean value of u changes little as the size increases. The relative size of the fluctuations in U^{REV} decreases in proportion to the linear size of the candidate REVs.

This example indicates that it makes sense to characterize the internal energy of a porous medium in terms of an internal energy density as defined by Equation (11), given that the size of the REV is appropriately large. About 100 links seem to be enough in this case. This will vary with the type of porous medium, cf. the 2D square network model of Savani et al. [28].

4. HOMOGENEITY ON THE MACRO-SCALE

Before we address any transport problems, consider again the system pictured in **Figure 1** (the white box). All REVs have variables and densities as explained above. By integrating to a somewhat larger volume V, using the densities defined, we obtain the set of basis variables, (U, S, M_i), in V. The internal energy U of the system is an Euler homogeneous function of first order in S, V, M_i:

$$U(\lambda S, \lambda V, \lambda M_i) = \lambda U(S, V, M_i) \tag{18}$$

where λ is a multiplication factor. The internal energy U, volume V, entropy S, and component mass M_i, obey therefore the Gibbs equation;

$$dU = \left(\frac{\partial U}{\partial S}\right)_{V,M_i} dS + \left(\frac{\partial U}{\partial V}\right)_{S,M_i} dV + \sum_{i=1}^{n} \left(\frac{\partial U}{\partial M_i}\right)_{S,V,M_j} dM_i \tag{19}$$

No special notation is used here to indicate that U, S, V, M_i are properties on the macro-scale. Given the heterogeneous nature on the micro-scale, the internal energy has contributions from all parts of the volume V, including from the excess surface and line energies. By writing Equation (18) we find that the normal thermodynamic relations apply for the heterogeneous system at equilibrium, for the additive properties U, S, V, M_i, obtained from sums of the bulk-, excess surface-, and excess line-contributions.

We can then move one more step and use Gibbs equation to *define* the temperature, the pressure, and chemical potentials on the macro-scale as partial derivatives of U:

$$T \equiv \left(\frac{\partial U}{\partial S}\right)_{V,M_i}, \quad p \equiv -\left(\frac{\partial U}{\partial V}\right)_{S,M_i}, \quad \mu_i \equiv \left(\frac{\partial U}{\partial M_i}\right)_{S,V,M_j} \tag{20}$$

The temperature, pressure, and chemical potentials on the macro-scale are, with these formulas, defined as partial derivatives of the internal energy. This is normal in

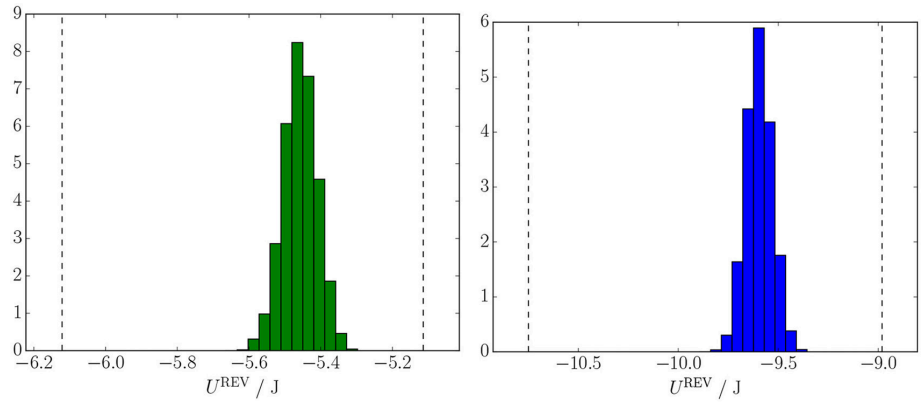

FIGURE 4 | Probability distributions of internal energy in two the candidate REVs. The left candidate REV (green) is 5.2 ×6 mm and the right candidate REV (blue) is 10.4 ×12 mm. In each plot, the left dashed line represents the internal energy the candidate REV would have if it contained non-wetting fluid only and the right dashed line represents the internal energy the candidate REV would have if it contained wetting fluid only.

thermodynamics, but the meaning is now extended. In a normal homogeneous, isotropic system at equilibrium, the temperature, pressure, and chemical equilibrium refer to a homogeneous volume element. The temperature of the REV is a temperature representing all phases, interfaces and lines combined, and the chemical potential of i is similarly obtained from the internal energy of all phases. Therefore, there are only one T, p, and μ_i for the REV. The state can be represented by the (blue) dots in **Figure 1**.

On the single pore level, the pressure and temperature in the REV will have a distribution. In the two immiscible-fluid-example the pressure, for instance, will vary between a wetting and a non-wetting phase because of the capillary pressure. One may also envision that small phase changes in one component (e.g., water) leads to temperature variations due to condensation or evaporation. Variations in temperature will follow changes in composition.

The intensive properties are *not* averages of the corresponding entities on the pore-scale over the REV. This was pointed out already by Gray and Hassanizadeh [3]. The definitions are derived from the total internal energy only, and this makes them uniquely defined. It is interesting that the intensive variables do not depend on how we split the energy into into bulk and surface terms inside the REV.

By substituting Equation (20) into Equation (19) we obtain the Gibbs equation for a change in total internal energy on the macro-scale

$$dU = TdS - pdV + \sum_{i=1}^{n} \mu_i dM_i \tag{21}$$

As a consequence of the condition of homogeneity of the first order, we also have

$$U = TS - pV + \sum_{i=1}^{n} \mu_i M_i \tag{22}$$

The partial derivatives T, p and μ_i are homogeneous functions of the zeroth order. This implies that

$$T(\lambda S, \lambda V, \lambda M_i) = T(S, V, M_i) \tag{23}$$

Choosing $\lambda = 1/V$ it follows that

$$T(S, V, M_i) = T(s, 1, \rho_i) = T(s, \rho_i) \tag{24}$$

The temperature therefore depends only on the subset of variables $s \equiv S/V, \rho_i \equiv M_i/V$ and not on the complete set of variables S, V, M_i. The same is true for the pressure, p, and the chemical potentials, μ_i. This implies that T, p and μ_i are not independent. We proceed to repeat the standard derivation of the Gibbs-Duhem equation which makes their interdependency explicit.

The Gibbs equation on the macro-scale in terms of the densities follows using Equations (21) and (22)

$$du = Tds + \sum_{i=1}^{n} \mu_i d\rho_i \tag{25}$$

which can alternatively be written as

$$ds = \frac{1}{T}du - \frac{1}{T}\sum_{i=1}^{n} \mu_i d\rho_i \tag{26}$$

The Euler equation implies

$$u = Ts - p + \sum_{i=1}^{n} \mu_i \rho_i \tag{27}$$

By differentiating Equation (27) and subtracting the Gibbs equation (25), we obtain in the usual way the Gibbs-Duhem equation:

$$dp = sdT + \sum_{i=1}^{n} \rho_i d\mu_i$$

This equation makes it possible to calculate p as a function of T and μ_i and shows how these quantities depend on one another.

We have now described the heterogeneous porous medium by a limited set of coarse-grained thermodynamic variables. These average variables and their corresponding temperature, pressure, and chemical potentials, describe a coarse-grained homogeneous mixture with variables which reflect the properties of the class of porous media. In standard equilibrium thermodynamics, Gibbs' equation applies to a homogeneous phase. We have extended this use to be applicable for heterogeneous systems at the macro-scale. On this scale, the heterogeneous system (the REV) is then regarded as being in local equilibrium. Whether or not the chosen procedure is viable, remains to be tested. We refer to the section 7 of this paper for more discussion and to a paper to follow [18] for an experimental program.

5. ENTROPY PRODUCTION IN POROUS MEDIA

Gradients in mass- and energy densities produce changes in the variables on the macro-scale. These lead to transport of heat and mass. Our aim is to find the equations that govern this transport across the REV. We therefore expose the system to driving forces and return to **Figure 1**.

The balance equations for masses and internal energy of a REV are

$$\frac{\partial \rho_i}{\partial t} = -\frac{\partial}{\partial x} J_i \tag{28}$$

$$\frac{\partial u}{\partial t} = -\frac{\partial}{\partial x} J_u = -\frac{\partial}{\partial x}\left[J_q^{'} + \sum_{i=1}^{n} J_i H_i \right] \tag{29}$$

The transport on this scale is in the $x-$direction only. The mass fluxes, J_i, and the flux of internal energy, J_u, are all macro-scale fluxes. The internal energy flux is the sum of the measurable (or sensible) heat flux, $J_q^{'}$ and the partial specific enthalpy (latent heat), H_i (in J.kg^{-1}) times the component fluxes, J_i, see [3, 9, 11] for further explanations. Component m (the porous medium) is not moving and is the convenient frame of reference for the fluxes.

The entropy balance on the macro-scale is

$$\frac{\partial s}{\partial t} = -\frac{\partial}{\partial x} J_s + \sigma \tag{30}$$

Here J_s is the entropy flux, and σ is the entropy production which is positive definite, $\sigma \geq 0$ (the second law of thermodynamics). We can now derive the expression for σ in the standard way [9, 11], by combining the balance equations with Gibbs' equation. The entropy production is the sum of all contributions within the REV.

In the derivations, we assume that the Gibbs equation is valid for the REV also when transport takes place. Droplets can form at high flow rates, while ganglia may occur at low rates. We have seen above that there is a minimum size of the REV, for which the Gibbs equation can be written. When we assume that the Gibbs equation applies, we implicitly assume that there exists a uniquely defined state. The existence of such an ergodic state was postulated by Hansen and Ramstad [29]. Valavanides and Daras used it in their DeProF model for two-phase flow in pore networks [30]. Experimental evidence for the assumption was documented by Erpelding [31].

Under the conditions that we demand valid for the REV, the Gibbs Equation (26) keeps its form during a time interval dt, giving

$$\frac{\partial s}{\partial t} = \frac{1}{T}\frac{\partial u}{\partial t} - \frac{1}{T}\sum_{i=1}^{n} \mu_i \frac{\partial \rho_i}{\partial t} \tag{31}$$

We can now introduce the balance equations for mass and energy into this equation, see [11] for details. By comparing the result with the entropy balance, Equation (30), we identify first the entropy flux, J_s,

$$J_s = \frac{1}{T} J_q' + \sum_{i=1}^{n} J_i S_i \tag{32}$$

The entropy flux is composed of the sensible heat flux over the temperature plus the sum of the specific entropies carried by the components. The form of the entropy production, σ, depends on our choice of the energy flux, J_u or J_q'. The choice of form is normally motivated by practical wishes; what is measurable or computable. We have

$$\begin{aligned} \sigma &= J_u \frac{\partial}{\partial x}\left(\frac{1}{T}\right) - \sum_{i=1}^{n} J_i \frac{\partial}{\partial x}\left(\frac{\mu_i}{T}\right) \\ &= J_q' \frac{\partial}{\partial x}\left(\frac{1}{T}\right) - \frac{1}{T}\sum_{i=1}^{n} J_i \frac{\partial}{\partial x}\mu_{i,T} \end{aligned} \tag{33}$$

These expressions are equivalent formulations of the same physical phenomena. When we choose J_u as variable with the conjugate force $\partial(1/T)/\partial x$, the mass fluxes are driven by minus the gradient in the Planck potential μ_i/T. When, on the other hand we choose J_q' as a variable with the conjugate force $\partial(1/T)/\partial x$, the mass fluxes are driven by minus the gradient in the chemical potential at constant temperature over this temperature. The entropy production defines the independent thermodynamic driving forces and their conjugate fluxes. We have given two possible choices above to demonstrate the flexibility. The last expression is preferred for analysis of experiments.

In order to find the last line in Equation (33) from the first, we used the thermodynamic identities $\mu_i = H_i - TS_i$ and $\partial(\mu_i/T)/\partial(1/T) = H_i$ as well as the expression for the energy flux given in Equation (29). Here S_i is the partial specific entropy (in J.kg^{-1}.K^{-1}).

5.1. The Chemical Potential at Constant Temperature

The derivative of the chemical potential at constant temperature is needed in the driving forces in the second line for σ in Equation

(33). For convenience we repeat its relation to the full chemical potential [9]. The differential of the full chemical potential is:

$$d\mu_i = -S_i dT + V_i dp + \sum_{j=1}^{n} \left(\frac{\partial \mu_i}{\partial M_j}\right)_{p,T,M_i} dM_j \tag{34}$$

where S_i, V_i, and $(\partial\mu_i/\partial M_j)_{p,T,M_i}$ are partial specific quantities. The partial specific entropy and volume are equal to:

$$S_i = -\left(\frac{\partial \mu_i}{\partial T}\right)_{p,M_j}, \; V_i = \left(\frac{\partial \mu_i}{\partial p}\right)_{T,M_j} \tag{35}$$

and the last term of Equation (33) is denoted by

$$d\mu_i^c = \sum_{j=1}^{n} \left(\frac{\partial \mu_i}{\partial M_j}\right)_{p,T,M_i} dM_j \tag{36}$$

By reshuffling, we have the quantity of interest as the differential of the full chemical potential plus an entropic term;

$$d\mu_{i,T} \equiv d\mu_i + S_i dT = V_i dp + d\mu_i^c \tag{37}$$

The differential of the chemical potential at constant temperature is

$$\frac{d\mu_{i,T}}{dx} = \frac{d\mu_i^c}{dx} + V_i \frac{dp}{dx} \tag{38}$$

With equilibrium in the gravitational field, the pressure gradient is $dp/dx = -\rho g$, where ρ is the total mass density and g is the acceleration of free fall [32]. The well known separation of components in the gravitational field is obtained, with $d\mu_{i,T} = 0$ and

$$\frac{d\mu_i^c}{dx} = \frac{RT}{W_i} \frac{d\ln(\hat{S}_i y_i)}{dx} = V_i \rho g \tag{39}$$

where W_i is the molar mass (in kg.mol^{-1}), $\hat{S}_i$ the saturation, and y_i the activity coefficient of component *i*. The gas constant, R, has dimension J.K^{-1}.mol^{-1}. The gradient of the mole fraction of methane and decane in the geothermal gradient of the fractured carbonaceous Ekofisk oil field, was estimated to 5×10^{-4}m^{-1} [33], in qualitative agreement with observations. We replace $d\mu_{i,T}$ below using these expressions.

It follows from Euler homogeneity that the chemical potentials in a (quasi-homogeneous) mixture are related by $0 = SdT - Vdp + \sum_{j=1}^{n} \rho_j d\mu_j$, which is Gibbs-Duhem's equation. By introducing Equation 37 into this equation we obtain an equivalent expression, to be used below:

$$0 = \sum_{j=1}^{n} \rho_j d\mu_j^c \tag{40}$$

6. TRANSPORT OF HEAT AND TWO-PHASE FLUIDS

Consider again the case of two immiscible fluids of single components, one more wetting (w) and one more non-wetting (n). The entropy production in Equation (33) gives,

$$\sigma = J_q' \frac{\partial}{\partial x}\left(\frac{1}{T}\right) - \frac{1}{T}\left(J_w \frac{\partial \mu_{w,T}}{\partial x} + J_n \frac{\partial \mu_{n,T}}{\partial x}\right) \tag{41}$$

The solid matrix is the frame of reference for transport, $J_r = 0$ and does not contribute to the entropy production. The volume flux is frequently measured, and we wish to introduce this as new variable

$$J_V = J_n V_n + J_w V_w \tag{42}$$

Here J_V has dimension (m^3.m^{-2}.s^{-1} = m.s^{-1}), and the partial specific volumes have dimension m^3.kg^{-1}. The volume flows used by Hansen et al. [16] are related to ours by $J_n \upsilon_n = \hat{S}_n \upsilon_n$, $J_w \upsilon_w = \hat{S}_w \upsilon_w$ and $J_V = \upsilon = \hat{S}_n \upsilon_n + \hat{S}_w \upsilon_w$.

The chemical potential of the solid matrix may not vary much if the composition of the solid is constant across the system. We assume that this is the case ($d\mu_m^c \approx 0$), and use Equation (40) to obtain

$$0 = \rho_n d\mu_n^c + \rho_w d\mu_w^c \tag{43}$$

The entropy production is invariant to the choice of variables. We can introduce the relations above and the explicit expression for $d\mu_{i,T}$ into Equation (41), and find the practical expression:

$$\sigma = J_q' \frac{\partial}{\partial x}\left(\frac{1}{T}\right) - J_V \frac{1}{T}\frac{\partial p}{\partial x} - \nu_D \frac{\rho_w}{T}\frac{\partial \mu_w^c}{\partial x} \tag{44}$$

In the last line, the difference velocity ν_D is

$$\nu_D = \frac{J_w}{\rho_w} - \frac{J_n}{\rho_n} \tag{45}$$

This velocity (in m/s) describes the relative movement of the two components within the porous matrix on the macro-scale. In other words, it describes the ability of the medium to separate components. The main driving force for separation is the chemical driving force, related to the gradient of the saturation. The equation implies that also temperature and pressure gradients may play a role for the separation.

The entropy production has again three terms, one for each independent driving force. With a single fluid, the number of terms is two. The force conjugate to the heat flux is again the gradient of the inverse temperature. The entropy production, in the form we can obtain, Equations (41) or (44), dictates the constitutive equations of the system.

6.1. A Path of Sister Systems

As pointed out above, through the construction of the REV we were able to create a continuous path through the system, defined by the thermodynamic variables of the REVs. The path was illustrated by a sequence of dots in **Figure 1**. Such a path

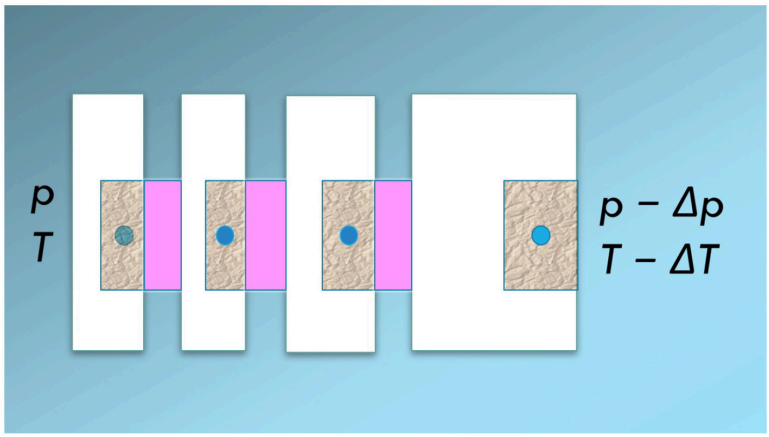

FIGURE 5 | A one-dimensional heterogeneous system cut into slices. Each cut is brought in equilibrium with a homogeneous (pink) mixture at the same temperature and pressure as the REV.

must exist, to make integration possible. Also continuum mixture theory hypothesizes such a path [4]: Hilfer introduced a series of *mixture* states, to define an integration path across the porous system, see e.g., [4].

The path created in section 2 is sufficient as a path of integration across the medium. The access to and measurement of properties in the REVs is another issue. It is difficult, if not impossible, to measure *in situ* as stated upfront. The measurement probe has a minimum extension (of some mm), and the measurement will represent an average over the surface of the probe. For a phase with constant density, the average is well-defined and measurable. A link between the state of the REV and a state where measurements are possible, is therefore needed. We call the state that provides this link a sister state.

Consider again the path of REVs in the direction of transport. To create the link between the REV and its sister state, consider the system divided into slices, see **Figure 5**. The slice (the sister system) contains homogeneous (pink) phases in equilibrium with the REV at the chosen location.

We hypothesize that we can find such sister states; in the form of a multi-component mixture with temperature, pressure, and composition such that equilibrium can be obtained with the REV-variables at any slice position. The variables of the sister state can then be measured the normal way. The chemical potential of a component in the sister state can, for instance, be found by introducing a vapor phase above this state and measure the partial vapor pressure. We postulate thus that a sister state can be found, that obey the conditions

$$T = T^s \tag{46}$$

$$p = p^s \tag{47}$$

$$\mu_i = \mu_i^s \tag{48}$$

Here $i = 1, ..., n$ are the components in the REV, and superscript s denotes the sister state. With the sister states available, we obtain an experimental handle on the variables of the porous medium. The hypothesis must be checked, of course.

The series of sister states have the same boundary conditions as the REV-states, by construction, and the overall driving forces will be the same. Between the end states, we envision the non-equilibrium system as a staircase. Each step in the stair made up of a REV is in equilibrium with a step of the sister-state-stair. Unlike the states inside the porous medium, the sister states are accessible for measurements, or determination of T, p, and μ_i. The driving forces of transport can then be described by the sequence of the sister states.

7. DISCUSSION

We have shown in this work how it is possible to extend the method of classical non-equilibrium thermodynamics [9] to describe transport in porous media. This was possible by

- constructing a REV in terms of a basis set of additive variables
- assuming that the REV is Euler homogeneous of degree one in the basis set.

The method is developed in the same manner as the classical theory is, but it extends the classical theory through the variable choice. The assumption about Euler homogeneity is the same for homogeneous (classical) as well as the heterogeneous porous media. The new variable set is necessary in order to account for the presence of the porous medium, i.e., the contributions from interfaces and contact line energies. Film formation in the pore is excluded. The properties of the porous medium will therefore enter in the definition of the variable set. The consequences of the choice will be elaborated in an article to come [18].

The classical equations have been written for single-phase systems, as these can be regarded as homogeneous on the molecular scale [34]. Equations (41) and (44), for instance, are well-established in theory of transport for polymer membranes,

see e.g., [34]. The idea of the sister states to define the state of a porous media with larger pores and immiscible phases was inspired by this. The way of dealing with lack of knowledge of variables inside the system was for instance used in polymer membrane transport long ago, see [35, 36]. The procedure, to introduce a series of equilibrium states, each state in equilibrium with the membrane at some location between the external boundaries, was first used by Scatchard [35], and experimentally verified much later [36, 37].

With the condition of Euler homogeneity we can set up the Gibbs equation, which is essential in the derivation of the entropy production. The total entropy production follows directly from the new set of variables and Euler homogeneity. This procedure is new, when compared to the literature where focus was set on the single phases, interfaces and contact lines [2, 3, 5].

The REV obeys local equilibrium in the sense that it obeys Gibbs equation. Some support for this can be found in the literature. Prigogine and Mazur [38] investigated a mixture of two fluids using non-equilibrium thermodynamics. Their system consisted of superfluid - and normal helium. Two pressures were defined, one for each of the two fluids. The interaction between the two fluids was small, meaning that one phase flowed as if the other one (aside from a small frictional force) was not there. The situation here is similar, as we may have different liquid pressures inside the REV. But the interaction between the two immiscible components in our porous medium is large, not negligible as in the helium case.

We are adding the contributions from each phase, interface, and line to overall variables for the REV. But unlike Gray and Miller [5] and others [39], we do not need to require that thermodynamic equilibrium relations are obeyed within the REV. This may seem to be drastic, but the Gibbs-Duhem equation follows from Euler homogeneity alone, cf. section 5. The assumption of Euler homogeneity is sufficient to obtain the Gibbs-Duhem equation. In this aspect, we agree with those who use that equation for porous media, see e.g., [6].

The surface areas and the contact line lengths are not *independent* variables in our representation of the REV. These variables have been included through the assumption that the basic variables of the REV are additive. This means that a REV of a double size has double the energy, entropy, and mass, but also double the surface areas of various types and double the line lengths. The contraction to the small set of variables depend on this assumption. Otherwise, we need to expand the variable set. This can be done, however. A promising route seems to include Minkovski integrals [40]. Our approach can be compared to the up-scaling method used in Smoothed Particle Hydrodynamics [20]. Inspired by the idea behind smoothed particle hydrodynamics, we can also define a normalized weight function $W(\mathbf{r})$, such that a microscopic variable $a(\mathbf{r})$ may be represented by its average, defined as

$$\overline{a}(\mathbf{r}) \equiv \int d\mathbf{r}' W(\mathbf{r}-\mathbf{r}')a(\mathbf{r}'). \tag{49}$$

For example, if $a(\mathbf{r}')$ is the local void fraction in a porous material as determined from samples of the material, $\overline{a}(\mathbf{r})$ is the average porosity of the medium. The average is assigned to the point $\mathbf{r}$ and varies smoothly in space. The average porosity $\overline{a}(\mathbf{r})$ would then be suitable for e.g., a reservoir simulation at the macro-scale.

In general, the system is subject to external forces and its properties are non-uniform. The choice of $W(\mathbf{r})$ is therefore crucial in that it defines the extent of the coarse-graining and the profile of the weighting. The illustration in **Figure 1** alludes to a weight function that is constant inside a cubic box and zero outside, but other choices are possible. Popular choices used in mesoscale simulations are the Gaussian and spline functions (see [20] for details). A convenient feature of the coarse-graining is that the average of a gradient of a property a is equal to the gradient of the average.

$$\nabla\overline{a}(\mathbf{r}) = \overline{\nabla a(\mathbf{r})} \tag{50}$$

Similarly the average of a divergence of a flux is equal to the divergence of the average. This implies that balance equations, which usually contain the divergence of a flux, remain valid after averaging. Time averages can also be introduced along the same lines.

Time scales relevant to porous media transport are usually large (minutes, hours); and much larger than times relevant for the molecular scale. Properties can change not only along the coordinate axis, but also on the time scale. In the present formulation, any change brought about in the REV must retain the validity of the Gibbs equation. As long as that is true, we can use the equations, also for transient phenomena.

The outcome of the derivations will enable us to deal with a wide range of non-isothermal phenomena in a systematic manner, from frost heave to heterogeneous catalysis, or multi-phase flow in porous media. We will elaborate on what this means in the next part of this work. In particular, we shall give more details on the meaning of the additive variables and the consequences for the REV pressure in a paper to come [18]. We will there return to the meaning of the REV variables and how they will contribute and help define new driving forces of transport.

8. CONCLUDING REMARKS

We have derived the entropy production for transport of heat and immiscible, single components (phases) in a porous medium. The derivations have followed standard non-equilibrium thermodynamics for heterogeneous systems [11]. The only, but essential, difference to current theories, has been the fact that we write all these equations for a porous medium on the macro-scale for the REV of a minimum size using its total entropy, energy and mass. These equations are mostly written for the separate contributions. Broadly speaking, we have been zooming out our view on the porous medium to first define some states that we take as thermodynamic states because they obey Euler homogeneity. The states are those illustrated by the dots in **Figure 1**. In order to define these states by experiments, we constructed the sister states of **Figure 5**.

The advantage of the present formulations is this; it is now possible to formulate the transport problem on the scale of a flow experiment in accordance with the second law of thermodynamics, with far less variables, see [18]. This opens up

the possibility to test the thermodynamic models for consistency and compatibility with the second law. Such tests will be explicitly formulated together with the constitutive equations, in the next part of this work [18].

AUTHOR CONTRIBUTIONS

SK and DB defined the variables of the REV and the sister states and wrote the first draft. AH, BH, and OG critically examined all proposals and contributed to revisions on the MS.

FUNDING

The authors are grateful to the Research Council of Norway through its Centers of Excellence funding scheme, project number 262644, PoreLab.

ACKNOWLEDGMENTS

Per Arne Slotte is thanked for stimulating discussions.

REFERENCES

1. Bedford A. Theories of immiscible and structured mixtures. *Int J Eng Sci.* (1983) **21**:863–960.
2. Hassanizadeh SM, Gray WG. Mechanics and thermodynamics of multiphase flow in porous media including interphase boundaries. *Adv Water Resour.* (1990) **13**:169–86.
3. Gray WG, Hassanizadeh SM. Macroscale continuum mechanics for multiphase porous-media flow including phases, interfaces, common lines and commpon points. *Adv Water Resour.* (1998) **21**:261–81.
4. Hilfer R. Macroscopic equations of motion for two phase flow in porous media. *Phys Rev E* (1998) **58**:2090.
5. Gray WG, Miller CT. *Introduction to the Thermodynamically Constrained Averaging Theory for Porous Medium Systems.* Cham: Springer (2014).
6. Revil A. Transport of water and ions in partially water-saturated porous media. *Adv Water Resour.* (2017) **103**:119–38. doi: 10.1016/j.advwatres.2016.07.016
7. Onsager L. Reciprocal relations in irreversible processes. I. *Phys Rev.* (1931) **37**:405–26.
8. Onsager L. Reciprocal relations in irreversible processes. II. *Phys Rev.* (1931) **38**:2265–79.
9. de Groot SR, Mazur P. *Non-Equilibrium Thermodynamics.* London: Dover (1984).
10. Bedeaux D, Albano AM, Mazur P. Boundary conditions and non-equilibrium thermodynamics. *Phys A* (1976) **82**:438–62.
11. Kjelstrup S, Bedeaux D. *Non-Equilibrium Thermodynamics of Heterogeneous Systems.* Singapore: Wiley (2008).
12. Zhu L, Koper GJM, Bedeaux D. Heats of transfer in the diffusion layer before the surface and the surface temperature for a catalytic hydrogen oxidation reaction (H_2+(1/2)O_2 = H_2O). *J Phys Chem A* (2006) **110**:4080–8. doi: 10.1021/jp056301i
13. Richter F, Gunnarshaug AF, Burheim OS, Vie PJS, Kjelstrup S. Single electrode entropy change for $LiCoO_2$ electrodes. *ECS Trans.* (2017) **80**:219–38. doi:10.1149/08010.0219ecst
14. Førland T, Ratkje SK. Irreversible thermodynamic treatment of frost heave. *Eng Geol.* (1981) **18**:225–9.
15. Huyghe JM, Nikooee E, Hassanizadeh SM. Bridging effective stress and soil water retention equations in deforming unsaturated porous media: a thermodynamic approach. *Transp Porous Med.* (2017) 117:349–65. doi: 10.1007/s11242-017-0837-9
16. Hansen A, Sinha S, Bedeaux D, Kjelstrup S, Gjennestad MA, Vassvik M. Relations between seepage velocities in immiscible, incompressible two-phase flow in porous media. arXiv:1712.06823. Availbale online at: https://arxiv.org/abs/1712.06823
17. Kjelstrup S, Bedeaux D, Hansen A, Hafskjold B, Galteland O. Non-isothermal two-phase flow in porous media. The entropy production. (2018) *arXiv.1805.03943*.
18. Kjelstrup S, Bedeaux D, Hansen A, Hafskjold B, Galteland O. Non-isothermal two-phase flow in porous media. Constitutive equations. (2018) *arXiv.1809.10378*.
19. Tallakstad KT, Løvoll G, Knudsen HA, Ramstad T, Flekkøy EG, Måløy KJ. Steady-state, simultaneous two-phase flow in porous media: an experimental study. *Phys Rev E* (2009) **80**:036308. doi: 10.1103/PhysRevE.80.036308
20. Monaghan JJ. Smoothed particle hydrodynamics. *Annu Rev Astron Astrophys.* (1992) **30**:543–74.
21. Gibbs JW. *The Scientific Papers of J.W. Gibbs.* New York, NY: Dover (1961).
22. Sinha S, Hansen A, Bedeaux D, Kjelstrup S, Savani I, Vassvik M. Effective rheology of bubbles moving in a capillary tube. *Phys Rev E* (2013) **87**:025001. doi: 10.1103/PhysRevE.87.025001
23. Aker E, Måløy KJ, Hansen A, Batrouni G. A two-dimensional network simulator for two-phase flow in porous media. *Trans Porous Media* (1998) **32**:163–86.
24. Gjennestad MA, Vassvik M, Kjelstrup S, Hansen A. Stable and efficient time integration at low capillary numbers of a dynamic pore network model for immiscible two-phase flow in porous media. *Front Phys.* (2018) 6:56. doi: 10.3389/fphy.2018.00056
25. Linstrom PJ, Mallard WG, editors. *NIST Chemistry WebBook, NIST Standard Reference Database Number 69.* Gaithersburg MD: National Institute of Standards and Technology (2018).
26. Neumann A. Contact angles and their temperature dependence: thermodynamic status, measurement, interpretation and application. *Adv Colloid Interfaces* (1974) **4**:105–91.
27. Zeppieri S, Rodríguez J, López de Ramos A. Interfacial tension of alkane + water systems. *J Chem Eng Data* (2001) **46**:1086–8. doi: 10.1021/je000245r
28. Savani I, Sinha S, Hansen A, Kjelstrup S, Bedeaux D, Vassvik M. A Monte Carlo procedure for two-phase flow in porous media. *Transp Porous Med.* (2017) **116**:869–88. doi: 10.1007/s11242-016-0804-x
29. Hansen A, Ramstad T. Towards a thermodynamics of immiscible two-phase steady-state flow in porous media. *Comp Geosci.* (2009) **13**:227. doi: 10.1007/s10596-008-9109-7
30. Valavanides MS, Daras T. Definition and counting of configurational microstates in steady-state two-phase flows in pore networks. *Entropy* (2016) **18**:1–28. doi: 10.3390/e18020054
31. Erpelding M, Sinha S, Tallakstad KT, Hansen A, Flekkøy EG, Måløy KJ. History independence of steady state in simultaneous two-phase flow through two-dimensional porous media. *Phys Rev E* (2013) **88**:053004. doi: 10.1103/PhysRevE.88.053004
32. Førland KS, Førland T, Ratkje SK. *Irreversible Thermodynamics. Theory and Applications.* Chichester: Wiley (1988).
33. Holt T, Lindeberg E, Ratkje SK. *The Effect of Gravity and Temperature Gradients on the Methane Distribution in Oil Reservoirs*. Society of Petroleum Engineers, SPE-11761-MS (1983).
34. Katchalsky A, Curran PF. *Nonequilibrium Thermodynamics in Biophysics.* Harvard University Press (1965).
35. Scatchard G. Ion exchanger electrodes. *Am Chem Soc.* (1953) **75**: 2883–7.
36. Lakshminarayanaiah N, Subrahmanyan V. Measurement of membrane potentials and test of theories. *J Polym Sci Part A* (1964) **2**:4 491–502.

37. Ratkje SK, Holt T, Skrede M. Cation membrane transport:evidence for local validity of nernst–planck equations. *Berich Bunsen Gesell.* (1988) **92**: 825–32.
38. Prigogine I, Mazur P. About two formulations of hydrodynamics and the problem of liquid helium II. *Physica* (1951) **17**: 661–79.
39. Helmig R. *Multiphase Flow and Transport Processes in the Subsurface.* Berlin: Springer (1997).
40. McClure JE, Armstrong RT, Berrill MA, Schluter S, Berg S, Gray WG, et al. A geometric state function for two-fluid flow in porous media. *Phys Rev Fluids* (2018) **3**:084306. doi: 10.1103/PhysRevFluids.3.084306

Conflict of Interest Statement: The authors declare that the research was conducted in the absence of any commercial or financial relationships that could be construed as a potential conflict of interest.

APPENDIX

Mathematical symbols, superscripts, subscripts.

Symbol	Explanation
d	differential
∂	partial derivative
Δ	change in a quantity or variable
Σ	sum
i	subscript meaning component i
m	number of phases
n	subscript meaning non-wetting fluid
w	subscript meaning wetting fluid
p	superscript meaning pore
REV	abbreviation meaning representative elementary volume
r	superscript meaning solid matrix of porous medium
s	superscript meaning interface
u	superscripts meaning internal energy
$\alpha\beta$	superscripts meaning contact area between phases $\alpha\beta$
$\alpha\beta\delta$	superscripts meaning contact line between phases α, β, δ
$\bar{x}$	average of x

Greek symbols

Symbol	Dimension	Explanation
α		superscripts meaning a phase
β		superscript meaning an interface
δ		superscript meaning a contact line
ϕ		porosity of porous medium
γ	$N.m^{-1}$ (N)	surface tension (line tension)
Λ	m	length of contact line
λ		Euler scaling parameter
μ_i	$J.kg^{-1}$	chemical potential of i
ρ_i	$kg.m^{-3}$	density, $\equiv M_i/V$
σ	$J.s^{-1}.K^{-1}.m^{-3}$	entropy production in a homogeneous phase
σ^s	$J.s^{-1}.K^{-1}.m^{-2}$	surface excess entropy production
σ^c	$J.s^{-1}.K^{-1}.m^{-1}$	line excess entropy production
Ω	m^2	surface or interface area

Latin symbols.

Symbol	Dimension	Explanation
G	J	Gibbs energy
M	kg	mass
m	$kg.mol^{-1}$	
d	m	pore length
H_i	$J.kg^{-1}$	partial specific enthalpy of i
J_i	$kg.s^{-1}.m^{-2}$	mass flux of i
J_u	$J.s^{-1}.m^{-2}$	energy flux
J'_q	$J.s^{-1}.m^{-2}$	sensible heat flux
J_V	$m^3.s^{-1}.m^{-2}$	volume flux
l	m	characteristic length of representative elementary volume
L	m	characteristic length of experimental system
L_{jj}, ℓ_{ij}		Onsager conductivity
p	Pa	pressure of REV
Q	$m^3.s^{-1}$	volume flow
$\bar{r}$	m	avarage pore radius
S	$J.K^{-1}$	entropy
s	$J.K^{-1}.m^{-3}$	entropy density
S_i	$J.kg^{-1}K^{-1}$	partial specific entropy of i
$\hat{S}$		degree of saturation, $\equiv V_l/V$
T	K	temperature
t	s	time
U	J	internal energy
u	$J.m^{-3}$	internal energy density
V	m^3	volume
V_i	$m^3.kg^{-1}$	partial specific volume
v_D	$m.s^{-1}$	difference velocity
x	m	coordinate axis
x_i	-	mass fraction of i
W_i	-	$kg.mol^{-1}$ molar mass of i

Article II

Signe Kjelstrup, Dick Bedeaux, Alex Hansen, Bjørn Hafskjold, **Olav Galteland**

Non-isothermal Transport of Multi-Phase Fluids in Porous Media. Constitutive Equations

Frontiers in Physics, 6, 150. (2019)
DOI: 10.3389/fphy.2018.00150

Article II

Article II

frontiers in Physics

ORIGINAL RESEARCH
published: 04 January 2019
doi: 10.3389/fphy.2018.00150

Non-isothermal Transport of Multi-phase Fluids in Porous Media. Constitutive Equations

Signe Kjelstrup[1]*, *Dick Bedeaux*[1], *Alex Hansen*[2], *Bjørn Hafskjold*[1] and *Olav Galteland*[1]

[1] PoreLab, Department of Chemistry, Norwegian University of Science and Technology, Trondheim, Norway, [2] PoreLab, Department of Physics, Norwegian University of Science and Technology, Trondheim, Norway

We define a representative elementary volume of a porous medium in terms of lumped extensive variables, including properties of homogeneous phases, interfaces, and contact lines. Using the grand potential, we define the pressure of the REV in a porous medium in a new manner. From the entropy production expressed in these variables, we develop new constitutive equations for multi-component, multi-phase, macro-scale flow. The system is exposed to temperature, composition, and pressure gradients. New contributions due to varying porosity or surface tension offer explanations for non-Darcy behavior, and predict thermal osmosis special for porous media. An experimental program is suggested to verify Onsager symmetry in the transport coefficients. The analysis is limited to non-deformable systems, which obey Euler homogeneity on the REV level.

Keywords: porous media, energy dissipation, two-phase flow, representative elementary volume, macro-scale, excess surface energy, pressure, non-equilibrium thermodynamics

OPEN ACCESS

Edited by:
Jürgen Vollmer,
Institut für Theoretische Physik,
Universität Leipzig, Germany

Reviewed by:
Constantinos Siettos,
University of Naples Federico II, Italy
Soren Taverniers,
Stanford University, United States

***Correspondence:**
Signe Kjelstrup
signe.kjelstrup@ntnu.no

Specialty section:
This article was submitted to Interdisciplinary Physics, a section of the journal Frontiers in Physics

Received: *08 October 2018*
Accepted: *11 December 2018*
Published: *04 January 2019*

Citation:
Kjelstrup S, Bedeaux D, Hansen A, Hafskjold B and Galteland O (2019) Non-isothermal Transport of Multi-phase Fluids in Porous Media. Constitutive Equations. Front. Phys. 6:150. doi: 10.3389/fphy.2018.00150

1. INTRODUCTION

We have recently [1] derived a coarse-grained form of the entropy production, σ, of a representative elementary volume (REV) in a non-deformable porous medium with multi-phase, multi-component, non-isothermal fluids. The coarse-grained description of the REV was formulated for systems that obey Euler homogeneity. A Gibbs equation could therefore be formulated for the REV itself, and used as a starting point, as is normal in non-equilibrium thermodynamics [2].

Once the entropy production has been found, the driving forces and the constitutive equations can be given. These will be specified here. We shall see that we can obtain the same form of the constitutive equations as for homogeneous systems, but that the driving forces are particular for the porous medium. To write out this particularity, is one aim of the present paper. We shall see that we can obtain a new definition for the pressure in a porous medium and use this and the chemical potential to find the constitutive equations. We are also giving internal relations between experiments particular for the flows, as derived for instance from the Onsager relations.

We consider, as a premise, the REV as a complete thermodynamic system. Hansen and Ramstad [3] suggested this possibility already some time ago. Since then, the hypothesis has been supported through measurements on Hele-Shaw cells [4] and through network simulations [5]. The coarse-grained variables of the REV will fluctuate similar to the variables in a normal thermodynamic state around a mean value.

The procedure that we used to obtain the Gibbs equation for coarse-grained variables [1], assumes that the additive thermodynamic variables of the REV are Euler homogeneous functions of

order one. We give first a brief review of the procedure that defines the basis set of thermodynamic variables (section 2.1). The consequences for the chemical potential and the pressure in the context of porous media is next described (sections 2.2, 2.3). A new definition of the pressure is proposed in section 2.3.

The constitutive equations that follow from the new set of variables, allow us to revisit previously published experimental results. We shall see, for instance, that they can explain deviations from Darcy's law. Such deviations have been observed for small volume flows, also for single fluids like water and water solutions [6–10]. Thresholds and/or deviations from straight lines in plots of flow vs. the overall pressure difference, have been reported. Boersma et al. [8] found a dependency of such a threshold on the average pore radius, $\bar{r}$, for flow in a porous medium made of glass-beads. The observations have, as of yet, no final explanation. When dealing with immiscible fluids, Tallakstad et al. [11] observed a dependence of the flow rate on the square of the pressure difference under steady-state flow conditions. Sinha and Hansen [12] attributed this square dependence to a change in the conductivity, arising from the successive opening of pores due to the mobilization of interfaces when the pressure difference across the sample is increased. The explanation was supported by a mean-field calculation and numerical experiments with a network model. Sinha et al. [10] followed up the original Tallakstad study, done in a two-dimensional model porous medium, both experimentally and computationally in three-dimensional porous media, with the same result.

There is not only a need to better understand deviations from Darcy's law for volume transport. Other driving forces than those related to the pressure difference, are also relevant to porous media transport. Counter-current transport of components can lead to gradients in composition (chemical potential) or chemical driving forces. Injection of cold seawater into a warm hydrocarbon reservoir can create thermal driving forces. This leads to thermal diffusion. The separation of components in a temperature gradient is an example of the Soret effect [13]. A temperature gradient may also lead to a pressure gradient, a phenomenon called thermal osmosis. These effects are not much studied in porous media, see [14] for a review on membranes. There are, for instance, contradictory findings in the literature with respect to the impact of the porous medium on thermal diffusion. Costeseque et al. [15] found that the porous medium had no significant effect on the Soret coefficient, as determined with a horizontal thermodiffusion cell (although the component diffusion was slower in the porous medium). On the other hand, Colombani et al. [16] found by molecular dynamics simulations that both the porosity and the wettability of the porous medium had an effect on the Soret coefficient. The presence of a porous matrix had an impact on the flow pattern and therefore the Soret coefficient according to Davarzani et al. [17]. The role of a thermal driving force is therefore at best unclear. A better understanding of its role could be important. An emerging concept for water cleaning is, for instance, based on thermal osmosis [18]. This process could help produce clean water using industrial and natural heat sources, a very important topic in the world today.

It is thus an open question in porous media theory, how driving forces like the ones mentioned interact, and how the porous medium makes these interactions special [17]. It is therefore also the aim of this work to clarify the coupling that can take place due to some central forces, by constructing a non-equilibrium thermodynamic theory, particular for porous media.

The paper is structured as follows. Section 2 gives first a brief repetition of the variables used to obtain the coarse-grained Gibbs equation and the corresponding entropy production [1]. As before, the analysis applies to systems that obeys Euler homogeneity of the first order. We restrict ourselves to non-deformable media, and systems with a constant ratio of fluid surface area to volume (no film formation). For such systems we proceed to find expressions for the chemical potential and the pressure in the context of non-deformable porous media, cf. sections 2.2, 2.3. We intend to extend the theory to deformable media later.

The expression for the entropy production with these variables is detailed in section 3. The driving forces, due to temperature -, pressure -, and chemical potential gradients, are specified in section 4. They obtain new contributions compared to their normal form in homogeneous systems. In the last section 5, we detail specific cases of component and volume flow in combination with heat transport. An experimental program is suggested in the end to verify Onsager symmetry in the transport coefficients.

2. THERMODYNAMIC VARIABLES FOR THE REV

2.1. The Basis Set of Variables

The central concept in this analysis is the representative elementary volume; the REV [19, 20]. Its characteristic size, l, is small compared to the size (length) of the full system, L, but large compared to the characteristic pore length and diameter. An illustration of the REV is given by the squares in **Figure 1**. The REV (square) consists of several phases and components. The problem is to find the representation on the larger scale. For each point in the porous system, represented by a (blue) dot in **Figure 1**, Kjelstrup et al. [1] used the REV around the dot to obtain the variables of the REV ($U^{\mathrm{REV}}, S^{\mathrm{REV}}, V^{\mathrm{REV}}, M_i^{\mathrm{REV}}$). The variables were given superscript REV to indicate that they constituted the only *independent* variables of the REV. From the Euler homogeneity of these variables, the possibility followed to define the temperature, pressure, and chemical potentials of the REV, (T, p, μ_i). We refer to Kjelstrup et al. [1] and to **Tables A1–A3** in the Appendix for further details, terminology and symbols.

The value of each of these REV-variables was obtained as a sum of contributions from each phase, interface and three-phase contact line present [19, 20]. The contributions are pore-scale variables; they are not *independent* variables on the macro-scale. To assume Euler homogeneity, means to assume that a REV of the double size, for example, has double the energy, entropy, and mass, as well as double the surface areas and double the line

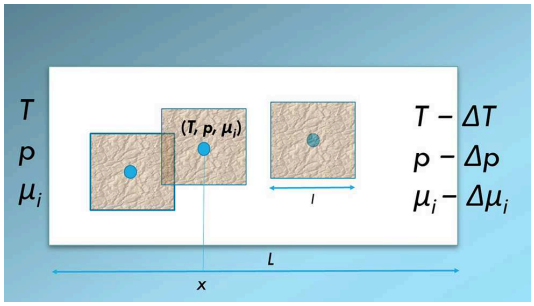

FIGURE 1 | A representative elementary volume (REV) (magenta squares, length l) in a system (white box of length L) that is exposed to for instance a pressure difference, Δp, a temperature difference, ΔT, and differences in chemical potentials $\Delta\mu_i$. A (blue) dot is used to represent the state that characterizes the REV. The set of state variables are positioned on the x-axis: The temperature, pressure and the chemical potentials, $(T, p, \mu_i)(x)$. The figure is adapted from Kjelstrup et al. [1].

lengths of various types. The average surface area, pore length and pore radius, as well as the curvature of the surfaces per unit of volume of the REV, are then everywhere the same. We limit ourselves to non-deformable systems with a constant ratio of fluid surface area to volume, for which this is the case. The extension to deformable systems is more complicated and will be considered later.

A system of k components in m homogeneous phases, has a volume, V^{REV}, with contributions from the homogeneous bulk phases $V^{\alpha,\mathrm{REV}}$, $m \geq \alpha \geq 1$, and the excess line volumes, $V^{\alpha\beta\delta,\mathrm{REV}}$, $m \geq \alpha > \beta > \delta \geq 1$.

$$V^{\mathrm{REV}} = \sum_{\alpha=1}^{m} V^{\alpha,\mathrm{REV}} + \sum_{\alpha>\beta>\delta=1}^{m} V^{\alpha\beta\delta,\mathrm{REV}} \approx \sum_{\alpha=1}^{m} V^{\alpha,\mathrm{REV}} \quad (1)$$

The superscripts denote the relevant phases, surfaces or contact lines. The surface area between phases α, β is denoted $\Omega^{\alpha\beta,\mathrm{REV}}$ while the contact line length between phases $\alpha\beta\delta$ is denoted $\Lambda^{\alpha\beta\delta,\mathrm{REV}}$. The surface area (line length) of the REV is the sum over all areas (lines) in the REV. The excess surface volumes are by construction zero. The excess line volumes are not, because the dividing surfaces in general cross each other along three different lines.

In this first exposition, we neglect contributions to the volume from the contact lines, which are normally small also in porous media. The volume of the pores is

$$V^{p,\mathrm{REV}} = \sum_{\alpha=1}^{m-1} V^{\alpha,\mathrm{REV}} \quad (2)$$

Superscript p is used for pore. The porosity, ϕ, and the degree of saturation, $\hat{S}^{\alpha}$ (saturation for short), are

$$\phi \equiv \frac{V^{p,\mathrm{REV}}}{V^{\mathrm{REV}}} \quad \text{and} \quad \hat{S}^{\alpha} \equiv \frac{V^{\alpha,\mathrm{REV}}}{V^{p,\mathrm{REV}}} = \frac{V^{\alpha,\mathrm{REV}}}{\phi V^{\mathrm{REV}}} \quad (3)$$

Superscript α is used for a component, which is equal to the phase in the present case. The porosity and the saturation do not depend on the size of the REV, and have therefore no REV-superscript.

The mass of component i in the REV, M_i^{REV}, is the sum of the masses in the homogeneous phases of the REV, α, $M_i^{\alpha,\mathrm{REV}}$, $m \geq \alpha \geq 1$, the excess interfacial masses, $M_i^{\alpha\beta,\mathrm{REV}}$, $m \geq \alpha > \beta \geq 1$, and the excess line masses, $M_i^{\alpha\beta\delta,\mathrm{REV}}$, $m \geq \alpha > \beta > \delta \geq 1$. We obtain:

$$M_i^{\mathrm{REV}} = \sum_{\alpha=1}^{m} M_i^{\alpha,\mathrm{REV}} + \sum_{\alpha>\beta=1}^{m} M_i^{\alpha\beta,\mathrm{REV}} + \sum_{\alpha>\beta>\delta=1}^{m} M_i^{\alpha\beta\delta,\mathrm{REV}} \quad (4)$$

where the first term on the right-hand side also can be written in terms of the (constant) densities ρ_i^{α}

$$\sum_{\alpha=1}^{m} M_i^{\alpha,\mathrm{REV}} = \sum_{\alpha=1}^{m} \rho_i^{\alpha} V_i^{\alpha,\mathrm{REV}} \quad (5)$$

Similar contributions follow for the other terms.

We shall often use the example of two immiscible one-component phases w and n in a solid porous material r of porosity ϕ, where contact line contributions are negligible. We can think of phase w as wetting, and n as non-wetting. The mass variables from Equation (4) are for n:

$$M_n^{\mathrm{REV}} = \rho_n V_n^{\mathrm{REV}} \quad (6)$$

while for the other components we obtain also surface excess contributions:

$$\begin{aligned} M_w^{\mathrm{REV}} &= M_w^{\mathrm{REV}} + M_w^{wn,\mathrm{REV}} \\ M_r^{\mathrm{REV}} &= M_r^{\mathrm{REV}} + M_r^{rn,\mathrm{REV}} + M_r^{rw,\mathrm{REV}} \end{aligned} \quad (7)$$

When an interface is formed between two phases, we are free to choose the position of the interface such that one of the components has a zero excess mass. This is the position of the equimolar surface of this component. This position is convenient because the number of variables are reduced. When we use the equimolar surface of n, $M_n^{rn} = M_n^{wn} = 0$, and when we use the equimolar surface of w at the surface of the solid, $M_w^{rw} = 0$. These choices simplify the description of the REV. Therefore, we shall later use the chemical potential of component n, which has a bulk contribution only, see section 2.2.

The expressions for U^{REV} and S^{REV} are similar to Equation (4). This way to construct a REV is reminiscent of the geometric construction of a state function, proposed for flow in porous media by McClure et al. [21].

The basis set of macro-scale variables of the REV $(U^{\mathrm{REV}}, S^{\mathrm{REV}}, V^{\mathrm{REV}}, M_i^{\mathrm{REV}})$ apply to the whole REV. The temperature, pressure and chemical potentials of the REV, (T, p, μ_i), on the macro-scale were next defined, as is normal in thermodynamics, as partial derivatives of the internal energy. These definitions are normal in the sense that they have the same form as they have in homogeneous systems. They are new because the variables (say U^{REV}) have contributions from all

parts of the heterogeneous REV. The intensive variables T, p, and μ_i are then *not* averages of the corresponding variables on the pore-scale. The importance of this was also pointed out by Hassanizadeh and Gray [11,12].

The macro-scale densities of internal energy, entropy and mass; in the example, u, s, ρ_i, do not depend on the *size* of the REV. The densities are therefore convenient when we need to integrate across the system [1]. They are, however, functions of the position of the REV, cf. **Figure 1**.

2.2. The Gibbs Energy of the REV

We proceed to define the Gibbs energy, G, as this variable is needed in the definition of driving forces of transport, see section 3. The general expression for Gibbs energy is

$$G \equiv U + pV - ST = \sum_{i=1}^{k} \mu_i M_i = \sum_{i=1}^{k} G_i \tag{8}$$

where G applies to the REV and G_i is defined for component i in the last identity. All REV variables need be taken into account. In principle, each component can exist in all phases in the REV. But component contributions to the REV are additive, cf. Equation (4). For component i we therefore have

$$\begin{aligned} G_i^{\mathrm{REV}} &\equiv \mu_i^{\mathrm{REV}} M_i^{\mathrm{REV}} \\ &= \sum_{\alpha=1}^{m} G_i^{\alpha,\mathrm{REV}} + \sum_{\alpha>\beta=1}^{m} G_i^{\alpha\beta,\mathrm{REV}} \\ &= \sum_{\alpha=1}^{m} g_i^{\alpha} V^{\alpha,\mathrm{REV}} + \sum_{\alpha>\beta=1}^{m} g_i^{\alpha\beta} \Omega^{\alpha\beta,\mathrm{REV}} \end{aligned} \tag{9}$$

The expression gives the Gibbs energy contributions of component i to the REV. We neglected again possible contributions from contact lines.

In the case of two immiscible, one-component fluids in a non-deformable porous rock, we can take advantage of the simpler description of the non-wetting fluid (see previous subsection) giving

$$G_n^{\mathrm{REV}} \equiv \mu_n M_n^{\mathrm{REV}} = G_n^{n,\mathrm{REV}} = g_n^n V^{n,\mathrm{REV}} \tag{10}$$

For immiscible, one-component fluids, the label indicating the components also gives the phase. The density g_n^n is an average over $V^{n,\mathrm{REV}}$. The local density in the pores may vary around the average.

The total differential of U is used with the definition (8), and we obtain

$$dG = -SdT + Vdp + \sum_i \mu_i dM_i \tag{11}$$

where the superscript REV is skipped for convenience.

2.3. The Pressure of the REV

We find the pressure of the REV by starting, as above, with the extensive property that holds the pressure as the variable. This is the grand potential. The compressional energy of the REV is equal to minus the grand potential:

$$\Upsilon^{\mathrm{REV}}\left(T, V^{\mathrm{REV}}, \mu_i\right) \equiv -pV^{\mathrm{REV}} = U^{\mathrm{REV}} - S^{\mathrm{REV}} T - \sum_{i=1}^{k} \mu_i M_i^{\mathrm{REV}} \tag{12}$$

The grand potential of the REV is additive, which gives

$$\Upsilon^{\mathrm{REV}} = \sum_{\alpha=1}^{m} \Upsilon^{\alpha,\mathrm{REV}} + \sum_{\alpha>\beta=1}^{m} \Upsilon^{\alpha\beta,\mathrm{REV}} + \sum_{\alpha>\beta>\delta=1}^{m} \Upsilon^{\alpha\beta\delta,\mathrm{REV}} \tag{13}$$

We introduce contributions from all phases, surfaces and contact lines. This allows us the possibility to define, in a new way, the pressure of the REV:

$$\begin{aligned} p = \frac{1}{V^{\mathrm{REV}}} \Bigg(& \sum_{\alpha=1}^{m} p^{\alpha} V^{\alpha,\mathrm{REV}} - \sum_{\alpha>\beta=1}^{m} \gamma^{\alpha\beta} \Omega^{\alpha\beta,\mathrm{REV}} \\ & - \sum_{\alpha>\beta>\delta=1}^{m} \gamma^{\alpha\beta\delta} \Lambda^{\alpha\beta\delta,\mathrm{REV}} \Bigg) \end{aligned} \tag{14}$$

The last equation makes it possible to compute the pressure of the REV, p, from the pressures in the bulk phases, the surface tensions and the line tensions. With knowledge of the pressure in the REV, we can find the driving force, $-dp/dx$, in the entropy production, see below, Equation (29).

We explain now how we can define and compute the pressure from Equation (14), using the example of two immiscible single fluids in a non-deformable medium. We shall neglect contact line contributions for simplicity. Such contributions can be added by the same procedure. We follow Equation (14) and sum over the n, w and r bulk phases, and the nr, wr, and nw—interfaces. The situation can be illustrated for a single cylindrical pore, see **Figure 2**.

The figure shows two phases n and w in a tube with the average radius. The wall material is r. Contact areas are therefore $\Omega^{nr,\mathrm{REV}}$, $\Omega^{wr,\mathrm{REV}}$, and $\Omega^{nw,\mathrm{REV}}$. The total surface area of the pore

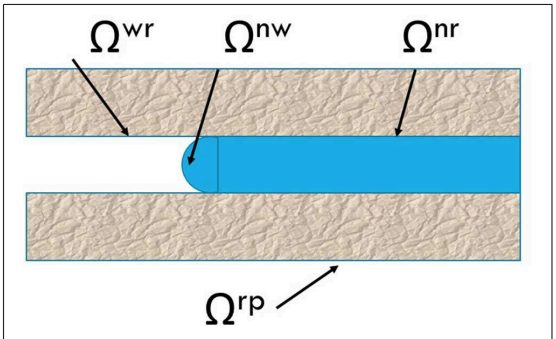

FIGURE 2 | Illustration of contact areas between the phases. A cylindrical pore is chosen as example.

is $\Omega^{rp,\mathrm{REV}} \equiv \Omega^{nr,\mathrm{REV}} + \Omega^{wr,\mathrm{REV}}$. The area $\Omega^{nw,\mathrm{REV}}$ is the smallest contact area shown in the figure. The volumes in Equation (14) depend on the saturation of the non-wetting component, $\hat{S}^n$ and the porosity, ϕ. Neither of the fluids form a film between the surface and the other fluid, so the surfaces satisfy in good approximation

$$\begin{aligned}\Omega^{nr,\mathrm{REV}} &= \hat{S}^n \Omega^{rp,\mathrm{REV}} \text{ and } \Omega^{wr,\mathrm{REV}} = \hat{S}^w \Omega^{rp,\mathrm{REV}} \\ &= (1-\hat{S}^n)\Omega^{rp,\mathrm{REV}} \end{aligned} \tag{15}$$

The pressure of the REV from Equation (14) can then be written as:

$$\begin{aligned} p = &[p^n \hat{S}^n \phi + p^w (1-\hat{S}^n)\phi + p^r(1-\phi)] \\ &-[\hat{S}^n \gamma^{nr} + (1-\hat{S}^n)\gamma^{wr}] \frac{\Omega^{rp,\mathrm{REV}}}{V^{\mathrm{REV}}} - \gamma^{nw} \frac{\Omega^{nw,\mathrm{REV}}}{V^{\mathrm{REV}}} \end{aligned} \tag{16}$$

Contact-line contributions were again not taken along, for simplicity. A consequence of the porous medium being homogeneous is that $\Omega^{rp,\mathrm{REV}}/V^{\mathrm{REV}}$ is the same everywhere. The ratio can be used as a measure of the average curvature of the pore surface, as will be explained below.

The volume-averaged contributions to the pressure from the homogeneous phases is given the symbol $\bar{p}$:

$$\begin{aligned}\bar{p} &= p^n \hat{S}^n \phi + p^w (1-\hat{S}^n)\phi + p^r(1-\phi) \\ &= \left(p^n - p^w\right)\hat{S}^n \phi + p^w \phi + p^r(1-\phi) \end{aligned} \tag{17}$$

The first term in the last equality shows that the saturation gives an important contribution to the volume-averaged pressure. The contributions of the 2nd and 3rd terms are due to p^w and p^r. These contributions are usually constant.

The surface-averaged contributions to the pressure are likewise given a separate symbol:

$$\bar{p}^c = [\hat{S}^n \gamma^{nr} + (1-\hat{S}^n)\gamma^{wr}] \frac{\Omega^{rp,\mathrm{REV}}}{V^{\mathrm{REV}}} + \gamma^{nw} \frac{\Omega^{nw,\mathrm{REV}}}{V^{\mathrm{REV}}} \tag{18}$$

The contribution of $\bar{p}^c$ to the total pressure, p, may be called the capillary pressure. The total pressure of the REV is thus, for short:

$$p = \bar{p} - \bar{p}^c \tag{19}$$

2.3.1. The Case of Approximately Cylindrical Pores

With an (approximately) cylindrical pore geometry, we can define the average radius of the pores by

$$\bar{r} \equiv \frac{2V^{p,\mathrm{REV}}}{\Omega^{rp,\mathrm{REV}}} \tag{20}$$

By introducing $\bar{r}$ into Equation (18) we obtain the capillary pressure

$$\bar{p}^c = \left(\gamma^{nr} - \gamma^{wr}\right)\hat{S}^n \frac{2\phi}{\bar{r}} + \gamma^{wr}\frac{2\phi}{\bar{r}} + \gamma^{nw}\frac{\Omega^{nw,\mathrm{REV}}}{V^{\mathrm{REV}}} \tag{21}$$

Again the first term shows that saturation gives an important contribution. The 2nd term only depends on the temperature and is usually constant. The 3rd term is proportional to the surface area of the fluid-fluid interface. In many experiments this surface area is much smaller than $\Omega^{rp,\mathrm{REV}}$. When that is the case, this term is negligible.

The three equations above give an expression for the REV pressure p for the example system.

To estimate the size of the various contributions, it is convenient to use mechanical equilibrium for the contact line and for the surface, although this condition may not apply to the REV, not even under steady flow conditions. With a balance of forces at the three-phase contact lines, Young's law applies for the surface tensions: $\gamma^{nr} - \gamma^{wr} = \gamma^{nw}\cos\theta$, where θ is the (average) contact angle. When there is furthermore mechanical equilibrium at the fluid-fluid interfaces, the pressure difference between the fluids is given by Young-Laplace's law, $p^n - p^w = 2\gamma^{nw}\cos\theta/\bar{r}$.

In the single-fluid (w) case, Equation (16) simplifies. There are volume-averaged and surface averaged contributions,

$$p = p^w\phi + p^r(1-\phi) - \gamma^{wr}\frac{2}{\bar{r}}\phi \tag{22}$$

We have defined above in detail what we mean by the pressure of a REV. We have found, using the grand potential, that it can be regarded as result of volume- and surface average properties, and we have given some examples. These contributions enter the driving force in Equations (23, 29), to be further discussed below.

3. THE ENTROPY PRODUCTION OF NON-ISOTHERMAL TWO-PHASE FLOW

Pressure-driven mass flows through porous media can lead to gradients in composition and temperature, and vice versa; temperature gradients can lead to mass flow, separation of components and pressure gradients. The interaction of such flows is of interest, and motivated the search for convenient forms of the entropy production [1].

3.1. Expression in Terms of Component Flows

From the Gibbs equation for the REV, we derived the entropy production for transport of heat and two immiscible fluid phases through the REV [1]. With transport in the x-direction only, the entropy production σ of the example system was

$$\sigma = J'_q \frac{\partial}{\partial x}\left(\frac{1}{T}\right) - \frac{1}{T}\left(J_w \frac{\partial \mu_{w,T}}{\partial x} + J_n \frac{\partial \mu_{n,T}}{\partial x}\right) \tag{23}$$

The frame of reference for the mass transport is the non-deformable solid matrix, $J_r \equiv 0$. Here J'_q is the sensible heat flux (in $\mathrm{J.m^{-2}.s^{-1}}$), T is the temperature (in K), J_i is a component flux (in $\mathrm{kg.m^{-2}.s^{-1}}$) and $\partial\mu_{i,T}/\partial x$ is the gradient of the chemical potential (in $\mathrm{J.kg^{-1}.m^{-1}}$) evaluated at constant temperature. All properties are for the REV, so superscript REV is omitted.

The thermal force conjugate to the heat flux is the gradient of the inverse temperature, where the temperature was defined for the REV as a whole, see Kjelstrup et al. [1]. The chemical force

conjugate to the mass flux is the negative gradient of $\mu_{i,T}$ over the temperature. The chemical driving forces are obtained from the full chemical potential, which is the derivative of G with respect to M_i:

$$\mu_i \equiv \left(\frac{\partial G}{\partial M_i}\right)_{T,p} \tag{24}$$

The total differential of the chemical potential is thus from Equation (11);

$$d\mu_i = -S_i dT + V_i dp + \sum_{j=1}^{k} \mu_{i,j}^c dM_j \equiv -S_i dT + V_i dp + d\mu_i^c \tag{25}$$

where $S_i = -(\partial \mu_i/\partial T)_{p,M_j}$ and $V_i = \left(\partial \mu_i/\partial p\right)_{T,M_j}$ and $\mu_{i,j}^c = (\partial \mu_i/\partial M_j)_{p,T,M_k}$ are partial specific quantities. The last term describes the change in the chemical potential by changing composition of the medium. The $d\mu_{i,T}$ is now defined as a part of the whole differential:

$$d\mu_{i,T} \equiv d\mu_i + S_i dT = V_i dp + d\mu_i^c \tag{26}$$

The last term is zero when the composition is uniform. In the expression of the entropy production in terms of component flows, Equation (23), the driving force has contributions from the composition variation and from the pressure gradient.

3.2. Expression in Terms of Volume Flow

The volume flow, rather than the component flows, is often the measured variable. A description with the volume flow is thus of interest. The volume flow of several components is $J_V = \Sigma_i j_i V_i$. We take the example of two fluids to demonstrate the principles.

$$J_V \equiv J_n V_n + J_w V_w \tag{27}$$

With two fluids in a uniform, non-deformable rock, there are three components. On the coarse-grained level, these are mixed. We assume that $d\mu_r^c = 0$, and obtain Gibbs-Duhem's equation on the form

$$\rho_n d\mu_n^c + \rho_w d\mu_w^c = 0 \tag{28}$$

where ρ_i is the density of i in the REV (in kg.m^3). This can be used with Equation (26) and J_V to change Equation (23) into

$$\sigma = J_q' \frac{\partial}{\partial x}\left(\frac{1}{T}\right) - J_V \frac{1}{T}\frac{\partial}{\partial x} p + \upsilon_D \frac{\rho_n}{T}\frac{\partial \mu_n^c}{\partial x} \tag{29}$$

We have chosen to keep the chemical potential of n, which has a simpler form than the other chemical potential ($\mu_n = \mu_n^n$), cf. section 2.2. The entropy production in Equation (23) is invariant, and this invariance defines υ_D as the relative velocity of component w and n (in m.s^{-1}):

$$\upsilon_D \equiv \frac{J_w}{\rho_w} - \frac{J_n}{\rho_n} \tag{30}$$

The entropy production 29 has also three terms. While the first term on the right-hand side is the same as before, the second term is the volume flow with minus the pressure gradient over the temperature as driving force, and the third term is the velocity difference with the chemical potential gradient times the density over the temperature as driving force.

Equations (23, 29) are equivalent. They describe the same entropy production or flow dissipation. They provide alternative choices of conjugate thermodynamic force-flux pairs. The choice to use in the particular case, is determined by practical reasons; what can be measured or not, or which terms are zero. For instance, under isothermal conditions we need not take the term containing the heat flux along, even if heat may be transported reversibly. One set may give a negative contribution to the entropy production (work is done), but the overall entropy production is positive, of course. Each set can be used to obtain constitutive equations for transport on the macro-scale. We shall proceed to find these for porous media flow, finding first more detailed expressions for the driving forces.

In the simple case of a single fluid, say w, we obtain directly from Equations (23, 26) that

$$\sigma = J_q' \frac{\partial}{\partial x}(\frac{1}{T}) - J_V \frac{1}{T}\frac{\partial p}{\partial x} \tag{31}$$

In the absence of a gradient in composition, $d\mu_i^c = 0$, the same expression applies also for more components. We may follow Hansen et al. [22] and write the component contributions as $J_n V_n = \hat{S}^n v_n$, $J_w V_w = \hat{S}^w v_w$ and $J_V = v = \hat{S}^n v_n + \hat{S}^w v_w$. where the saturation has been introduced, and v_i is the volume flow of i.

4. DEFINITION OF THE DRIVING FORCES IN THE CONTEXT OF A POROUS MEDIUM

We expand on the basis presented earlier [1], and give definitions of the driving forces in the context of porous media flow.

4.1. The Saturation-Dependent Contributions to the Chemical Potential Gradient

The specific contribution to the chemical potential gradients in the entropy production in Equation (23) is of interest. The concentration dependent part of the chemical potential of i, μ_i, for an ideal system is (in J.kg^{-1})

$$\mu_i = \mu_i^0 + \frac{RT}{W_i} \ln \frac{\rho_i}{\rho_i^{0,\mathrm{REV}}} \tag{32}$$

Here R is the gas constant (in J.K^{-1}.mol^{-1}) and W_i is the molar mass (in kg.mol^{-1}). The chemical potential is measured referred to a standard state, μ_i^0, having the local concentration ρ_i^0 in all the pores. In the description of porous media, a convenient reference state may be the state when one component is filling all pores, or when the saturation is unity, $\hat{S}^i = 1$. The mass density of i in the REV for the standard state is $\rho_i^{0,\mathrm{REV}} = \rho_i^0 V_p^{\mathrm{REV}}/V^{\mathrm{REV}} = \rho_i^0 \phi$. Away from this state $\rho_i = \rho_i^0 \hat{S}^i \phi$ for $i = n, w$. When ϕ is constant, this gives

$$\frac{\rho_i}{\hat{S}^i} = \rho_i^0 \phi \tag{33}$$

By introducing these definitions into Equation (32), we obtain for the concentration dependent part of the chemical driving force of n

$$\frac{\partial \mu_n^c}{\partial x} = \frac{RT}{W_n}\frac{1}{\hat{S}^n}\frac{\partial \hat{S}^n}{\partial x} \tag{34}$$

We see that any variation in saturation between REVs along the x-axis (cf. **Figure 1**), will lead to a driving force. We integrate between two REVs and obtain the chemical driving force for porous media flow

$$\rho_n \Delta \mu_n^c = \phi \frac{\rho_n^0 RT}{W_n}\Delta \hat{S}^n \tag{35}$$

We have seen that the return to the Gibbs energy of the porous medium helped define the chemical potential in terms of properties relevant to porous media. All variables are measurable.

4.2. The Pressure Dependent Contribution

The driving force for volume flow is the negative gradient of the REV pressure over the temperature. To measure the pressure p inside the REV is difficult. The pressure in the fluid phases adjacent to the porous medium can be determined. Tallakstad et al. [11] defined the measured pressure difference, $\Delta p'$, at steady state, as an average over the value $\Delta p(t)$ over the time of measurement:

$$\Delta p' = \frac{1}{t_e - t_s}\int_{t_s}^{t_e} \Delta p(t) dt \tag{36}$$

Here t is the time and Δ refers to the extension of the system. Subscript 's' denotes the start and 'e' denotes the end of the measurement. We will take this pressure difference as our Δp. The pressure differences Δp^w and Δp^n can also be measured when there is continuity in the fluids, w and n, respectively.

The pressure variation across the REV is given by Equation (19), we have an interpretation of the pressure difference external to the porous medium;

$$\frac{d}{dx}p = \frac{d}{dx}(\bar{p} - \bar{p}^c) \tag{37}$$

We integrate over the system and obtain an interpretation of the total pressure difference:

$$\Delta p = \Delta \bar{p} - \Delta \bar{p}^c \tag{38}$$

We can assess the right-hand side of this equation using Equations (17, 18).

4.2.1. The Case of Large Pressure Differences

When the pressure drop across the porous plug is large compared to the capillary pressure contribution, the surface contributions and therefore $\bar{p}^c$ can be neglected. This is the case of large capillary numbers. Furthermore $p^n = p^w$. In the pressure difference, the terms with constant ϕ and p^r disappears, and the pressure difference is:

$$\Delta p = \Delta \bar{p} = \phi \Delta p^w \tag{39}$$

The pressure is applied to the whole cross-sectional area. This explains that the net driving force becomes a fraction, ϕ, of Δp^w. In other words, the force applies to the fraction ϕ of the pore area.

The conditions leading to Equation (39) are common in the laboratory. Some numerical values for the air-glycerol system, [4], can illustrate when the conditions apply. The value of $2\phi\gamma^{wr}/\bar{r}$ is of the same order of magnitude as $p^c\hat{S}^n\phi$ (400 Pa) when the surface tension $\gamma = 6.4 \cdot 10^{-2}$N m^{-2}, the average pore radius $\bar{r} = 0.2$ mm and the porosity $\phi = 0.63$. A typical value of $\Delta\bar{p}$ in the experiments is close to 30 kPa, which is far from the limit where capillary effects are significant.

4.2.2. The Case of Small Pressure Differences

For small capillary numbers the effective pressure drop across a porous plug is comparable to or smaller than the capillary pressure. Surface contributions need be taken into account. Equation (38) gives the effective pressure difference. When we can assume a constant average radius $\bar{r}$, and constant porosity, we obtain

$$\Delta p = \Delta \bar{p} - \frac{2\phi}{\bar{r}}\Delta\left[\left(\gamma^{nr} - \gamma^{wr}\right)\hat{S}^n + \gamma^{wr}\right] - \Delta\left(\gamma^{nw}\frac{\Omega^{nw,\mathrm{REV}}}{V^{\mathrm{REV}}}\right) \tag{40}$$

A fluid will be transported when the surface tensions of the fluids with the wall are different and there is a difference in the saturation. When there is only one fluid in the porous medium, cf. Equation (22), and we have constant $\bar{r}$ and porosity, the pressure difference becomes

$$\Delta p = \Delta \bar{p} - \frac{2\phi}{\bar{r}}\Delta\gamma^{wr} \tag{41}$$

The last term can lead to mass transport, when the surface tension changes.

5. CONSTITUTIVE EQUATIONS. EXAMPLES

5.1. Constitutive Equations for Non-isothermal, Two-Phase, Immiscible Fluids

The constitutive equations follow from the entropy production. We present these on differential form for two incompressible flows. From Equation (23) we have:

$$\begin{aligned}
J_q' &= l_{qq}\frac{\partial}{\partial x}(\frac{1}{T}) - l_{qw}\frac{1}{T}\frac{\partial \mu_{w,T}}{\partial x} - l_{qn}\frac{1}{T}\frac{\partial \mu_{n,T}}{\partial x}\\
J_w &= l_{wq}\frac{\partial}{\partial x}(\frac{1}{T}) - l_{ww}\frac{1}{T}\frac{\partial \mu_{w,T}}{\partial x} - l_{wn}\frac{1}{T}\frac{\partial \mu_{n,T}}{\partial x}\\
J_n &= l_{nq}\frac{\partial}{\partial x}(\frac{1}{T}) - l_{nw}\frac{1}{T}\frac{\partial \mu_{w,T}}{\partial x} - l_{nn}\frac{1}{T}\frac{\partial \mu_{n,T}}{\partial x}
\end{aligned} \tag{42}$$

We can also use Equation (29) and obtain

$$\begin{aligned}
J_q' &= l_{qq}\frac{\partial}{\partial x}\left(\frac{1}{T}\right) - l_{qp}\frac{1}{T}\frac{\partial}{\partial x}p + l_{qd}\frac{\rho_n}{T}\frac{\partial \mu_n^c}{\partial x}\\
J_V &= l_{pq}\frac{\partial}{\partial x}\left(\frac{1}{T}\right) - l_{pp}\frac{1}{T}\frac{\partial}{\partial x}p + l_{pd}\frac{\rho_n}{T}\frac{\partial \mu_n^c}{\partial x}\\
\upsilon_D &= l_{dq}\frac{\partial}{\partial x}\left(\frac{1}{T}\right) - l_{dp}\frac{1}{T}\frac{\partial}{\partial x}p + l_{dd}\frac{\rho_n}{T}\frac{\partial \mu_n^c}{\partial x}
\end{aligned} \tag{43}$$

The flux-force relations are linear on the REV-level. Our construction of the coarse-grained entropy production has followed the standard line in non-equilibrium thermodynamic theory, meaning that the Onsager relations holds for each matrix of coefficients. They may not hold, when the REV no longer can be constructed using Euler homogeneity (i.e., can be regarded as a thermodynamic state) or when the balance equations fail. Some evidence exists that the REV is a thermodynamic state [4, 5]. Also, there is theoretical and computational proof that the Onsager relations apply, $l_{ij} = l_{ji}$ [23–25]. Experimental proof for the Onsager relations exists for one-phase flow in porous media[26], but as far as we know, not for two-phase flow. We continue to specify how this possibly can be achieved.

One set of conductivities can be expressed by the other, using entropy production invariance. The element l_{qq} is the same in both formulations.

We have discussed above how the local and overall driving forces can be determined. We integrate across the system in order to relate experimental results to theory. We integrate the linear laws 43 across the REV, and obtain

$$\begin{aligned} J'_q &= L_{qq}\Delta(\frac{1}{T}) - L_{qw}\frac{1}{T}\Delta\mu_{w,T} - L_{qn}\frac{1}{T}\Delta\mu_{n,T} \\ J_w &= L_{wq}\Delta(\frac{1}{T}) - L_{ww}\frac{1}{T}\Delta\mu_{w,T} - L_{wn}\frac{1}{T}\Delta\mu_{n,T} \\ J_n &= L_{nq}\Delta(\frac{1}{T}) - L_{nw}\frac{1}{T}\Delta\mu_{w,T} - L_{nn}\frac{1}{T}\Delta\mu_{n,T} \end{aligned} \tag{44}$$

and

$$\begin{aligned} J'_q &= L_{qq}\Delta\left(\frac{1}{T}\right) - L_{qp}\frac{1}{T}\Delta p + L_{qd}\frac{\rho_n}{T}\Delta\mu_n^c \\ J_V &= L_{pq}\Delta\left(\frac{1}{T}\right) - L_{pp}\frac{1}{T}\Delta p + L_{pd}\frac{\rho_n}{T}\Delta\mu_n^c \\ \upsilon_D &= L_{dq}\Delta\left(\frac{1}{T}\right) - L_{dp}\frac{1}{T}\Delta p + L_{dd}\frac{\rho_n}{T}\Delta\mu_d^c \end{aligned} \tag{45}$$

Here $L_{ij} \equiv l_{ij}/l$ and l is the length of the REV, and the driving forces are defined by Equations (35, 38).

The coefficients may become dependent on the force through the integration as shown by Sinha et al. [27]. The averaging procedure gave the conductivity as a function of ($\Delta\bar{p}$ - Δp^c) in the terminology of this paper. In the remainder of this work we will discuss experimental conditions that allow us to determine these coefficients. The presentation follows closely the derivation of Stavermann [28] and Katchalsky et al. [29]. For transport in discrete systems with polymer membranes, see also [30]. We refer to these works for further definitions of transport coefficients.

5.2. Constitutive Equation for Isothermal, Single Fluid

For an isothermal single fluid *w*, flowing inside a porous medium, the entropy production 45 has one term; the volume flow times the negative pressure difference over the temperature. By including the constant temperature in the transport coefficient, we obtain the common linear law. With the permeability L_p, we write

$$J_V = -L_p\Delta p \tag{46}$$

where $L_p \equiv L_{pp}/T$. The permeability is normally a function of state variables (pressure, temperature). In the hydrodynamic regime it is a function of viscosity, $L_p = L_p(p, T, \eta)$. By introducing the new expression for the pressure, Equation (22), we obtain

$$J_V = -L_{VV}\left(\Delta p^w - \frac{2}{\bar{r}}\Delta\gamma^{wr}\right) \tag{47}$$

When the permeability and porosity are constant, $L_{VV} \equiv L_p\phi$. The equation predicts a threshold value for flow if there is a (significant) change in the surface tension across the REV. Transport will take place, when $\Delta p^w > 2\Delta\gamma^{wr}/\bar{r}$. The permeability L_{VV} is inversely proportional to the viscosity η of the fluid in the hydrodynamic regime. Interestingly, Boersma et al. [8] and Miller et al. [7] plotted the volume flow vs. the hydrostatic pressure difference Δp^w and found a deviation from Darcy's law in the form of a pressure threshold, for water or water solutions in clay. They offered no explanation for this. Also Bernadiner et al. [9] and Swartzendruber [6] plotted the volume flow of water solution J_V vs. the pressure gradient in sandstone with low clay content [9], and in NaCl-saturated Utah bentonite [6]. The thresholds that they observed depended on the content of salt in the permeating solution. They explained the thresholds by water adsorption and pore clogging by colloids [9]. According to Equation (47), a varying surface tension (due to a varying adsorption and clogging) might explain the existence of a threshold or a non-linear flux-force relation. There is no reason to believe that the non-linear flux-force relation is not caused by creation of system disorder, as was shown analytically for a tube [27] and in Sinha and Hansen [12] for a porous medium.

5.3. Constitutive Equations for Isothermal, Two-Phase Fluids

The entropy production in Equation (29) has two terms when two immiscible components flow at isothermal conditions. We choose the formulation that has variables J_V and υ_D; volume flux and interdiffusion flux, respectively. Equation (45) gives then:

$$\begin{aligned} J_V &= -L_{pp}\Delta p + L_{pd}\left(\rho_n\Delta\mu_n^c\right) \\ \upsilon_D &= -L_{dp}\Delta p + L_{dd}\left(\rho_n\Delta\mu_n^c\right) \end{aligned} \tag{48}$$

where $L'_{ij} \equiv L_{ij}/T$. The coefficients reflect, as above, the mechanism of flow (pressure, diffusion). Four experiments can be done to determine the four coefficients. There are only three independent coefficients. When four experiments are done, we can check the Onsager relations.

5.3.1. Main Coefficient: The Hydraulic Permeability

The (hydraulic) permeability K is related to the mobility coefficient L_{pp}, by $L_{pp} = K/\eta$ where η is the fluid viscosity. Both coefficients are measured at uniform composition. By

introducing the driving force for the volume flow from Equation (38), we obtain [the last term on Equation (48)] is zero:

$$J_V = -L_{pp}\Delta p = -L_{pp}\Delta(\bar{p} - \bar{p}^c) \tag{49}$$

With the present definition of variables the equation applies to the overall behavior of the system. A plot of J_V vs. $\Delta\bar{p}$ may show a threshold. This threshold has more contributions than in the single component system, as there are contributions to the pressure from surface and line energies. A threshold may be detectable at low capillary numbers.

The hydraulic permeability, is found by measuring the volume flow caused by the overall pressure difference at uniform composition;

$$K = -\eta\left(\frac{J_V}{\Delta p}\right)_{d\mu_n^c=0} \tag{50}$$

The mobility is a function of the saturation, $L_{pp} = L_{pp}(p, T, \eta, \hat{S}^w)$. In the hydrodynamic regime, the coefficient can be modeled, assuming Poiseuille flow and the effective viscosity $\eta^{\text{eff}} = \eta_w\hat{S}^w + \eta_n\hat{S}^n$ [27]. Using a pore model, Sinha et al. [27] found a dependence of the coefficient L_{pp} on the threshold pressure. This non-linearity does not prevent the use of non-equilibrium thermodynamics.

5.3.2. Main Coefficient: The Interdiffusion Coefficient

The main coefficient L_{dd} is an interdiffusion coefficient. It is defined at uniform pressure from the difference flux created by a difference in saturation;

$$L_{dd} = \left(\frac{\upsilon_D}{\rho_n\Delta\mu_n^c}\right)_{\Delta p=0} = \frac{W_n}{\phi RT\rho_n^0}\left(\frac{\upsilon_D}{\Delta\hat{S}^n}\right)_{\Delta p=0} \tag{51}$$

where we used Equation (35) for the driving force.

5.3.3. The Two Coupling Coefficients

The coupling coefficients in Equations (48) express that a separation of components can be caused by a pressure gradient (L_{dp}) and that a volume flow can be promoted by a gradient in saturation (L_{pd}).

Consider first the determination of L_{dp}. A pressure gradient may build as a consequence of a difference in composition [30]. The volume flux continues until a balance of forces is reached:

$$\Delta p = \frac{L_{pd}}{L_{pp}}\rho_n\Delta\mu_n^c \tag{52}$$

From the force-balance across the system, we obtain:

$$\left(\frac{\Delta p}{\Delta\hat{S}_n}\right)_{J_V=0} = \frac{L_{pd}}{L_{pp}}\phi\frac{\rho_n^0 RT}{W_n} \tag{53}$$

This condition can be used to find the unknown coupling coefficient, once the hydraulic permeability is known.

The remaining coupling coefficient can be found from the flux ratio, r, that has been called the reflection coefficient r, see also [30]. At constant saturation, we have

$$r = -\left(\frac{\upsilon_D}{J_V}\right)_{\Delta\mu_n^c=0} = -\frac{L_{dp}}{L_{pp}} \tag{54}$$

We are now in a position to compare L_{pd} and L_{dp} and verify the Onsager relations. The state of the system must be (approximately) the same, when the comparison is made.

5.4. Constitutive Equations for Non-isothermal, Two-Phase Fluids

The full set of equations given in Equation (45) must be used to describe non-isothermal flow in porous media. The coefficients, L_{pp}, $L_{pd} = L_{dp}$, L_{dd} in the lower right-hand side corner of the conductivity matrix, were discussed above. The new coefficients are those related to heat transport. The coefficient L_{qq} represents the Fourier type heat conductivity at uniform composition and pressure. The coefficients L_{pq} and L_{dq} are coupling coefficients.

Non-zero coefficients L_{pq} and L_{dq} mean that we can obtain separation in a temperature gradient. Injection of cold water into warm reservoirs may thus lead to separation. Likewise, a pressure difference can arise from a temperature difference. This is thermal osmosis [14].

Separation caused by a thermal driving force was observed in clay-containing soils where water was transported in clay capillaries against a pressure gradient. The coefficient, measured at constant pressure, was called the segregation potential [31]. The coefficient L_{pq} can be obtained from Equation (45), setting $\Delta p = 0$ and $\Delta\mu_n^c = 0$ ($\Delta\hat{S}^n$=0) in the second line. We obtain

$$\left(\frac{J_V}{\Delta T}\right)_{\Delta p=0,\Delta\mu_n^c=0} = -\frac{1}{T^2}L_{pq} \tag{55}$$

This coefficient can also be found from steady state conditions, when the thermal gradient is balanced by a gradient in saturation (chemical potential)

$$\begin{aligned} L_{pq}\frac{1}{T^2}\Delta T &= L_{pd}\rho_n\Delta\mu_n^c = L_{pd}\phi\frac{RT\rho_n^0}{W_n}\Delta\hat{S}^n \\ \left(\frac{\Delta\hat{S}^n}{\Delta T}\right)_{\upsilon_D=0} &= \frac{W_n}{RT^3\rho_n^0}\frac{L_{pq}}{L_{pd}} \end{aligned} \tag{56}$$

This determination of L_{pq} requires knowledge of L_{pd}. Alternatively, we may obtain the coefficient from the thermal osmosis experiment

$$\left(\frac{\Delta p}{\Delta T}\right)_{J_V=0,\Delta\mu_n^c=0} = -\frac{1}{T}\frac{L_{pq}}{L_{pp}} \tag{57}$$

The coupling coefficient L_{qp} can also be found by measuring the heat flux that accompanies the volume flux for constant composition and at isothermal conditions.

$$\left(\frac{J_q'}{J_V}\right)_{\Delta T=0,\Delta\mu_n^c=0} = \frac{L_{qp}}{L_{pp}} \tag{58}$$

These interrelated effects are well-known in homogeneous media [14], but have to the best of our knowledge, not been measured for porous media with two-phase flow.

6. DISCUSSION AND CONCLUSION

We have further developed a new coarse-grained formulation of the entropy production [1] for porous media, and specified the constitutive equations for flow of two immiscible fluids under uniform or varying temperature, pressure and composition. Several of the equations are new in the context of porous media, but they follow well-documented tracks in classical non-equilibrium thermodynamics [1, 28–30]. Experimental observations exist on single fluid flow, that give support to the theoretical description.

We have given a new definition of the pressure of the representative elementary volume (REV), and used it to obtain the pressure part of the driving force. The force obtains contributions from homogeneous phases, surfaces—and, in principle also line—tensions of the system. This distinguishes the present formulation from their counterpart for homogeneous systems [1, 28–30].

We have seen that surface contributions can be spelled out for varying conditions, under the assumption that the additive properties of the REV are Euler homogeneous of the first order. Doing this, we have been able to explain for instance deviations from Darcy's law, or the occurrence of threshold pressures in plots of flow vs pressure difference. We have pointed at possibilities to describe non-isothermal phenomena.

As for instance sections 5.1–5.3 show, there is a multitude of scenarios that can be further investigated, and used to check the theory. The expressions open up the possibility to test the thermodynamic models in use, for their compatibility with the second law.

The basic assumption used is that the REV set of basis variables are Euler homogeneous functions of degree one. This means in essence that *one* temperature, *one* pressure and *one* chemical potential per component can be defined for the REV. Some evidence already supports the idea that the REV is a thermodynamic state [4], [5], originally proposed by Hansen and Ramstad [3] and Tallakstad et al. [11]. We did neither consider surface areas, nor their curvature or the contact line length as independent variables, but these may be included, cf.[21].

We have illustrated relations for some specific cases; the non-isothermal flow of one or two immiscible single fluids in a non-deformable medium. It is straight forward to include more terms in the chemical potential (*e.g.* gravity). To include stress fields or other fields that deform the porous medium is more problematic, and has been postponed.

Flow of two isothermal, immiscible fluids in a porous medium has often been described by Darcy's law, using the relative permeability concept. The seepage velocities v_n and v_w are related to fluxes used here by $v_n = J_n V_n$ and $v_w = J_w V_w$. The expressions for the seepage velocities must be contained or be equivalent to the expressions given here, using the condition of invariance for the entropy production. A comparison can elucidate assumptions that are made. Hilfer and Standnes et al. [32, 33] gave a set of linear relations for the seepage velocities. Their driving forces were the gradients in the single component pressures, obtained by pressure measurements in the single phases. Their description implies e.g., that the composition is uniform.

We have seen through these examples how non-equilibrium thermodynamic theory can provide a fundamental basis for constitutive equations, also in porous media. For systems that obey entropy production invariance and Onsager symmetry, we have obtained relations between variables, which have been used to a limited degree for two-phase systems.

AUTHOR CONTRIBUTIONS

SK and DB defined the variables of the REV and wrote the first draft. AH, BH, and OG critically examined all proposals and contributed to revisions of the Manuscript.

ACKNOWLEDGMENTS

Per Arne Slotte is thanked for stimulating discussions. The authors are grateful to the Research Council of Norway through its Centers of Excellence funding scheme, project number 262644, PoreLab.

REFERENCES

1. Kjelstrup S, Bedeaux D, Hansen A, Hafskjold B, Galteland O. Non-isothermal two-phase flow in porous media. The entropy production. *Front Phys.* (2018) **6**:126. doi: 10.3389/fphy.2018.00126
2. de Groot SR, Mazur P. *Non-Equilibrium Thermodynamics*. London: Dover (1984).
3. Hansen A, Ramstad T. Towards a thermodynamics of immiscible two-phase steady-state flow in porous media. *Comp Geosci.* (2009) **13**:227–34. doi: 10.1007/s10596-008-9109-7
4. Erpelding M, Sinha S, Tallakstad KT, Hansen A, Flekkøy EG, Måløy KJ. History independence of steady state in simultaneous two-phase flow through two-dimensional porous media. *Phys Rev E* (2013) **88**:053004. doi: 10.1103/PhysRevE.88.053004
5. Savani I, Sinha S, Hansen A, Kjelstrup S, Bedeaux D, Vassvik M. A Monte Carlo procedure for two-phase flow in porous media. *Transp Porous Med.* (2017) **116**:869–88. doi: 10.1007/s11242-016-0804-x
6. Swartzendruber D. Non-Darcy flow behaviour in liquid-saturated porous media. *J Geophys Res.* (1962) **67**:5205. doi: 10.1029/JZ067i013p05205
7. Miller RJ, Low PF. Threshold Gradient for Water Flow in Clay Systems. *Soil Sci Soc Am Proc.* (1963) **27**:605–9.
8. Boersma L, Lindstrom FT, Saxena SK. Limitations of Darcy's law in glass bead porous media. *Soil Sci Soc Am Proc.* (1973) **37**:333–5.
9. Bernadiner MG, Protopapas AL. Progress on the theory of flow in geologic media with treshold gradient. *J Environ Sci Health* (1994) **A29**:249–75.
10. Sinha S, Bender AT, Danczyk M, Keepseagle K, Prather CA, Bray JM, et al. Effective rheology of two-phase flow in three-dimensional porous media: experiment and simulation. *Transp Porous Med.* (2017) **119**:77–94. doi: 10.1007/s11242-017-0874-4
11. Tallakstad KT, Knudsen HA, Ramstad T, Løvoll G, Måløy KJ, Toussaint R, et al. Steady-state, two-phase flow in porous media: Statistics and transport properties. *Phys Rev Lett.* (2009) **102**:074502. doi: 10.1103/PhysRevLett.102.074502

12. Sinha and Hansen Sinha S, Hansen A. Effective rheology of immiscible two-phase flow in porous media. *Europhys Lett.* (2012) **99**:44004. doi: 10.1209/0295-5075/99/44004
13. Kjelstrup S, Bedeaux D. *Non-Equilibrium Thermodynamics of Heterogeneous Systems*. Singapore: Wiley (2008).
14. Barragan VM, Kjelstrup S. Thermo-osmosis in membrane systems. *J NonEq Thermodyn.* (2017) **42**:217–36. doi: 10.1515/jnet-2016-0088
15. Costeseque P, Pollak T, Platten JK, Marcoux M. Transient-state method for coupled evaluation of Soret and Fick coefficients, and related tortuosity factors, using free and porous packed thermodiffusion cells: applications to $CuSO_4$ aqueous solution (0.25 M). *Eur Phys J E* (2004) **15**:249–53. doi: 10.1140/epje/i2004-10064-6
16. Colombani J, Galliero G, Duguay B, Caltagirone JP, Montel F, Bopp PA. A molecular dynamics study of the thermal diffusion in a porous medium. *Phys Chem Chem Phys.* (2002) **4**:313–21. doi: 10.1039/B106800H
17. H Davarzani MQ M Marcoux. Theoretical predictions of the effective thermodiffusion coefficients in porous media. *Int J Heat and Mass Transfer* (2010) **53**:1514–28. doi: 10.1016/j.ijheatmasstransfer.2009.11.044
18. Keulen L, van der Ham LV, Kuipers NJM, Hanemaaijer JH, Vlugt TJH, Kjelstrup S. Membrane distillation against a pressure difference. *J Membr Sci.* (2017) **524**:151–62. doi: 10.1016/j.memsci.2016.10.054
19. Hassanizadeh SM, Gray WG. Mechanics and thermodynamics of multiphase flow in porous media including interphase boundaries. *Adv Water Resour.* (1990) **13**:169–86.
20. Gray WG, Hassanizadeh SM. Macroscale continuum mechanics for multiphase porous-media flow including phases, interfaces, common lines and commpon points. *Adv Water Resour.* (1998) **21**:261–81.
21. McClure JE, Armstrong RT, Berrill MA, Schluter S, Berg S, Gray WG, et al. A geometric state function for two-fluid flow in porous media. *arXiv:1805.11032* (2018). doi: 10.1103/PhysRevFluids.3.084306
22. Hansen A, Sinha S, Bedeaux D, Kjelstrup S, Gjennestad MA, Vassvik M. Relations between seepage velocities in immiscible, incompressible two-phase flow in porous media. *Transp Porous Med.* (2018) **125**:565–87. doi: 10.1007/s11242-018-1139-6
23. Flekkøy EG, Pride SR, Toussaint R. Onsager symetry from mesoscopic time reversibility and the hydrodynamic dispersion tensor for coarse-grained systems. *Phys Rev E.* (2017) **95**:022136. doi: 10.1103/PhysRevE.95.022136
24. Pride S, Vasco D, Flekkøy E, Holtzmann R. Dispersive transport and symmetry of the dispersion tensor in porous media. *Phys Rev E* (2017) **95**:043103. doi: 10.1103/PhysRevE.95.043103
25. Burelbach J, Bruckner DB, Frenkel D, Eiser E. Thermophoretic forces on a mesoscopic scale. *Soft Matter.* (2018) **14**:7446–54. doi: 10.1039/C8SM01132J
26. Li SX, Pengra DB, Wong P. Onsager's reciprocal relation and the hydraulic permeability of porous media. *Phys Rev E.* (1995) **51**: 5748–51.
27. Sinha S, Hansen A, Bedeaux D, Kjelstrup S, Savani I, Vassvik M. Effective rheology of bubbles moving in a capillary tube. *Phys Rev E* (2013) **87**:025001. doi: 10.1103/PhysRevE.87.025001
28. Stavermann AJ. Non-equilibrium thermodynamics of membrane processes. *Trans Farad Soc.* (1952) **48**:176–85.
29. Katchalsky A, Curran PF. *Nonequilibrium Thermodynamics in Biophysics*. Cambridge, MA: Harvard University Press (1965).
30. Førland KS, Førland T, Ratkje SK. *Irreversible Thermodynamics. Theory and Applications.* Chichester: Wiley (1988).
31. Konrad JM. Frost susceptibility related to soil index properties. *Can Geotech J.* (1999) **36**:403–17.
32. Hilfer R. Macroscopic equations of motion for two phase flow in porous media. *Phys Rev E* (1998) **58**:2090.
33. Standnes DC, Evje S, Andresen PØ. A novel relative permeability model based on mixture theory approach accounting for solid-fluid and fluid-fluid interaction. *Transp Porous Med.* (2017) **119**:707–38. doi: 10.1007/s11242-017-0907-z

Conflict of Interest Statement: The authors declare that the research was conducted in the absence of any commercial or financial relationships that could be construed as a potential conflict of interest.

APPENDIX
Symbol Lists

TABLE A1 | Mathematical symbols, superscripts, subscripts.

Symbol	Explanation
c	Superscript meaning capillary pressure
d	Differential
∂	Partial derivative
Δ	Change in a quantity or variable
$\Delta_{f,t}$	The change is taken from f on the right to t On the left hand side
Σ	Sum
i	Subscript meaning component i
m	Number of fluids
n	Subscript meaning non-wetting fluid
w	Subscript meaning wetting fluid
p	Superscript meaning pore
REV	Abbreviation meaning representative elementary volume
r	Superscript meaning rock, solid matrix of medium
s	Superscript meaning interface
u	Subscript meaning internal energy
α, β	Superscripts meaning surface between phases α and β
α, β, δ	Superscripts meaning contact line between phases α, β, δ
θ	Contact angle, average

TABLE A2 | latin symbols

Symbol	Dimension	Explanation
G	J	Gibbs energy
M	kg	Mass
d	m	Pore length
H_i	$\mathrm{J.kg^{-1}}$	Partial specific enthalpy of i
J	$\mathrm{kg.s^{-1}.m^{-2}}$	Mass flux
J'_q	$\mathrm{J.s^{-1}.m^{-2}}$	Sensible heat flux
l	m	Characteristic length of representative elementary volume
L	m	Characteristic length of experimental system
L_{ij}		Onsager conductivity
p	Pa	Pressure of REV
$\bar{r}$	m	Average pore radius
S	$\mathrm{J.K^{-1}}$	Entropy
s	$\mathrm{J.K^{-1}.m^{-3}}$	Entropy density
S_i	$\mathrm{J\ kg^{-1}.K^{-1}}$	Partial specific entropy of i
$\hat{S}_i$		Degree of saturation of i, $\equiv V_i/V$
T	K	Temperature
t	s	Time
U	J	Internal energy
u	$\mathrm{J.m^{-3}}$	Internal energy density
V	$\mathrm{m^3}$	Volume
V_i	$\mathrm{m^3.kg^{-1}}$	Partial specific volume
x	m	Axis of transport
W_i	$\mathrm{kg.mol^{-1}}$	Molar mass of i

TABLE A3 | greek symbols, continued

Symbol	Dimension	Explanation
α		Superscripts meaning a phase
β		Superscript meaning an interface
δ		Superscript meaning a contact line
ϕ		Porosity of porous medium
γ	$\mathrm{N.m^{-1}}$	Surface tension
μ_i	$\mathrm{J.kg^{-1}}$	Chemical potential of i
ρ_i	$\mathrm{kg.m^{-3}}$	Density, $\equiv M_i/V_i$
σ	$\mathrm{J.s^{-1}.K^{-1}.m^{-3}}$	Entropy production in a homogeneous phase
Ω	$\mathrm{m^2}$	Surface or interface area

Article III

Olav Galteland, Dick Bedeaux, Bjørn Hafskjold, and Signe Kjelstrup.

Pressures Inside a Nano-Porous Medium. The Case of a Single Phase Fluid

Frontiers in Physics, 7, 60. (2019)
DOI: 10.3389/fphy.2019.00060

Article III

Article III

frontiers in Physics

ORIGINAL RESEARCH
published: 24 April 2019
doi: 10.3389/fphy.2019.00060

Pressures Inside a Nano-Porous Medium. The Case of a Single Phase Fluid

Olav Galteland, Dick Bedeaux, Bjørn Hafskjold and Signe Kjelstrup*

PoreLab, Department of Chemistry, Norwegian University of Science and Technology, Trondheim, Norway

We define the pressure of a porous medium in terms of the grand potential and compute its value in a nano-confined or nano-porous medium, meaning a medium where thermodynamic equations need be adjusted for smallness. On the nano-scale, the pressure depends in a crucial way on the size and shape of the pores. According to Hill [1], two pressures are needed to characterize this situation; the integral pressure and the differential pressure. Using Hill's formalism for a nano-porous medium, we derive an expression for the difference between the integral and the differential pressures in a spherical phase α of radius R, $\hat{p}^{\alpha} - p^{\alpha} = \gamma/R$. We recover the law of Young-Laplace for the differential pressure difference across the same curved surface. We discuss the definition of a representative volume element for the nano-porous medium and show that the smallest REV is a unit cell in the direction of the pore in the fcc lattice. We also show, for the first time, how the pressure profile through a nano-porous medium can be defined and computed away from equilibrium.

Keywords: nano-porous media, thermodynamics of small systems, representative elementary volume, single phase fluid, molecular dynamics simulations

OPEN ACCESS

Edited by:
Daniel Bonamy, Commissariat á l'Energie Atomique et aux Energies Alternatives (CEA), France

Reviewed by:
Alberto Rosso, Centre National de la Recherche Scientifique (CNRS), France
Reinaldo Roberto Rosa, Instituto Nacional de Pesquisas Espaciais (INPE), Brazil

****Correspondence:***
Olav Galteland
olav.galteland@ntnu.no

Specialty section:
This article was submitted to Interdisciplinary Physics, a section of the journal Frontiers in Physics

Received: *30 January 2019*
Accepted: *29 March 2019*
Published: *24 April 2019*

Citation:
Galteland O, Bedeaux D, Hafskjold B and Kjelstrup S (2019) Pressures Inside a Nano-Porous Medium. The Case of a Single Phase Fluid. Front. Phys. 7:60. doi: 10.3389/fphy.2019.00060

1. INTRODUCTION

The description of transport processes in porous media poses many challenges that are well described in the literature (see e.g., [2–6]). There is, for instance, no consensus, neither on the definition nor on the measurement or the calculation, of the pressure in a porous medium with flow of immiscible fluids. The problem with the ill-defined microscopic pressure tensor [5, 7] is accentuated in a heterogeneous system with interfaces between solids and fluids. In a homogeneous fluid phase one may define and calculate a pressure and a pressure gradient from the equation of state. In a porous medium the presence of curved surfaces and fluid confinements makes it difficult to apply accepted methods for calculation of the microscopic pressure tensor and, consequently, the pressure gradient as driving force for fluid flow. The scale at which we choose to work will be decisive for the answer. Moreover, the scale that the hydrodynamic equations of transport refer to, remains to be given for nano-porous as well as micro-porous media.

A central element in the derivation of the equations of transport on the macro-scale is the definition of a representative elementary volume (REV) (see e.g., [8, 9]). The size of the REV should be large compared to the pore size and small compared to size of the porous medium. It should contain a statistically representative collection of pores. We have recently discussed [10] a new scheme to define a basis set of additive variables: the internal energy, entropy, and masses of all the components of the REV. These variables are additive in the sense that they are sums of contributions of all phases, interfaces and contact lines within the REV. Using Euler homogeneity of the first kind, we were able to derive the Gibbs equation for the REV. This equation defines

the temperature, pressure and chemical potentials of the REV as partial derivatives of the internal energy of the REV [10].

As discussed in Kjelstrup et al. [11] the grand potential, Υ, of the REV is given by minus $k_B T$ times the logarithm of the grand partition function, Z_g, where k_B is Boltzmann's constant and T is the temperature. The grand potential is equal to minus the contribution to the internal energy from the pressure-volume term, $k_B T \ln Z_g = \Upsilon = -pV$, which we will from now on refer to as the compressional energy. For a single fluid f in a porous medium r, the result was [10, 11]

$$pV = p^f V^f + p^r V^r - \gamma^{fr}\Omega^{fr}, \tag{1}$$

where p and V are the pressure and the volume of the REV. Furthermore p^f and V^f are the pressure and the volume of the fluid in the REV, p^r and V^r are the pressure and the volume in the grains in the REV, and γ^{fr} and Ω^{fr} are the surface tension and the surface area between the fluid and the grain. The assumption behind the expression was the additive nature of the grand potential. This definition of the REV, and the expression for the grand potential, opens up a possibility to define the pressure on the hydrodynamic scale. The aim of this work is to explore this possibility. We shall find that it will work very well for flow of a single fluid in a porous medium. As a non-limiting illustrative example, we use grains positioned in a fcc lattice. The work can be seen as a continuation of our earlier works [10, 11].

The work so far considered transport processes in micro-porous, not nano-porous media. In micro-porous media, the pressure of any phase (the surface tension of any interface) is independent of the volume of the phase (the area between the phases). This was crucial for the validity of equation 1. For nano-porous systems, we need to step away from Equation (1). Following Hill's procedure for small systems' thermodynamics [1], we generalize Equation (1) to provide an expression for the thermodynamic pressure in a nano-porous medium. We shall see that not only one, but two pressures are needed to handle the additional complications that arise at the nano-scale; the impact of confinement and of radii of curvature of the interfaces. In the thermodynamic limit, the approach presented for the nano-scale must simplify to the one for the macro-scale. We shall see that this is so. In order to work with controlled conditions, we will first investigate the pressure of a fluid around a single solid nano-scale grain and next around a lattice of solid nano-scale grains. The new expression, which we propose as a definition of the pressure in a nano-porous medium, will be investigated for viability and validity for this case. The present work can be seen as a first step in the direction toward a definition and use of pressure and pressure gradients in real porous media.

The pressure is not uniquely defined at molecular scale. This lack of uniqueness becomes apparent in molecular dynamics (MD) simulations, for which the computational algorithm has to be carefully designed [7]. The predominant method for pressure calculations in particular systems is using the Irving-Kirkwood contour for the force between two particles [12]. This algorithm works for homogeneous systems, but special care must be taken for heterogeneous systems [5, 6]. However, if the control volume (REV) used for pressure calculation is large compared with the heterogeneity length scale, one may argue that the algorithm for homogeneous systems gives a good approximation to the true result. We are interested in the isotropic pressure averaged over the REV, on a scale where the porous medium can be considered to be homogeneous.

The paper is organized as follows. In section 2 we derive the pressure of a REV for one solid grain surrounded by fluid particles (Case I) and for a three-dimensional face-centered cubic (fcc) lattice of solid grains (Case II). Section 3 describes the molecular dynamics simulation technique when the system is in equilibrium and in a pressure gradient. In section 4 we use the theory to interpret results of equilibrium molecular dynamics simulations for one solid grain and for an array of solid grains in a fluid. Finally we apply the results to describe the system under a pressure gradient. We conclude in the last section that the expressions and the procedure developed provide a viable definition of the pressures and pressure gradients in nano-porous media.

2. THE PRESSURE OF A NANO-POROUS MEDIUM

Equation (1) applies to a micro-porous medium, a medium where the pore-size is in the micrometer range or larger [10, 11]. For a nano-porous medium we need to apply the thermodynamics of small systems [1]. In nano-porous media, this technique is therefore well suited for the investigation. The thermodynamic properties like internal energy, entropy and masses of components of a small system are not proportional to the system's volume. As Hill explained, this leads to the definition of two different pressures, for which he introduced the names integral and differential pressure, $\hat{p}$ and p, respectively. For a system with a volume V, these pressures are related by

$$p(V) = \frac{\partial\left(\hat{p}\left(V\right)V\right)}{\partial V} = \hat{p}\left(V\right) + V\frac{\partial\left(\hat{p}\left(V\right)\right)}{\partial V}. \tag{2}$$

The symbol p (the differential pressure) is given to the variable that we normally understand as the pressure on the macroscopic level. It is only when $\hat{p}$ depends on V, that the two pressures are different. For large systems, $\hat{p}$ does not depend on V and the two pressures are the same.

The integral and differential pressures connect to different types of mechanical work on an ensemble of small systems. The differential pressure times the change of the small system volume is the work done on the surroundings by this volume change. The name differential derives from the use of a differential volume. This work is the same, whether the system is large or small. The integral pressure times the volume per replica, however, is the work done by adding one small system of constant volume to the remaining ones, keeping the temperature constant. This work is special for small systems. It derives from an ensemble view, but is equally well measurable. The word integral derives from the addition of a small system.

From statistical mechanics of macro-scale systems, we know that pV equals $k_B T$ times the natural logarithm of the grand-canonical partition function. For a small (nano-sized) system,

Hill ([1], Equations 1–17), showed that this logarithm gives $\hat{p}V$. In nano-porous media this product is different from pV, cf. Equation (1). Energies are still additive and the total compressional energy within the small system is similar to Equation (1). We replace Equation (1) by:

$$\hat{p}V = \hat{p}^f V^f + \hat{p}^r V^r - \hat{\gamma}^{fr}\Omega^{fr}, \tag{3}$$

where $\hat{p}^f$, $\hat{p}^r$ are integral pressures of the sub-volumes V^f and V^r, and $\hat{\gamma}^{fr}$ is the integral surface tension.

We consider here a nano-porous medium, so integral pressures and integral surface tensions apply. The integral pressure and integral surface tension normally depend on the system size. In the porous medium there are two characteristic sizes: the size of a grain and the distance between the surfaces of two grains[1]. The quantities $\hat{p}$, $\hat{p}^f$, $\hat{p}^r$ and $\hat{\gamma}^{fr}$ may depend on both. We shall here examine a system (cf. section 3) of spherical, monodisperse grains, for which the radius R is a good measure of the size. The volume of the grains may be a good alternative measure, which we will also use. The dependence on the grain size and on the distance between the surfaces of the grains will be studied in an effort to establish Equation (3).

In the following, we consider a single spherical grain confined by a single phase fluid (Case I) and a face-centered cubic (fcc) lattice of spherical grains confined by a single phase fluid (Case II). The size of the REV does not need to be large, and we will show in section 4.2 that the smallest REV is a unit cell in the direction of the pore in the fcc lattice.

2.1. Case I. Single Spherical Grain

Consider the inclusion of a spherical grain r in a box with fluid phase f. This is system A in **Figure 1**. Phase f has volume V^f and phase r has volume V^r. The total volume is $V = V^f + V^r$. The surface area between phase f and r is Ω^{fr}. The compressional energy of system A has contributions, in principle, from all its small parts

$$\hat{p}^A V = \hat{p}^f V^f + \hat{p}^r V^r - \hat{\gamma}^{fr}\Omega^{fr} \tag{4}$$

where $\hat{p}^A$ is the unknown pressure in Equation (3). There is a hat on the pressures and the surface tension, in the outset, because the system is small. The pressure of the fluid in A is, however, p^f, meaning that $\hat{p}^f = p^f$. When the surface tension depends on the curvature, there is a dependence of $\hat{\gamma}^{fr}$ on Ω^{fr} [13, 14]. This interesting effect, which we will not consider here, becomes relevant as the grain size decreases. Only $\hat{p}^r$ depends on the volume of the phase, V^r. This gives

$$\hat{p}^A V = p^f V^f + \hat{p}^r V^r - \gamma^{fr}\Omega^{fr} \tag{5}$$

We now introduce a system B in contact with A. System B has volume V, contains pure fluid, and is tuned so that it is in thermodynamic equilibrium with A. The equilibrium condition requires that their grand canonical partition functions are equal,

[1]Another valid characteristic size is the size of the pores between the grains, but this follows from the two we have chosen.

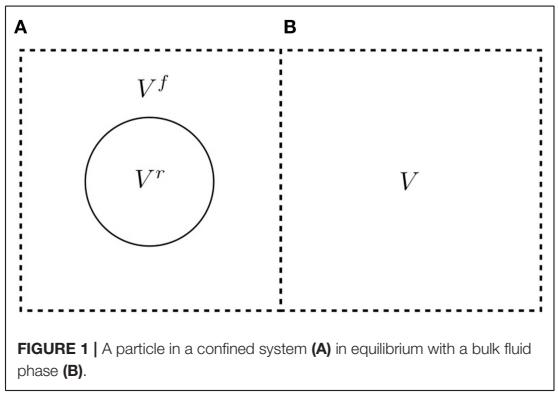

FIGURE 1 | A particle in a confined system **(A)** in equilibrium with a bulk fluid phase **(B)**.

which implies $\hat{p}^A V = \hat{p}^B V$, and with equal volumes this means $\hat{p}^A = \hat{p}^B$. Furthermore, system B is not a small system in Hill's sense, which leads to:

$$\hat{p}^A = \hat{p}^B = p^B = p^f \tag{6}$$

The fluid pressure p^f is the same in phases A and B. We obtain

$$p^f V = p^f V^f + \hat{p}^r V^r - \gamma^{fr}\Omega^{fr}, \tag{7}$$

and by rearranging the terms,

$$\hat{p}^r = p^f + \frac{\gamma^{fr}\Omega^{fr}}{V^r} = p^f + \frac{3\gamma^{fr}}{R}. \tag{8}$$

where we have used that $V^r + V^f = V$ and $\frac{\Omega^{fr}}{V^r} = \frac{3}{R}$ for a spherical phase r.

The pressure of the rock particle depends on the volume of the particle. The relation of the two pressures is according to Hill

$$p^r = \frac{\partial(\hat{p}^r V^r)}{\partial V^r} \tag{9}$$

When this is combined with the equation right above, we find the relation we are after

$$p^r - p^f = \frac{2\gamma}{R}, \tag{10}$$

which is the familiar Young-Laplace's law. By subtracting Equation (10) from Equation (8), we obtain an interesting new relation

$$\hat{p}^r - p^r = \frac{\gamma^{fr}}{R} \tag{11}$$

The expression relates the integral and differential pressure for a spherical phase r of radius R. It is clear that this pressure difference is almost equally sensitive to the radius of curvature as is the pressure difference in Young-Laplace's law.

We see from this example how the integral pressure enters the description of small systems. The integral pressure is not equal

to our normal bulk pressure, called the differential pressure by Hill, $\hat{p}^r \neq p^r$. While two differential pressures satisfy Young-Laplace's law in Equation (10), the integral pressures do not. The integral pressure has the property that when averaged over system A using Equation (4), it is the same as in system B, cf. Equation (6). This analysis shows that system A is a possible, or as we shall see proper, choice of a REV that contains the solid grain, while system B is a possible choice of a REV that contains only fluid.

2.2. Case II. Lattice of Spherical Grains

The above explanation concerned a single spherical grain and was a first step in the development of a procedure to determine the pressure of a nano-porous medium. To create a more realistic model, we introduce now a lattice of spherical grains. The integral pressure of a REV containing n grains is given by an extension of Equation (3)

$$\hat{p}^A V = p^f V^f + \sum_{i=1}^{n} \hat{p}_i^r V_i^r - \sum_{i=1}^{n} \hat{\gamma}_i^{fr} \Omega_i^{fr}, \tag{12}$$

For each grain one may follow the same derivation for the integral and differential pressure as for the single grain. By using Equation (8), we obtain

$$\hat{p}_i^r = p^f + \gamma_i^{fr} \frac{\Omega_i^{fr}}{V_i^r} = p^f + \frac{3\gamma_i^{fr}}{R_i}, \tag{13}$$

where the last identity applies to spherical grains only. The differential pressure of the grains is given by a generalization of Equation (10)

$$\begin{aligned} p_i^r &= \frac{\partial(\hat{p}_i^r V_i^r)}{\partial V_i^r} = \frac{\partial(p^f V_i^r)}{\partial V_i^r} + \gamma_i^{fr} \frac{\partial \Omega_i^{fr}}{\partial V_i^r} \\ &= p^f + \gamma_i^{fr} \frac{\partial \Omega_i^{fr}}{\partial V_i^r} = p^f + \frac{2\gamma_i^{fr}}{R_i}, \end{aligned} \tag{14}$$

where the last identity is only for spherical grains. The differential pressures again satisfy Young-Laplace's law at equilibrium.

When all grains are identical spheres and positioned on a fcc lattice, a properly chosen layer covering half the unit cell can be a proper choice of the REV. We shall see how this can be understood in more detail from the molecular dynamics simulations below. The REV is larger if the material is amorphous.

3. MOLECULAR DYNAMICS SIMULATIONS

Cases I and II were simulated at equilibrium, while case II was simulated also away from equilibrium. **Figures 3–8** illustrate the equilibrium simulations of the two cases.

3.1. Systems

The simulation box was three-dimensional with side lengths L_x, L_y, L_z.The box was elongated in the x-direction, $L_x > L_y = L_z$. Periodic boundary conditions were used in all directions in the equilibrium simulations. In the non-equilibrium simulation, reflecting particle boundaries [15] were applied to the x-direction, cf. section 3.5. Along the x-axis, the simulation box was divided into n rectangular cuboids (called layers) of size $\Delta x, L_y, L_z$, where $\Delta x = L_x/n$. The volume of each layer is $V_l = \Delta x L_y L_z$. There are two regions A and B in the simulation box. Region A contains fluid (red particles) and grains (blue particles) and region B contains only fluid, see **Figure 2**. The regions, B = B_1 + B_2 and A do not have the same size, but the layers have the same thickness, Δx. The compressional energy of the fluid in one layer is, $\hat{p}_l^f V_l^f = p_l V_l^f$.

The simulation was carried out with LAMMPS [16] in the canonical ensemble using the Nosé-Hoover thermostat [17], at constant temperature $T^* = 2.0$ (in Lennard-Jones units). The critical temperature for the Lennard-Jones/spline potential (LJ/s) is approximately $T_c^* \approx 0.9$. Fluid densities range from $\rho^* = 0.01$ to $\rho^* = 0.7$.

3.2. Case Studies

In case I the single spherical grain was placed in the center of the box. A periodic image of the spherical grain is a distance L_x, L_y and L_z away in the x, y and z-directions, see **Figure 4A**. The surface to surface distance of the spherical grains is $d = L_\alpha - 2R$, where R is the radius of the grain, and $\alpha = y, z$. In case I, each spherical grain has four nearest neighbors in the periodic lattice that is built when we use periodic boundary conditions. We considered two nearest neighbor distances; $d = 4\sigma_0$ and $d = 11\sigma_0$, where σ_0 is the diameter of the fluid particles.

In case II, the spherical grains were placed in a fcc lattice with lattice constant a. The two shortest distances between the surfaces were characterized by $d_1 = \frac{1}{2}(\sqrt{2}a - 4R)$ and $d_2 = a - 2R$, see **Figure 2**, where $d_1 < d_2$. We used $d_1 = 4.14\sigma_0$ and $d_1 = 11.21\sigma_0$, which is almost the same as the distances considered in case I. The corresponding other distances were $d_2 = 10\sigma_0$ and $d_2 = 20\sigma_0$. Each grain has 12 nearest neighbors at a distance d_1.

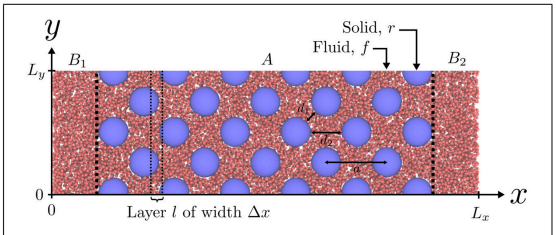

FIGURE 2 | A slice of the simulation box in case II. The box has side lengths L_x, L_y, L_z, and properties are calculated along the x-axis in layers l of width Δx. Blue particles are grain r and red particles are fluid f. The A is the lattice constant of the fcc lattice, d_1 and d_2 are the two shortest surface-to-surface distances.

In all cases we computed the volume of the grains V_l^r, the surface area Ω_l^{fr} and the compressional energy of each layer, l, in the x-direction.

3.3. Particle Interaction Potential

The particles interact with the Lennard-Jones/spline potential,

$$u_{ij}(r) = \begin{cases} \infty & \text{if } r < R_{ij} \\ 4\epsilon_{ij}\left[\left(\frac{\sigma_{ij}-R_{ij}}{r-R_{ij}}\right)^{12} - \left(\frac{\sigma_{ij}-R_{ij}}{r-R_{ij}}\right)^{6}\right] & \text{if } R_{ij} < r < r_{s,ij} \\ a_{ij}(r-r_{c,ij})^2 + b_{ij}(r-r_{c,ij})^3 & \text{if } r_s < r < r_{c,ij} \\ 0 & \text{if } r > r_{c,ij} \end{cases}. \tag{15}$$

Each particle type has a hard-core diameter R_{ii} and a soft-core diameter σ_{ii}. There were two types of particles, small particles with $\sigma_{ff} = \sigma_0$, $R_{ff} = 0$ and large particles with $\sigma_{rr} = 10\sigma_0$, $R_{rr} = 9\sigma_0$. The small particles are the fluid (f), and the large particles are the grain (r). The hard-core and soft-core diameters for fluid-grain pairs are given by the Lorentz mixing rule

$$R_{fr} = \frac{1}{2}\left(R_{ff} + R_{rr}\right) \quad \text{and} \quad \sigma_{fr} = \frac{1}{2}\left(\sigma_{ff} + \sigma_{rr}\right). \tag{16}$$

We define the radius of the grain particles as $R \equiv (\sigma_{ff} + \sigma_{rr})/2 = 5.5\sigma_0$, which is the distance from the grain center where the potential energy is zero. Fluid particles can occupy a position closer to the grain than this, this is illustrated in **Figure 3**. The figure shows the radial distribution function, $g(r)$, of fluid particles around a single spherical grain. The density of fluid varied between $\rho^* = 0.1$ and $\rho^* = 0.7$. This shows that the average distance from the grain particle and the closest fluid particle is approximately $5.5\sigma_0$, but the fluid particles are able to occupy positions closer to the grain particle.

The interaction strength ϵ_{ij} was set to ϵ_0 for all particle-particle pairs. The potential and its derivative are continuous in $r = r_{c,ij}$. The parameters a_{ij}, b_{ij} and $r_{s,ij}$ were determined so that the potential and the derivative of the potential (the force) are continuous at $r = r_{s,ij}$.

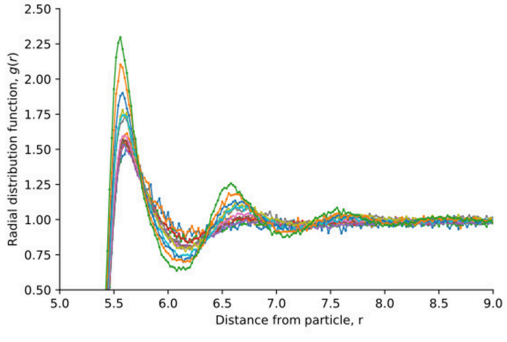

FIGURE 3 | The radial distribution function of fluid particles around a grain, as shown in **Figure 4**. Results are shown for densities that vary between $\rho^* = 0.1$ and $\rho^* = 0.7$.

3.4. Pressure Computations

The contribution of the fluid to the grand potential of layer l is [12]

$$p_l^f V_l^f = \frac{1}{3}\left\langle \sum_{i\in l} m_i(\mathbf{v}_i \cdot \mathbf{v}_i)\right\rangle - \frac{1}{6}\left\langle \sum_{i\in l}\sum_{j=1}^{N}(\mathbf{r}_{ij} \cdot \mathbf{f}_{ij})\right\rangle, \tag{17}$$

where p_l^f is the fluid differential pressure, V_l^f the fluid volume, m_i and $\mathbf{v}_i$ are the mass and velocity of fluid particle i. The first two sums are over all fluid particles i in layer l, while the second sum is over all other particles j. Half of the virial contribution, the second term in Equation (17), is assigned to particle i and the other half to particle j. The virial contribution assigned to the solid particles are not included. $\mathbf{r}_{ij} \equiv \mathbf{r}_i - \mathbf{r}_j$ is the vector connecting particle i and j, and $\mathbf{f}_{ij} = -\partial u_{ij}/\partial \mathbf{r}_{ij}$ is the force between them. The $\cdot$ means an inner product of the vectors. The computation gives $\hat{p}_l^f$, which is the contribution to the integral pressure in layer l from the fluid particles, accounting for their interaction with the grain particles.

3.5. The Porous Medium in a Pressure Gradient

We used the reflecting particle boundary method developed by Li et al. [15] to generate a pressure difference across the system along the x-axis. Particles moving from right to left pass the periodic boundary at $x = 0$ and $x = L_x$ with probability $(1 - \alpha_p)$ and reflected with probability α_p, whereas particles moving from left to right pass freely through the boundary. A large α_p gives a high pressure difference and a low α_p gives a low pressure difference.

4. RESULTS AND DISCUSSION

The results of the molecular dynamics simulations are shown in **Figures 4–8** (equilibrium) and **Figures 9**, **10** (away from equilibrium). The porous medium structure was characterized by its pair correlation function, cf. **Figure 3**. The compressional energy was computed according to equation 4 in case I with a single spherical grain and case II with a lattice of spherical grains.

We computed the compressional energy, $p_l V_l$, in the bulk liquid (region B) and in the nano-porous medium (region A). In the bulk liquid we computed the pressure directly from the compressional energy, because $p_l V_l = p_l^f V_l^f$ (not shown).

Figures 4, **6** show the various contributions to the compressional energy, cf. equation 4. The grain particles were identical and the system was in equilibrium, so the integral pressure in the grains was everywhere the same, $\hat{p}_l^r = \hat{p}^r$. Similarly, the surface tension was everywhere the same, $\gamma_l^{fr} = \gamma^{fr}$.

The grain pressure $\hat{p}^r$ and surface tension γ^{fr} were fitted such that the pressure is everywhere the same and are plotted as a function of the fluid pressure p^f. The results for case II were next used in **Figures 9**, **10** to determine the pressure gradient across the sequence of REVs in the porous medium.

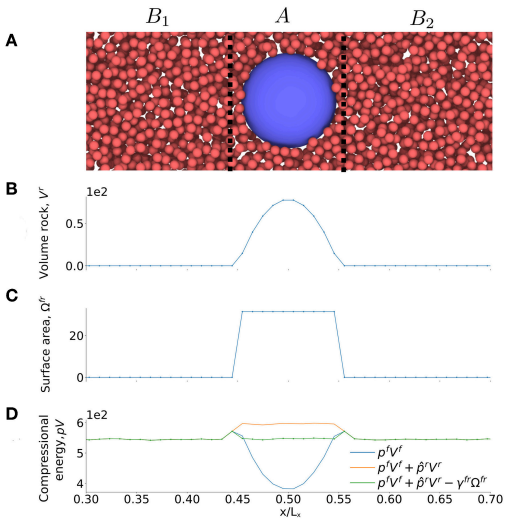

FIGURE 4 | (A) Illustration of case I, a single spherical grain surrounded by a fluid phase with $d = 4\sigma_0$. **(B)** Volume of grain, V^r, **(C)** surface area Ω^{fr} and **(D)** compressional energy pV as a function of the x-axis of the simulation box.

4.1. Case I. Single Spherical Grain. Equilibrium

The single sphere case is illustrated in **Figure 4A**. **Figures 4B,C** show the variation in the volume of the porous medium (rock), V_l^r, and the surface area between the rock and the fluid, Ω^{fr}, along the x-axis of the simulation box. The two quantities were determined for all layers, l, and these results were used in the plots of **Figures 4B,C**. To be representative, the REV must include the solid sphere with boundaries left and right of the sphere. In order to obtain $p^{\text{REV}}V^{\text{REV}}$ we summed $p_l V_l$ over all the layers in the REV. At equilibrium, $p^{\text{REV}} = p$, where p is the pressure in the fluid in region B. For the REV we then have

$$pV^{\text{REV}} = \sum_{l\in\text{REV}} p_l^f V_l^f + \hat{p}^r \sum_{l\in\text{REV}} V_l^r - \gamma^{fr} \sum_{l\in\text{REV}} \Omega_l^{fr}, \qquad (18)$$

where we used that $\hat{p}_l^r = \hat{p}^r$ and $\gamma_l^{fr} = \gamma^{fr}$. We know the values of all the elements in this equation, except $\hat{p}^r$ and γ^{fr}. The values of $\hat{p}^r$ and γ^{fr} are fitted such that the pressure, p in Equation (18) is everywhere the same. With these fitted values available, we calculated $p_l V_l$ of each layer from

$$p_l V_l = p_l^f V_l^f + \hat{p}^r V_l^r - \gamma^{fr}\Omega_l^{fr}. \qquad (19)$$

The contributions to the compressional energy in this equation for case I are shown in the bottom **Figure 4D**. We see the contribution from (1) the bulk fluid $p_l^f V_l^f$, (2) the bulk fluid and grain $p_l^f V_l^f + \hat{p}^r V_l^r$ and (3) the total compressional energy, $p_l V_l = p_l^f V_l^f + \hat{p}^r V_l^r - \gamma^{fr}\Omega^{fr}$, which gives the pressure of the REV when summed and divided with the volume of the REV.

Figure 4D shows clearly that the bulk pressure energy gives the largest contribution, as one would expect. It is also clear that the surface energy is significant. As the surface to volume ratio increases, the bulk contributions may become smaller than the surface contribution (not shown). In the present case, this will happen when the radius of the sphere is $2.25\sigma_0$. For our grains with $R = 5.5\sigma_0$, this does not happen.

The plots of $\hat{p}^r$ and γ^{fr} as functions of p in region B are shown in **Figure 5**. The values for $d = 4\sigma_0$ and $d = 11\sigma_0$ are given in the same plots. We see that the plots fall on top of each other. This shows that the integral pressure and the surface tension are independent of the distance d in the interval considered. If confinement effects were essential, we would expect that $\hat{p}^r$ and γ^{fr} were functions of the distance d between the surfaces of the spheres. When the value of d decreases below $4\sigma_0$, deviations may arise, for instance due to contributions from the disjoining pressure. Such a contribution is expected to vary with the surface area, and increase as the distance between interfaces become shorter. In plots like **Figure 5**, we may see this as a decrease in the surface tension.

4.2. Case II. Lattice of Spherical Grains. Equilibrium

Consider next the lattice of spherical grains, illustrated in **Figure 6A**. **Figures 6B,C** give the variation in the volume of the porous medium V_l^r and surface area, Ω^{fr}, along the x-axis.

When the REV in region A is properly chosen, we know that $p^{\text{REV}} = p$. In equilibrium, the pressure of the REV is constant in the bulk liquid phases, in regions B_1 or B_2, where p is the pressure of the fluid in region B. In order to obtain pV^{REV} in region A, we sum $p_l V_l$ over all the layers that make up the REV, and obtain

$$pV^{\text{REV}} = \sum_{l\in\text{REV}} p_l^f V_l^f + \hat{p}^r \sum_{l\in\text{REV}} V_l^r - \gamma^{fr} \sum_{l\in\text{REV}} \Omega_l^{fr}, \qquad (20)$$

To proceed, we find first the values of all the elements in this equation, except $\hat{p}^r$ and γ^{fr}. The values of $\hat{p}^r$ and γ^{fr} are fitted such that the pressure is everywhere the same. Using these fitted values, we next calculated $\hat{p}_l V_l$ of each layer using

$$p_l V_l = p_l^f V_l^f + \hat{p}^r V_l^r - \gamma^{fr}\Omega_l^{fr} \qquad (21)$$

The contributions to the compressional energy in this equation are shown in three stages in **Figure 6D**: (1) bulk fluid contribution $p_l^f V_l^f$, (2) bulk fluid and grain contribution $p_l^f V_l^f + \hat{p}^r V_l^r$ and (3) the total compressional energy, $p_l V_l = p_l^f V_l^f + \hat{p}^r V_l^r - \gamma^{fr}\Omega^{fr}$. **Figure 6D** shows clearly that the bulk contribution is largest, as is expected. However, the surface energy is significant.

From **Figure 6B** it follows that a proper choice of the REV is a unit cell, because all REVs are then identical, (except the REVs at the boundaries). The integral over $p_l V_l$ in these REVs is the same and equal to pV^{REV}. The layers l are smaller than the REV and as a consequence $\hat{p}_l V_l$ will vary, a variation that is seen in **Figure 6D**.

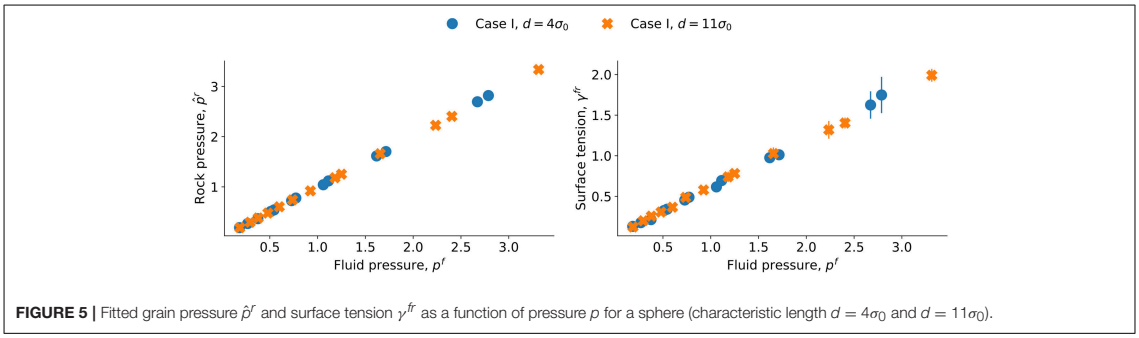

FIGURE 5 | Fitted grain pressure $\hat{p}^r$ and surface tension γ^{fr} as a function of pressure p for a sphere (characteristic length $d = 4\sigma_0$ and $d = 11\sigma_0$).

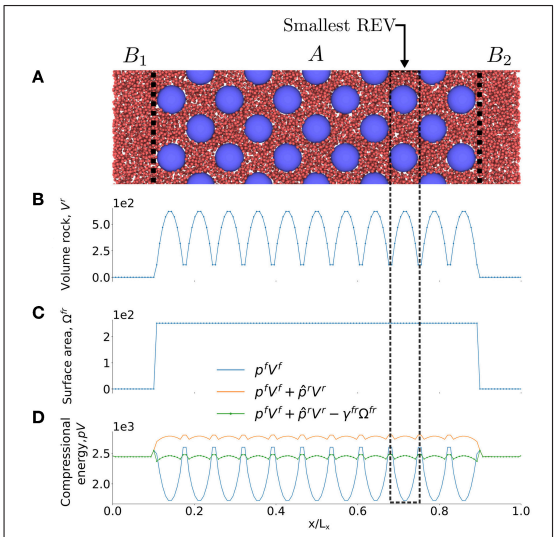

FIGURE 6 | (A) Illustration of case II, a lattice spherical grain surrounded by a fluid phase with $a = 20\sigma_0$. **(B)** Volume of grain, V^r, **(C)** surface area Ω^{fr} and **(D)** compressional energy pV as a function of the x-axis of the simulation box. The smallest REV is a unit cell.

The values for $\hat{p}^r$ and γ^{fr} are shown as a function of p^f for case II in **Figure 7** for $d_1 = 4.14\sigma_0$ and $d_1 = 11.21\sigma_0$. We see now a systematic difference between the values of $\hat{p}^r$ and γ^{fr} in the two cases. The integral pressure and the surface tension increases as the distance between the grains decreases. The difference in one set can be estimated from the other. Say, for a difference in surface tension $\Delta\gamma^{fr}$ we obtain for the same fluid pressure from equation 11, a difference in integral pressure of $\Delta\hat{p}^r = 3\Delta\gamma^{fr}/R$. This is nearly what we find by comparing the lines in **Figure 6**, the lines can be predicted from one another using $R = 6.5\sigma_0$ while the value in **Figure 3** is $R = 5.5\sigma_0$. The difference may be due to the disjoining pressure. Its distribution is not spherically symmetric, which may explain the difference between $6.5\sigma_0$ and $5.5\sigma_0$.

The results should be the same as for case I for the larger distance, and indeed that is found, cf. **Figure 8**. As the distance between the grain surfaces increases, we expect the dependence on confinement to disappear, and this is documented by **Figure 8** where the two cases are shown with distances $d = 11\sigma_0$ and $d_1 = 11.21\sigma_0$, respectively. The curves for the single grain and lattice of grains overlap.

The knowledge gained above on the various pressures at equilibrium is needed to construct the REV. The size of the REV includes the complete range of potential interactions available in the system, but not more. To find a REV-property, we need to sample the whole space of possible interactions. The thickness of the REV is larger than the layer thickness used in the simulations.

Our analysis therefore shows that the pressure inside grains in a fcc lattice and the surface tension, depends in particular on the distances between the surfaces of the spheres, including on their periodic replicas. A procedure has been developed to find the pressure of a REV, from information of the (equilibrium) values of $\hat{p}^r$ and γ^{fr} as a function of p^f. It has been documented in particular for nano-porous medium, but is likely to hold for other lattices, even amorphous materials when the REV can be defined properly.

4.3. Case II. Lattice of Spherical Grains. Non-equilibrium

Figure 9 illustrates the system in the pressure gradient, where **Figure 9B** shows the compressional energy, pV, along the x-axis. The dip in the pressure close to $x = 0$ is caused by the reflecting particle boundary, cf. section 3.5. The reflecting particle boundary introduces a surface between the high pressure on the left side and the low pressure on the right side.

To show first how a REV-property is determined from the layer-property, consider again the compressional energies of each layer. In the analysis we used the fcc lattice with lattice parameter $a = 20\sigma_0$. The volume of the grain, V^r, and the surface area, Ω^{fr}, varied of course in the exact same way as in **Figures 6B,C**. The pressure gradient was generated as explained in section 3.5. The pressure difference between the external reservoirs B_1 and B_2 was large, giving a gradient with order of magnitude 10^{12} bar/m. The fluid on the left side is liquid-like, while the fluid on the right side is gas-like. The smallest REV as obtained in the analysis at equilibrium is indicated in the figure.

In order to compute a REV variable away from equilibrium, we therefore follow the procedure described by Kjelstrup et al.

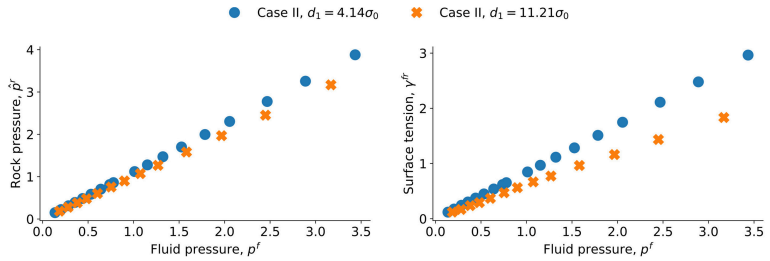

FIGURE 7 | Fitted grain pressure $\hat{p}^r$ and surface tension γ^{fr} as a function of pressure p for the lattice of spheres (characteristic length $d_1 = 4.14\sigma_0$ and $d_1 = 11.21\sigma_0$).

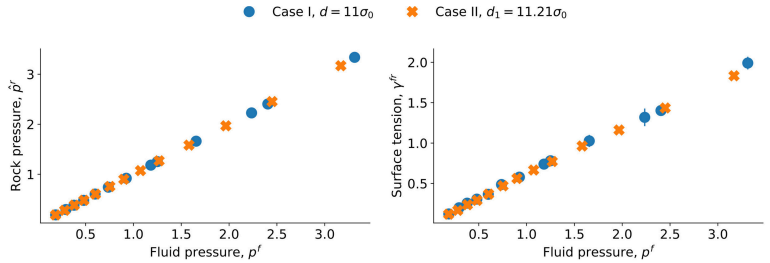

FIGURE 8 | Fitted grain pressure $\hat{p}^r$ and surface tension γ^{fr} as a function of pressure p for the sphere (characteristic length $d = 11\sigma_0$) and a lattice of spheres (characteristic length $d_1 = 11.21\sigma_0$).

[10] and choose a layer as a reference point. We then compute the average using five layers, two to the left, two to the right and the central layer. Moving one layer down the gradient, we repeat the procedure, and in this manner we obtain the property variation on the REV scale. The results of the simulation gave, for each individual layer, $p_l^l V_l^l$, as plotted in **Figure 9B**. The profile created by the REV-centers is shown in **Figure 10**. We see a smooth linear profile (central curve) as one would expect from the boundary conditions that are imposed on the system. Some traces of oscillation are still left in the separate contributions to the total compressional energy.

We have seen that a nano-porous medium is characterized by pressures in the fluid and the solid phases, as well as the surface tension between the fluid and the solid. When one reduces the size of a thermodynamic system to the nano-meter size, the pressures and the surface tensions become dependent on the size of the system. An important observation is then that there are two relevant pressures rather than one. Hill [1] called them the integral and the differential pressure, respectively. It is maybe surprising that the simple virial expression works so well for all pressure calculations in a fluid, but we have found that it can be used. We will next be able to study transport processes, where the external pressure difference is a driving force. The method, to compute the mechanical force intrinsic to the porous medium, may open interesting new possibilities to study the effects that are characteristic for porous media.

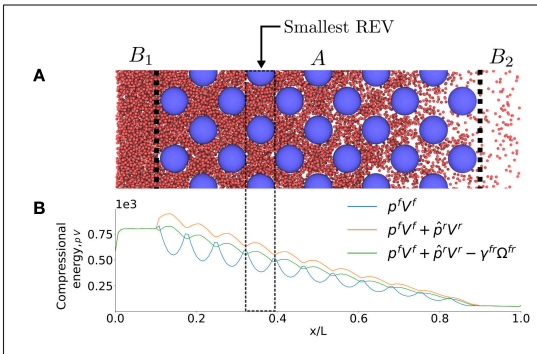

FIGURE 9 | (A) Illustration of case II in a pressure gradient. **(B)** Compressional energy pV variation across the system.

In a macro-scale description, the so-called representative elementary volume (REV) is essential. The REV makes it possible to obtain thermodynamic variables on this scale. We have here discussed how the fact that the macro-scale pressure is constant in equilibrium makes it possible to obtain the integral pressure in the solid, as well as the surface tension, of the liquid-solid contacts in the REV. An observation which confirms the soundness of the procedure is that we recover Young-Laplace's law for the differential pressures. The existence of a REV for

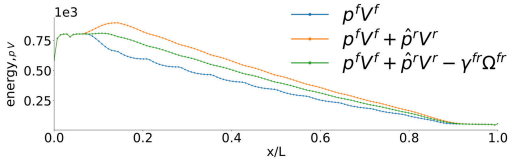

FIGURE 10 | Compressional energy pV variation across the system smoothed over the representary elementary volume.

systems on the nano-scale supports the idea of a REV that can be defined for pores also of micrometer dimension [10]. There is no conflict between the levels of description as they merge in the thermodynamic limit. The REV, as defined in the present work, may allow us to develop a non-equilibrium thermodynamic theory for the nano-scale.

5. CONCLUSIONS

The following conclusions can be drawn from the above studies

- We have obtained the first support for a new way to compute the pressure in a nano-porous medium. The integral pressure of the medium is defined by the grand potential. The definition applies to the thermodynamic limit, as well as to systems which are small, according to the definition of Hill [1].
- It follows that nano-porous media need two pressures in their description, the integral and the differential pressure. This is new knowledge in the context of nano-porous media.
- For a spherical rock particle of radius R, we derive a relation between the integral and the differential pressure in terms of the surface tension, $\hat{p}^r - p^r = \gamma/R$. Their difference is non-negligible in the cases where Young-Laplace's law applies.
- We have constructed two models of a porous medium, case I with a single spherical grain and case II with a fcc lattice of spherical grains. The new method to compute the pressure in these nano-porous mediums is not specific to these two cases, it is general. The method can be used on, e.g., a random distribution of spherical grains, but the REV will need to be larger in order to include all possible microstates. The REV needs in general to be larger as the heterogeneity of the porous medium increases.
- To illustrate the concepts, we have constructed a system with a single fluid. The rock pressure and the surface tension are constant throughout the porous medium at equilibrium. The assumptions were confirmed for a porosity change from $\phi = 0.74$ to 0.92, for a REV with minimum size of a unit cell.
- From the assumption of local equilibrium, we can find the pressure internal to a REV of the porous medium, under non-equilibrium conditions, and a continuous variation in the pressure on a macro-scale.

To obtain these conclusions, we have used molecular dynamics simulations of a single spherical grain in a pore and then for face-centered lattice of spherical grains in a pore. This tool is irreplaceable in its ability to test assumptions made in the theory. The simulations were used here to compute the integral rock pressure and the surface tension, as well as the pressure of the representative volume, and through this to develop a procedure for porous media pressure calculations.

Only one fluid has been studied here. The situation is expected to be more complicated with two-phase flow and an amorphous medium. Nevertheless, we believe that this first step has given useful information for the work to follow. We shall continue to use the grand potential for the more complicated cases, in work toward a non-equilibrium thermodynamic theory for the nano-scale.

AUTHOR CONTRIBUTIONS

All authors contributed equally to the work done. OG carried out the simulations.

ACKNOWLEDGMENTS

The calculation power was granted by The Norwegian Metacenter of Computational Science (NOTUR). We thank the Research Council of Norway through its Centres of Excellence funding scheme, project number 262644, PoreLab.

REFERENCES

1. Hill TL. *Thermodynamics of Small Systems*. New York, NY: Dover (1964).
2. Gray WG, Miller CT. Thermodynamically constrained averaging theory approach for modeling flow and transport phenomena in porous medium systems: 8. Interface and common curve dynamics. *Adv Water Resour.* (2010) **33**:1427–43. doi: 10.1016/j.advwatres.2010.07.002
3. Bennethum LS, Weinstein T. Three pressures in porous media. *Transp Porous Media.* (2004) **54**:1–34. doi: 10.1023/A:1025701922798
4. Magda J, Tirrell M, Davis H. Molecular dynamics of narrow, liquid-filled pores. *J Chem Phys.* (1985) **83**:1888–901. doi: 10.1063/1.449375
5. Todd B, Evans DJ, Daivis PJ. Pressure tensor for inhomogeneous fluids. *Phys Rev E.* (1995) **52**:1627. doi: 10.1103/PhysRevE.52.1627
6. Ikeshoji T, Hafskjold B, Furuholt H. Molecular-level calculation scheme for pressure in inhomogeneous systems of flat and spherical layers. *Mol Simulat.* (2003) **29**:101–9. doi: 10.1080/10286620210000 2518a
7. Hafskjold B, Ikeshoji T. Microscopic pressure tensor for hard-sphere fluids. *Phys Rev E.* (2002) **66**:1–4. doi: 10.1103/PhysRevE.66.0 11203
8. Hassanizadeh SM, Gray WG. Mechanics and thermodynamics of multiphase flow in porous media including interphase boundaries. *Adv Water Resour.* (1990) **13**:169–86. doi: 10.1016/0309-1708(90)90040-B
9. Gray WG, Hassanizadeh SM. Macroscale continuum mechanics for multiphase porous-media flow including phases, interfaces. *Adv Water Resour.* (1998) **21**:261–81. doi: 10.1016/S0309-1708(96)0 0063-2
10. Kjelstrup S, Bedeaux D, Hansen A, Hafskjold B, Galteland O. Non-isothermal transport of multi-phase fluids in porous media. the entropy production. *Front Phys.* (2018) **6**:126. doi: 10.3389/fphy.2018.00126

11. Kjelstrup S, Bedeaux D, Hansen A, Hafskjold B, Galteland O. Non-isothermal transport of multi-phase fluids in porous media. Constitutive Equations. *Front Phys.* (2019) **6**:150. doi: 10.3389/fphy.2018.00150
12. Irving JH, Kirkwood JG. The statistical mechanical theory of transport processes. IV. The equations of hydrodynamics. *J Chem Phys*. (1950) **18**:817–29. doi: 10.1063/1.1747782
13. Tolman RC. The effect of droplet size on surface tension. *J Chem Phys*. (1949) **17**:333–7. doi: 10.1063/1.1747247
14. Helfrich W. Elastic properties of lipid bilayers: theory and possible experiments. *Zeitschrift für Naturforschung C*. (1973) **28**:693–703.
15. Li J, Liao D, Yip S. Coupling continuum to molecular-dynamics simulation: reflecting particle method and the field estimator. *Phys Rev E*. (1998) **57**:7259–67. doi: 10.1103/PhysRevE.57.7259
16. Plimpton S. Fast parallel algorithms for short - range molecular dynamics. *J Comput Phys*. (1995) **117**:1–19. doi: 10.1006/jcph.1995.1039
17. Hoover WG, Holian BL. Kinetic moments method for the canonical ensemble distribution. *Phys Lett Sect A*. (1996) **211**:253–7. doi: 10.1016/0375-9601(95)00973-6

Conflict of Interest Statement: The authors declare that the research was conducted in the absence of any commercial or financial relationships that could be construed as a potential conflict of interest.

Article IV

Mate Erdős, **Olav Galteland**, Dick Bedeaux, Signe Kjelstrup, Othonas A. Moultos, Thijs J. H. Vlugt

Gibbs Ensemble Monte Carlo Simulation of Fluids in Confinement: Relation Between the Differential and Integral Pressures

Nanomaterials, 10(2), 293. (2020)

DOI: 10.3390/nano10020293

Article IV

Article IV

nanomaterials

MDPI

Article

Gibbs Ensemble Monte Carlo Simulation of Fluids in Confinement: Relation between the Differential and Integral Pressures

Máté Erdős [1], Olav Galteland [2], Dick Bedeaux [2], Signe Kjelstrup [2], Othonas A. Moultos [1] and Thijs J. H. Vlugt [1,*]

[1] Engineering Thermodynamics, Process & Energy Department, Faculty of Mechanical, Maritime and Materials Engineering, Delft University of Technology, Leeghwaterstraat 39, 2628CB Delft, The Netherlands; m.erdos-2@tudelft.nl (M.E.); o.moultos@tudelft.nl (O.A.M.)

[2] PoreLab, Department of Chemistry, Norwegian University of Science and Technology, 7031 Trondheim, Norway; olav.galteland@ntnu.no (O.G.); dick.bedeaux@ntnu.no (D.B.); signe.kjelstrup@ntnu.no (S.K.)

* Correspondence: t.j.h.vlugt@tudelft.nl

Received: 12 January 2020; Accepted: 5 February 2020; Published: 9 February 2020

Abstract: The accurate description of the behavior of fluids in nanoporous materials is of great importance for numerous industrial applications. Recently, a new approach was reported to calculate the pressure of nanoconfined fluids. In this approach, two different pressures are defined to take into account the smallness of the system: the so-called differential and the integral pressures. Here, the effect of several factors contributing to the confinement of fluids in nanopores are investigated using the definitions of the differential and integral pressures. Monte Carlo (MC) simulations are performed in a variation of the Gibbs ensemble to study the effect of the pore geometry, fluid-wall interactions, and differential pressure of the bulk fluid phase. It is shown that the differential and integral pressure are different for small pores and become equal as the pore size increases. The ratio of the driving forces for mass transport in the bulk and in the confined fluid is also studied. It is found that, for small pore sizes (i.e., $<5\sigma_{\text{fluid}}$), the ratio of the two driving forces considerably deviates from 1.

Keywords: nanothermodynamics; porous systems; molecular simulation; differential pressure; integral pressure

1. Introduction

The widespread application of nanoporous materials in several fields, such as chromatography, membrane separation, catalysis, etc., has lead to a growing interest in the accurate description of the thermodynamic behavior of fluids confined in nanopores [1–6]. The pressure of a nanoconfined fluid is one of the most important thermodynamic properties which is needed for an accurate description of the flow rate, diffusion coefficient, and the swelling of the nanoporous material [7–10]. Various approaches for calculating the pressure of a fluid in a nanopore have been proposed [1,11–13]. The main difficulty of the pressure calculation arises from the ambiguous definition of the pressure tensor inside porous materials due to the presence of curved surfaces and confinement effects [7,14,15]. Traditional thermodynamic laws and concepts, such as Gibbs surface dynamics, Kelvin equation, etc., may not be applicable at the nano-scale [16]. In the past decade, several methods were reported using different simulation techniques i.e., classical density functional theory [17,18], equation of state modeling [19], etc., to model the behavior of fluids in confinement.

Recently, Galteland et al. [11] reported a new approach for the calculation of pressure in nanoporous materials using Hill's thermodynamics for small systems [20]. In this approach, two

different pressures are needed to account for confinement effects in nanoporous materials: the differential pressure P, and the integral pressure $\hat{p}$. In an ensemble of small systems, the differential pressure times the volume change of the small systems is equal to the work exerted on the surroundings by the volume change. The differential pressure corresponds to the macroscopic pressure and does not depend on the size of the system. The addition of a small system to an ensemble of small systems exerts work on the surroundings which is equal to the integral pressure times the volume of the added small system. The differential and integral pressures are different for small systems and become equal in the thermodynamic limit. For a system with volume V, the two pressures are related by [11,20]:

$$P(V) = \left(\frac{\partial(\hat{p}(V)V)}{\partial V}\right)_{T,\mu} = \hat{p}(V) + V\left(\frac{\partial(\hat{p}(V))}{\partial V}\right)_{T,\mu}. \quad (1)$$

As shown in Equation (1), the two pressures are different only when the integral pressure $\hat{p}$ depends on the volume of the system. Galteland et al. [11] performed equilibrium and non-equilibrium molecular dynamics simulations of Lennard–Jones (LJ) fluids in a face-centered lattice of spherical grains representing a porous medium. Using Hill's thermodynamics of small systems [20] and the additive property of the grand potential, Galteland et al. [11] defines the compressional energy ($\hat{p}V$) of the representative elementary volume (REV) in the simulations as follows:

$$\hat{p}V = \hat{p}^{\mathrm{f}}V^{f} + \hat{p}^{\mathrm{r}}V^{\mathrm{r}} - \hat{\gamma}^{\mathrm{fr}}\omega^{\mathrm{fr}}, \quad (2)$$

where $\hat{p}$ is the integral pressure of volume V, $\hat{p}^{\mathrm{f}}$ and V^{f} are the integral pressure and volume of the fluid, $\hat{p}^{\mathrm{r}}$ and V^{r} are the integral pressure and volume of the grain particles, and the $\hat{\gamma}^{\mathrm{fr}}$ and ω^{fr} are the integral surface tension and surface area between the fluid and grain particles. Based on the obtained results, it was concluded that the definition of two pressures is needed to calculate the pressure of the fluid in nanoporous medium.

In this study, the relation between the differential and integral pressure is investigated by performing Monte Carlo (MC) simulations of LJ fluids. The simulations are carried out in a modified Gibbs ensemble, using two simulation boxes in equilibrium with each other. One box represents the bulk fluid, while the other simulation box represents the nanoconfined system, including walls that interact with the fluid particles, as shown in Figure 1. The effect of confinement on the integral pressure is investigated by considering different fluid-wall interaction strengths and pore geometries, namely, a cylinder and a slit pore. To investigate the relation between the differential and integral pressure, the difference of the two pressures, $P - \langle\hat{p}\rangle$, and the ratio of driving forces for mass transport, $\frac{\mathrm{d}\langle\hat{p}\rangle}{\mathrm{d}P}$, are computed. In Section 2, the devised ensemble and the equations used to calculate the pressure and energy of the system are presented. In Section 3, a rigorous derivation of the used expression to compute the ratio of driving forces is shown. In Section 4, the results for the different differential pressures and pore geometries are shown. In Section 5, our conclusions are summarized.

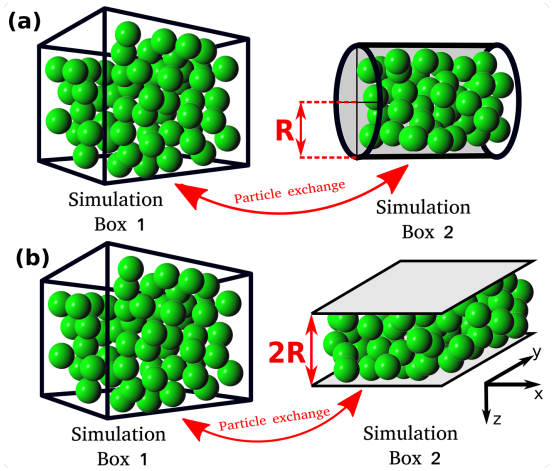

Figure 1. Schematic representation of the Monte Carlo (MC) simulation scheme. Simulation Box 1 represents the bulk fluid with differential pressure P. Simulation Box 2 contains the confined fluid with (average) integral pressure $\langle \hat{p} \rangle$. (**a**,**b**) The two investigated systems are shown where the bulk fluid is in equilibrium with the nanoconfined fluid in a cylinder and in a slit pore, respectively. Due to the particle exchange, the chemical potential of the two boxes are equal, but in general $P \neq \langle \hat{p} \rangle$.

2. Simulation Details

All MC simulations are carried out using an in-house simulation code. The MC simulations consist of two simulation domains, Simulation Box 1 and Simulation box 2 (see Figure 1). Throughout the manuscript the terms Simulation Box 1 and 2 are used to refer to the two domains, however, simulation domain 2 does not correspond to an actual box. The total number of particles in the system, N_T, is fixed and particles can be exchanged between the simulation boxes. Box 1 is cubic and has periodic boundary conditions imposed in all directions. Box 1 represents a bulk fluid. The differential pressure, P, and temperature, T, in Simulation Box 1 are imposed, while the volume, V_1, and the number of particles, N_1, can fluctuate. Simulation Box 2 is a cylinder or a slit pore with a fixed volume V_2. The size of the cylinder and the slit pore are defined by the radius, R, and by the distance between the two parallel planes, $2R$, respectively (Figure 1). In Box 2, periodic boundary conditions are applied only in the axial direction for the cylinder and in the x and y directions for the slit pore (see Figure 1). Box 2 represents the confined fluid which has an integral pressure $\hat{p}$. In Simulation Box 2, the volume, V_2, and temperature T are imposed, while the number of particles N_2 can fluctuate by exchanging particles with Box 1. The instantaneous integral pressure fluctuates, and by definition [20] its ensemble average, $\langle \hat{p} \rangle$, will be equal to P only for macroscopic systems ($R \to \infty$). The ensemble used is a variation of the NPT-Gibbs ensemble [21]. The main difference between the ensemble used in this work and the conventional NPT-Gibbs ensemble is that in our simulations the volume of Box 2 is fixed [21]. Essentially, Box 2 corresponds to the grand canonical ensemble with the reservoir explicitly modeled in Box 1. This computational setup was also used in other studies, i.e., A. Z. Panagiotopoulos et al. [21], P. Bai et al. [22], etc.

In the MC simulations, three types of trial moves are used: translation, volume change, and particle exchange. The translation and particle exchange trial moves are used in both simulation boxes, while volume change trial moves are only performed in Simulation Box 1. The acceptance rules of the trial moves can be found elsewhere [23]. The particle exchange trial move, ensures that Box 1 and Box 2 are in chemical equilibrium, i.e., the chemical potentials of the two boxes are equal ($\mu_1 = \mu_2$). The chemical potentials of the boxes are defined as the sum of the ideal and excess chemical potentials of the fluid in the respective box ($\mu_1 = \mu_1^{\text{id}} + \mu_1^{\text{ex}}, \mu_2 = \mu_2^{\text{id}} + \mu_2^{\text{ex}}$). The ideal gas chemical potentials ($\mu_1^{\text{id}}, \mu_2^{\text{id}}$) are calculated based on the density and temperature of the fluid. The excess chemical potential

(μ_1^{ex}, μ_2^{ex}) can be calculated using different methods, i.e., Widom's test particle insertion method [23], Contionous Fractional Component Monte Carlo method [24,25], Bennet acceptance ratio method [26], etc. Although the Bennet acceptance ratio method is computationally more efficient than the Widom's test particle insertion method, the Widom's test particle method is sufficient for the systems considered in this study. Separate simulations are carried out using different cylinder radii R, while imposing $P = 0.2$ (in reduced units) in Box 1. In Figure 2, the chemical potential of Box 1 and Box 2 (Figure 2a), as well as the density of Box 1 and Box 2 (Figure 2b), are shown as a function of the cylinder radius at $P = 0.2$. As can be seen from Figure 2a, the chemical potentials of Box 1 and Box 2 are equal within the uncertainties of the simulations.

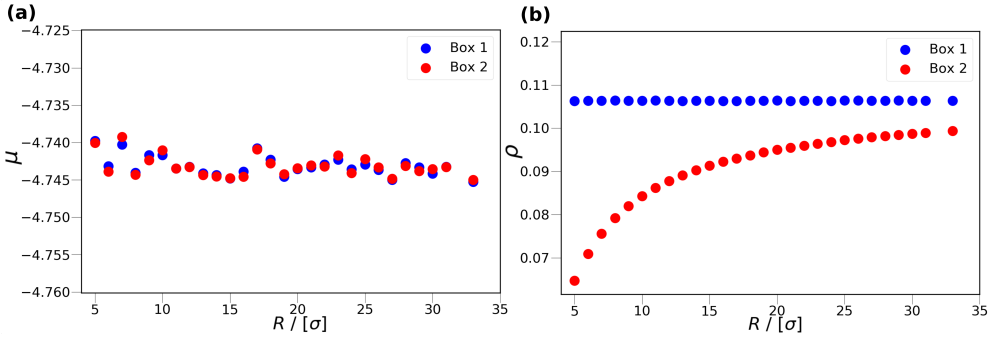

Figure 2. The chemical potential (**a**) and density (**b**) of the bulk, Box 1, and confined fluids, Box 2, as a function of the cylinder radius, R, at $P = 0.2$ (in Simulation Box 1). The blue and red colors represent Box 1 and Box 2, respectively. The temperature is fixed at $T = 2$. All values are presented in reduced units. The error bars are smaller than the symbol sizes.

In all simulations, the total potential energy, U, is calculated using the 12-6 LJ interaction potential:

$$U = U_{\text{fluid}-\text{fluid}} + U_{\text{fluid}-\text{wall}}, \tag{3}$$

where $U_{\text{fluid}-\text{fluid}}$ is the potential energy due to interaction between the fluid particles, and $U_{\text{fluid}-\text{wall}}$ represents the potential energy contribution from the interactions between the fluid particles and the wall of Box 2. $U_{\text{fluid}-\text{fluid}}$ in both simulation boxes is calculated according to:

$$U_{\text{fluid}-\text{fluid}} = \begin{cases} \sum_{i<j} \left[4\epsilon_{\text{fluid}} \left(\left(\frac{\sigma_{\text{fluid}}}{r_{ij}} \right)^{12} - \left(\frac{\sigma_{\text{fluid}}}{r_{ij}} \right)^{6} \right) - U_{\text{shift}} \right] & r_{ij} < 2.5\sigma_{\text{fluid}} \\ 0, & \text{otherwise} \end{cases}, \tag{4}$$

where r_{ij} is the distance of particle i and j, U_{shift} makes the interaction potentially continuous at the cut-off distance ($2.5\sigma_{\text{fluid}}$), and ϵ_{fluid}, σ_{fluid} are the LJ parameters. In the past, several studies were reported using different types of interaction potentials to model the fluid-solid interactions in confined spaces [22,27,28]. Since the aim of this study is to show the difference between the differential and integral pressures and not to simulate some specific adsorption system, only two types of interaction potentials are considered for the interaction of fluid particles with the wall in Simulation Box 2. In the first case, the wall has only repulsive interactions with the fluid particles. The potential energy contribution of this type is calculated based on the Weeks–Chandler–Andersen potential [29]:

$$U_{\text{fluid}-\text{wall}} = \begin{cases} \sum_{i=0}^{N_2} \left[4\epsilon_{\text{fw}} \left(\left(\frac{\sigma_{\text{fw}}}{r_{wi}} \right)^{12} - \left(\frac{\sigma_{\text{fw}}}{r_{wi}} \right)^{6} \right) + 1 \right] & r_{wi} < 2^{1/6}\sigma_{\text{fw}} \\ 0, & \text{otherwise} \end{cases}, \tag{5}$$

where N_2 is the number of particles in Box 2, r_{wi} is the closest distance of particle i from the walls, and ϵ_{fw} and σ_{fw} are the LJ parameters for the interaction between the wall and the fluid particles. In the second case, the attractive interactions between the wall and fluid particles are taken into account using the traditional form of the 12-6 LJ interaction potential:

$$U_{\text{fluid}-\text{wall}} = \begin{cases} \sum_{i=0}^{N_2} \left[4\epsilon_{\text{fw}} \left(\left(\frac{\sigma_{\text{fw}}}{r_{wi}} \right)^{12} - \left(\frac{\sigma_{\text{fw}}}{r_{wi}} \right)^{6} \right) - U_{\text{shift}-\text{fw}} \right] & r_{\text{wi}} < 2.5\sigma_{\text{fw}} \\ 0, & \text{otherwise} \end{cases}, \tag{6}$$

where $U_{\text{shift}-\text{fw}}$ makes the interaction potential continuous at the cut-off distance, and ϵ_{fw} and σ_{fw} are the LJ parameters.

The expression for calculating the integral pressure in Box 2 is as follows[30]:

$$\hat{p} = \frac{N_2}{V_2} k_{\text{B}} T + \hat{p}_{\text{fluid}-\text{fluid}} + \hat{p}_{\text{fluid}-\text{wall}}, \tag{7}$$

where $\hat{p}_{\text{fluid}-\text{fluid}}$ represents the contribution of the fluid-fluid interaction to the integral pressure, k_B is the Boltzmann constant, and $\hat{p}_{\text{fluid}-\text{wall}}$ represents the contribution of the fluid-wall interaction to the integral pressure. The $\hat{p}_{\text{fluid}-\text{fluid}}$, and $\hat{p}_{\text{fluid}-\text{wall}}$ terms represent the virial contributions of the integral pressure. The terms are calculated based on the virial theorem [7], i.e., using the derivative of the potential energy function with respect to r. The pressure term $\hat{p}_{\text{fluid}-\text{fluid}}$ is calculated as follows [7]:

$$\hat{p}_{\text{fluid}-\text{fluid}} = \frac{48}{3V_2} \epsilon_{\text{fluid}} \sum_{i<j} \left(\left(\frac{\sigma_{\text{fluid}}}{r_{ij}} \right)^{12} - 0.5 \left(\frac{\sigma_{\text{fluid}}}{r_{ij}} \right)^{6} \right). \tag{8}$$

The third term in Equation (7) represents the pressure contribution related to the interactions of the LJ particles with the wall of Box 2. The term $\hat{p}_{\text{fluid}-\text{wall}}$ for the repulsive wall potential is derived based on Equation (5) [7]. The following expression is obtained:

$$\hat{p}_{\text{fluid}-\text{wall}} = \begin{cases} \sum_{i=1}^{N_2} \frac{24}{3V_2} \epsilon_{\text{fw}} \left(\left(\frac{\sigma_{\text{fw}}}{r_{wi}} \right)^{12} - 0.5 \left(\frac{\sigma_{\text{fw}}}{r_{wi}} \right)^{6} \right) & r_{wi} < 2^{1/6} \sigma_{\text{fw}} \\ 0, & \text{otherwise} \end{cases}. \tag{9}$$

The following expression is used to calculate the $\hat{p}_{\text{fluid}-\text{wall}}$ when the wall has also attractive interactions with the fluid [7]:

$$\hat{p}_{\text{fluid}-\text{wall}} = \begin{cases} \sum_{i=1}^{N_2} \frac{24}{3V_2} \epsilon_{\text{fw}} \left(\left(\frac{\sigma_{\text{fw}}}{r_{wi}} \right)^{12} - 0.5 \left(\frac{\sigma_{\text{fw}}}{r_{wi}} \right)^{6} \right) & r_{wi} < 2.5\sigma_{\text{fw}} \\ 0, & \text{otherwise} \end{cases}. \tag{10}$$

By comparing Equations (8)–(10), it can observed that the multiplication factor 48 in Equation (8) is replaced by the factor 24 in Equations (9) and (10). This difference means that only 50 % of the fluid-wall interactions are taken into account at the calculation of the $\hat{p}_{\text{fluid}-\text{wall}}$ term [7]. In the MC simulations, Equations (7)–(10) yield instantaneous values from which ensemble averages are computed, i.e., $\langle \hat{p} \rangle$.

In all simulations, the LJ parameters of the fluid particles are $\epsilon_{\text{fluid}} = 1$, $\sigma_{\text{fluid}} = 1$, and the cut-off radius is $r_{\text{cut}} = 2.5\sigma_{\text{fluid}}$ for the fluid-fluid interactions. Regardless of the type of interaction potential used to calculate the interaction of the fluid particles and the wall in Simulation Box 2, the LJ parameter, $\sigma_{\text{fw}} = 1$ is used. In the case of the purely repulsive wall potential, the LJ parameter $\epsilon_{\text{fw}} = 1$ is used. In case of the attractive wall potential, five different values for the ϵ_{fw} LJ parameters are considered: $\epsilon_{\text{fw}} = 0.3, 0.5, 0.7, 1.0, 1.5$. In this study, all of the reported parameters are in dimensionless units. The LJ interactions are truncated and shifted (i.e., no tail corrections are applied). To avoid phase transitions, the temperature is fixed at $T = 2$ [31,32].

3. Theory

To investigate the difference between the differential and integral pressures, the ratio $\frac{d\langle\hat{p}\rangle}{dP}$ is calculated. The term $\frac{d\langle\hat{p}\rangle}{dP}$ is the ratio of the pressure gradient for mass transport in the bulk phase, $\frac{dP}{dL}$, and in the confined space $\frac{d\langle\hat{p}\rangle}{dL}$ (see Figure 3). Essentially, the ratio of driving forces, $\frac{d\langle\hat{p}\rangle}{dP}$, equals the ratio of transport coefficients when either P or $\hat{p}$ is used as driving force for mass transport in the corresponding transport equation. $\frac{d\langle\hat{p}\rangle}{dP}$ is referred to as the ratio of driving forces throughout this work. One possible approach to compute the ratio of driving forces is to perform simulations at different imposed differential pressures and calculate the difference in the differential and integral pressures. To avoid the necessity of performing several simulations, in this study the ratio of driving forces is calculated based on the fluctuation theory. Using this approach, the ratio of driving forces can be obtained by performing a single simulation.

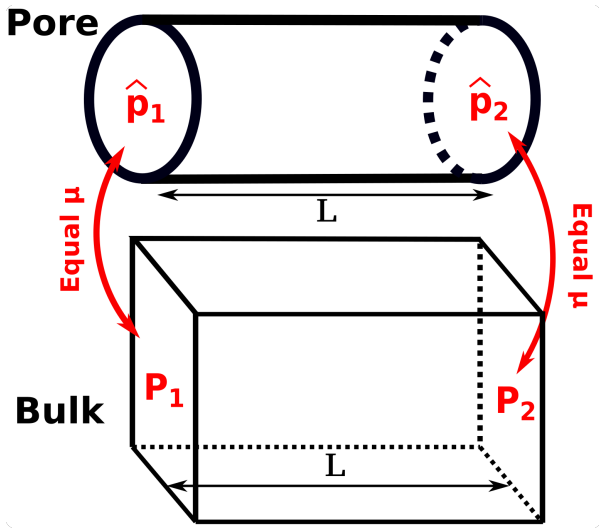

Figure 3. Schematic representation of a bulk fluid in equilibrium with a nanoconfined fluid in a pore. The concept of the ratio of driving forces for mass transport, $\frac{d\langle\hat{p}\rangle}{dP}$, can be introduced based on the definition of ratio of driving forces in the two systems, $\frac{d\langle\hat{p}\rangle}{dL}$ and $\frac{dP}{dL}$.

To obtain an expression for $\frac{d\langle\hat{p}\rangle}{dP}$, the partition function of the system is needed [23]:

$$Q = C \sum_{N_1=0}^{N_T} \frac{V_2^{N_T-N_1}}{N_1!\,(N_T-N_1)!} \int_0^\infty dV_1\, V_1^{N_1}\, e^{-\beta P V_1} \int dr^{N_T}\, e^{-\beta U}, \tag{11}$$

where C is a constant, $\beta = \frac{1}{k_B T}$, N_1 is the number of particles in Box 1, N_T is total number of particles in the simulation, V_1 is the volume of Box 1, V_2 is the volume of Box 2, and U is the potential energy. The ensemble average of a thermodynamic property X can be obtained using:

$$\langle X\rangle = \frac{\sum_{N_1=0}^{N_T} \frac{V_2^{(N_T-N_1)}}{N_1!\,(N_T-N_1)!} \int_0^\infty dV_1\, V_1^{N_1}\, e^{-\beta P V_1} \int dr^{N_T}\, e^{-\beta U} X}{\sum_{N_1=0}^{N_T} \frac{V_2^{(N_T-N_1)}}{N_1!\,(N_T-N_1)!} \int_0^\infty dV_1\, V_1^{N_1}\, e^{-\beta P V_1} \int dr^{N_T}\, e^{-\beta U}}. \tag{12}$$

Therefore, to obtain the expression for $\frac{\mathrm{d}\langle\hat{p}\rangle}{\mathrm{d}P}$, the following relation is used:

$$\frac{\mathrm{d}\langle\hat{p}\rangle}{\mathrm{d}P} = \frac{\mathrm{d}}{\mathrm{d}P}\frac{\sum_{N_1=0}^{N_T}\frac{V_2^{(N_T-N_1)}}{N_1!\,(N_T-N_1)!}\int_0^\infty \mathrm{d}V_1\, V_1^{N_1}\, e^{-\beta P V_1}\int \mathrm{d}r^{N_T}\, e^{-\beta U}\hat{p}}{\sum_{N_1=0}^{N_T}\frac{V_2^{(N_T-N_1)}}{N_1!\,(N_T-N_1)!}\int_0^\infty \mathrm{d}V_1\, V_1^{N_1}\, e^{-\beta P V_1}\int \mathrm{d}r^{N_T}\, e^{-\beta U}}. \tag{13}$$

By switching the order of the integration and differentiation, the following expression is obtained:

$$\begin{aligned}
&\frac{\mathrm{d}\langle\hat{p}\rangle}{\mathrm{d}P} = \\
&\frac{\left(\sum_{N_1=0}^{N_T}\int_0^\infty \mathrm{d}V_1\int \mathrm{d}r^{N_T}\,\frac{V_2^{(N_T-N_1)}\,V_1^{N_1}}{N_1!\,(N_T-N_1)!}\,(-\beta\,V_1)e^{-\beta P V_1}\,e^{-\beta U}\hat{p}\right)}{\left(\sum_{N_1=0}^{N_T}\int_0^\infty \mathrm{d}V_1\int \mathrm{d}r^{N_T}\,\frac{V_2^{(N_T-N_1)}\,V_1^{N_1}}{N_1!\,(N_T-N_1)!}\,e^{-\beta P V_1}\,e^{-\beta U}\right)^2} \\
&\times\left(\sum_{N_1=0}^{N_T}\int_0^\infty \mathrm{d}V_1\int \mathrm{d}r^{N_T}\,\frac{V_2^{(N_T-N_1)}\,V_1^{N_1}}{N_1!\,(N_T-N_1)!}\,e^{-\beta P V_1}\,e^{-\beta U}\right) \\
&-\frac{\left(\sum_{N_1=0}^{N_T}\int_0^\infty \mathrm{d}V_1\int \mathrm{d}r\,\frac{V_2^{(N_T-N_1)}\,V_1^{N_1}}{N_1!\,(N_T-N_1)!}\,(-\beta\,V_1)e^{-\beta P V_1}\,e^{-\beta U}\right)}{\left(\sum_{N_1=0}^{N_T}\int_0^\infty \mathrm{d}V_1\int \mathrm{d}r^{N_T}\,\frac{V_2^{(N_T-N_1)}\,V_1^{N_1}}{N_1!\,(N_T-N_1)!}\,e^{-\beta P V_1}\,e^{-\beta U}\right)^2} \\
&\times\left(\sum_{N_1=0}^{N_T}\int_0^\infty \mathrm{d}V_1\int \mathrm{d}r^{N_T}\,\frac{V_2^{(N_T-N_1)}\,V_1^{N_1}}{N_1!\,(N_T-N_1)!}\,e^{-\beta P V_1}\,e^{-\beta U}\hat{p}\right) \\
&=\langle-\beta V_1\hat{p}\rangle-(\langle-\beta V_1\rangle\langle\hat{p}\rangle)=\beta(\langle V_1\rangle\langle\hat{p}\rangle-\langle V_1\hat{p}\rangle)=\frac{\langle V_1\rangle\langle\hat{p}\rangle-\langle V_1\hat{p}\rangle}{k_bT}.
\end{aligned} \tag{14}$$

The final expression in Equation (14) is essentially the cross correlation between V_1 and $\hat{p}$. In this study, this expression is used to calculate the ratio of driving forces.

4. Results and Discussion

In this work, the difference between the differential and integral pressure, $P-\langle\hat{p}\rangle$, and the ratio of driving forces $\frac{\mathrm{d}\langle\hat{p}\rangle}{\mathrm{d}P}$, are investigated. Two different pore geometries, a cylinder and a slit pore, are studied with varying fluid-wall interaction potentials. The effect of confinement is investigated for gas ($\rho\approx 0.1$) and liquid ($\rho = 0.58, 0.8$) phases, corresponding to $P = 0.2, 2.0, 6.0$, respectively.

4.1. Difference between the Differential and Integral Pressure

In Figure 4, the difference between the differential, P, and the ensemble average of the integral pressure, $\langle\hat{p}\rangle$, is shown as a function of the inverse radius, R^{-1}, of Box 2 for the cylindrical and slit pore cases for the two types of wall potentials. As can be seen in Figure 4, as R^{-1} decreases, the difference between the differential and integral pressure decreases in all cases. The data are fitted to $AR^{-1}+B$, where A and B are constants. The coefficient of determination of the fitted lines is above 0.99 showing that the relation between the R^{-1} and $P-\langle\hat{p}\rangle$ is indeed linear. For large radii ($R > 30\sigma$), where the fluid in Box 2 behaves like in the bulk, $P-\langle\hat{p}\rangle$ approaches 0, which is also indicated by the fitted lines. In Figure 4a,c,e, the difference between the two pressures are shown for the cylindrical pore. In Figure 4b,d,f, the difference in the pressures are shown for the slit pore. By comparing the magnitude of $P-\langle\hat{p}\rangle$ for the cylindrical and slit pore cases, it can be seen that the pressure difference is larger in the cylindrical pore than in the slit pore. The larger value of $P-\langle\hat{p}\rangle$ for the cylindrical pores can be attributed to the stronger confinement effects compared to the slit pore. The stronger confinement effects are also indicated by the steeper slopes (constant A in the fitted lines) of the cylindrical pore compared to the slit pore. It can also be observed that by increasing the interaction strength between

the wall of Box 2 and the fluid, ϵ_{wf}, the difference between the differential and integral pressure at the same pore size decreases. By comparing the calculated values of $P - \langle \hat{p} \rangle$ for $P = 0.2$ and $P = 6.0$, it can be seen that the effect of the interaction strength between the wall in Box 2 and the fluid, ϵ_{wf}, is considerably larger at the lower differential pressure. For example, in the case of the slit pore, the ratio of slopes of the fitted line for $\epsilon_{wf} = 1.0$ and $\epsilon_{wf} = 1.5$ at $P = 0.2$ is 0.88, as shown in Figure 4b, and at $P = 6.0$ is 0.96, as shown in Figure 4f. This can be caused by the different number of particles inside the pore at the two differential pressures. In the case of $P = 0.2$, by increasing the interaction strength, more particles can enter the pore which results in larger integral pressures, while at $P = 6.0$, the pore is practically saturated for all ϵ_{wf}; therefore, the interaction strength has a lower effect on the integral pressure.

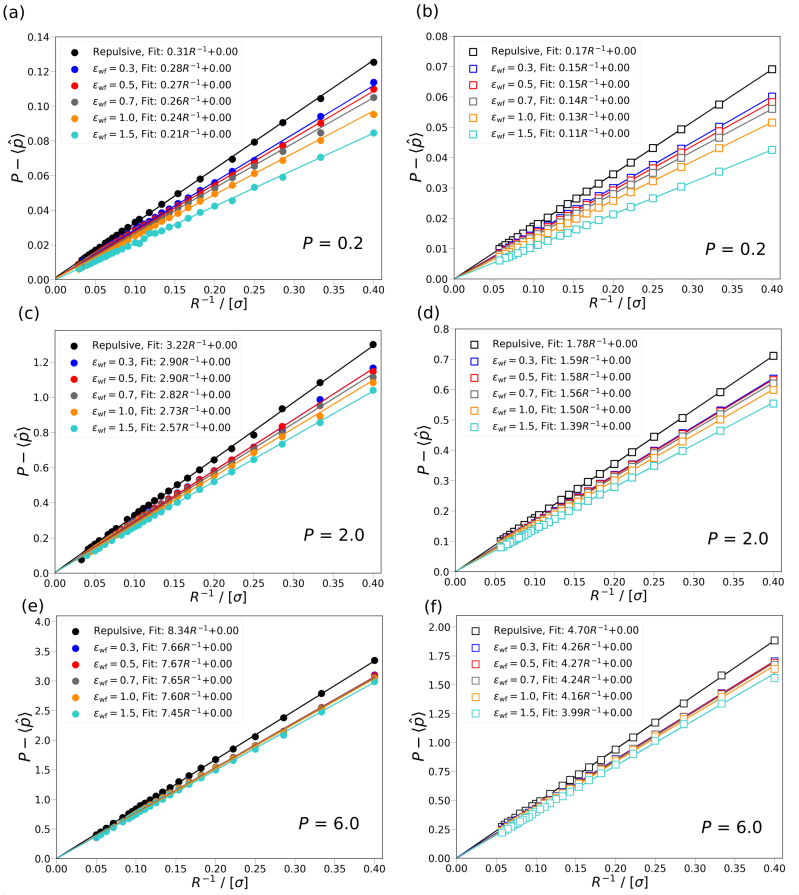

Figure 4. The difference between the differential, P, and the ensemble average of integral pressure, $\langle \hat{p} \rangle$, is shown as a function of the inverse radius R^{-1} of Box 2 at $P = 0.2$, 2.0, and 6.0 for cylindrical and slit pores with fluid-wall interactions. (**a**,**c**,**e**) The pressure difference is shown for cylindrical pores at differential pressure $P = 0.2$, 2.0, and 6.0, respectively. (**b**,**d**,**f**) The pressure difference is shown for slit pores at differential pressure $P = 0.2$, 2.0, and 6.0, respectively. The simulation results are shown with symbols, while the lines are fits to the data points. The equation used for the fitting is $AR^{-1} + B$, where A and B are constants. The colors denote the different level of attraction between the wall of Box 2 and the fluid, repulsive wall potential (black), $\epsilon_{wf} = 0.3$ (blue), 0.5 (red), 0.7 (gray), 1.0 (orange), and 1.5 (cyan). The results for the cylindrical pore are shown with closed circles and for the slit pores with open rectangles. The temperature of both boxes is set to $T = 2$. The average densities of Box 1 are $\rho \approx$ 0.10, 0.58, and 0.8 at $P = 0.2$, 2.0, and 6.0, respectively.

Based on the work of Galteland et al. [11], the slope of the fitted line can also be related to the effective surface tension between the fluid particles and the wall in Box 2, i.e., $P - \langle \hat{p} \rangle \sim \frac{\hat{\gamma}^{\mathrm{fr}}_{\mathrm{effective}}}{R}$. The linear relation between $P - \langle \hat{p} \rangle$ and R^{-1} shows that the effective surface tension does not depend on the curvature of the wall. In Figure 4, it can be observed that the effective surface tension decreases as the fluid-wall interactions become more attractive. In Figure 4a–f, it can be seen that the ratio of the effective surface tensions (slopes of the fitted lines) for the same ϵ_{wf} with the slit and cylindrical pore is nearly constant. For example, at $\epsilon_{\mathrm{wf}} = 0.5$ and $P = 2.0$, the ratio of the slope of the fitted lines for the slit and cylindrical pore is ~ 0.54, as shown in Figure 4c,d, and at $\epsilon_{\mathrm{wf}} = 0.3$ and $P = 0.2$, the ratio of the two slopes is also ~ 0.54, as shown in Figure 4a,b. The ratio of the effective surface tensions between the slit and cylindrical pores are in the range of ∼0.52–0.56 and considered constant since it is within the uncertainties of simulations. The constant ratio of effective surface tension between the slit and cylindrical pore also indicates the larger confinement effects in the cylindrical pore.

4.2. Ratio of Driving Forces

In Figure 5, the ratio of driving forces for mass transport, $\frac{\mathrm{d}\langle \hat{p} \rangle}{\mathrm{d}P}$, is shown as a function of the inverse radius of Box 2, R^{-1}, at three different pressures, $P = 0.2, 2.0, 6.0$, for both the slit and cylindrical pores. From Figure 5, it can be observed that $\frac{\mathrm{d}\langle \hat{p} \rangle}{\mathrm{d}P}$ is considerably smaller than 1 for small pore sizes. This means that a change in the differential pressure, P, of Box 1 results in a smaller change in the integral pressure, $\langle \hat{p} \rangle$, of Box 2. This difference underlines the effect of the confinement on the pressure of the fluid in nanopores and shows the difference in driving forces in the bulk and confined fluid. As R increases, $\frac{\mathrm{d}\langle \hat{p} \rangle}{\mathrm{d}P}$ approaches 1, i.e., the fluid in the pore behaves more like a bulk fluid. As can be seen in Figure 5, $\frac{\mathrm{d}\langle \hat{p} \rangle}{\mathrm{d}P}$ is larger for the slit pore than for the cylindrical pore at the same conditions. This means that in case of the slit pore a change in the differential pressure, P, results in a larger difference in the integral pressure, $\langle \hat{p} \rangle$, than for the cylindrical pore. The larger change in the integral pressure indicates that the confinement effects are weaker in the slit pore. In Figure 5a,b, it can be observed that by increasing the interaction strength between the wall of the pore and the fluid particles, the ratio of the driving forces decreases. At higher differential pressures the decrease in the ratio of driving forces due to the increasing fluid-wall interaction strength becomes less pronounced, as shown in Figure 5c–f. The smaller influence of the interaction strength, ϵ_{fw}, on the ratio of driving forces may be caused by the increasing contribution of the fluid-fluid interactions to the integral pressure due to the larger number of fluid particles in the pore at higher differential pressure. In Figure 5a–f, the ratio of driving force is shown for the slit and cylindrical pores at the same differential pressure. It can be seen that the ratio of the slopes of the fitted lines for the same value of ϵ_{wf} with the slit and cylindrical pore is constant within the uncertainties of the simulations. The ratio of the slopes is in the range of ∼0.52–0.58, which indicates that the confinement effects in the cylindrical pore are almost twice as strong as in the slit pore.

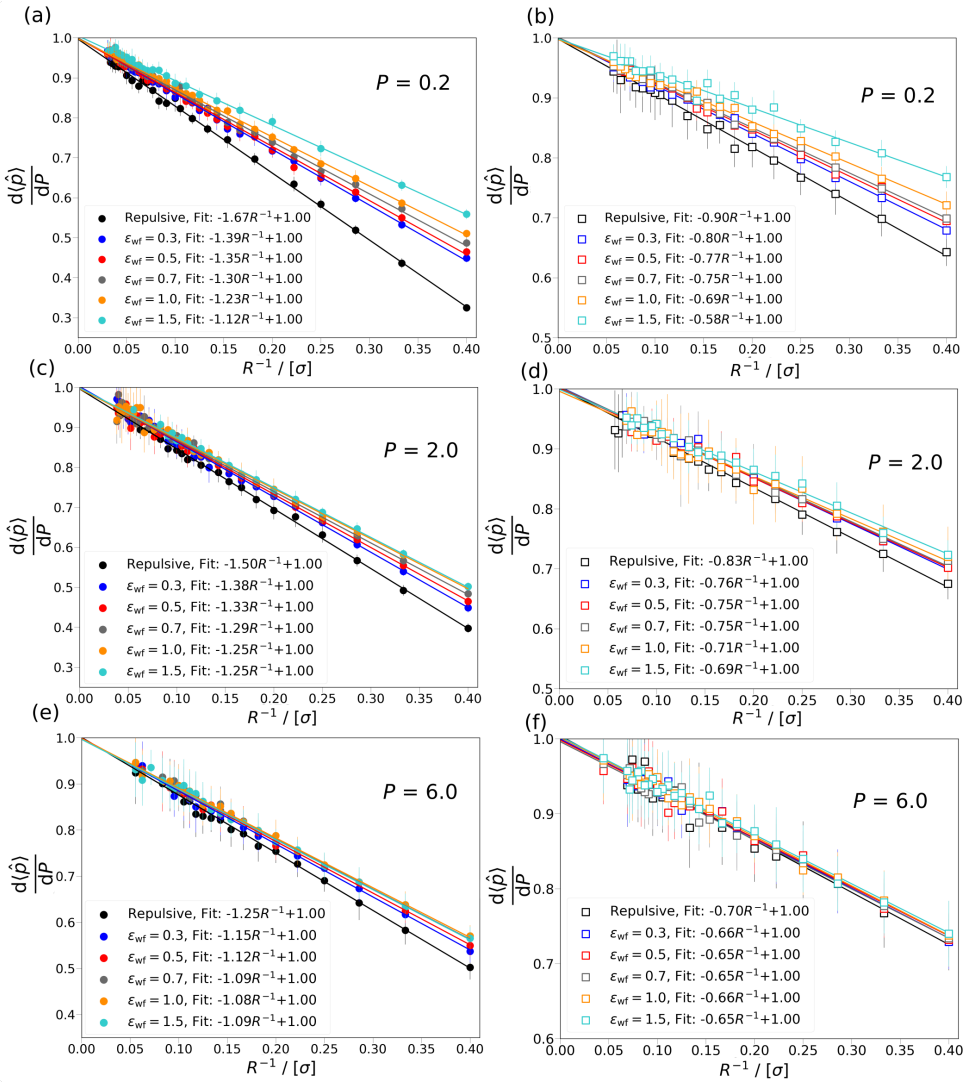

Figure 5. The ratio of driving forces, $\frac{\mathrm{d}\langle\hat{p}\rangle}{\mathrm{d}P}$, is shown as a function of the inverse radius, R^{-1}, of Box 2 at $P = 0.2, 2.0$, and 6.0 for the cylindrical and slit pore cases with repulsive and attractive wall potentials. (**a**,**c**,**e**) $\frac{\mathrm{d}\langle\hat{p}\rangle}{\mathrm{d}P}$ is shown for cylindrical pores at differential pressure $P = 0.2$, 2.0, and 6.0, respectively. (**b**,**d**,**f**) $\frac{\mathrm{d}\langle\hat{p}\rangle}{\mathrm{d}P}$ is shown for slit pores at differential pressures $P = 0.2$, 2.0, and 6.0, respectively. The simulation results are shown with symbols, while the lines are fits to the data points. The equation used for the fitting is $AR^{-1} + B$, where A and B are constants. The results for the cylindrical pore are shown with closed circles and for the slit pores with open rectangles. The colors denote the different wall potential used in Box 2, repulsive wall potential (black), $\epsilon_{\mathrm{wf}} = 0.3$ (blue), $\epsilon_{\mathrm{wf}} = 0.5$ (red), $\epsilon_{\mathrm{wf}} = 0.7$ (gray), $\epsilon_{\mathrm{wf}} = 1.0$ (orange), and $\epsilon_{\mathrm{wf}} = 1.5$ (cyan). The temperature of both boxes is set to $T = 2$. The average densities of Box 1 are $\rho \approx 0.10$, 0.58, and 0.8 at $P = 0.2$, 2.0, and 6.0, respectively.

5. Conclusions

In this study, the new approach reported by Galteland et al. [11] is used to investigate the effects of confinement on a fluid in a nanopore by performing MC simulations. The simulations are carried out in a variation of the Gibbs ensemble with two simulation boxes in chemical equilibrium. One of the simulation boxes represents the bulk fluid with differential pressure P, and the other a slit or cylindrical pore with repulsive or attractive wall interaction potential. In case of the attractive wall potentials, several scenarios are considered for the strength of the interaction between the wall and the fluid particles. The effect of confinement is investigated for three differential pressures, $P = 0.2, 2.0, 6.0$, corresponding to gas ($\rho \approx 0.1$) and liquid phases ($\rho = 0.58, 0.8$). It is concluded that the difference between the differential and integral pressure $P - \langle \hat{p} \rangle$, for all studied cases, approaches 0 when $R \to \infty$. It is shown that the increase in the interaction strength between the wall and the fluid particles has smaller effect on the difference in the pressures, $P - \langle \hat{p} \rangle$, as the differential pressure increases. Based on the work of Galteland et al. [11], the difference of the differential and integral pressure is related to the effective surface tension between the fluid particles and wall of the pore. It is shown that the effective surface tension does not depend on the curvature of the wall. It is found that by considering a bulk fluid in equilibrium with a cylindrical or slit nanopore, the ratio of driving forces for mass transport in the bulk phase is larger than in the nanopore ($\frac{\mathrm{d}\langle \hat{p} \rangle}{\mathrm{d}P} << 1$) for small pore sizes. As R increases, $\frac{\mathrm{d}\langle \hat{p} \rangle}{\mathrm{d}P}$ approaches 1, i.e., the fluid in the pore behaves more like a bulk fluid. This clearly shows that the approximation that $\hat{p} \approx P$ does not hold on the nanoscale.

Author Contributions: T.J.H.V. and M.E. wrote the software, M.E. and O.G. carried out the simulations. S.K., D.B., and O.G. contributed to the conceptual design and the development of the work. The project was supervised by O.A.M., S.K., D.B., and T.J.H.V. All authors contributed to the writing of the manuscript and the scientific discussions. All authors have read and agree to the published version of the manuscript.

Funding: This research was funded by the Center of Excellence funding scheme of the Research Council of Norway, project no 262644, PoreLab. This work was also sponsored by NWO Exacte Wetenschappen (Physical Sciences) for the use of supercomputer facilities, with financial support from the Nederlandse Organisatie voor Wetenschappelijk Onderzoek (Netherlands Organisation for Scientific Research, NWO).

Acknowledgments: T.J.H.V. acknowledges NWO-CW (Chemical Sciences) for a VICI grant.

Conflicts of Interest: The authors declare no conflict of interest.

References

1. Gubbins, K.E.; Long, Y.; Śliwinska Bartkowiak, M. Thermodynamics of confined nano-phases. *J. Chem. Thermodyn.* **2014**, *74*, 169–183. [CrossRef]
2. Furukawa, H.; Cordova, K.; O'Keeffe, M.; Yaghi, O. The chemistry and applications of metal-organic frameworks. *Science* **2013**, *341*. [CrossRef] [PubMed]
3. Gu, Z.Y.; Yang, C.X.; Chang, N.; Yan, X.P. Metal-organic frameworks for analytical chemistry: From sample collection to chromatographic separation. *Accounts Chem. Res.* **2012**, *45*, 734–745. [CrossRef]
4. Yilmaz, B.; Müller, U. Catalytic applications of zeolites in chemical industry. *Top. Catal.* **2009**, *52*, 888–895. [CrossRef]
5. Glaser, R.; Weitkamp, J. The application of zeolites in catalysis. *Springer Ser. Chem. Phys.* **2004**, *75*, 159–212.
6. Erdős, M.; de Lange, M.F.; Kapteijn, F.; Moultos, O.A.; Vlugt, T.J.H. In Silico Screening of Metal–Organic Frameworks for Adsorption-Driven Heat Pumps and Chillers. *ACS Appl. Mater. Interfaces* **2018**, *10*, 27074–27087. [CrossRef]
7. Irving, J.H.; Kirkwood, J.G. The Statistical Mechanical Theory of Transport Processes. IV. The Equations of Hydrodynamics. *J. Chem. Phys.* **1950**, *18*, 817–829. [CrossRef]
8. Férey, G.; Serre, C. Large breathing effects in three-dimensional porous hybrid matter: Facts, analyses, rules and consequences. *Chem. Soc. Rev.* **2009**, *38*, 1380–1399. [CrossRef]
9. Song, H.; Yu, M.; Zhu, W.; Wu, P.; Lou, Y.; Wang, Y.; Killough, J. Numerical investigation of gas flow rate in shale gas reservoirs with nanoporous media. *Int. J. Heat Mass Transf.* **2015**, *80*, 626–635. [CrossRef]

10. Huber, P. Soft matter in hard confinement: phase transition thermodynamics, structure, texture, diffusion and flow in nanoporous media. *J. Phys. Condens. Matter* **2015**, *27*, 103102. [CrossRef]
11. Galteland, O.; Bedeaux, D.; Hafskjold, B.; Kjelstrup, S. Pressures Inside a Nano-Porous Medium. The Case of a Single Phase Fluid. *Front. Phys.* **2019**, *7*, 60. [CrossRef]
12. Todd, B.D.; Evans, D.J.; Daivis, P.J. Pressure tensor for inhomogeneous fluids. *Phys. Rev. E* **1995**, *52*, 1627–1638. [CrossRef]
13. Ikeshoji, T.; Hafskjold, B.; Furuholt, H. Molecular-level Calculation Scheme for Pressure in Inhomogeneous Systems of Flat and Spherical Layers. *Mol. Simul.* **2003**, *29*, 101–109. [CrossRef]
14. Walton, J.; Tildesley, D.; Rowlinson, J.; Henderson, J. The pressure tensor at the planar surface of a liquid. *Mol. Phys.* **1983**, *48*, 1357–1368. [CrossRef]
15. Blokhuis, E.M.; Bedeaux, D. Pressure tensor of a spherical interface. *J. Chem. Phys.* **1992**, *97*, 3576–3586. [CrossRef]
16. Wang, G.M.; Sevick, E.M.; Mittag, E.; Searles, D.J.; Evans, D.J. Experimental Demonstration of Violations of the Second Law of Thermodynamics for Small Systems and Short Time Scales. *Phys. Rev. Lett.* **2002**, *89*, 050601. [CrossRef]
17. Nilson, R.H.; Griffiths, S.K. Influence of atomistic physics on electro-osmotic flow: An analysis based on density functional theory. *J. Chem. Phys.* **2006**, *125*, 164510. [CrossRef]
18. Lee, J.W.; Nilson, R.H.; Templeton, J.A.; Griffiths, S.K.; Kung, A.; Wong, B.M. Comparison of Molecular Dynamics with Classical Density Functional and Poisson–Boltzmann Theories of the Electric Double Layer in Nanochannels. *J. Chem. Theory Comput.* **2012**, *8*, 2012–2022. [CrossRef]
19. Gjennestad, M.A.; Øivind Wilhelmsen. Thermodynamic stability of droplets, bubbles and thick films in open and closed pores. *Fluid Phase Equilibria* **2020**, *505*, 112351. [CrossRef]
20. Hill, T.L. *Thermodynamics of Small Systems*, 1st ed.; NY:Dover: New York, NY, USA, 1964.
21. Panagiotopoulos, A.Z. Direct determination of phase coexistence properties of fluids by Monte Carlo simulation in a new ensemble. *Mol. Phys.* **1987**, *61*, 813–826. [CrossRef]
22. Bai, P.; Siepmann, J.I. Selective adsorption from dilute solutions: Gibbs ensemble Monte Carlo simulations. *Fluid Phase Equilibria* **2013**, *351*, 1–6. [CrossRef]
23. Frenkel, D.; Smit, B. *Understanding Molecular Simulation*, 2nd ed.; Academic Press: London, UK, 2001.
24. Shi, W.; Maginn, E.J. Continuous Fractional Component Monte Carlo : An Adaptive Biasing Method for Open System Atomistic Simulations. *J. Chem. Theory Comput.* **2007**, *3*, 1451–1463. [CrossRef] [PubMed]
25. Poursaeidesfahani, A.; Torres-Knoop, A.; Dubbeldam, D.; Vlugt, T.J.H. Direct Free Energy Calculation in the Continuous Fractional Component Gibbs Ensemble. *J. Chem. Theory Comput.* **2016**, *12*, 1481–1490. [CrossRef] [PubMed]
26. Bennett, C.H. Efficient estimation of free energy differences from Monte Carlo data. *J. Comput. Phys.* **1976**, *22*, 245–268. [CrossRef]
27. Stecki, J. Steele (10-4-3) Potential due to a Solid Wall. *Langmuir* **1997**, *13*, 597–598. [CrossRef]
28. Jiménez-Serratos, G.; Cárdenas, H.; Müller, E.A. Extension of the effective solid-fluid Steele potential for Mie force fields. *Mol. Phys.* **2019**, *117*, 3840–3851. [CrossRef]
29. Weeks, J.D.; Chandler, D.; Andersen, H.C. Role of Repulsive Forces in Determining the Equilibrium Structure of Simple Liquids. *J. Chem. Phys.* **1971**, *54*, 5237–5247. [CrossRef]
30. Allen, M.P.; Tildesley, D.J. *Computer Simulation of Liquids*, 2nd ed.; Oxford University Press: Oxford, UK, 2017.
31. Smit, B. Phase diagrams of Lennard–Jones fluids. *J. Chem. Phys.* **1992**, *96*, 8639–8640. [CrossRef]
32. Potoff, J.J.; Panagiotopoulos, A.Z. Critical point and phase behavior of the pure fluid and a Lennard–Jones mixture. *J. Chem. Phys.* **1998**, *109*, 10914–10920. [CrossRef]

Article V

Michael T. Rauter, **Olav Galteland**, Mate Erdős, Othonas A. Moultos, Thijs J. H. Vlugt, Sondre K. Schnell, Signe Kjelstrup.

Two-Phase Equilibrium Conditions in Nanopores

Nanomaterials, 10(4), 608. (2020)
DOI: 10.3390/nano10040608

Article V

Article V

nanomaterials

MDPI

Article

Two-Phase Equilibrium Conditions in Nanopores

Michael T. Rauter [1,*], Olav Galteland [1], Máté Erdős [2], Othonas A. Moultos [2], Thijs J. H. Vlugt [2], Sondre K. Schnell [3], Dick Bedeaux [1] and Signe Kjelstrup [1]

1 PoreLab, Department of Chemistry, Norwegian University of Science and Technology, NO-7491 Trondheim, Norway; olav.galteland@ntnu.no (O.G.); dick.bedeaux@ntnu.no (D.B.); signe.kjelstrup@ntnu.no (S.K.)

2 Engineering Thermodynamics, Process and Energy Department, Delft University of Technology, Leeghwaterstraat 39, 2628CB Delft, The Netherlands; m.erdos-2@tudelft.nl (M.E.); o.moultos@tudelft.nl (O.A.M.); T.J.H.Vlugt@tudelft.nl (T.J.H.V.)

3 Department of Materials Science and Engineering, Norwegian University of Science and Technology, NO-7491 Trondheim, Norway; sondre.k.schnell@ntnu.no

* Correspondence: michael.t.rauter@ntnu.no

Received: 25 February 2020; Accepted: 21 March 2020; Published: 26 March 2020

Abstract: It is known that thermodynamic properties of a system change upon confinement. To know how, is important for modelling of porous media. We propose to use Hill's systematic thermodynamic analysis of confined systems to describe two-phase equilibrium in a nanopore. The integral pressure, as defined by the compression energy of a small volume, is then central. We show that the integral pressure is constant along a slit pore with a liquid and vapor in equilibrium, when Young and Young–Laplace's laws apply. The integral pressure of a bulk fluid in a slit pore at mechanical equilibrium can be understood as the average tangential pressure inside the pore. The pressure at mechanical equilibrium, now named differential pressure, is the average of the trace of the mechanical pressure tensor divided by three as before. Using molecular dynamics simulations, we computed the integral and differential pressures, $\widehat{p}$ and p, respectively, analysing the data with a growing-core methodology. The value of the bulk pressure was confirmed by Gibbs ensemble Monte Carlo simulations. The pressure difference times the volume, V, is the subdivision potential of Hill, $(p - \widehat{p})V = \epsilon$. The combined simulation results confirm that the integral pressure is constant along the pore, and that ϵ/V scales with the inverse pore width. This scaling law will be useful for prediction of thermodynamic properties of confined systems in more complicated geometries.

Keywords: pressure; confinement; equilibrium; thermodynamic; small-system; hills-thermodynamics; pore; nanopore; interface

1. Introduction

It is well known that thermodynamic properties of fluids significantly change when the fluid phases become confined [1,2]. Given the importance of porous media for applications in for example fuel cells [3], batteries [4], and membranes for drinking water production [5–7], it is essential to understand how properties change upon confinement. In particular, one would like to be able to predict how thermodynamic properties of the system change with size. We have earlier documented how the thermodynamic factors and the pressures of some systems scale with a characteristic inverse system size (surface area over volume) [8–10]. The aim of the present work is to continue this line of work and present a geometric scaling law for the pressure of a nanopore. This work can, in a general context, be seen as an extension of Hill's thermodynamics of small systems [11]. The essential idea of Hill was to introduce a large ensemble of $\mathcal{N}$ small systems, enabling the use of standard thermodynamic tools for the ensemble. System properties were obtained by dividing the ensemble value by $\mathcal{N}$. In this way, he was able to deal with the impact of shape- and size-variation of the

small system, within the normal structure of thermodynamics. The dimensions of a nano-pore, which make molecular interactions at the pore surface important, can promote changes in phase transitions, surface adsorption, pore vapor pressure, and phase stability [2,12–14]. The literature offers, however, several definitions of the pressure inside a nano-porous material [15,16]. This situation calls for a robust definition of the representative elementary volume (REV) of the small system, to serve as a basis for a definition of pressure. Kjelstrup et al. [17] offered a definition of the REV-pressure based on the compression energy of the REV. Galteland et al. [18] showed, by evaluating this property for a single component in a nanoporous system, that the REV was not sufficiently described by the bulk fluid pressure. Also the integral pressure, $\widehat{p}$, as defined by Hill was required to describe the degree of confinement in the REV. In Hill's [11] terminology, one distinguishes between the integral pressure $\widehat{p}$, and the differential pressure, p. Erdos et al. [10] provided an expression for the ratio of the driving forces for adsorption into a pore, by means of the integral and differential pressures. They expressed the ratio by the cross-correlation of the volume and the integral pressure.

Hill defined the difference of the two pressures times the volume by the subdivision potential $\epsilon = (p - \widehat{p})V$ [11]. The integral pressure can differ significantly from the differential pressure in confined systems [10,18]. In the limit of a bulk fluid, they are the same, however. Galteland et al. studied pores between an fcc type-lattice of spheres [18], and found that the difference in the differential and integral pressure depended on the inverse radius of the spheres in the lattice. Here, we investigate a slit pore of nano-scale dimensions, with a constant pore slit-width ranging from 3 to 5 nm, and filled with a vapor and liquid phase of the same component. The purpose is to find thermodynamic and mechanical equilibrium conditions in terms of the pressures defined by Hill, and compare these to existing descriptions in terms of Young's and Young–Laplace's laws. The analysis leads to a new equilibrium condition, stated in terms of the integral pressure: This property is constant along the nano-sized pore. When this condition is combined with Youngs' equation for the contact angles, one recovers the Young–Laplace equation.

For the geometry studied here, it is possible to derive a scaling law for the integral pressure. The pore shape is kept constant in the derivations, as shape is a variable in small system thermodynamics [19]. The new scaling law relates properties of one system size to another size, with the same shape. This is helpful in a situation where measurements are lacking. Hill extended the thermodynamic variable set, including an ensemble of the small system, thereby providing a new basis for introduction and examination of size effects in thermodynamics. Hill's formulation of surface thermodynamics contain Gibbs' method [20].

Molecular dynamics and Monte Carlo simulations [10,21] are excellent tools for equilibrium studies of confined systems. Two fluid phases will be simulated in a slit pore of varying width. Focus is directed to the equilibrium conditions, when single phases are in contact with each other and the wall. The choice of the system was motivated by the simple geometry, which makes it possible to test particular scaling laws for slit pores and cylindrical pores.

The structure of the paper is as follows: We first present the equations of a REV leading to the relation between the differential pressure p and the integral pressure $\widehat{p}$. We next test the derived equations for slit pores of different sizes and different interactions between pore wall and fluid. The new growing-core methodology, brings out the difference between the differential and the integral pressure. Finally, results are discussed and put in perspective.

2. Theory

2.1. Thermodynamic Relations for Small Systems

Hill used the name "small system" for systems with properties that are not extensive in the system volume [11]. Such systems are frequently confined, i.e., bounded by the surroundings. To obtain a generalized thermodynamic description of small systems, and to deal with size and shape-dependencies, Hill [11] introduced an ensemble of $\mathcal{N}$ identical and independent replicas of the

small system. Keeping the total entropy S_t, and particle number, N_t, constant, while increasing the number of small systems $\mathcal{N}$ (each with constant volume V) in the ensemble, an extended version of the Gibbs equation was obtained:

$$\mathrm{d}U_t = T\mathrm{d}S_t - p\mathcal{N}\mathrm{d}V + \sum_j \mu_j \mathrm{d}N_{j,t} - \widehat{p}V\mathrm{d}\,\mathcal{N} \tag{1}$$

which we call the Hill-Gibbs equation. Here, U_t is the total internal energy of the ensemble, T is the temperature, p is the pressure, and μ_j is the chemical potential of component j. The new term, $-\widehat{p}V\mathrm{d}\,\mathcal{N}$, is the reversible work needed to change the total volume, by changing the number of small systems, keeping S_t, V, and $N_{t,j}$ constant.

Hill [11] distinguished between p and $\widehat{p}$ by calling the properties the differential and integral pressure, respectively. This work aims to elucidate the difference of these variables for a small system which is confined to a pore, in the grand-canonical ensemble.

The average values in the grand-canonical ensemble for a single small system are

$$U = \frac{U_t}{\mathcal{N}}, \quad N_j = \frac{N_{j,t}}{\mathcal{N}}, \quad S = \frac{S_t}{\mathcal{N}}. \tag{2}$$

By introducing these equations into Equation (1), we obtain the usual Gibbs equation for dU, and what we call the Hill-Gibbs-Duhem's equation.

$$\mathrm{d}(\widehat{p}V) = S\mathrm{d}T + \sum_j N_j \mathrm{d}\mu_j + p\mathrm{d}V \tag{3}$$

The equation reduces to the usual Gibbs-Duhem equation when $\widehat{p} = p$. When T and μ_j are constant in Equation (3), we obtain a relation between the integral and differential pressure when the shape of the system is controlled [11]:

$$p = \left(\frac{\partial \widehat{p}V}{\partial V}\right)_{T,\mu} = \widehat{p} + V\left(\frac{\partial \widehat{p}}{\partial V}\right)_{T,\mu}. \tag{4}$$

The expression shows that p and $\widehat{p}$ differ for small systems, for which $\widehat{p}$ depends on the volume. In a macroscopic system, with $V \to \infty$, p and $\widehat{p}$ are the same. The relation clarifies the chosen names; p is obtained by differentiation.

The above equations will be applied to a two-phase system in a slit pore and a cylindrical pore. Inside the pore, the differential pressure of the liquid differ from that of the vapor phase. For the time being, we introduce the notation p_d^v and p_d^l for the differential pressure of the vapor and liquid, respectively, and p_d^f to indicate either of the two. The difference of the differential and the integral pressure times the volume is equal to the subdivision potential [11], ϵ. By rearranging Equation (4), using $p_d^f = p$, we obtain:

$$p - \widehat{p} = \frac{\epsilon(T, V, \mu_j)}{V} = V\left(\frac{\partial \widehat{p}}{\partial V}\right)_{T,\mu_j}. \tag{5}$$

The subdivision potential is an additive thermodynamic property [11]. When such a property is divided by the small system volume, a scaling law can be found; of a similar type as we have found earlier [8,9]. The ratio ϵ/V is proportional to the the inverse characteristic size Ω/V of the system, where Ω is the surface area between the fluid and the solid [18]. In general terms,

$$p - \widehat{p} = \frac{\epsilon}{V} = \zeta^{\infty} + \zeta^{s}\left(\frac{\Omega}{V}\right) + \zeta^{se}\left(\frac{\Omega}{V}\right)^2 + \ldots \tag{6}$$

The coefficients ζ^{∞}, ζ^{s} and ζ^{se} do not depend on Ω/V, but are functions of T and μ_j. As p and $\widehat{p}$ are equal in the thermodynamic limit, it follows that the coefficient $\zeta^{\infty} = 0$.

2.2. The Integral Pressure of a Representative Volume Element

To define the differential and integral pressures, and the conditions for thermodynamic and mechanical equilibrium between two phases within a pore, we need suitable REVs. In a porous medium with two fluid phases, we need more than one type of REV, one for each phase. A REV needs, as the name says, to be representative for all molecular interactions in the system [17]. It should be large enough to contain a statistically representative amount of the fluids and solids. The purpose of the REV is to define a volume element, to be used to define equilibrium, but also to define local equilibrium in a large system where fluid transports take place [17].

A liquid droplet in equilibrium with its vapor inside a slit pore is an example of a two-phase confined fluid. The droplet system is illustrated in Figure 1. Various REVs are possible. Each REV need to cover the whole cross section of the pore. In the following we are concerned with two REVs, one in the vapor- and one in the liquid phase. None of them includes the surface between liquid and vapor. Two examples of REVs (REV_1 and REV_2) are illustrated in Figure 1. The x-axis is located at the center of the pore.

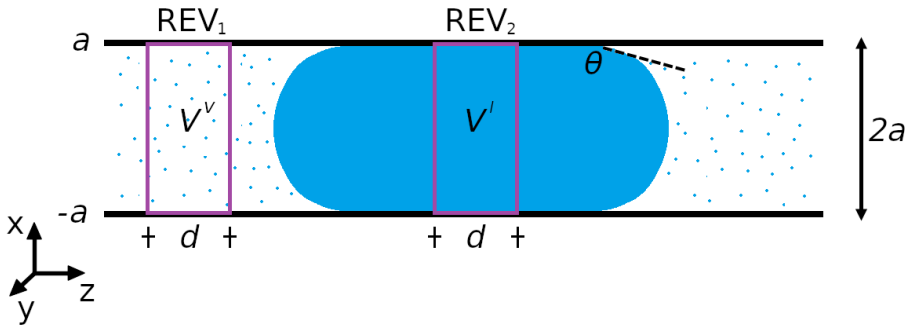

Figure 1. Slit pore of width $2a$ with a liquid droplet in the middle, which is in equilibrium with a vapor phase on both sides. The representative volume elements are REV_1 (vapor of volume V^v) and REV_2 (liquid of volume V^l), both with length d. The x-axis is located at the center of the pore.

The integral pressure of an isothermal REV with constant chemical potentials is expressed in terms of the compression energy, $\widehat{p}V$, which is defined by the grand potential, Y [11].

$$\widehat{p}V = -\mathrm{Y} \equiv k_\mathrm{B} T \ln \Xi \tag{7}$$

Here k_B is the Boltzmann constant and Ξ the grand-canonical partition function. Similar to ϵ, also the compression energy is additive. It is the sum of contributions from all phases and interfaces present within the REV. The grand potential provides then the statistical mechanical link to particle behaviour, and is a tool for pressure computations (see below). The system is small in the sense of Hill, when the integral pressure deviate from the (bulk) fluid pressure.

The general expression for the compression energy for a REV_n, with $n = 1, 2$ is then

$$\widehat{p}_{\mathrm{REV}_n} V = \widehat{p}^f V^f - \widehat{\gamma}^{fs} \Omega^{fs} \tag{8}$$

where V is the volume of the REV, V^f is the volume of the fluid, Ω^{fs} is the surface area between the fluid and the wall, and $\widehat{\gamma}^{fs}$ is the integral surface tension at the wall, or the surface tension of the small system. In the present case, the two REVs are completely filled with a fluid; a vapor (REV_1) or a liquid (REV_2). The REV volume in both cases obeys $V = V^f = V^v = V^l = 2adw$, where a is the slit pore half width, d the REV length and w the width of the REV. Superscripts v and l refer again to the vapor and the liquid. The surface area between fluid and solid is $\Omega^{fs} = 2dw$. The surface tension between fluid

and pore surface are $\widehat{\gamma}^{ls}$ and $\widehat{\gamma}^{vs}$, respectively, where the hat indicate that the system may be small. In that case, the surface tension is a function of the contact area/system geometry.

For sufficiently large values of a, the fluid in the center of the pore has macroscopic bulk properties. In that case; the integral pressure in the vapor $\widehat{p}^{v}$ and the liquid $\widehat{p}^{l}$ are independent of V^{v} or V^{l}, respectively, and

$$\widehat{p}^{v} = p^{v}, \qquad \widehat{p}^{l} = p^{l}. \tag{9}$$

Here, p^{l} and p^{v} are bulk pressures of the liquid and vapor, respectively.

In a slit pore, the wall surface is not curved. When the distance between the walls ($2a$) is sufficiently large, the fluid–solid surface tension show macroscopic behaviour, and:

$$\widehat{\gamma}^{vs} = \gamma^{vs}, \qquad \widehat{\gamma}^{ls} = \gamma^{ls}. \tag{10}$$

By introducing the expressions, Equations (9) and (10), the volume and the fluid–solid surface area into Equation (8), we obtain expressions for the integral pressure of the liquid and vapor REVs:

$$\widehat{p}_{\mathrm{REV}_2} = p^{l} - \frac{\gamma^{ls}}{a}, \qquad \widehat{p}_{\mathrm{REV}_1} = p^{v} - \frac{\gamma^{vs}}{a}. \tag{11}$$

Suppose now that integral pressure is constant everywhere at equilibrium, or that:

$$\widehat{p}_{\mathrm{REV}_2} = \widehat{p}_{\mathrm{REV}_1}. \tag{12}$$

This means we can write:

$$p^{l} = p^{v} + \frac{\gamma^{ls} - \gamma^{vs}}{a} \tag{13}$$

Young's law derives from a force balance at phase equilibrium:

$$\gamma^{ls} = \gamma^{vs} + \gamma^{lv}\cos\theta, \tag{14}$$

Here γ^{lv} is the liquid-vapor surface tension. We introduce this law in the equation above and obtain:

$$p^{l} = p^{v} + \frac{\gamma^{lv}}{a}\cos\theta = p^{v} + \frac{\gamma^{lv}}{R}. \tag{15}$$

This is Young–Laplace's equation for a slit pore. Young–Laplace's equation has been verified in the experimental literature numerous times [22,23]. The radius of curvature of the liquid-vapor surface, $R = a/\cos\theta$, was used, where θ is the contact angle at the pore wall, see Figure 1. We have found this equation without examining the liquid-vapor interface per se.

Equation (12) is thus equivalent to validity of the laws of Young and Young–Laplace. These familiar laws apply to thermodynamic and mechanical equilibrium, so we expect the equality to do the same. In this sense we have derived a new way to express phase equilibrium in nanopores.

Consider again a state of equilibrium where the integral pressure is constant. The integral pressures of the fluids are shown by Equation (11). For each fluid, the difference of the differential and integral pressure for the slit pore follows from Equation (4):

$$p - \widehat{p} = a^{3}\left(\frac{\partial \widehat{p}}{\partial a^{3}}\right)_{T,\mu} = \frac{\gamma^{fs}(\alpha)}{3a}. \tag{16}$$

where we have indicated that the surface tension depends on a parameter α which characterizes the molecular interactions of the fluid and the wall. The shape is a variable in small system thermodynamics, and remains constant when we determine the derivative. To keep the shape constant, means to take the isomorphic derivative of the integral pressure in Equation (16).

A change from the slit pore to a cylindrical pore, will change the proportionality factor in a concrete way. The ratio of the area over the volume in the REV of a cylindrical pore is double the value in a slit pore. The ratio of the slope in a cylindrical pore over that from a slit pore is therefore equal to 2. The corresponding scaling law for a cylindrical pore becomes:

$$p - \widehat{p} = a^3 \left(\frac{\partial \widehat{p}}{\partial a^3} \right)_{T,\mu} = \frac{2\gamma^{fs}(\alpha)}{3a}. \tag{17}$$

By changing the geometry of the pore only, keeping the fluid wall interactions constant, we predict that the slope of pressure difference vs the surface tension will change by a factor 2.

For large systems (when $a \to \infty$), the difference between p and $\widehat{p}$ disappears, leading to $p = \widehat{p} = p^f$ in the REV. For small systems, however, the difference between p and $\widehat{p}$ is described by the ratio between fluid–solid surface tension and the half channel width (γ^{fs}/a) divided by 3. We have thus found that the pressure difference follows a scaling law, similar to the one proposed by the Small System Method [8,9], and given in Equation (6).

Equation (16) can be tested by molecular dynamics simulations. In such a test, one can identify independently all terms in the equation, and confirm that the condition $\widehat{p}_{REV_1} = \widehat{p}_{REV_2}$ holds. Essential in the calculation is that p and $\widehat{p}$ refer to the same volume.

These theoretical results demonstrate why it may pay to take the effort to invoke the perhaps more complicated thermodynamic scheme of Hill. Young and Young–Laplaces' laws describe the same physical phenomenon as Equations (16) and (17). Hill's theory shows how the two Equations (16) and (17) are linked to each other and to new variables (e.g., ϵ), in manners which can be tested.

2.3. A Mechanical Interpretation of the Pressures

The above derivation showed that the condition of constant integral pressure at equilibrium is required by Young's and Young–Laplace's laws. The integral and differential pressures are therefore also related to the mechanical pressure tensor. The mechanical pressure tensor will from now be denoted with upper case P, while the thermodynamic pressures are denoted as before, with lower case p. A complete set of relations between P and p is provided in the Appendix A. Here, we present the main relations.

Consider again the liquid droplet in a slit pore, as shown in Figure 1. The slit pore wall is parallel to the yz-plane. The pressure tensor component acting normal to the wall is the xx-component, $P_N = P_{xx}$ (cf. the Appendix A). There are two tangential components of the pressure tensor, the yy-component and the zz-component, which are equal in equilibrium. The tangential pressure tensor component is the average of the two, $P_T = \frac{1}{2}(P_{yy} + P_{zz})$. The surface tension is minus the excess of the tangential pressure tensor [24],

$$\gamma^{fs} = \frac{1}{2} \int_{-a}^{a} (P_N(x) - P_T(x)) \mathrm{d}x. \tag{18}$$

The factor of one half accounts for the fact that the integral is for two fluid–solid surfaces. By introducing the fluid–solid surface tension into the equation for the integral pressure of a single fluid phase, cf. Equation (11), we obtain

$$\widehat{p} = p^f - \frac{1}{2a} \int_{-a}^{a} (P_N(x) - P_T(x)) \mathrm{d}x, \tag{19}$$

where superscript f again refers to either the liquid or vapor. The normal component of the mechanical pressure tensor is constant through flat surfaces at mechanical equilibrium. The integral of the normal component divided by $2a$ is therefore equal to P_N. We assume that the normal component is equal to the differential pressure of the bulk fluid, $p^f = P_N$. Below, the assumption is shown to hold.

The differential pressure of the bulk fluid and the integral over the normal component of the pressure cancel each other, and the integral pressure is equal to the average tangential component,

$$\widehat{p} = \frac{1}{2a}\int_{-a}^{a} P_T(x)\mathrm{d}x = \langle P_T \rangle. \tag{20}$$

This equation shows that the integral pressure of a bulk fluid in a slit pore at mechanical equilibrium can be understood as the average tangential pressure.

The differential pressure can also be related to the mechanical pressure tensor. The difference between the differential and integral pressures is equal to the fluid–solid surface tension divided by $3a$. By introducing Equation (18) for the fluid–solid surface tension, we obtain

$$p - \widehat{p} = \frac{1}{6a}\int_{-a}^{a} (P_N(x) - P_T(x))\mathrm{d}x \tag{21}$$

By reorganizing and inserting the average of the tangential pressure for the integral pressure,

$$p = \frac{1}{3}\left(\langle P_N \rangle + 2\langle P_T \rangle\right) = \frac{1}{3}\mathrm{Tr}\langle P \rangle \tag{22}$$

The differential pressure is equal to the average of the trace of the mechanical pressure tensor divided by 3.

3. Simulations

3.1. Molecular Dynamic Simulations

3.1.1. System

Simulations were carried out for a droplet in a slit pore. The droplet in the middle of the pore was surrounded by its vapor phase on both sides (see Figure 2). The simulation box, with the side lengths $L_x = L_y \neq L_z$ had periodic boundary conditions in all directions.

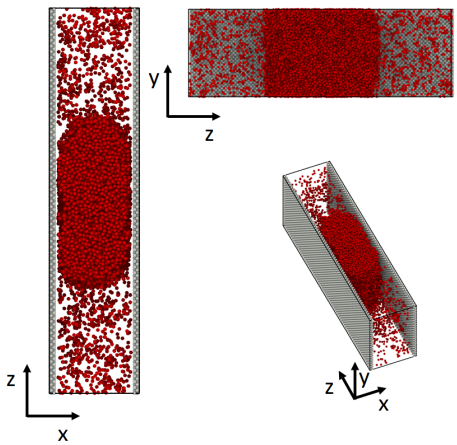

Figure 2. System used in the simulation. The droplet in the middle of the slit pore is surrounded by a vapor phase on both sides.

The simulation box was divided into n rectangular layers along the z-axis with a layer thickness of $\Delta z = L_z/n$. Both the pore-wall (grey) and the fluid (red) consisted of Lennard-Jones/spline particles [25]. The particles of the wall were immobilized, such that the particles were able to interact with the fluid particles, but not move. Due to periodic boundary conditions, the wall thickness was

$t = 3.5\sigma_0$ and had a density of $\rho_{wall} = 1.05$. The fluid inside the pore was initialized in a way that the overall density inside the pore was $\rho_{fluid} = 0.27$, thus in the two phase regime [25]. The averaged density of the bulk liquid was $\rho_{liquid} = 0.75 \pm 0.0015$ and the one of the vapor $\rho_{vapor} = 0.03 \pm 0.0025$.

The simulations were carried out using LAMMPS [26] in the canonical (NVT) ensemble at a temperature of $T^* = 0.70$. The Nosé-Hoover thermostat [27] was used to keep the temperature constant. We used Lennard-Jones reduced units, which are indicated by superscript * [28]. The system was simulated for four slit widths, $a = 8.7\sigma_0$, $10.45\sigma_0$, $12.2\sigma_0$ and $13.7\sigma_0$. The half channel widths were chosen so that both, the pressure of the fluid in the center, p^f, as well as the fluid–solid surface tension, γ^{fs}, are independent of the distance a, i.e., they show macroscopic bulk properties. Furthermore, the slit widths are large enough to avoid the effect of the disjoining pressure, as discussed in [13].

3.1.2. Particle Interaction Potential

The interaction between particles of type i and j was defined by the Lennard-Jones/spline potential [25,28],

$$u_{ij}(r) = \begin{cases} 4\varepsilon_{ij}\left[\left(\frac{\sigma_{ij}}{r}\right)^{12} - \alpha_{ij}\left(\frac{\sigma_{ij}}{r}\right)^{6}\right] & \text{if } r < r_{s,ij} \\ a_{ij}(r - r_{c,ij})^2 + b_{ij}(r - r_{c,ij})^3 & \text{if } r_{s,ij} < r < r_{c,ij} \\ 0 & \text{if } r > r_{c,ij} \end{cases} \tag{23}$$

where r is the distance between the particles. The interaction parameters, ε_{ij} and σ_{ij}, were set to 1 for all particle pairs (Lennard-Jones units). The interaction parameter α_{ij} is used to control the attractive interaction between the wall and the fluid, where we used $\alpha_{sf} = 0.05$, 0.15 and 0.25. For wall-wall and fluid-fluid interactions the interaction parameter was set to $\alpha_{ss} = \alpha_{ff} = 1$. All α_{sf} values represent a strong, repulsive interaction between wall and fluid, thus a non-wetting behaviour. The parameters a_{ij}, b_{ij}, $r_{c,ij}$ and $r_{s,ij}$ were determined such that the potential and its derivative are continuous functions at $r_{s,ij} = 1.24\sigma$ and $r_{c,ij} = 1.74\sigma$ [25].

3.1.3. Computation of REV Pressures and Wall-Fluid Surface Tension

The mechanical pressures in any layer l or combination of layers, or in a REV (core plus all layers included), were computed following Kirkwood [24]:

$$P_{\beta\kappa} = \frac{1}{3V}\sum_{i\in l} m_i(v_{i,\beta} - v_{m,\beta})(v_{i,\kappa} - v_{m,\kappa}) - \frac{1}{6V}\sum_{i\in l}\sum_{j=1}^{N}(r_{ij,\beta}f_{ij,\kappa}). \tag{24}$$

The subscripts β and κ denote the Cartesian coordinates, x, y and z, while V is the volume of the layer, m_i is the mass of particle i, $v_{i,\beta}$ is the velocity of fluid particle i in the β-direction, and $v_{m,\beta}$ is the average velocity in the β-direction. This velocity is zero in our equilibrium simulations. The properties $r_{ij,\beta}$ and $f_{ij,\beta}$ are, respectively, the distance and the force between particle i and j in the β-direction. The first term is the kinetic energy contribution from the particles, and the second term arise from pairwise interactions. Because of isotropy, the tensor is diagonal (see Appendix A).

Half the value of the pairwise energy contribution is assigned to the layer that contains particle i, while the other half is assigned to the layer that contains particle j. A more precise distribution of the contributions is available [29–32], but the present method has sufficiently small errors for the volumes used.

The pressure of a fluid volume element was calculated, starting with the core of the pore (lightest color in Figure 3), which has volume V_1. Volume was gradually added to the core, including in the end also the wall (black color in Figure 3). In this manner, the volume of the core was growing, layer by layer, until in the end $s - 1$ layers were added to the central core. The pressure was computed for the core (V_1), for the core plus one subsequent layer (V_2), and for the total volume (V_{tot}). The total volume, V_{tot}, is equal to the volume V of the REV (see Figure 1). Thus, the pressure was computed

in growing pore core -volumes until the volume was large enough to cover the whole width ($2a$) of the pore. This new growing-core methodology enabled an calculation of the pressure in the center of the pore (the core) and the averaged pressure of the whole cross section of the pore, including all interactions with the pore wall. When all layers plus the wall inside the pore were included (V_{tot}), we obtained $\widehat{p}$ of the REV. As long as there is no impact of the wall, (the core plus layers is sufficiently far away from the wall) we observed the bulk fluid pressure, p^f. This procedure was applied to two REVs, one in the liquid and one in the vapor phase.

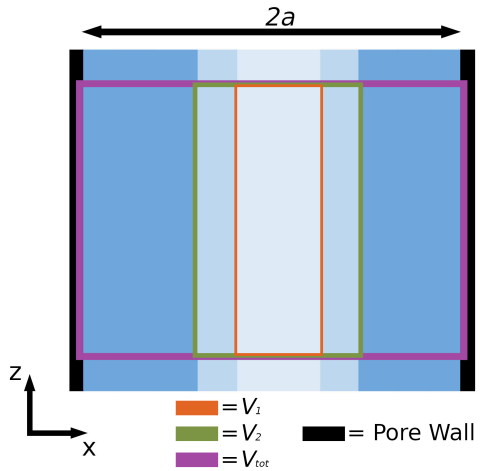

Figure 3. The core layer of the slit pore (lightest color) and subsequent layers (progressively darker color) used in the calculation of the pressure tensor of the fluid. V_1 and V_2 are the volumes of the core and the core plus one layer, respectively. V_{tot} is the total volume, covering all interactions with the pore wall.

The fluid–solid surface tension was computed as the excess of the tangential pressure tensor component [24] from Equation (18).

The extrapolated normal component P_N was taken to be equal to the pressure in core, where the fluid–solid surface has no effect on the pressure. The tangential component of the pressure was calculated using $P_T = \frac{1}{2}(P_{yy} + P_{zz})$. The value was obtained using a low resolution in x-direction and by averaging over multiple chunks of the liquid phase, along the pore in the z-direction.

3.2. Gibbs Ensemble Monte Carlo

In the derivation of Equation (20), the pressure tensor normal to the slit pore wall, P_N, is assumed to be equal to the bulk pressure p^f. This assumption was tested using Gibbs ensemble Monte Carlo simulations for two values of p^f (0.2 and 6.0 reduced units). The method is the same as reported recently by Erdős et al. [10]. In the simulations, two simulation boxes were defined. Simulation box 1 represents a reservoir of a bulk fluid with periodic boundary conditions applied in all directions. The fluid particles interact with the shifted and truncated Lennard-Jones potential with $\sigma = 1$, $\epsilon = 1$ and cut-off $r_c = 2.5$. The pressure, p^f, and temperature, T, of the fluid in simulation box 1 are imposed, while the number of particles, N_1, and the volume of the box can fluctuate. Simulation box 2 was a slit pore with fixed volume and temperature. The size of the slit pore was defined by the distance between the two parallel planes, $2a$. In simulation box 2, periodic boundary conditions were applied in the directions parallel to the planes. The total number of particles, $N_1 + N_2$, was fixed in the simulations. Simulation box 1 and 2 can exchange particles, which ensured that the two boxes were in chemical equilibrium. The pressure of the fluid in simulation box 2 was equal to the differential pressure in

equilibrium with the pressure imposed in the reservoir (box 1), p^f. A more detailed description of the simulation setup is given by Erdős et al. [10]. The high and low pressures were computed for varying pore sizes a.

4. Results and Discussion

The results for the independent computations of the pressure of a bulk fluid and corresponding pressure in the pore, using Gibbs ensemble Monte Carlo simulations, are shown in Table 1 in Section 4.1. The results of the molecular dynamics simulations are shown in Figures 4–7 in Sections 4.2–4.5. The figures show the pressure variation from the center of the slit to the wall, in the direction perpendicular to the wall (Figure 4) and parallel to the wall (Figure 5). The next figures confirm, as we shall see, that we can use a constant $\widehat{p}$ to define equilibrium, and that a small system scaling law applies.

4.1. Pressure Component Normal to the Pore Wall

The normal component of the pressure tensor in simulation box 2 and bulk pressure in simulation box 1 are shown in Table 1.

Table 1. The pressure tensor normal to the slit pore wall, P_N, and the bulk pressure p^f with varying pore sizes a. Two total pressures are studied for various pore sizes.

Pore Size a/σ_0	Normal Pressure, $P_N\sigma_0^3/\varepsilon_0$	Bulk Fluid Pressure, $p^f\sigma_0^3/\varepsilon_0$
5	6.178 ± 0.005	6.023 ± 0.005
6	6.017 ± 0.005	6.011 ± 0.005
9	6.014 ± 0.005	5.995 ± 0.006
12	6.011 ± 0.005	5.995 ± 0.003
15	6.029 ± 0.004	5.995 ± 0.004
21	6.011 ± 0.004	6.000 ± 0.003
27	5.997 ± 0.004	6.002 ± 0.003
35	5.998 ± 0.004	5.997 ± 0.003
5	0.2011 ± 0.0009	0.2002 ± 0.0002
6	0.1988 ± 0.0009	0.2005 ± 0.0002
9	0.2007 ± 0.0008	0.2000 ± 0.0002
12	0.2020 ± 0.0007	0.2002 ± 0.0002
15	0.1980 ± 0.0007	0.1997 ± 0.0002
21	0.1993 ± 0.0006	0.1997 ± 0.0001
27	0.2005 ± 0.0006	0.2000 ± 0.0001
35	0.2000 ± 0.0005	0.2001 ± 0.0001

The pressure tensor normal to the pore wall in simulation box 2 is according to Table 1 equal to the bulk pressure in simulation box 1 within the accuracy of the simulation. The results show that this assumption is correct. Therefore, the integral pressure can be understood as the average value of the pressure tensor components tangential to the pore wall, $\widehat{p} = \langle P_T \rangle$.

4.2. Pressure Variation in the Direction Normal to the Pore Wall

The variation in the pressure component normal to the surface walls is shown for the liquid (top) and the vapor phases (bottom) in Figure 4, for pore widths, $2a = 17.4\sigma_0$ (left) and $2a = 27.4\sigma_0$ (right), using $\alpha_{sf} = 0.15$ (repelling interactions). The horizontal straight line in all sub-figures is the xx-component extrapolated to the walls. We know there is bulk fluid in the core, as the pressures in V_1 and V_2 are the same, so this component is equal to the bulk pressure. For the other curves in the figure, the tangential components of the pressures (the yy- and zz-components) fall on top of each other. The distances $2a$, b and c between the 4 dashed lines and the pore wall (grey) in the figure represent three fluid volumes, of increasing size (V_1, V_2 and V_{tot}). These are the core volume (width c,

volume V_1), the core plus layer 1 (width b, volume V_2) and the whole volume (width $2a$, volume V_{tot}). The distance $2a$ is the width of the channel.

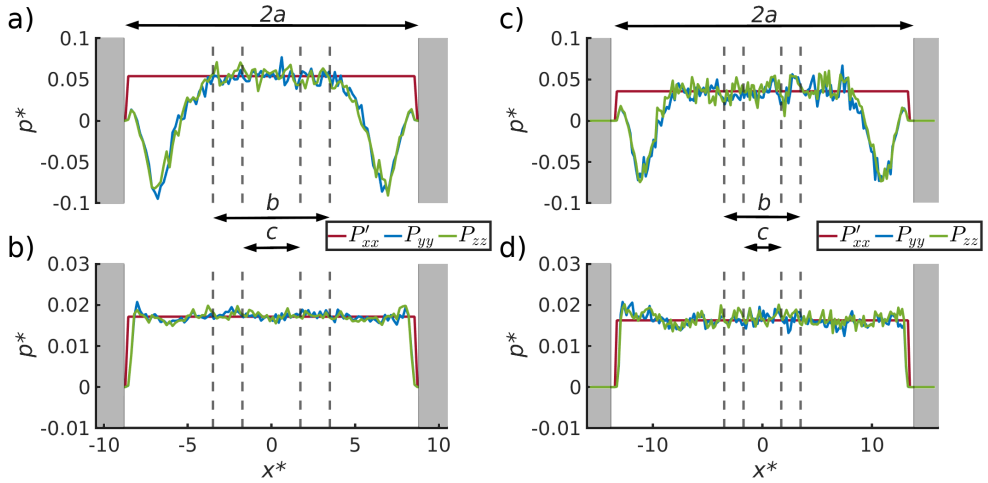

Figure 4. Pressure variation of the three pressure components normal to the surface shown for (**a**) the liquid phase with pore width $17.4\sigma_0$, (**b**) the vapor phase with pore width $17.4\sigma_0$, (**c**) the liquid phase with pore width $27.4\sigma_0$ and (**d**) the vapor phase with pore width $27.4\sigma_0$, for $\alpha_{sf} = 0.15$. The normal component of the pressure, P'_{xx}, is extrapolated from the center of the slit pore.

In the liquid phase (top), the tangential pressure component becomes negative close to the surface. This variation was used to compute the surface tension between solid and liquid from Equation (18). The value was found, within the accuracy of the calculation, to be independent of the distance between the two surface walls, see Table 2.

For the vapor phase, there is no dip in the pressure tensor into the negative regime. In the vapor, not only the extrapolated normal pressure component, P'_{xx}, but also the two tangential components, P_{yy} and P_{zz}, are constant and independent of the distance between the two surfaces. Therefore, the surface tension between the vapor and the wall is negligible.

The pressure in the pore core depends on the distance between the surface walls, i.e., it is larger in the pore with a smaller distance (left) than in the one with a larger distance (right). The bulk fluid pressures are related to the curvature of the liquid-vapor meniscus by Young–Laplace's law, which depends on the slit pore width $2a$.

4.3. Pressure Variation along the Pore

The pressure tensor components were computed for three volumes of increasing size (V_1, V_2 and V_{tot}) using the growing-core methodology. V_1 and V_2 are subvolumes in the center of the REVs and V_{tot} is the volume covering the whole REV, i.e., $V_{\text{tot}} = V^l = V^v$ (see Figures 1 and 3). In Figure 5, the pressure components are plotted as a function of the z-direction. The z-direction is parallel to the pore wall and passes through the vapor and the liquid droplet.

The volumes V_1 and V_2 contain bulk fluid, and are not influenced by the pore wall. The pressure components of the two volumes in the center of the box are equal. It was shown (Table 1) that the pressure was that of a bulk fluid in equilibrium with the pore. Therefore, the liquid bulk pressure is p^l. The pressures are equal to the vapor bulk pressure, p^v, on both sides of the liquid droplet.

The volume V_{tot} includes the fluid and its interface with the pore wall. The pressure component normal to the fluid wall is still equal to the fluid pressure, $P_{xx} = p^f$. The pressure components tangential to the fluid wall in the bulk liquid and bulk vapor, are equal to the integral pressure,

$\widehat{p} = \langle P_T \rangle$. The integral pressure is the same in the liquid and vapor phases, in agreement with Equation (20).

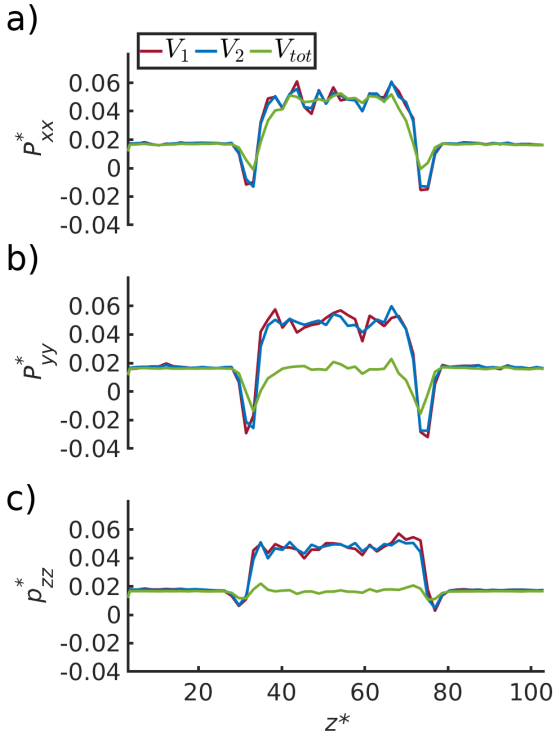

Figure 5. Pressure components (**a**) P_{xx}, (**b**) P_{yy} and (**c**) P_{zz}, as a function of the z- direction for three regions defined using the growing-core methodology. The liquid droplet is in the center of the box, from $z = 30\sigma_0$ to $z = 75\sigma_0$. There is a vapor phase on both sides of the liquid droplet.

4.4. Pressure Differences Across the Liquid-Vapor Interface

Figure 6 (left) shows the difference between the normal components of the bulk pressures in the liquid and vapor. The pressure difference is shown as a function of the inverse half channel width, a, for three values of the interaction parameter α, all values representing wall-fluid repulsive forces. Figure 6 (right) shows the difference between the liquid and vapor for the tangential components of the pressures, i.e., the integral pressure $\widehat{p}$ (dashed lines) and the bulk pressure $= p^f$ (solid lines). Results are shown as a function of the inverse half channel width between the two pore walls, $1/a$, and three fluid–solid interactions parameters α. These plots allow us to test Equations (10) and (12).

We first observe that the integral pressure differences for the two fluids are zero, meaning that the integral pressure is constant along the pore, see Figure 6 right bottom. The results support Equation (12). In the bulk phases, the tangential and normal components are the same. This confirms the soundness of the calculation procedures.

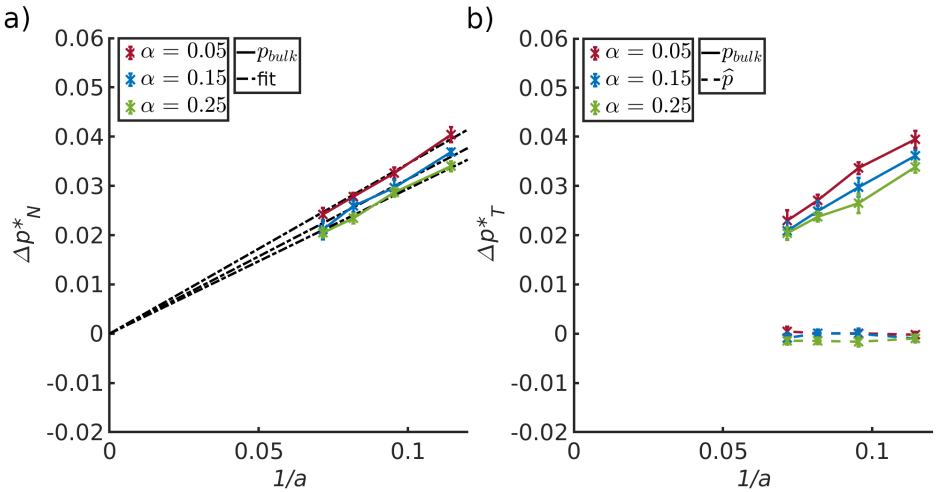

Figure 6. Difference between (**a**) the normal components of the pressure of the bulk liquid and vapor and (**b**) the difference in the tangential component of the pressure of the bulk liquid and vapor, for three different solid-fluid interactions (α) plotted as a function of the inverse half pore width. The bulk pressure, p^f and the integral pressure are represented by solid and dashed lines, respectively.

Both figures show that the difference in bulk pressure components depends on the distance between the two pore walls and the interaction parameter α. This is a consequence of a corresponding decrease of the liquid-vapor curvature. The uncertainties in the results, did not allow a determination of θ. We have therefore not computed the liquid-vapor surface tension, to confirm directly the law Young–Laplace. However, results of the two REVs combined, imply the validity of this law. The liquid–solid and vapor–solid surface tensions, computed with Equation (18), are given in Table 2 for the three α-values. The surface tension changes slightly with α.

Within the accuracy of the calculation, it was possible to estimate the slope of the three data sets. Lines to guide the eye were fitted through zero in the left-hand side figure, following Young–Laplace or the scaling law. The values of the slopes were 0.35/0.31/0.29, for α= 0.05/0.15/0.25, respectively. The slope is equal to $\gamma^{lv}\cos\theta$ which is approximately equal to γ^{ls} since $\gamma^{vs} \approx 0$ (see Equation (14) and Table 2).

The slopes depended on the interaction parameter α. The value increased for decreasing values of α. This is expected: The more repelling the surface is, the higher is the surface tension. The slopes are in agreement with the liquid-solid surface tensions given in Table 2.

Table 2. Surface tensions for the liquid/solid and vapor/solid interfaces. Values are presented for three interaction parameters α in the Lennard-Jones potential used in the computations. The surface tensions were computed via the excess of the tangential pressure tensor (see Equation (18)).

α	γ^{ls}	γ^{vs}
0.05	0.36 ± 0.02	0.0067 ± 0.0026
0.15	0.33 ± 0.01	0.005 ± 0.0035
0.25	0.31 ± 0.01	0.004 ± 0.0045

4.5. The Small System Scaling Law and the Subdivison Potential

Following the definition of Hill, the difference between the differential pressure, p, and the integral pressure, $\widehat{p}$, was given by Equation (16), or $\epsilon/V = \gamma^{fs}/(3a)$. The relation is an example of a small system scaling law, cf. Equation (6).

To investigate this further, the differential pressure, p, of the liquid REV minus the integral pressure $\widehat{p}$ of the same was plotted in Figure 7 as a function of the inverse half channel width for $\alpha = 0.15$. The difference between p and $\widehat{p}$ was proportional to $1/a$, and the slope was as predicted by the liquid/solid surface tension from Table 2 divided by the half channel width, a, and a factor of 3. The line goes through zero, when $1/a$ becomes zero. This is the thermodynamic limit value.

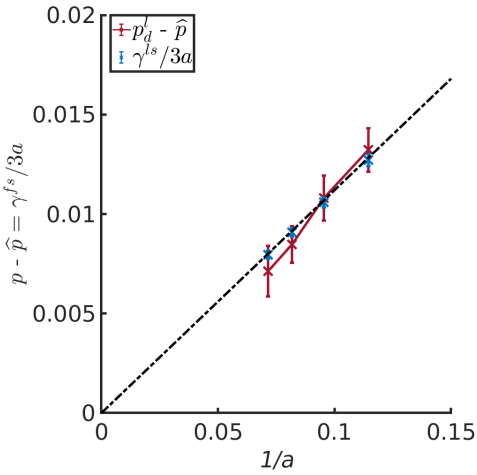

Figure 7. Difference between p and $\widehat{p}$ for the liquid REV_2 as a function of the inverse half channel width for $\alpha = 0.15$..

Erdos et al. [10] reported slopes for cylinder pores in addition to slit pores. The ratio of slopes between slit and cylinder pore was 0.52–0.58. From Equations (16) and (17), we obtain the ratio 0.50, when the surface tension is constant. The surface tension is a function of the interaction parameter, as we have seen. The surface tension may also depend on curvature. It follows that results from two pores with different geometries, having the same α, and a surface tension which is independent of curvature, will fall on top of each other.

The scaling law, that relate the integral and differential pressure of a REV, offer a new procedure for calculation of surface tensions. This defined dependence on the inverse characteristic length, may help distinguish between various other types of dependencies (curvature).

5. Conclusions

In this work we have confirmed, using molecular dynamics simulations, that the integral pressure in a nano-confined single fluid in two phases is constant along a pore. This supports and extends earlier investigations of Galteland et al. [18] for a single fluid between spheres arranged in a fcc lattice. The results imply, that Young's and Young–Laplace equations apply, equations which have been validated experimentally numerous times. The integral pressure in mechanical equilibrium can be understood as the average tangential component of the pressure. It is this component that is constant through a pore at equilibrium. The differential pressure at mechanical equilibrium can be understood as the average of the trace of the mechanical pressure tensor divided by 3.

The integral pressure, introduced by Hill, is relevant for descriptions of nano-pores. Using this, we have developed a small system scaling law for nano-pores. Equation (6) is valid for a slit pore and a cylindrical pore. The findings allowed us to speculate on wider applications of the scaling law. One may imagine using the law for more complex geometries, where higher order terms are relevant (line tension contributions). Once the subdivision potential is known, other thermodynamic quantities,

like the enthalpy-hat, can also be computed for the confined system [33]. This opens up new ways to study confined systems.

Author Contributions: M.T.R. and O.G. wrote software and carried out the calculations. M.E. did the Monte Carlo simulations. S.K., D.B., M.T.R. and O.G. contributed to the conceptual design and development. The project was supervised by O.A.M., S.K.S., S.K., D.B., and T.J.H.V. All authors contributed to the writing of the manuscript and the scientific discussions. All authors have read and agreed to the published version of the manuscript.

Funding: This research was funded by the Center of Excellence funding scheme of the Research Council of Norway, project no 262644, PoreLab. The work was also sponsored by NWO ExacteWetenschappen (Physical Sciences) for the use of supercomputer facilities, with financial support from the Nederlandse Organisatie voor Wetenschappelijk Onderzoek (Netherlands Organisation for Scientific Research, NWO).

Acknowledgments: The calculation power was granted by The Norwegian Metacenter of Computational Science (NOTUR). Thanks to the Research Council of Norway through its Centres of Excellence funding scheme, project number 262644, PoreLab, and SKS acknowledges funding through the Research Council of Norway and the Young Research Talents Scheme with project number 275754. TJHV acknowledges NWO-CW (Chemical Sciences) for a VICI grant. Discussions with Øivind Wilhelmsen were highly appreciated.

Conflicts of Interest: The authors declare no conflict of interest.

Appendix A

In an isotropic system, the differential pressure p is normally defined by the trace of the pressure tensor [34]:

$$p = \frac{P_{xx} + P_{yy} + P_{zz}}{3} \tag{A1}$$

where P_{ii} is the pressure component in the direction ii. Also the integral pressure can be understood in terms of these pressure components. The integral pressure, $\widehat{p}$, in the present slit pore was expressed by Equation (20):

$$\widehat{p} = \frac{1}{2a}\int_{-a}^{a} P_T \mathrm{d}x = \langle P_T \rangle = \frac{P_{yy} + P_{zz}}{2} \tag{A2}$$

where P_{yy} and P_{zz} are the pressure components in tangential direction, and x is the direction normal to the surface. The difference between p and $\widehat{p}$ can then be written as

$$p - \widehat{p} = \frac{P_{xx} + P_{yy} + P_{zz}}{3} - \frac{P_{yy} + P_{zz}}{2} \tag{A3}$$

which results in

$$p - \widehat{p} = \frac{P_{xx}}{3} - \frac{P_{yy} + P_{zz}}{6} \tag{A4}$$

By using the definition for the tangential pressure from Equation (A2), we obtain

$$p - \widehat{p} = \frac{P_{xx}}{3} - \frac{\langle P_T \rangle}{3} \tag{A5}$$

The normal pressure is equal to the tangential pressure in the thermodynamic limit (the bulk fluid). For the bulk fluid;

$$P_{xx} = \langle P_T \rangle = p^f \tag{A6}$$

These relations mean that there is no difference between p and $\widehat{p}$.

With the assumption used in Equation (A2), P_{xx}, is constant in the direction perpendicular to the pore surface, and

$$P_{xx} = p^f \tag{A7}$$

also away from the thermodynamic limit. By combining Equation (A2) with the definition of $\widehat{p}$, Equation (11), we obtain

$$\langle P_T \rangle = p^f - \frac{\gamma^{fs}}{a} \tag{A8}$$

By introducing Equations (A7) and (A8) into Equation (A5), we obtain

$$p - \widehat{p} = \frac{p^f}{3} - \frac{p^f}{3} + \frac{\gamma^{fs}}{3a} \tag{A9}$$

which is

$$p - \widehat{p} = \frac{\gamma^{fs}}{3a} \tag{A10}$$

The difference between the differential pressure p and the integral pressure $\widehat{p}$ in this equation is the same as the difference in Equation (16), which was obtained using Hills formalism.

References

1. Keshavarzi, E.; Kamalvand, M. Energy effects on the structure and thermodynamic properties of nanoconfined fluids (a density functional theory study). *J. Phys. Chem. B* **2009**, *113*, 5493–5499. [CrossRef] [PubMed]
2. Braun, E.; Chen, J.J.; Schnell, S.K.; Lin, L.C.; Reimer, J.A.; Smit, B. Nanoporous Materials Can Tune the Critical Point of a Pure Substance. *Angew. Chem.* **2015**, *127*, 14557–14560. [CrossRef]
3. Pharoah, J.; Karan, K.; Sun, W. On effective transport coefficients in PEM fuel cell electrodes: Anisotropy of the porous transport layers. *J. Power Sources* **2006**, *161*, 214–224. [CrossRef]
4. Newman, J.; Tiedemann, W. Porous-electrode theory with battery applications. *AIChE J.* **1975**, *21*, 25–41. [CrossRef]
5. Guo, H.; Wyart, Y.; Perot, J.; Nauleau, F.; Moulin, P. Low-pressure membrane integrity tests for drinking water treatment: A review. *Water Res.* **2010**, *44*, 41–57. [CrossRef]
6. Alklaibi, A.M.; Lior, N. Transport analysis of air-gap membrane distillation. *J. Membr. Sci.* **2005**, *255*, 239–253. [CrossRef]
7. Kuipers, N.; Hanemaaijer, J.H.; Brouwer, H.; van Medevoort, J.; Jansen, A.; Altena, F.; van der Vleuten, P.; Bak, H. Simultaneous production of high-quality water and electrical power from aqueous feedstock's and waste heat by high-pressure membrane distillation. *Desalin. Water Treat.* **2015**, *55*, 2766–2776. [CrossRef]
8. Schnell, S.K.; Vlugt, T.J.H.; Simon, J.M.; Bedeaux, D.; Kjelstrup, S. Thermodynamics of small systems embedded in a reservoir: A detailed analysis of finite size effects. *Mol. Phys.* **2012**, *110*, 1069–1079. [CrossRef]
9. Strøm, B.; Simon, J.M.; Schnell, S.; Kjelstrup, S.; He, J.; Bedeaux, D. Size and shape effects on the thermodynamic properties of nanoscale volumes of water. *Phys. Chem. Chem. Phys.* **2017**, *19*, 9016. [CrossRef]
10. Erdős, M.; Galteland, O.; Bedeaux, D.; Kjelstrup, S.; Moultos, O.A.; Vlugt, T.J.H. Gibbs Ensemble Monte Carlo Simulation of Fluids in Confinement: Relation between the Differential and Integral Pressures. *Nanomaterials* **2020**, *10*, 293. [CrossRef]
11. Hill, T.L. *Thermodynamics of Small Systems*; Dover Publications Inc.: New York, NY, USA, 1994.
12. Dong, X.; Liu, H.; Hou, J.; Wu, K.; Chen, Z. Phase equilibria of confined fluids in nanopores of tight and shale rocks considering the effect of capillary pressure and adsorption film. *Ind. Eng. Chem. Res.* **2016**, *55*, 798–811. [CrossRef]
13. Gubbins, K.E.; Long, Y.; Śliwinska-Bartkowiak, M. Thermodynamics of confined nano-phases. *J. Chem. Thermodyn.* **2014**, *74*, 169–183. [CrossRef]
14. Giovambattista, N.; Rossky, P.J.; Debenedetti, P.G. Phase transitions induced by nanoconfinement in liquid water. *Phys. Rev. Lett.* **2009**, *102*, 050603. [CrossRef] [PubMed]
15. Eslami, H.; Mehdipour, N. Local chemical potential and pressure tensor in inhomogeneous nanoconfined fluids. *J. Chem. Phys.* **2012**, *137*, 144702. [CrossRef] [PubMed]
16. Bennethum, L.S.; Weinstein, T. Three pressures in porous media. *Transp. Porous Med.* **2004**, *54*, 1–34. [CrossRef]
17. Kjelstrup, S.; Bedeaux, D.; Hansen, A.; Hafskjold, B.; Galteland, O. Non-isothermal transport of multi-phase fluids in porous media. Constitutive equations. *Front. Phys.* **2019**, *6*, 150. [CrossRef]
18. Galteland, O.; Bedeaux, D.; Kjelstrup, S.; Hafskjold, B. Pressures inside a nano-porous medium. The case of a single phase fluid. *Front. Phys.* **2019**, *7*, 60. [CrossRef]

19. Bedeaux, D.; Kjelstrup, S.; Schnell, S.K. *Nanothermodynamics. General Theory*; PoreLab, NTNU Grafisk: Trondheim, Norway, 2020.
20. Bedeaux, D.; Kjelstrup, S. Hill's thermodynamics is equivalent with Gibb's thermodynamics for surfaces of constant curvatures. *Chem. Phys. Lett.* **2018**, *707*, 40–43. [CrossRef]
21. Tsai, D. The virial theorem and stress calculation in molecular dynamics. *J. Chem. Phys.* **1979**, *70*, 1375–1382. [CrossRef]
22. Chatterjee, J. Prediction of coupled menisci shapes by Young–Laplace equation and the resultant variability in capillary retention. *J. Colloid Interface Sci.* **2007**, *314*, 199–206. [CrossRef]
23. Gras, J.P.; Delenne, J.Y.; El Youssoufi, M.S. Study of capillary interaction between two grains: A new experimental device with suction control. *Granular Matter* **2013**, *15*, 49–56. [CrossRef]
24. Kirkwood, J.G.; Buff, F.P. The statistical mechanical theory of surface tension. *J. Chem. Phys.* **1949**, *17*, 338–343. [CrossRef]
25. Hafskjold, B.; Travis, K.P.; Hass, A.B.; Hammer, M.; Aasen, A.; Wilhelmsen, Ø. Thermodynamic properties of the 3D Lennard-Jones/spline model. *Mol. Phys.* **2019**, *117*, 3754–3769. [CrossRef]
26. Plimpton, S. Fast parallel algorithms for short-range molecular dynamics. *J. Comput. Phys.* **1995**, *117*, 1–19. [CrossRef]
27. Braga, C.; Travis, K.P. A configurational temperature Nosé-Hoover thermostat. *J. Chem. Phys.* **2005**, *123*, 134101. [CrossRef]
28. Frenkel, D.; Smit, B. *Understanding Molecular Simulation: From Algorithms to Applications*; Elsevier: Amsterdam, The Netherlands, 2001; Volume 1.
29. Hafskjold, B.; Ikeshoji, T. Microscopic pressure tensor for hard-sphere fluids. *Phys. Rev. E* **2002**, *66*, 011203. [CrossRef]
30. Ikeshoji, T.; Hafskjold, B.; Furuholt, H. Molecular-level calculation scheme for pressure in inhomogeneous systems of flat and spherical layers. *Mol. Simul.* **2003**, *29*, 101–109. [CrossRef]
31. Todd, B.; Evans, D.J.; Daivis, P.J. Pressure tensor for inhomogeneous fluids. *Phys. Rev. E* **1995**, *52*, 1627. [CrossRef]
32. Todd, B.D.; Daivis, P.J. *Nonequilibrium Molecular Dynamics: Theory, Algorithms and Applications*; Cambridge University Press: Cambridge, UK, 2017.
33. Skorpa, R.; Simon, J.M.; Bedeaux, D.; Kjelstrup, S. The reaction enthalpy of hydrogen dissociation calculated with the Small System Method from simulation of molecular fluctuations. *Phys. Chem. Chem. Phys.* **2014**, *16*, 19681. [CrossRef]
34. Daivis, P.J.; Evans, D.J. Comparison of constant pressure and constant volume nonequilibrium simulations of sheared model decane. *J. Chem. Phys.* **1994**, *100*, 541–547. [CrossRef]

Article VI

Olav Galteland, Dick Bedeaux, Signe Kjelstrup

Nanothermodynamic Description and Molecular Simulation of a Single-Phase Fluid in a Slit Pore

Nanomaterials, 11(1), 165. (2021)
DOI: 10.3390/nano11010165

Article VI

Article VI

nanomaterials

MDPI

Article

Nanothermodynamic Description and Molecular Simulation of a Single-Phase Fluid in a Slit Pore

Olav Galteland *, Dick Bedeaux and Signe Kjelstrup

PoreLab, Department of Chemistry, Norwegian University of Science and Technology, 7491 Trondheim, Norway; dick.bedeaux@ntnu.no (D.B.); signe.kjelstrup@ntnu.no (S.K.)

* Correspondence: olav.galteland@ntnu.no

Abstract: We have described for the first time the thermodynamic state of a highly confined single-phase and single-component fluid in a slit pore using Hill's thermodynamics of small systems. Hill's theory has been named nanothermodynamics. We started by constructing an ensemble of slit pores for controlled temperature, volume, surface area, and chemical potential. We have presented the integral and differential properties according to Hill, and used them to define the disjoining pressure on the new basis. We identified all thermodynamic pressures by their mechanical counterparts in a consistent manner, and have given evidence that the identification holds true using molecular simulations. We computed the entropy and energy densities, and found in agreement with the literature, that the structures at the wall are of an energetic, not entropic nature. We have shown that the subdivision potential is unequal to zero for small wall surface areas. We have showed how Hill's method can be used to find new Maxwell relations of a confined fluid, in addition to a scaling relation, which applies when the walls are far enough apart. By this expansion of nanothermodynamics, we have set the stage for further developments of the thermodynamics of confined fluids, a field that is central in nanotechnology.

Keywords: Hill's thermodynamics of small systems; porous media; integral pressure; molecular simulation

Citation: Galteland, O.; Bedeaux, D.; Kjelstrup, S. Nanothermodynamic Description and Molecular Simulation of a Single-Phase Fluid in a Slit Pore. *Nanomaterials* **2021**, *11*, 165. https://doi.org/10.3390/nano11010165

Received: 2 December 2020
Accepted: 6 January 2021
Published: 11 January 2021

1. Introduction

The thermodynamic state of a fluid in confinement is important for the understanding of adsorption to walls, chemical reactions, film formation and transport in porous media [1–6]. The molecular structuring at the walls and the forces between particles and walls are central. The change in thermodynamic properties upon confinement is substantial. This has been known for a long time [1,7]. Derjaguin considered the measurable force that attracts or repels two walls that are close together, and defined from this the disjoining pressure [7]. The disjoining pressure has also been called the solvation pressure [1]. When the walls are far apart, the disjoining pressure vanishes. It is not well known, however, how size and shape, as variables, affect the disjoining pressure or other properties of the confined fluid.

Confinement is considered to be important, for instance, in the context of CO_2 separation and sequestration by metal-organic frameworks [2] or for adsorption in zeolites [3]. The disjoining pressure is of interest when studying aggregation of colloidal particles, suspended or adsorbed [4–6]. It is likely to be important also for film flow on the macroscale [8].

More knowledge of confined fluids on the nanoscale is therefore needed. It may, for instance, help us solve the well-known up-scaling problem in porous media science [9]. The central problem is to understand how to integrate properties on the pore scale to the macroscale where Darcy's law applies. In order to account for shape and size effects, it was recently proposed to use the four Minkowski functionals [10–12]. This simplifies the description of a representative elementary volume (REV). Another procedure using the grand potential for average variables in the REV was also proposed [13,14].

In this work, we want to further examine this procedure [13,14], by looking for a way to describe the confined fluid in a pore. We are looking for a way to deal with size- and shape-dependent variables in a systematic and general manner. Two thermodynamic approaches are common. The approach following Gibbs is most popular [15–19]. However, the method of Hill may offer an attractive alternative [20–25], partly because it may provide an independent check on Gibbs procedure, but also because general geometric scaling relations are obtainable from Hill's method. We will see that this is also the case in the present study.

We will pursue the method of Hill. This starts with the observation that a small system has surface energy comparable to its bulk energy. A consequence is that the properties are not Euler homogeneous. Hill proposed to deal with such systems in an original manner [26]. His idea was to introduce an ensemble of replicas of the small systems, on which standard thermodynamics could be applied. Hill's method has not gained much attention, in spite of a renewed effort to spur interests [27,28].

The long-range aim of this work is to contribute to the effort of finding variables that characterize the confined fluid, for instance in a REV. The grand potential offers one option to describe the pressure and other variables [13,14]. We will pursue this route and study a single-phase and single-component fluid in a slit pore using Hill's method. The so-called integral and differential pressures introduced by Hill are central. Hill did not consider the disjoining pressure, however, it is a small system property and we will see that this concept has benefited from insights of nanothermodynamics. The purpose of this paper is to clarify the use of Hill's nanothermodynamics, by applying the method to a fluid in a slit pore with walls of large surface areas. This is a well-studied case in the literature [1,29], and is well suited to bring out new results on the confined state, the disjoining pressure and other properties. Grand canonical Monte Carlo and molecular dynamics simulation techniques are well suited to investigate thermodynamic relations. We will use these tools to simulate a single-phase fluid in a slit pore in the grand canonical ensemble. A particular advantage of this technique is that the simulations offer a mechanical picture of the system.

Solid–fluid and fluid–fluid interactions are considered here, but not solid–solid interactions. The solid–solid interactions will have a large effect on the thermodynamic state of the system at very small slit pore heights. We do not consider quantum effects that follow from system smallness in this work. We will consider slit pores of height $h/\lambda_B = 6$ to 71, where λ_B is the thermal de Broglie wavelength.

Section 2.1 introduces the reader to Hill's nanothermodynamics. We show in Section 2.2 how this theory can be used to define size- and shape-dependent properties, and new Maxwell relations that follow from these. A definition of the disjoining pressure follows naturally in Section 2.3. In order to be able to verify relations with molecular simulations as a tool, we need to identify the integral pressures and surface tension in terms of the mechanical pressure tensor components. This is done in Section 2.4. In Section 3 we describe the molecular simulations.

We proceed in Section 4 to investigate relations in the theory, and illustrate them with numerical results. We compute the local mechanical and thermodynamic variables according to Hill; i.e., the integral and differential pressures, and the integral and differential surface tensions. The grand potential, or the replica energy, is equal to minus the integral pressure times the volume. The set of thermodynamic variables of the nanothermodynamic framework, in terms of mechanical properties, is found to be self-consistent. We offer concluding remarks in Section 5.

2. Theory

2.1. Hill's Nanothermodynamics

Consider an ensemble of $\mathcal{N}$ slit pores, where each slit pore is filled with a single-phase and single-component fluid. The slit pores do not interact with each other. The j-th slit pore has two parallel plane walls of area Ω_j, separated by a distance h_j. The ensemble of slit pores has the total internal energy U_t, total entropy S_t, total volume $V_t = \sum_{j=1}^{\mathcal{N}} h_j \Omega_j$, total

surface area $2\Omega_t = 2\sum_{j=1}^{\mathcal{N}} \Omega_j$, and total number of particles N. The factor of two in the total surface area arises because there are two fluid–solid surfaces of equal area per slit pore. By construction, the ensemble variables $U_t, S_t, V_t, \Omega_t, N$, and $\mathcal{N}$ are Euler homogeneous functions of the first order in the number $\mathcal{N}$ of slit pores. The total differential of the total internal energy is

$$\mathrm{d}U_t = T\mathrm{d}S_t - p_\perp \mathrm{d}V_t + 2\gamma \mathrm{d}\Omega_t + \mu \mathrm{d}N_t + \varepsilon \mathrm{d}\mathcal{N}. \tag{1}$$

This type of equation for the total internal energy we call the Hill-Gibbs equation [25]. The last term was added by Hill. The partial derivatives of the total internal energy define the temperature T, the normal pressure $p_\perp$, the surface tension γ and the chemical potential μ

$$\begin{aligned} \left(\frac{\partial U_t}{\partial S_t}\right)_{V_t,\Omega_t,N_t,\mathcal{N}} &= T, & \left(\frac{\partial U_t}{\partial V_t}\right)_{S_t,\Omega_t,N_t,\mathcal{N}} &= -p_\perp, \\ \left(\frac{\partial U_t}{\partial \Omega_t}\right)_{S_t,V_t,N_t,\mathcal{N}} &= 2\gamma, & \left(\frac{\partial U_t}{\partial N_t}\right)_{S_t,V_t,\Omega_t,\mathcal{N}} &= \mu. \end{aligned} \tag{2}$$

The control variables in subscripts are kept constant while taking the derivatives. The volume derivative is taken while keeping the total surface area constant, which implies that the volume is changed by changing the distance between the surfaces $h_j \equiv V_j/\Omega_j$. The surface derivative is taken while keeping the volume constant, which implies that both the pore heights and surface areas are changed in such a way that the change in the total volume is zero.

The new thermodynamic variable ε is the *subdivision potential*. It is

$$\left(\frac{\partial U_t}{\partial \mathcal{N}}\right)_{S_t,V_t,\Omega_t,N_t} = \varepsilon. \tag{3}$$

The subdivision potential is defined here as the increase in the total internal energy as the number of slit pores $\mathcal{N}$ increases while keeping S_t, V_t, Ω_t, and N_t constant. This definition is different from the definition in a previous article by us [23], where only the entropy, volume and number of particles were kept constant and not the surface area. This led to a different expression for the subdivision potential.

The subdivision potential is the work done on the system when adding a new slit pore while keeping the other control variables constant. The subdivision potential may be positive or negative, depending on whether work is needed or gained by adding new slit pore replicas.

We are aiming to describe the disjoining pressure, see Section 2.3, of an open slit pore when the volume, surface area, temperature and chemical potential are control variables. We will change to this ensemble. This ensemble is useful for describing experiments and simulations. We use the average volume per slit pore $V = V_t/\mathcal{N}$ and the average surface area per slit pore $2\Omega = 2\Omega_t/\mathcal{N}$, rather than the total volume V_t and the total surface area $2\Omega_t$. In order to obtain an appropriate Hill-Gibbs equation for this case, we substitute the total volume with the average volume $V_t = V\mathcal{N}$ and total surface area with the average surface area $2\Omega_t = 2\Omega\mathcal{N}$. The total differentials of the volume and surface area are

$$\mathrm{d}(V\mathcal{N}) = \mathcal{N}\mathrm{d}V + V\mathrm{d}\mathcal{N} \quad \text{and} \quad \mathrm{d}(\Omega\mathcal{N}) = \mathcal{N}\mathrm{d}\Omega + \Omega\mathrm{d}\mathcal{N}. \tag{4}$$

By introducing this into the Hill–Gibbs equation, see Equation (1), we obtain

$$\mathrm{d}U_t = T\mathrm{d}S_t - p_\perp \mathcal{N}\mathrm{d}V + 2\gamma\mathcal{N}\mathrm{d}\Omega + \mu \mathrm{d}N_t + (\varepsilon - p_\perp V + 2\gamma\Omega)\mathrm{d}\mathcal{N}. \tag{5}$$

The parenthesis define the replica energy

$$X(T, V, \Omega, \mu) \equiv \varepsilon - p_\perp V + 2\gamma\Omega. \tag{6}$$

The subdivision potential ε, normal pressure $p_\perp$, and surface tension γ depend on the control variable set T, V, Ω, and μ. The replica energy density will be used to define the disjoining pressure.

The grand partition function covers all microstates available to the slit pore. In order to calculate this partition function one chooses a volume V and a surface area Ω. Both can be varied independently. For large h and Ω only a change in the volume $V = h\Omega$, and not in h and Ω separately, matters. For a small volume, it is necessary to use the volume V and the surface area Ω as independent variables. This is because the same volume change due to a change of the pore height $h = V/\Omega$ or due to a change of the surface area Ω produces different changes in the partition function, and therefore in the thermodynamic variables.

The replica energy was identified by Hill as the grand potential, here equal to minus the integral pressure times the volume [26],

$$X(T, V, \Omega, \mu) = -\hat{p}V = -\hat{p}_\perp V + 2\hat{\gamma}\Omega. \tag{7}$$

In the last equality, we have chosen to identify the integral pressure as the integral normal pressure times the volume minus the integral surface tension times the surface area. We will refer to $\hat{p}_\perp$, $\hat{\gamma}$ and $\hat{p}$ as the integral normal pressure, the integral surface tension and the integral pressure, respectively, while $p_\perp$ and γ are the differential normal pressure and the differential surface tension, respectively. The names integral and differential pressure were coined by Hill to reflect that the differential pressure involves the differential of the integral pressure. We have chosen a control variable set with volume and surface area, such that we do not have a differential pressure but a differential normal pressure $p_\perp$ and differential surface tension γ in its place.

From Equations (6) and (7) it follows that the subdivision potential is

$$\varepsilon = (p_\perp - \hat{p}_\perp)V - 2(\gamma - \hat{\gamma})\Omega. \tag{8}$$

The subdivision potential ε indicates that the integral normal pressure and the integral surface tension may be different from the corresponding differential variables.

2.2. Maxwell Relations for a Slit Pore

Using that the total internal energy is Euler homogeneous of the first order in the number of slit pores, see Equation (5), we integrate it at constant T, V, μ and Ω

$$U_t = TS_t + \mu N_t + X\mathcal{N}. \tag{9}$$

We introduce the average internal energy, entropy and number of particles per slit pore

$$U_t = U\mathcal{N}, \qquad S_t = S\mathcal{N}, \quad \text{and} \quad N_t = N\mathcal{N}. \tag{10}$$

By introducing the average properties into the total internal energy in Equation (9) we obtain the internal energy per slit pore

$$U = TS + \mu N + (\varepsilon - p_\perp V + 2\gamma\Omega) = TS + \mu N + X. \tag{11}$$

Substituting the average properties per slit pore in Equation (10) into the corresponding Hill-Gibbs equation, see Equation (5), and using the internal energy in Equation (11), we obtain the total differential of the internal energy

$$\mathrm{d}U = T\mathrm{d}S - p_\perp \mathrm{d}V + 2\gamma\mathrm{d}\Omega + \mu\mathrm{d}N. \tag{12}$$

By differentiating the internal energy in Equation (11) and using the total differential of the internal energy in Equation (12), we obtain the total differential of the replica energy

$$\mathrm{d}X = -\mathrm{d}(\hat{p}_\perp V - 2\hat{\gamma}\Omega) = -\mathrm{d}(\hat{p}V) = -S\mathrm{d}T - p_\perp \mathrm{d}V + 2\gamma\mathrm{d}\Omega - N\mathrm{d}\mu. \tag{13}$$

This equation was termed the Hill-Gibbs-Duhem Equation [25], because it reduces to the Gibbs-Duhem equation for a large system. It follows that the partial derivatives of the grand potential is

$$\begin{aligned}
\left(\frac{\partial(\hat{p}V)}{\partial T}\right)_{V,\Omega,\mu} &= -\left(\frac{\partial X}{\partial T}\right)_{V,\Omega,\mu} = S,\\
\left(\frac{\partial(\hat{p}V)}{\partial V}\right)_{T,\Omega,\mu} &= -\left(\frac{\partial X}{\partial V}\right)_{T,\Omega,\mu} = p_\perp,\\
\left(\frac{\partial(\hat{p}V)}{\partial \Omega}\right)_{T,V,\mu} &= -\left(\frac{\partial X}{\partial \Omega}\right)_{T,V,\mu} = -2\gamma,\\
\left(\frac{\partial(\hat{p}V)}{\partial \mu}\right)_{T,V,\Omega} &= -\left(\frac{\partial X}{\partial \mu}\right)_{T,V,\Omega} = N.
\end{aligned} \tag{14}$$

Rather than the names replica energy or grand potential, we name from now $X = -\hat{p}V$ by minus the integral pressure times the volume. In Section 2.4 we will define the integral pressure in terms of the average tangential mechanical pressure which can be calculated from molecular simulations. In the simulations, we consider surface areas Ω much larger than the diameter of the fluid particles and heights $h = V/\Omega$ comparable to the diameter of the fluid particles. This implies that $\hat{p}$, $\hat{p}_\perp$, $\hat{\gamma}$, $u \equiv U/V$, $s \equiv S/V$, $p_\perp$, γ, and $\rho \equiv N/V$ do not depend on Ω, but the variables will depend on the height h and therefore on the volume V.

The volume and surface derivative can be rewritten in terms of derivatives of the slit pore height and surface area. These derivatives are needed to calculate the differential normal pressure and differential surface tension. The differential normal pressure is

$$p_\perp = \left(\frac{\partial(\hat{p}V)}{\partial V}\right)_{T,\Omega,\mu} = \hat{p} + V\left(\frac{\partial \hat{p}}{\partial V}\right)_{T,\Omega,\mu} = \hat{p} + h\left(\frac{\partial \hat{p}}{\partial h}\right)_{T,\Omega,\mu}. \tag{15}$$

The differential surface tension is

$$\gamma = -\frac{V}{2}\left(\frac{\partial \hat{p}}{\partial \Omega}\right)_{T,V,\mu} = \frac{h^2}{2}\left(\frac{\partial \hat{p}}{\partial h}\right)_{T,\Omega,\mu} - \frac{V}{2}\left(\frac{\partial \hat{p}}{\partial \Omega}\right)_{T,h,\mu}. \tag{16}$$

Combining the equations for the differential normal pressure and surface tension it follows that the integral pressure is

$$\hat{p} = p_\perp - \frac{2}{h}\gamma - \Omega\left(\frac{\partial \hat{p}}{\partial \Omega}\right)_{T,\mu,h}. \tag{17}$$

The last term is the equal to minus the subdivision potential divided by volume, see Equations (7) and (8). The subdivision potential is

$$\varepsilon = \Omega V\left(\frac{\partial \hat{p}}{\partial \Omega}\right)_{T,\mu,h}. \tag{18}$$

This implies that in the grand canonical ensemble with T, V, Ω, μ as control variables, the thermodynamic description of the slit pore with a small height is the same as for the slit pore with a large height. However, it changes when the integral pressure depends on the surface area. This may not be the case for any other set of control variables. In general, the properties of a small system (confined fluid) depend on the set of control variables.

In this work, we deal with large surface areas, such that the integral pressure does not depend on it. As a consequence the subdivision potential is zero. We will find that the integral and differential normal pressure are equal. Using that $\varepsilon = 0$, it follows that the integral and differential surface tensions are also equal for a large surface area, see Equation (8),

$$\hat{p}_\perp = p_\perp \quad \text{and} \quad \hat{\gamma} = \gamma. \tag{19}$$

We will investigate the first identity for large surface areas using molecular simulations.

From Equation (13) we obtain the following Maxwell relations of the differential surface tension,

$$\begin{aligned}
\left(\frac{\partial \gamma}{\partial T}\right)_{V,\Omega,\mu} &= -\frac{1}{2}\left(\frac{\partial S}{\partial \Omega}\right)_{T,\mu,V} = \frac{h^2}{2}\left(\frac{\partial s}{\partial h}\right)_{T,\mu,\Omega}, \\
\left(\frac{\partial \gamma}{\partial \mu}\right)_{T,V,\Omega} &= -\frac{1}{2}\left(\frac{\partial N}{\partial \Omega}\right)_{T,\mu,V} = \frac{h^2}{2}\left(\frac{\partial \rho}{\partial h}\right)_{T,\mu,\Omega}, \\
\left(\frac{\partial \gamma}{\partial V}\right)_{T,\Omega,\mu} &= -\frac{1}{2}\left(\frac{\partial p_\perp}{\partial \Omega}\right)_{T,\mu,V} = \frac{h}{2\Omega}\left(\frac{\partial p_\perp}{\partial h}\right)_{T,\mu,\Omega}.
\end{aligned} \tag{20}$$

In the second identity, we have used that the entropy density, fluid number density and differential normal pressure are independent of the surface area for large surface areas. Other Maxwell relations are possible, see the Hill–Gibbs–Duhem Equation (13). The last equality can be written as

$$\left(\frac{\partial \gamma}{\partial h}\right)_{T,\mu} = \frac{h}{2}\left(\frac{\partial p_\perp}{\partial h}\right)_{T,\mu,\Omega}. \tag{21}$$

The important implication of this expression is that the constant nature of one variable implies the constant nature of the other for large pore heights. With the mechanical description of the integral properties given in Section 2.4 the consistency of all the above thermodynamic relations can be tested.

2.3. The Disjoining Pressure

We define the excess replica energy as the replica energy of a slit pore of height h minus the replica energy of the slit pore where the slit pore height approaches infinity,

$$X^{\text{ex}} = X - \lim_{h\to\infty} X. \tag{22}$$

We denote the thermodynamic variables where the slit pore height approaches infinity with ∞ in superscript,

$$\lim_{h\to\infty} X = X^\infty. \tag{23}$$

The excess replica energy can be written in terms of the excess integral pressure $\hat{p}^{\text{ex}}$, excess integral normal pressure $\hat{p}^{\text{ex}}_\perp$, and excess integral surface tensions $\hat{\gamma}^{\text{ex}}$

$$X^{\text{ex}} = -\hat{p}^{\text{ex}}\, V = -\hat{p}^{\text{ex}}_\perp V + 2\hat{\gamma}^{\text{ex}}\Omega. \tag{24}$$

We define now the disjoining pressure as the excess normal pressure,

$$\Pi(h) \equiv \hat{p}^{\text{ex}}_\perp \equiv \hat{p}_\perp - p^\infty_\perp. \tag{25}$$

Other possible names are minus the excess replica density, or the excess grand potential density.

This definition of the disjoining pressure is different from the typical definition found in the literature [7,29,30]. Typically the disjoining pressure is defined to be equal to what we in this work call the excess differential normal pressure, where the excess is relative to a bulk fluid. For large surface areas we will show with molecular simulations that $\hat{p}_\perp = p_\perp$. We will furthermore show that the integral normal pressure, as the slit pore height approaches infinite separation, equals the bulk fluid pressure $p^\infty_\perp = p^b$. This shows that our choice is equivalent to the usual definition.

2.4. A Mechanical Description of the Slit Pore

The thermodynamic description of integral and differential pressures and surface tensions has its mechanical equivalent description in terms of components of the mechanical pressure tensor. A recent discussion on this topic clarified the challenge of translating the mechanical pressure tensor into a thermodynamic scalar variable in a meaningful manner [31–33]. We will identify the integral normal pressure, integral surface tension, and integral pressure in such a way that thermodynamic framework is self-consistent. However, we do not claim that this is the only valid choice of thermodynamic pressures and tensions in terms of the mechanical pressure tensor.

The mechanical pressure tensor of a heterogeneous system is ambiguously defined. This has been known for a long time, at least since the work by Irving and Kirkwood in the 1940s. It was shown by Schofield and Henderson [34] that the ambiguity is due to the arbitrary choice of the integration contour C_{ij}, which is needed to calculate the configurational contribution to the pressure tensor. The local mechanical pressure tensor is calculated in a subvolume V_l as a sum of the kinetic and the configurational contributions,

$$P_{\alpha\beta}(x) = P^k_{\alpha\beta} + P^c_{\alpha\beta}. \tag{26}$$

Upper case P is used to denote mechanical pressure tensor components in order to distinguish them from the thermodynamic pressures, which are denoted by the lower case p. The kinetic contribution is the ideal contribution to the mechanical pressure and is calculated as

$$P^k_{\alpha\beta} = \frac{1}{V_l}\left\langle \sum_{i\in V_l} m_i v_{i,\alpha} v_{i,\beta} \right\rangle. \tag{27}$$

The sum with subscript $i \in V_l$ represents a sum over all particles in the subvolume V_l. The particle mass is m_i and $v_{i,\alpha}$ is the velocity in the α-direction. The solid walls do not have a velocity and consequently do not directly contribute to the kinetic pressure. The brackets $\langle \dots \rangle$ represent ensemble average. The configurational contribution is the non-ideal contribution to the mechanical pressure and is calculated as

$$P^c_{\alpha\beta} = -\frac{1}{2V_l}\left\langle \sum_{i=1}^{N}\sum_{\substack{j=1\\ j\neq i}}^{N} f_{ij,\alpha} \int_{C_{ij}\in V_l} \mathrm{d}l_\beta \right\rangle. \tag{28}$$

The sum represents a sum over all particle pairs. The α-component of the force vector acting on particle i due to particle j is $f_{ij,\alpha}$. The fluid–fluid and fluid–solid interactions contribute to the configurational pressure, the solid–solid interaction is zero and does not contribute to the pressure. The line integral is the β-component of the part of the contour C_{ij} contained in the subvolume V_l.

The contour C_{ij} is the source of the ambiguity of the mechanical pressure tensor, it can be any continuous line from the centers of particles i to j. The Harasima [35] and the Irving–Kirkwood [36] contours are two common choices for C_{ij}. The Harasima contour is defined as two continuous line segments, a line from the center of particle i parallel to the surface and a line normal to the surface to the center of particle j. The Irving–Kirkwood is the straight line from particle i to j. For flat surfaces they are equal. However, for spherical surfaces, the Harasima contour does not obey momentum balance [37]. There are cases where the Harasima contour is more useful than the Irving–Kirkwood contour [38]. In this work, we will use the equations by Ikeshoji et al. [39] with the Irving–Kirkwoood contour to calculate the mechanical pressure tensor.

We will only consider surface areas Ω much larger in both directions than the fluid particle diameter. This implies the mechanical pressure tensor does not depend on Ω. It does, however, depend on the height $h \equiv V/\Omega$ and therefore on the volume V.

Using the translational symmetry of the slit pore in the y- and z-direction, where the x-direction is normal to the solid surface, the equilibrium mechanical pressure tensor in the slit pore has the form

$$\mathbf{P}(x;h) = P_{\perp}(h)\mathbf{e}_x\mathbf{e}_x + P_{\parallel}(x;h)(\mathbf{e}_y\mathbf{e}_y + \mathbf{e}_z\mathbf{e}_z), \tag{29}$$

where $\mathbf{e}_x$, $\mathbf{e}_y$ and $\mathbf{e}_z$ are the unit vectors in the x-, y- and z-directions. The normal pressure tensor component is equal to the xx-component, and tangential pressure tensor component is the average of the yy- and zz-components,

$$P_{\perp}(h) = P_{xx} \quad \text{and} \quad P_{\parallel}(x,h) = \frac{1}{2}(P_{yy} + P_{zz}). \tag{30}$$

Mechanical equilibrium requires that the tangential pressure is independent of the y- and z-coordinates, but depends on the x-coordinate. The normal pressure is independent of all spatial coordinates.

We identify the thermodynamic integral normal pressure in terms of the volume integral of the normal mechanical pressure divided by the volume. However, since the normal mechanical pressure and the area are constant everywhere, this simplifies to

$$\hat{p}_{\perp}(h) \equiv \frac{1}{h}\int_0^h P_{\perp}(h)x = P_{\perp}(h). \tag{31}$$

The integral normal pressure in a large pore is equal to the pressure in a bulk phase in equilibrium with the pore. The difference in the integral normal pressure in a liquid and vapor phase in a slit pore is described the Young–Laplace equation, while the integral pressure is the same in both the liquid and vapor phase [23]. An alternative route to the integral normal pressure is via the local fluid number density profile [40]

$$P_{\perp}(h) = \int_0^h f_{fs}(x)\rho(x,h)x, \tag{32}$$

where $f_{fs}(x)$ is the fluid–solid force and $\rho(x,h)$ is the local fluid number density. The fluid density and fluid–solid forces are uniquely defined, and do not have the inherent problem that the mechanical pressure tensor has. We can use this equation to validate our method of calculating the integral normal pressure.

We identify further the integral surface tension as the integral of the normal minus tangential pressure tensor components,

$$\hat{\gamma}(h) \equiv \frac{1}{2}\int_0^h \Big(P_{\perp}(h) - P_{\parallel}(x;h)\Big)\mathrm{d}x, \tag{33}$$

where the factor half is due to the fact that there are two fluid–solid surfaces. It follows from Equation (7) together with Equations (31) and (33) that the integral pressure is,

$$\hat{p}(h) = \frac{1}{h}\int_0^h P_{\parallel}(x;h)\mathrm{d}x. \tag{34}$$

As shown by Harasima [35] and Schofield and Henderson [34] a sufficiently large volume integral of the mechanical pressure tensor components does not depend on the choice of the integral contour C_{ij}. We have identified the integral normal pressure, integral surface tension and integral pressure in terms of the mechanical pressure tensor. The local mechanical pressure tensor has an inherent problem, specifically that the contour C_{ij} can be any continuous line from i to j. However, the thermodynamic variables do not have this inherent problem. This is because we integrate the local mechanical pressure tensor across the whole volume V. This volume integral includes all interactions.

The internal energy can be calculated as the sum of the kinetic and potential energy,

$$U = E_k + E_p. \tag{35}$$

By dividing the internal energy in Equation (11) by the volume we obtain the internal energy density $u = U/V$. We also use the entropy density $s = S/V$, and fluid number density $\rho = N/V$. By rearranging the equation we obtain the entropy density as

$$s = \frac{1}{T}(u + \hat{p} - \mu\rho), \tag{36}$$

where the internal energy density, integral pressure and fluid number density are known. The volume, chemical potential and temperature are imposed on the system.

3. Simulation Details

The thermodynamic state of slit pores of varying heights h was investigated by using grand-canonical Monte Carlo (GCMC) [41] in combination with molecular dynamic (MD) simulations with the Nosé–Hoover thermostat [42]. This produced the grand canonical ensemble, i.e., constant chemical potential, temperature, volume and surface area. The GCMC method inserted and deleted fluid particles to and from the simulation box from an imaginary fluid particle reservoir at the same temperature and chemical potential. This controlled the chemical potential of the fluid in the slit pore. The MD procedure updated the positions and velocities of the fluid particles and controlled the temperature with the Nosé–Hoover thermostat.

The simulations were carried out using LAMMPS [43]. The local mechanical pressure tensor was calculated by post-processing the particle trajectories with in-house software (available at D.O.I. 10.5281/zenodo.4405267). The chemical potential and temperature were kept constant at $\mu^* = 1$ and $T^* = 2$. The critical temperature of the Lennard–Jones/spline fluid is $T_c^* = 0.885$ [44]. All units in this work are in reduced Lennard–Jones units, see Table 1 for a definition.

Table 1. The reduced units are denoted with an asterisk in superscript, for example T^*. The variables are reduced using the molecular diameter σ, potential well depth ϵ, fluid particle mass m and Boltzmann constant k_B.

Description	Definition
Energy	$E^* = E/\epsilon$
Entropy	$S^* = S/k_B$
Temperature	$T^* = Tk_B/\epsilon$
Distance	$x^* = x/\sigma$
Pressure	$p^* = p\sigma^3/\epsilon$
Chemical potential	$\mu^* = \mu/\epsilon$

The simulation box was a rectangular cuboid of side lengths $L_x, L_y = L_z$. The side lengths $L_y = L_z$ were chosen such that the surface area was large. Large in this context indicates large enough for $\hat{p}$, $\hat{p}_\perp$, $\hat{\gamma}$, $p_\perp$, and γ to be independent of the surface area $\Omega = L_y L_z$. The simulation box size was decided such that the average number of fluid particles was approximately 2×10^4. The simulation box was periodic in the y- and z-directions, and non-periodic in the x-direction. This implies that the particles did not interact across the simulation box boundary in the x-direction.

The fluid–fluid and fluid–solid interaction was modeled with the Lennard-Jones/spline potential [44]. The fluid–fluid and fluid–solid interactions were equal. The potential energy of a fluid–fluid or fluid–solid pair separated by a distance r was

$$u^{LJ/s}(r) = \begin{cases} 4\epsilon\left[\left(\frac{\sigma}{r}\right)^{12} - \left(\frac{\sigma}{r}\right)^{6}\right] & \text{if } r < r_s \\ a(r - r_c)^2 + b(r - r_c)^3 & \text{if } r_s < r < r_c \\ 0 & \text{else,} \end{cases} \tag{37}$$

where r_s, a, b and r_c were chosen such that the potential energy and the force were continuous at the inflection point $r = r_s$ and the cut-off $r = r_c$. The solid walls were placed

at the simulation box boundaries $x = -L_x/2$ and $x = L_x/2$. The distance between the fluid and solids were $r = |x_f - L_x/2|$ and $r = |x_f + L_x/2|$, where x_f is the x-position of the fluid particle.

The dividing surfaces of the fluid–solid surfaces were chosen to be at $x = -L_x/2$ and $x = L_x/2$. The slit pore height was consequently determined to be $h = L_x$. Other choices of the dividing surface are possible, for example, the Gibbs dividing surface or the surface of tension. When $L_x < 2r_c$ the fluid particle can interact with both solid walls. See Figure 1 for an visualization of the simulation box for the case $L_x = 4\sigma$.

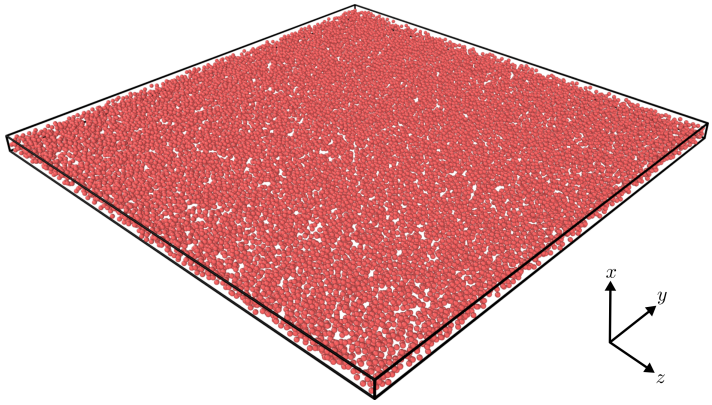

Figure 1. Visualization of the fluid particles in a slit pore of height $L_x = 4\sigma$, chemical potential $\mu^* = 1$, and temperature $T^* = 2$. The fluid particles are rendered in red, and their diameter is rendered at σ. The solid is not rendered. The solid lines illustrates the edges of the simulation box. The simulation was rendered with Open Visualization Tool (OVITO) [45].

The mechanical pressure tensor was calculated in thin rectangular cuboids, called layers l, of side lengths $\Delta x, L_y, L_z$. The thickness of the layers was $\Delta x = 0.005\sigma$ and the number of layers was $n_l = h/\Delta x$. The diagonal components of the mechanical pressure tensor was calculated using Equations (27)–(29).

The kinetic energy was calculated as the sum of the kinetic energy for each fluid particle and the potential energy was calculated as the sum of the potential energy of each fluid–fluid and fluid–solid pairs,

$$E_k = \frac{1}{2}\sum_{i=1}^{N} m_i(\mathbf{v}_i \cdot \mathbf{v}_i) \quad \text{and} \quad E_p = \sum_{i=1}^{N}\sum_{j>i}^{N} u^{LJ/s}(r_{ij}). \tag{38}$$

The sums of the kinetic and potential energies were used to calculate the internal energy and entropy densities.

4. Results and Discussion

The results are presented in Figures 2–10 and discussed in that order before general remarks are offered.

The normal mechanical pressure $P_\perp$ is presented in Figure 2a. It does not depend on the position x, but it depends strongly on the slit pore height h. The figure shows a straight line of various lengths for each of the three heights, which reflect the slit pore height h. The integral normal pressure was identified as this component, $\hat{p}_\perp = P_\perp$. We see that it is always constant, as demanded by Equation (31). For slit pore heights $h > 7\sigma$ we find that the normal mechanical pressure is equal to the bulk pressure. At $h = 2.04\sigma$ the normal mechanical pressure is at a global maximum and at $h = 2.59\sigma$ it has a local minimum for the given temperature and chemical potential. The normal mechanical pressures divided by the bulk pressure for the two cases are $P_\perp/p^\mathrm{b} = 2.5135 \pm 0.0008$ and $P_\perp/p^\mathrm{b} = 0.5539 \pm 0.0002$, respectively. The global minimum, which is zero, is at $h < 1.8\sigma$ when no fluid particles

fit in the slit pore. This is because solid–solid interactions and quantum effects are not considered in this work.

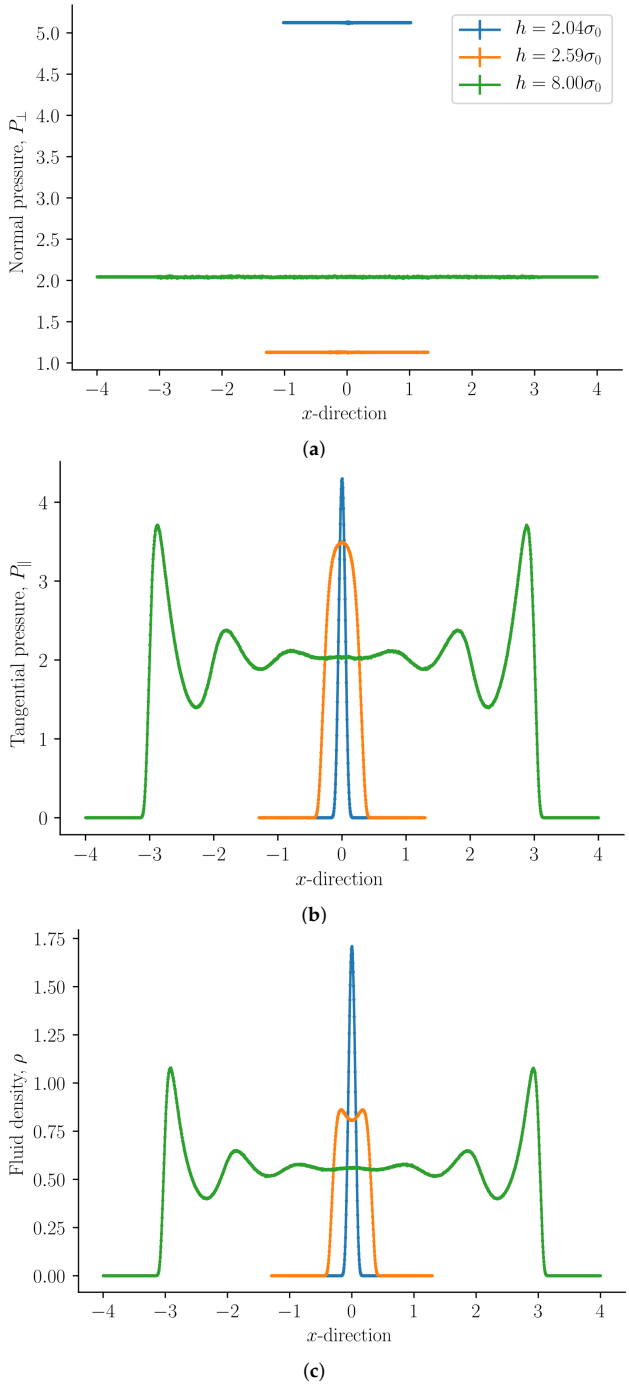

Figure 2. (**a**) Normal mechanical pressure, (**b**) tangential mechanical pressure, and (**c**) fluid number density ρ as a function of th e x-direction for slit pore heights $h = 2.04\sigma$, 2.59σ, and 8σ.

The tangential mechanical pressure $P_{\parallel}$, illustrated in Figure 2b, depends in contrast on the position x as well as on the slit pore height h. The integral pressure is the average of $P_{\parallel}$, see Equation (34). The tangential mechanical pressure follows the trend of the fluid number density, compare Figures 2b,c. For pore sizes $h > 7\sigma$ the tangential mechanical pressure is constant and equal to the bulk pressure p^{b} in the center of the pore. This indicates that the pore is large enough to accommodate bulk liquid in the center. The fluid is highly structured close to the fluid–solid surface [1]. As the slit pore height is decreased, fluid structures on the two sides overlap. When regions of structured fluids overlap, repulsive and attractive forces between the surfaces appear, and the disjoining pressure becomes non-zero.

The fluid number density $\rho = N/V$ is presented in Figure 3 as a function of the slit pore height h. The bulk fluid number density ρ^{b} in equilibrium with the slit pore is shown as a dashed line. The fluid number density converges to the bulk value as the slit pore height approaches infinity. The volume V depends on the choice of the fluid–solid dividing surfaces. We have chosen the dividing surfaces to be at $x = -L_x/2$ and $x = L_x/2$. The choice of the dividing surface determines how rapidly the slit pore values converge to the bulk values. A dividing surface closer to the fluid phase will reduce the volume and consequently the slit pore values will converge faster to the bulk values. Other choices of the dividing surface are possible.

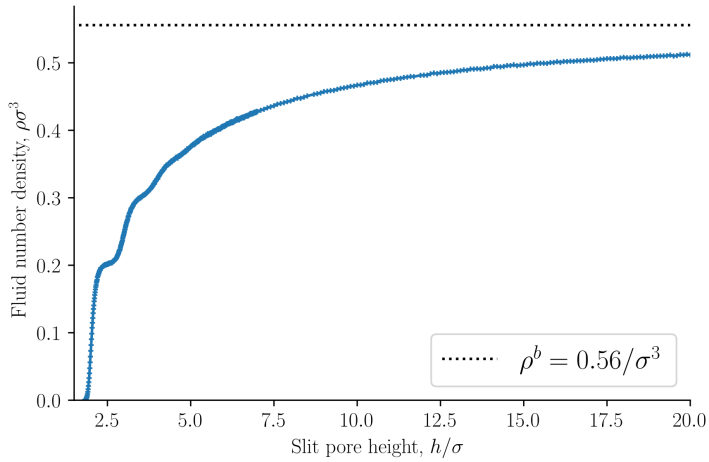

Figure 3. Fluid number density $\rho = N/V$ as a function of slit pore height h. The bulk fluid number density is shown as a dashed line.

The entropy density is presented in Figure 4 as a function of the slit pore height h. The entropy density is a monotonically increasing function of the height h. This confirms the observation by Israelachvili [1] that the origin of the oscillations of the disjoining pressure as a function of the height is not entropic. As a further confirmation of this point, we find that the internal energy density oscillates with a period equal to the particle diameter, see Figure 5. The oscillating forces or pressures are thus of energetic origin. The bulk entropy and internal energy densities are shown as dashed lines. The entropy and internal energy densities of the slit pore converge to the bulk values as the slit pore height is increased.

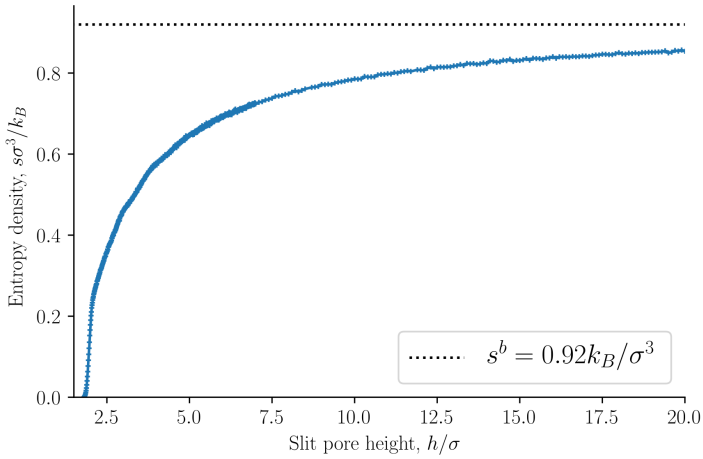

Figure 4. Entropy density $s = S/V$ as a function of slit pore height h. See Equation (36). The dashed line shows the entropy density of the bulk s^{b}.

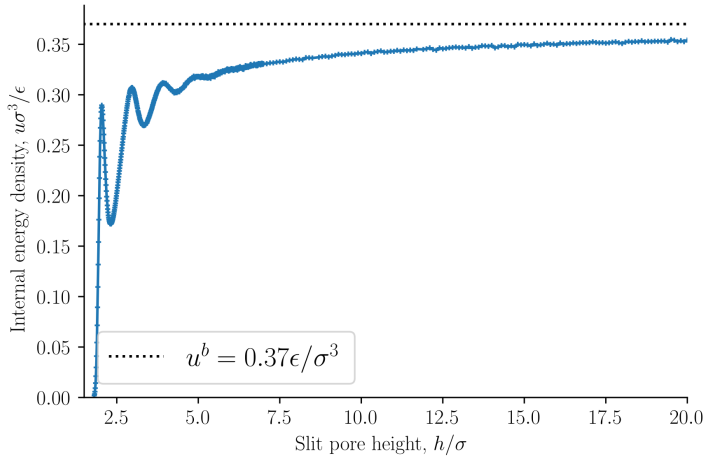

Figure 5. Internal energy density $u = U/V$ as a function of slit pore height h. See Equation (35). The dashed line shows the internal energy density of the bulk u^{b}.

The integral pressure is equal to the volume average tangential mechanical pressure $\hat{p} = h^{-1} \int_0^h P_{\parallel} \mathrm{d}x$. It is of special interest because it is equal to minus the grand potential divided by volume $\hat{p} = -X/V$, or the replica energy density. The grand potential is the starting point for the definition of the average thermodynamic properties of the REV [13]. The integral pressure is presented in Figure 6 as a function of the slit pore height h. The integral pressure converges to the bulk pressure p^{b} as the slit pore height approaches infinity, as expected. The bulk pressure is shown as a dashed line.

In previous works [13,14,21] we argued that the gradient of the integral pressure is the driving force for mass flux. In another work [23] we found the integral pressure of a two-phase system in a slit pore to be equal in the liquid and vapor in equilibrium. The identification of the integral pressure in this work is consistent with this interpretation. The gradient of the integral pressure is the driving force of the mass flux. For fluid flows tangential to the slit pore surfaces it is the gradient in the tangential mechanical pressure tensor component that gives the driving force when the system is out of equilibrium. In this work we identify the integral pressure as the average of the tangential mechanical pressure tensor components.

As stated in Section 2.2, the integral and differential normal pressures and integral and differential surface tensions are expected to be equal when the surface area is large. If this is correct, the integral pressure can be computed as

$$\hat{p}(h) = \frac{1}{h}\int_{h_0}^{h} \hat{p}_\perp h' \quad = \int_{h_0}^{h} \frac{2\hat{\gamma}}{h'^2} h'. \tag{39}$$

The lower integration limit is $h_0 = 1.8\sigma$, at which point the integral pressure is in good approximation zero. The integral pressure computed from Equation (39) is shown in Figure 6. The curves are identical. This implies that the integral and differential normal pressures are equal. As we have already shown that the subdivision potential is zero $\varepsilon = 0$ for large surface areas with this set of control variables, it follows that the integral and differential surface tensions are also equal. We will from now on refer to the integral normal pressure and integral surface tensions as the normal pressure and surface tension.

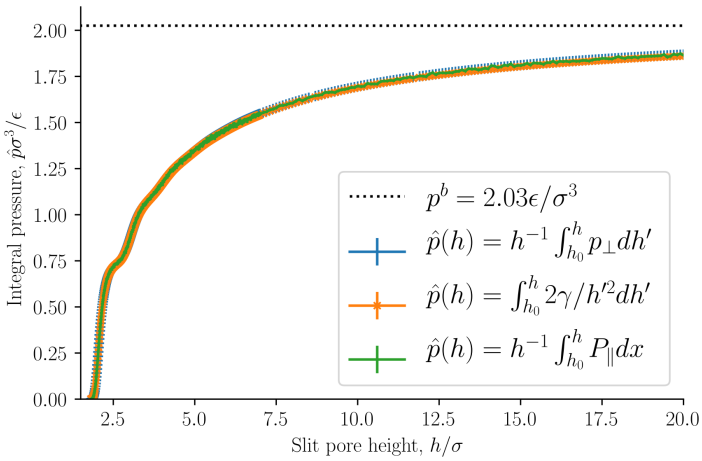

Figure 6. Integral pressure $\hat{p}$ as a function of slit pore height h. The integral pressure is computed as the average tangential mechanical pressure, see Equation (34), and from the normal pressure and surface tension, see Equation (39).

The normal pressure was identified as the normal mechanical pressure $p_\perp = P_\perp$ in Equation (31). It is presented in Figure 7 as a function of the slit pore height h. The normal pressure was also calculated from the local fluid density and the fluid–solid force using Equation (32). The two methods of calculating the normal pressure agree, which indicates that we have calculated the mechanical pressure tensor correctly.

The normal pressure oscillates with a period equal to the fluid particle diameter at small heights h. The oscillations decay as the height h increases. Such oscillations have been observed in experiments and are well known, see for example Israelachvili [1]. The oscillations are caused by the structuring of the fluid particles between the surfaces, and by the fact that the fluid particles all have the same diameter. As the height is increased above $h > 7\sigma$ the oscillations vanish and the normal pressure is constant and equal to the bulk pressure. The bulk pressure is shown as a dashed line in the figure. At heights $h > 7\sigma$ the fluid structuring near the walls do not overlap. At lower densities, smaller oscillations are expected with a faster decay. The normal pressure shows a similar trend to previous works [15,16,40]. At very small heights, the solid–solid interaction will dominate and completely overshadow the fluid-fluid and fluid–solid interactions presented here. We have not included any solid–solid interaction in this work, and as a consequence the normal pressure approaches zero because there is no room for any fluid particles to enter the slit pore.

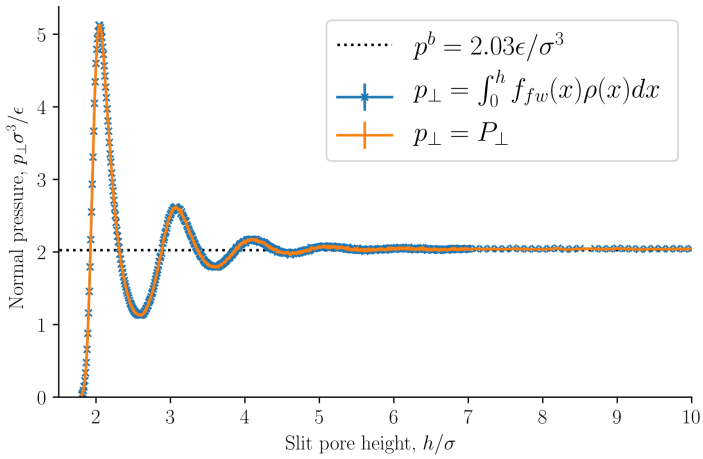

Figure 7. Normal pressure $p_\perp = P_\perp$ as a function of slit pore height h. It is computed as the normal mechanical pressure tensor component, see Equation (31), and as the integral of the fluid–solid force times the local fluid density, see Equation (32).

When $p_\perp = \hat{p}_\perp$ and $\varepsilon = 0$, it follows from Equation (8) that the integral and differential surface tensions are equal $\gamma = \hat{\gamma}$. The surface tension as a function of the slit pore height is presented in Figure 8, see Equation (33). The surface tension at infinite separation γ^∞ is computed as the average surface tension of the slit pore, with height $h > 10\sigma$, at which point the surface tension is independent of h.

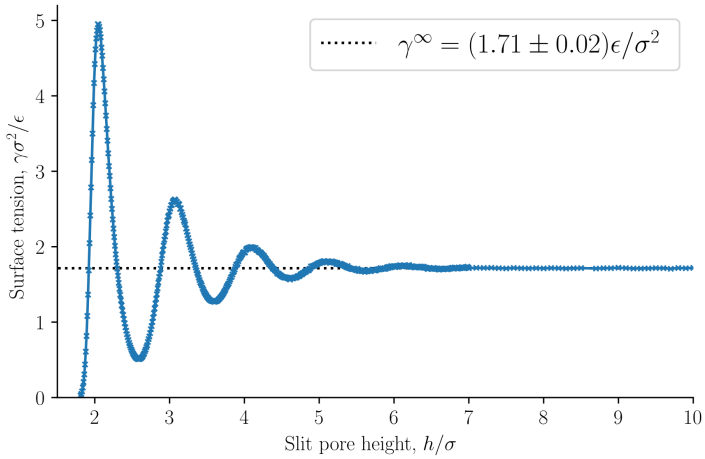

Figure 8. Surface tension γ as a function of slit pore height h, see Equation (33). The dashed line shows the surface tension at infinite separation γ^∞.

The disjoining pressure Π was computed from Equation (25), and is shown as a function of the slit pore height h in Figure 9. The disjoining pressure was here defined to be equal to the integral normal pressure minus the normal pressure at infinite separation. Because the integral and the differential normal pressures are the same and because the normal pressure at infinite separation is equal to the bulk pressure, in this case, the definition contain the commonly used definition of the disjoining pressure [7,29]. The normal pressure is constant for slit pore heights $h > 7\sigma$. Consequently, the normal pressure at infinite separation can be calculated as the normal pressure when $h > 7\sigma$. The normal pres-

sure at infinite separation is equal to the pressure in a bulk fluid with the same temperature and chemical potential.

For the present case, we can claim that our definition of the disjoining pressure is equivalent to the common definition. Our definition is general, as it also covers the cases where the integral and the differential normal pressures are unequal. Examples where this is the case are given below.

Figure 10 shows how the normal pressure minus the integral pressure scales with inverse slit pore height. It is equal to the scaling law presented in a previous work [23]. The slope of this ideal curve is equal to two times the surface tension. When the inverse slit pore height approaches zero, i.e., when the walls are far apart, the normal pressure and integral pressures are equal as predicted. For pores that are so small that no bulk fluid can form in the center, the structuring at the walls starts to overlap, and a fluctuating difference is seen in the difference of the normal and integral pressures. In the region of the straight line, we have a scaling law, that relates states of different heights. At heights smaller than approximately $h < 5\sigma$ the scaling law breaks down, the difference of the two pressures starts to oscillate. There are positive and negative deviations from the law.

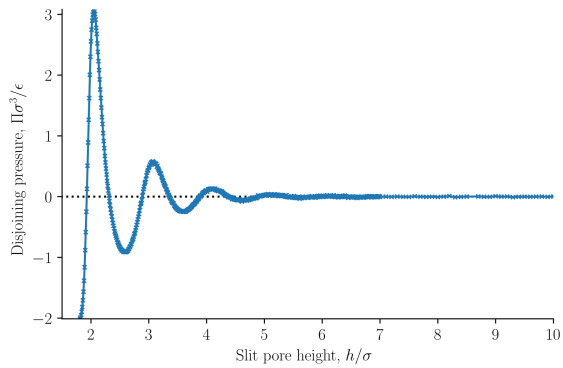

Figure 9. Disjoining pressure as a function the slit pore height h, see Equation (25).

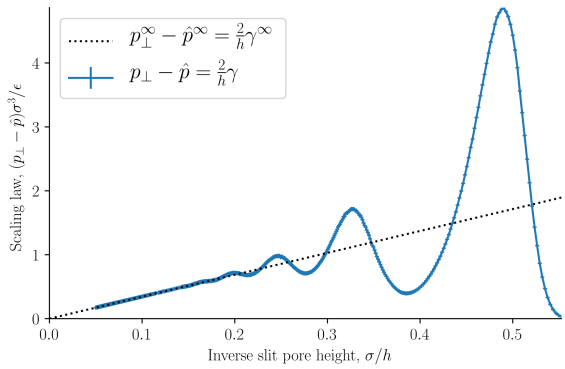

Figure 10. The scaling of normal pressure minus integral pressure as a function of the inverse slit pore height h.

In our earlier work [23], we studied liquid-vapor coexistence in a slit pore. In that work the surface area was not a control variable, and as a consequence the subdivision potential was found to be equal to two times the surface tension divided by the slit pore height, see Figure 10. Another reasonable set of control variables is the height h instead of

the volume V. For a control variable set consisting of temperature, height, surface area and chemical potential, the differential normal pressure is equal to

$$p_\perp = \frac{1}{\Omega}\left(\frac{\partial(\hat{p}V)}{\partial h}\right)_{T,\Omega,\mu} = \hat{p} + h\left(\frac{\partial \hat{p}}{\partial h}\right)_{T,\Omega,\mu}. \tag{40}$$

The differential surface tensions is

$$\gamma = -\frac{1}{2}\left(\frac{\partial(\hat{p}V)}{\partial \Omega}\right)_{T,\mu,h} = -\frac{\hat{p}h}{2} - \frac{V}{2}\left(\frac{\partial \hat{p}}{\partial \Omega}\right)_{T,\mu,h}. \tag{41}$$

For this set of control variables, the height h is kept constant instead of the volume V. The subdivision potential is accordingly

$$\begin{aligned} \varepsilon &= -\hat{p}V + p_\perp V + 2\gamma\Omega \\ &= \hat{p}V + hV\left(\frac{\partial \hat{p}}{\partial h}\right)_{T,\Omega,\mu} + \Omega V\left(\frac{\partial \hat{p}}{\partial \Omega}\right)_{T,h,\mu}. \end{aligned} \tag{42}$$

These relations also help us characterize the smallness of the slit pore with the large walls. The subdivision potential, introduced by Hill as a measure of smallness, deviates from zero in the last relation, also when the integral pressure does not depend on the size of the area, with height h and surface area Ω as control variables. A dependency on the area is relevant when adsorption takes place on small spheres [24]. A slit pore with large walls may be expected to be small for small heights h, since the confined fluid is not bulk-like. However, we have seen that when we use volume V and surface area Ω as control variables, the subdivision potential is zero for large surface areas. A zero subdivision potential means that the system also can be described perfectly using regular thermodynamics [18]. It is nevertheless meaningful to define a non-zero integral pressure, because the integral pressure enters the grand potential. It, therefore, determines the thermodynamic properties of a REV. Away from equilibrium, it will create a driving force.

The grand potential or minus the integral pressure times the volume are equal to the replica energy. The replica energy is not zero in the present case. Clearly, we have here an example where smallness is brought out in Hill's terms through the replica potential.

5. Conclusions

We have developed a nanothermodynamic description based on the ideas of Hill to describe single-phase and single-component fluids in slit pores in a new manner. As environmental control variables we chose the chemical potential, temperature, volume and surface area. We have seen that the outcome varies with the set chosen, but the procedure can be used for complex geometries and different sets.

Following Hill, we introduced the subdivision potential. It is non-zero only when the integral pressure depends on the surface area Ω. For large surface areas we have shown that the subdivision potential is zero, and that $p_\perp = \hat{p}_\perp$ and $\gamma = \hat{\gamma}$. In this sense, we have found that nanothermodynamics is equivalent to the usual thermodynamic description for all heights. The replica energy, and therefore the integral pressure, were shown to be non-zero. This allowed us to identify a scaling law, which confirms earlier results [22,23]. By choosing height h rather than volume V among the control variables, a non-zero subdivision potential appears.

We have identified the thermodynamic properties by their mechanical counterparts in a consistent manner. The integral pressure, which is equal to minus the grand potential divided by volume, can be understood as the average tangential mechanical pressure. The normal pressure is the normal mechanical pressure, and the surface tension is the integral of the normal minus the tangential mechanical pressure. The entropy and internal energy densities vary with the slit pore height, confirming the observations of Israelachvili [1]. The entropy density increases monotonically with increasing height, while

the energy density oscillates. This confirms that the disjoining pressure is not of entropic origin, it is of energetic origin [1].

By these investigations of the nanothermodynamic theory and the subsequent simulations, we hope to have expanded on the knowledge on Hill's method, making it more available for further studies, for instance of flow and reactions in porous media.

Author Contributions: O.G. contributed to investigation, methodology, software and visualization. D.B. and S.K. contributed to supervision. All authors contributed to conceptualization, formal analysis, writing original draft, reviewing and editing. All authors have read and agreed to the published version of the manuscript.

Funding: We are grateful to the Research Council of Norway for funding through its Center of Excellence funding scheme, project number 262644, PoreLab.

Institutional Review Board Statement: Not applicable.

Data Availability Statement: The data set is available at D.O.I. 10.5281/zenodo.4405271.

Acknowledgments: The computations were performed on resources provided by UNINETT Sigma2—the National Infrastructure for High Performance Computing and Data Storage in Norway.

Conflicts of Interest: The authors declare no conflict of interest.

References

1. Israelachvili, J.N. *Intermolecular and Surface Forces*; Academic Press: Cambridge, MA, USA, 1985.
2. McDonald, T.M.; Mason, J.A.; Kong, X.; Bloch, E.D.; Gygi, D.; Dani, A.; Crocella, V.; Giordanino, F.; Odoh, S.O.; Drisdell, W.S.; et al. Cooperative insertion of CO_2 in diamine-appended metal-organic frameworks. *Nature* **2015**, *519*, 303–308. [CrossRef] [PubMed]
3. Vlugt, T.; Krishna, R.; Smit, B. Molecular simulations of adsorption isotherms for linear and branched alkanes and their mixtures in silicalite. *J. Phys. Chem. B* **1999**, *103*, 1102–1118. [CrossRef]
4. Bresme, F.; Oettel, M. Nanoparticles at fluid interfaces. *J. Phys. Condens. Matter* **2007**, *19*, 413101. [CrossRef] [PubMed]
5. Bresme, F.; Lehle, H.; Oettel, M. Solvent-mediated interactions between nanoparticles at fluid interfaces. *J. Chem. Phys.* **2009**, *130*, 214711. [CrossRef]
6. Galteland, O.; Bresme, F.; Hafskjold, B. Solvent-Mediated Forces between Ellipsoidal Nanoparticles Adsorbed at Liquid–Vapor Interfaces. *Langmuir* **2020**, *36*, 48. [CrossRef]
7. Derjaguin, B. Untersuchungen über die Reibung und Adhäsion, IV. *Kolloid Z.* **1934**, *69*, 155–164. [CrossRef]
8. Moura, M.; Flekkøy, E.G.; Måløy, K.J.; Schäfer, G.; Toussaint, R. Connectivity enhancement due to film flow in porous media. *Phys. Rev. Fluids* **2019**, *4*, 094102. [CrossRef]
9. Das, D.; Hassanizadeh, S. *Upscaling Multiphase Flow in Porous Media*; Springer: Berlin, Germany, 2005.
10. Khanamiri, H.H.; Berg, C.F.; Slotte, P.A.; Schlüter, S.; Torsæter, O. Description of Free Energy for Immiscible Two-Fluid Flow in Porous Media by Integral Geometry and Thermodynamics. *Water Resour. Res.* **2018**, *54*, 9045–9059. [CrossRef]
11. Armstrong, R.T.; McClure, J.E.; Robins, V.; Liu, Z.; Arns, C.H.; Schlüter, S.; Berg, S. Porous media characterization using minkowski functionals: Theories, applications and future directions. *Transp. Porous Med.* **2019**, *130*, 305–335. [CrossRef]
12. Slotte, P.A.; Berg, C.F.; Khanamiri, H.H. Predicting Resistivity and Permeability of Porous Media Using Minkowski Functionals. *Transp. Porous Med.* **2020**, *131*, 705–722. [CrossRef]
13. Kjelstrup, S.; Bedeaux, D.; Hansen, A.; Hafskjold, B.; Galteland, O. Non-isothermal transport of multi-phase fluids in porous media. the entropy production. *Front. Phys.* **2018**, *6*, 126. [CrossRef]
14. Kjelstrup, S.; Bedeaux, D.; Hansen, A.; Hafskjold, B.; Galteland, O. Non-isothermal transport of multi-phase fluids in porous media. Constitutive equations. *Front. Phys.* **2019**, *6*, 150. [CrossRef]
15. Balbuena, P.B.; Berry, D.; Gubbins, K.E. Solvation pressures for simple fluids in micropores. *J. Phys. Chem.* **1993**, *97*, 937–943. [CrossRef]
16. Gubbins, K.E.; Long, Y.; Śliwinska-Bartkowiak, M. Thermodynamics of confined nano-phases. *J. Chem. Thermodyn.* **2014**, *74*, 169–183. [CrossRef]
17. Bedeaux, D.; Kjelstrup, S. Hill's nano-thermodynamics is equivalent with Gibbs' thermodynamics for surfaces of constant curvatures. *Chem. Phys. Lett.* **2018**, *707*, 40–43. [CrossRef]
18. Gjennestad, M.A.; Wilhelmsen, Ø. Thermodynamic stability of volatile droplets and thin films governed by the disjoining pressure in open and closed containers. *Langmuir* **2020**, *36*, 27. [CrossRef]
19. Gjennestad, M.A.; Wilhelmsen, Ø. Thermodynamic stability of droplets, bubbles and thick films in open and closed pores. *Fluid Phase Equilibr.* **2020**, *505*, 112351. [CrossRef]
20. Strøm, B.A.; Simon, J.M.; Schnell, S.K.; Kjelstrup, S.; He, J.; Bedeaux, D. Size and shape effects on the thermodynamic properties of nanoscale volumes of water. *Phys. Chem. Chem. Phys.* **2017**, *19*, 9016–9027. [CrossRef]

21. Galteland, O.; Bedeaux, D.; Hafskjold, B.; Kjelstrup, S. Pressures inside a nano-porous medium. The case of a single phase fluid. *Front. Phys.* **2019**, *7*, 60. [CrossRef]
22. Erdős, M.; Galteland, O.; Bedeaux, D.; Kjelstrup, S.; Moultos, O.A.; Vlugt, T.J. Gibbs Ensemble Monte Carlo Simulation of Fluids in Confinement: Relation between the Differential and Integral Pressures. *Nanomaterials* **2020**, *10*, 293. [CrossRef]
23. Rauter, M.T.; Galteland, O.; Erdős, M.; Moultos, O.A.; Vlugt, T.J.; Schnell, S.K.; Bedeaux, D.; Kjelstrup, S. Two-Phase Equilibrium Conditions in Nanopores. *Nanomaterials* **2020**, *10*, 608. [CrossRef] [PubMed]
24. Strøm, B.A.; He, J.; Bedeaux, D.; Kjelstrup, S. When Thermodynamic Properties of Adsorbed Films Depend on Size: Fundamental Theory and Case Study. *Nanomaterials* **2020**, *10*, 1691. [CrossRef] [PubMed]
25. Bedeaux, D.; Kjelstrup, S.; Schnell, S.K. *Nanothermodynamics. General Theory*; NTNU: Trondheim, Norway, 2020.
26. Hill, T.L. *Thermodynamics of Small Systems - Two Volumes Bound as One*; Dover: New York, NY, USA, 1964.
27. Hill, T.L.; Chamberlin, R.V. Extension of the thermodynamics of small systems to open metastable states: An example. *Proc. Natl. Acad. Sci. USA* **1998**, *95*, 12779–12782. [CrossRef] [PubMed]
28. Hill, T.L.; Chamberlin, R.V. Fluctuations in energy in completely open small systems. *Nano Lett.* **2002**, *2*, 609–613. [CrossRef]
29. Hansen, J.P.; McDonald, I.R. *Theory of Simple Liquids*; Elsevier: Amsterdam, The Netherlands, 1990.
30. Radke, C. Film and membrane-model thermodynamics of free thin liquid films. *J. Colloid Interf. Sci.* **2015**, *449*, 462–479. [CrossRef]
31. Long, Y.; Palmer, J.C.; Coasne, B.; Śliwinska-Bartkowiak, M.; Gubbins, K.E. Pressure enhancement in carbon nanopores: A major confinement effect. *Phys. Chem. Chem. Phys.* **2011**, *13*, 17163–17170. [CrossRef]
32. van Dijk, D. Comment on "Pressure enhancement in carbon nanopores: A major confinement effect" by Y. Long, J. C. Palmer, B. Coasne, M. Sliwinska-Bartkowiak and K. E. Gubbins, Phys. Chem. Chem. Phys., 2011, 13, 17163. *Phys. Chem. Chem. Phys.* **2020**, *22*, 9824–9825. [CrossRef]
33. Long, Y.; Palmer, J.C.; Coasne, B.; Shi, K.; Śliwińska-Bartkowiak, M.; Gubbins, K.E. Reply to the 'Comment on "Pressure enhancement in carbon nanopores: A major confinement effect"'by D. van Dijk, Phys. Chem. Chem. Phys., 2020, 22. *Phys. Chem. Chem. Phys.* **2020**, *22*, 9826–9830. [CrossRef]
34. Schofield, P.; Henderson, J.R. Statistical mechanics of inhomogeneous fluids. *Proc. R. Soc. Lon. Ser. A* **1982**, *379*, 231–246.
35. Harasima, A. Molecular theory of surface tension. *Adv. Chem. Phys.* **1958**, *1*, 203–237.
36. Irving, J.; Kirkwood, J.G. The statistical mechanical theory of transport processes. IV. The equations of hydrodynamics. *J. Chem. Phys.* **1950**, *18*, 817–829. [CrossRef]
37. Hafskjold, B.; Ikeshoji, T. Microscopic pressure tensor for hard-sphere fluids. *Phys. Rev. E* **2002**, *66*, 011203. [CrossRef] [PubMed]
38. Shi, K.; Shen, Y.; Santiso, E.E.; Gubbins, K.E. Microscopic pressure tensor in cylindrical geometry: Pressure of water in a carbon nanotube. *J. Chem. Theory Comput.* **2020**, *16*, 5548–5561. [CrossRef] [PubMed]
39. Ikeshoji, T.; Hafskjold, B.; Furuholt, H. Molecular-level calculation scheme for pressure in inhomogeneous systems of flat and spherical layers. *Mol. Simulat.* **2003**, *29*, 101–109. [CrossRef]
40. Evans, R.; Marini Bettolo Marconi, U. Phase equilibria and solvation forces for fluids confined between parallel walls. *J. Chem. Phys.* **1987**, *86*, 7138–7148. [CrossRef]
41. Frenkel, D.; Smit, B. *Understanding Molecular Simulation: From Algorithms to Applications*; Elsevier: Amsterdam, The Netherlands, 2001; Volume 1.
42. Shinoda, W.; Shiga, M.; Mikami, M. Rapid estimation of elastic constants by molecular dynamics simulation under constant stress. *Phys. Rev. B* **2004**, *69*, 134103. [CrossRef]
43. Plimpton, S. Fast parallel algorithms for short-range molecular dynamics. *J. Comput. Phys.* **1995**, *117*, 1–19. [CrossRef]
44. Hafskjold, B.; Travis, K.P.; Hass, A.B.; Hammer, M.; Aasen, A.; Wilhelmsen, Ø. Thermodynamic properties of the 3D Lennard-Jones/spline model. *Mol. Phys.* **2019**, *117*, 3754–3769. [CrossRef]
45. Stukowski, A. Visualization and analysis of atomistic simulation data with OVITO–the Open Visualization Tool. *Model. Simul. Mater. Sci.* **2009**, *18*, 015012. [CrossRef]

Article VII

Olav Galteland, Eivind Bering, Kim Kristiansen, Dick Bedeaux, Signe Kjelstrup

Legendre-Fenchel Transforms Capture Layering Transitions in Porous Media

Submitted 2021
DOI: 10.48550/arXiv:2111.15253

Article VII

Article VII

Legendre-Fenchel transforms capture layering transitions in porous media

Olav Galteland[1], Eivind Bering[2], Kim Kristiansen[1], Dick Bedeaux[1], and Signe Kjelstrup[1]

[1]PoreLab, Department of Chemistry, Norwegian University of Science and Technology
[2]PoreLab, Department of Physics, Norwegian University of Science and Technology

December 1, 2021

Abstract

We have investigated the state of a nanoconfined fluid in a slit pore in the canonical and isobaric ensembles. The systems were simulated with molecular dynamics simulations. The fluid has a transition to a close-packed structure when the height of the slit approaches the particle diameter. The Helmholtz energy is a non-convex function of the slit height if the number of particles does not exceed that of one monolayer. As a consequence, the Legendre transform cannot be applied to obtain the Gibbs energy. The Gibbs energy of a non-deformable slit pore can be transformed into the Helmholtz energy of a deformable slit pore using the Legendre-Fenchel transform. The Legendre-Fenchel transform corresponds to the Maxwell construction of equal areas.

1 Introduction

Over the last years, there has been an increasing number of observations of phase transitions in confined fluids. Fluids can for instance change their critical temperature by several tens of degrees [1, 2], a two-dimensional layer at an interface may develop more than one structure [3], and adsorption to droplets may depend largely on droplet size [4, 5]. Classical Gibbs thermodynamics ceases to exist on the nanoscale. The need for the inclusion of shape and size has been met in several ways. Gibbs and followers included curvature as a variable [6] to deal with droplet size dependence. Not only size and shape will matter for the outcome of the analysis of simulations; the thermodynamic properties will also depend on the small system's environment or the set of variables that control the system (the ensemble) according to Hill [7, 8]. Dong [9] argued that thermodynamic variables, like the surface tension, change as we shrink the small system, and proposed to add as variable the integral surface tension, to complement the normal (differential) surface tension. The pressure of fluids in porous media is of special interest as its gradient is the main driving force for mass transport [10, 11].

A systematic way to address these problems was given by Hill [7, 8] already 50 years ago. We have argued that the problems are best addressed by his method [12, 13, 14, 3], because the method provides a general description of small systems. We have for instance been able to write scaling laws for small system variables [15], and a new equilibrium criterion for pressure was developed for two-phase equilibria in slit pores [15]. Hill's method is therefore our first choice when the aim is to learn more about structural transitions in confined fluids or how variables change. We shall find here that a transforming procedure exists in terms of the Legendre-Fenchel transform. This is a more general transform than the Legendre transform and can be used for large as well as small systems. It will enable us to compute the Gibbs energy from the Helmholtz energy and vice versa.

We have recently reported the changes in free energy during polymer stretching. The free energy depends on the conditions used, whether the polymer is stretched at controlled length or force [16, 17]. For sufficiently short polymers, the Helmholtz energy is a non-convex function of the controlled length of the polymer. A convex function has a non-negative second derivative everywhere. To transform from the Helmholtz to the Gibbs energy the Legendre-Fenchel transform could be applied. Similarly, we observed that the grand potential of a fluid in a slit pore is a non-convex function of the distance between the parallel plates at constant chemical potential and temperature [3]. Also, the Helmholtz energy of solid colloids in solution is non-convex as a function of the controlled distance between the colloids, keeping the temperature, volume, and the number of particles constant [18]. Both cases can be explained by a disjoining pressure (also known as the solvation pressure) [19], which is the excess normal pressure relative to the bulk pressure due to the packing of fluid particles between the solids. The observations mentioned all stem from size effects. To obtain the free energy of the corresponding constant pressure ensemble the Legendre-Fenchel transform must be applied, and not the Legendre transform.

The three pillars that science progresses from are theory, experiments, and simulations. The theory part is lacking in nanotechnology. Energy converting devices are abundant, but there is little available general theory of energy conversion for the nanoscale. The laws of energy conversion are the laws of thermodynamics, and the question we are asking is which form these take. Nanothermodynamics has been constructed, mostly by adding terms to Gibbs's classical formulation for large-scale systems. While this mending

procedure may serve the purpose in some special cases, it does not present us with a systematic procedure to be used as a general tool. Here we argue that the theory of Hill presented more than 50 years ago, presents an underused opportunity for a systematic procedure. To show the advantage of this approach, we study a transition between two structural regimes in a molecular fluid in a porous media model and document the applicability of an important tool, namely the Legendre-Fenchel transform.

Several problems arise for systems dependent on size and shape. To which extent can we still use the thermodynamic tools on nanoscale systems that apply to macroscale systems? When additional independent variables are needed in the Gibbs equation, from which pool do we draw them and how?

The free energies of a molecular fluid in a slit pore will be investigated at two conditions; at constant volume and constant normal pressure. In the first case, the system is in the canonical ensemble, and in the second case, the system is in the isobaric ensemble. In the thermodynamic limit, where the free energy is convex, we can transform the free energy from one ensemble to another using the Legendre transform. For small systems, this is not always the case. However, in the case of polymer stretching, we have recently found that the Legendre-Fenchel transform can be used [17]. This experience has led us to wonder whether Legendre-Fenchel transforms can be used also for fluids confined to the slit pore, thereby motivating this paper. In the isochoric ensemble, the volume of the slit pore is controlled, and we will consider this as a simple model of a non-deformable porous medium. In the isobaric ensemble, the pore normal pressure is controlled, and the pore volume can fluctuate. We will consider this as a simple model of a deformable porous medium.

The paper is outlined as follows. We give the theoretical background in section 2, including the Legendre-Fenchel transform in section 2.1. We proceed to present the simulation technique in section 3 and show in section 4, that the Helmholtz energy of an isochoric slit pore can be transformed into the Gibbs energy of an isobaric slit pore using the Legendre-Fenchel transform. The findings are discussed and perspectives are pointed out. In short, we shall see that systems that are small in Hill's sense have additional transitions than the bulk systems have. The system is more restricted when we control the fluid height than when we control the normal pressure.

1.1 System description.

We investigate a single-phase fluid in a slit pore. This can be seen as a simple model suited to bring out the features described above. The system consists of a fluid placed between two parallel solid walls, see Fig. 1. The system has periodic boundary conditions in the y- and z-directions. In the canonical ensemble, the walls do not move, while in the isobaric ensemble, the top wall can move in the x-direction and will act as a piston with controlled normal pressure on the fluid.

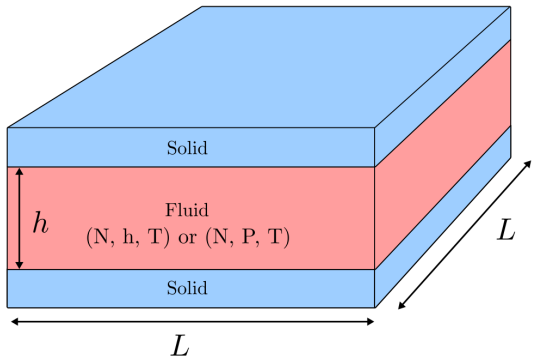

Figure 1: The fluid is placed between two parallel solid walls. The walls are separated by a distance h (height) and the side lengths of the walls are L. In the canonical ensemble the height h is controlled and the normal pressure P fluctuates, while in the isobaric ensemble the normal pressure P is controlled and the height h fluctuates.

In the canonical ensemble the volume of the system is controlled, and the normal pressure P fluctuates. In the isobaric ensemble, the normal pressure P is controlled, and the volume $V = L^2h = Ah$ fluctuates, where $A = L^2$ is the fluid-solid surface area of one of the walls. The side lengths in the y- and z-directions are fixed equal to L, and it is only the distance between the walls h (height) that fluctuates. The side lengths L are much larger than the height such that the system may be considered to be independent of the surface area A.

2 Theory

In the canonical ensemble, the Helmholtz energy describes the maximum obtainable work of the system. The total differential of the Helmholtz energy is

$$\mathrm{d}F(N,h,T) = -S\mathrm{d}T - PA\mathrm{d}h + \mu\mathrm{d}N, \tag{1}$$

where N is the number of fluid particles, T is the temperature, S is the entropy, P is the normal pressure, A is the fluid-solid surface area, and μ is the chemical potential. In the isobaric ensemble, it is the Gibbs energy that describes the maximum obtainable work of the system. The total differential of the Gibbs energy is

$$\mathrm{d}G(N,P,T) = -S\mathrm{d}T + Ah\mathrm{d}P + \mu\mathrm{d}N. \tag{2}$$

The normal pressure and height are defined in terms of the free energies as

$$P \equiv -\frac{1}{A}\left(\frac{\partial F}{\partial h}\right)_{T,N} \quad \text{and} \quad h \equiv \frac{1}{A}\left(\frac{\partial G}{\partial P}\right)_{T,N}. \tag{3}$$

The difference in the specific Helmholtz energy $\Delta f = F/M$, where M is the total mass of the fluid, is calculated by integrating the mean normal pressure as a function of the volume in the canonical ensemble

$$\Delta f = f(N,h,T) - f(N,h_0,T) = -\frac{A}{M}\int_{h_0}^{h}\langle P\rangle \mathrm{d}h', \quad (4)$$

where $\langle P\rangle$ is the mean normal pressure. Similarly, the difference in the specific Gibbs energy $\Delta g = G/M$ is calculated by integrating the mean height as a function of the normal pressure in the isobaric ensemble

$$\Delta g = g(N,P,T) - g(N,P_0,T) = \frac{A}{M}\int_{P}^{P_0}\langle h\rangle \mathrm{d}P', \quad (5)$$

where $\langle h\rangle$ is the mean height, and $f_0 = f(N,h_0,T)$ and $g_0 = g(N,P_0,T)$ are reference states at a large height h_0 and low pressure P_0. The difference in the specific entropy of the system in the isochoric ensemble is

$$\Delta s = \frac{1}{T}(\Delta u - \Delta f), \quad (6)$$

where Δu is the change in the specific internal energy of the system. The changes in specific entropy and internal energy are relative to a system at height h_0.

2.1 The Legendre-Fenchel transform.

In the isobaric ensemble, the control variables are temperature T, normal pressure P, and the number of fluid particles N. The normal pressure is equal to the absolute force acting on the walls divided by the surface area A. This is equal to the normal component of the mechanical pressure tensor of the fluid [3]. The isobaric partition function can be obtained by a Laplace transform of the canonical partition function

$$\mathcal{Z}(N,P,T) = \beta PA\int_0^\infty Z(N,h,T)\exp(-\beta PAh)\mathrm{d}h, \quad (7)$$

where $Z(N,h,T)$ is the canonical partition function and $\beta = (k_\mathrm{B}T)^{-1}$ where k_B is the Boltzmann constant. The Helmholtz and Gibbs energies are given by the corresponding partition functions

$$F(N,h,T) = -k_\mathrm{B}T\ln Z(N,h,T) \quad (8)$$

and

$$G(N,P,T) = -k_\mathrm{B}T\ln \mathcal{Z}(N,P,T), \quad (9)$$

respectively. From the three equations above it follows that the Gibbs energy can be obtained from the Helmholtz energy,

$$\exp[-\beta G(N,P,T)] = \beta PA\int_0^\infty \exp[-\beta(F(N,h,T)+PAh)]\mathrm{d}h. \quad (10)$$

For sufficiently high surface number densities $\Gamma = N/A$, the system is large and the Helmholtz energy F is a differentiable and convex function of the height, and the above expression reduces to the Legendre transform of the Helmholtz energy to the Gibbs energy,

$$G_\mathrm{L}(N,P,T) = G(N,h,T) + PhA. \quad (11)$$

For low surface number densities Γ, the system is small, and the Helmholtz energy is non-convex and the integral in equation 10 does not reduce to the Legendre transform. If the distribution of the normal pressure is sharply peaked it can however be calculated with a saddlepoint approximation [17, 20, 21],

$$G_\mathrm{LF}(N,P,T) = \min_h(F(N,h,T) + PhA). \quad (12)$$

This is the Legendre-Fenchel (LF) transform of the Helmholtz energy F to the Gibbs energy G_LF. The LF transform returns only convex functions. If we apply it again,

$$F^{**} = \max_p(G_\mathrm{LF} + PhA) = G_\mathrm{LF} + PhA, \quad (13)$$

we obtain the convex envelope of the Helmholtz energy F^{**}. The convex envelope is the largest function satisfying $F^{**} \le F$, which is only equal to the original Helmholtz energy F if it is a convex function. In other words, the LF transform is not self-inverse if the function is non-convex [20, 21]. The LF transform can be defined as either the maximum or minimum. Since G_LF must be convex, we can also obtain F^{**} from a Legendre transform of G_LF.

The Maxwell construction of equal areas for liquid-vapor coexistence is equivalent to the convex envelope of the Helmholtz energy F^{**}. The equal area rule states that for a liquid-vapor coexistence the system follows a constant pressure P_eq from volume V_l to V_g when the system evaporates, and conversely for condensation. The two volumes V_l and V_g at the pressure P_eq are the binodal points of the pressure-volume curve. The equal area rule states

$$\int_{V_\mathrm{l}}^{V_\mathrm{g}} P(V)\mathrm{d}V = P_\mathrm{eq}(V_\mathrm{l} - V_\mathrm{g}) \quad (14)$$

where $P(V)$ is a cubic equation of state, for example, the van der Waals equation, below the critical point. This corresponds to finding the double tangent line of the non-convex Helmholtz energy. The double tangent line is a tangent of the function at two different points. A double tangent line does not exist for convex functions. The double tangent line is exactly the convex envelope, as it is the largest function that satisfies $F^{**} \le F$.

3 Simulation details

A fluid between two parallel solid walls in the canonical and the isobaric ensemble was investigated with molecular dynamics simulations using LAMMPS [22, 23]. The temperature of the fluid was controlled using the Nosé-Hoover thermostat to $T = 2.26T_c = 2\varepsilon/k_\mathrm{B}$, where T_c is the critical temperature of the bulk fluid [24].

The walls were made up of solid particles in a face-centered cubic lattice with a number density $n_s^* = 1/\sigma^3$ corresponding to a lattice constant $a = 2^{2/3}\sigma$, where σ is the fluid particle diameter. Each wall had $N^p = 5 \times 10^4$ solid particles and side lengths $L = 100a \approx 159\sigma$. Each solid particle had a mass equal to the fluid particle mass, implying that the mass of the top solid wall (piston) was 5×10^4 times greater than a fluid particle. The mass of each particle were equal to m, which in reduced units is equal to one. The total mass of the fluid particles were $M = Nm$. In the canonical ensemble, the solid particles were fixed in space and could not move. In the isobaric ensemble, the solid particles in the lower wall were fixed in space, while the solid particles in the piston were free to move as a single rigid body in the x-direction. The piston could not rotate or move in the y- or z-directions. The fluid particles were placed between the walls. The system is visualized in Fig. 2 using OVITO [25]. The fluid particles are drawn in red and the solid particles are drawn in blue.

The fluid-fluid and fluid-solid particles interacted with the Lennard-Jones/spline potential [24],

$$u^{\mathrm{LJ/s}}(r) = \begin{cases} 4\varepsilon\left[\left(\frac{\sigma}{r}\right)^{12} - \left(\frac{\sigma}{r}\right)^{6}\right] & \text{if } r < r_s, \\ a(r-r_c)^2 + b(r-r_c)^3 & \text{if } r_s < r < r_c, \\ 0 & \text{else,} \end{cases} \quad (15)$$

where $r = |\boldsymbol{r}_j - \boldsymbol{r}_i|$ is the distance between particle i and j, σ is the particle diameter, and ε is the well-depth of the interactions. The parameters $r_s = (26/7)^{(1/6)}\sigma \approx 1.24\sigma$, $a = -24192/3211(\varepsilon/r_s^2)$, $b = -387072/61009(\varepsilon/r_s^3)$ and $r_c = 67/48r_s \approx 1.74\sigma$ were set such that the potential energy and the force were continuous at r_s and r_c. An advantage of the Lennard-Jones/spline potential is that the cut-off is much shorter than the regular Lennard-Jones potential with a typical cut-off at 2.5σ, which considerably decreases the computation time. See for more details on the properties of the Lennard-Jones/spline potential the work of Hafskjold *et al* [24] and Kristiansen [26]. The fluid-fluid and fluid-solid interactions were equal, while the solid-solid interaction was zero. The size of the timesteps was set equal to $\delta t = 0.002$. All units are in reduced Lennard-Jones units, meaning that they are reduced with the mass, particle diameter σ, the minimum of the interaction potential ε, and the Boltzmann constant k_{B}.

The system was initialized by creating one slab of fluid particles between two slabs of solid particles, all in a face-centered cubic lattice. The fluid particles were initialized with a velocity such that the temperature was equal to $T = 2\varepsilon/k_{\mathrm{B}}$, and they were free to move for 10^4 timesteps to melt the face-centered cubic lattice of the fluid. In the canonical ensemble, the piston was moved with a constant velocity for 10^5 timesteps to reach the desired height h, from here on defined as the minimum distance between the center of a solid particle in the bottom solid wall and the center of a solid particle in the piston. The controlled height was in the range $h \in [1.7, 110]\sigma$. Then the position of the piston was fixed, and the system was run for 10^6 timesteps to calculate

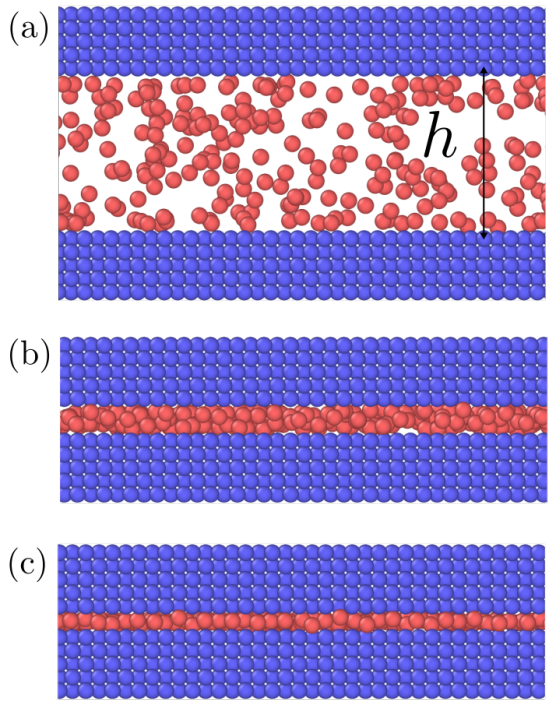

Figure 2: A rendering of simulations in the isobaric ensemble with surface number density $\Gamma = 0.81$. The top solid wall is the free to move in the normal direction and acts as a piston on the fluid with a controlled normal pressure P. The height h is shown in **(a)** and is defined as the minimum distance between the center of a solid particle in the bottom solid wall and the center of a solid particle in the piston. The normal pressure and mean height were equal to **(a)** $P = 0.164\varepsilon/\sigma^3$ and $\langle h \rangle = (10.2 \pm 0.09)\sigma$, **(b)** $P = 2.88\varepsilon/\sigma^3$ and $\langle h \rangle = (2.530 \pm 0.009)\sigma$ and, **(c)** $P = 2.89\varepsilon/\sigma^3$ and $\langle h \rangle = (1.865 \pm 0.003)\sigma$.

the mean normal pressure, $\langle P \rangle$.

The mean normal pressure was calculated as the arithmetic mean of the instantaneous forces of the particles in the piston at time t at time intervals $\Delta t = 0.2$

$$\langle P \rangle = \frac{1}{An} \sum_{t=0}^{n} \sum_{i=1}^{N^p} f_{x,i,t}, \tag{16}$$

where $f_{x,i,t}$ is the force in the x-direction acting on the solid particle i in the piston at time t, N^p is the number of solid particles, and $n = 10^6(\delta t/\Delta t) = 10^4$ is the number of samples where δt is the size of the timestep. Alternatively, the normal pressure could be calculated as the normal component of the mechanical pressure tensor in the fluid [3]. This has been done as a consistency check.

In the isobaric ensemble, an external force was added to the piston after melting the face-centered cubic lattice of the fluid. The simulations with controlled normal pressures were run sequentially from low to high normal pressure to obtain the compression curve, and from high to low normal pressure to obtain the expansion curve. This was done to reach all available states of the system in the isobaric ensemble. The controlled normal pressures were in the range $P \in [0.0045, 25]\varepsilon/\sigma^3$. Each of the simulations was run for 10^6 timesteps to calculate the mean height $\langle h \rangle$.

An external force f_x in the x-direction was applied to each solid particle in the piston,

$$f_x = \frac{PA}{N^p} \tag{17}$$

where N^p is the number of particles in the piston. The mean height $\langle h \rangle$ was calculated as the arithmetic mean of the instantaneous height at time t at time intervals of $\Delta t = 0.2$

$$\langle h \rangle = \frac{1}{n} \sum_{t}^{n} h_t. \tag{18}$$

The mean of the specific internal energy was calculated as the mean potential energy plus the mean kinetic energy of the fluid particles,

$$\langle u \rangle = \frac{1}{M} \left(\sum_{i=1}^{N} \sum_{j>i}^{N} u^{\mathrm{LJ/s}}(r) + \frac{1}{2} \sum_{i=1}^{N} m(\boldsymbol{v}_i \cdot \boldsymbol{v}_i) \right) \tag{19}$$

where $\boldsymbol{v}_i$ is the velocity of particle i, m is the mass of each fluid particle and $M = Nm$ is the total mass of the fluid particles. The specific internal energy was used together with the specific Helmholtz energy to calculate the specific entropy. The reference states f_0, u_0, and s_0 were calculated at height $h_0 = 110\sigma_0$, and g_0 was calculated at pressure P_0 corresponding to a mean height $\langle h_0 \rangle = 110\sigma_0$.

4 Results and discussion

The results are illustrated in Figs. 3 to 10. Fig. 3 shows the normal pressure-height relationship in isochoric conditions for various surface number densities. Figs. 4 to 6, give

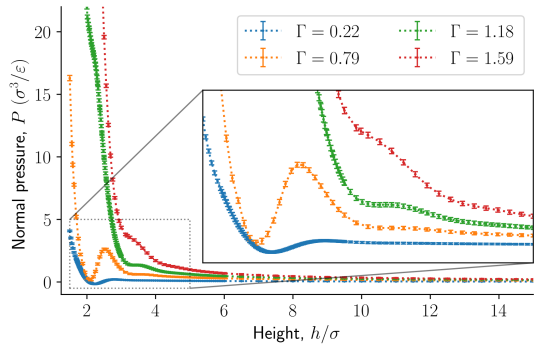

Figure 3: Normal pressure as a function of the height in isochoric conditions for varying surface number densities. The insert is an enlargement of the region where structural transitions occur.

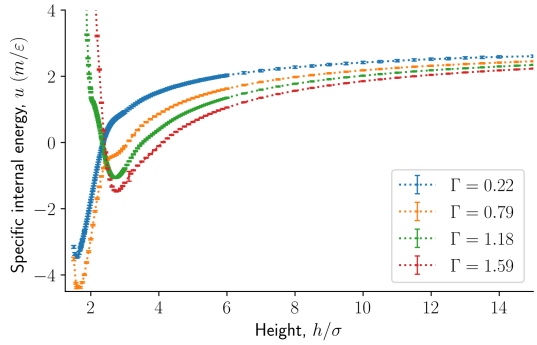

Figure 4: Specific internal energy as a function of the height in isochoric conditions for varying surface number densities.

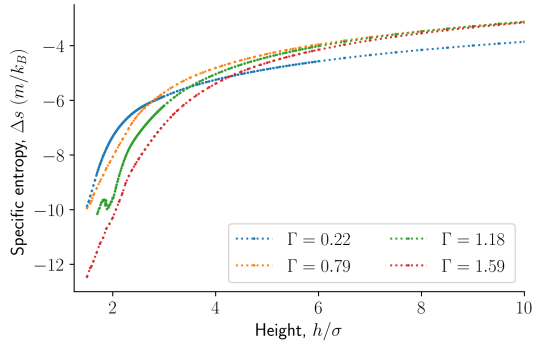

Figure 5: Difference in specific entropy as a function of the height in isochoric conditions for varying surface number densities.

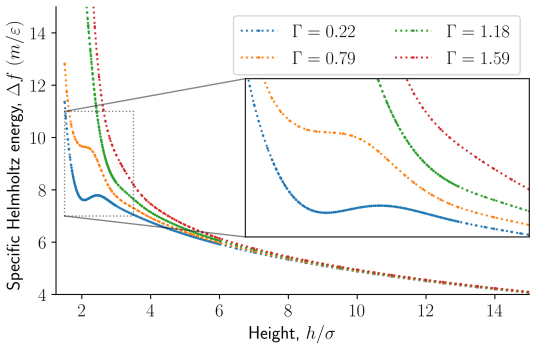

Figure 6: Difference in specific Helmholtz energy as a function of height for isochoric conditions for varying surface number densities.

the specific internal energy, difference in specific entropy, and difference in specific Helmholtz energy, respectively, all properties as a function of a controlled height. The difference in specific entropy and Helmholtz energy are given as the difference relative to the reference state at $h_0 = 110\sigma$. Fig. 7 is a visualisation of the monolayer in isochoric conditions when close to hexagonal packing appears.

The impact of the choice of environmental control variables on the normal pressure-height relationship, the basis of the findings reported, is illustrated in Fig. 8. This provides a basis for examination of Legendre and the Legendre-Fenchel transforms, see Figs. 9 and 10. The various results will now be explained and discussed.

4.1 The normal pressure, specific internal energy, entropy, and Helmholtz energy as a function of height.

The normal pressure-height relationship as a function of height and for various number densities was presented in Fig. 3. The thermodynamic limit behavior is seen for large heights or large surface number densities. The large system has a differentiable convex Helmholtz energy, approximately when the height $h > 3\sigma$ and when the surface number densities are $\Gamma \geq 1.18$. The typical small system behaviour appears for heights $h < 3\sigma$ and surface densities $\Gamma < 1.18$.

For smaller heights or surface number densities, the normal pressure goes through a local minimum and maximum as the height changes. This implies that the Helmholtz energy is non-convex. The specific internal energy has also a minimum, see Fig. 4. The entropy is monotonically increasing, except for the case $\Gamma = 1.18$ which has a local minimum, see Fig. 5. The Helmholtz energy in Fig. 6 captures the trade-off between the internal energy and the entropy. The Helmholtz energy as a function of height is non-convex for surface densities $\Gamma < 1.18$, which entails that the Legendre transform can not be applied. The insert in Fig. 6 magnifies the interesting region. The emerging structures are stabilized by the ability of the system to go to lower energy and higher entropy. The curves indicate a smooth structural transition.

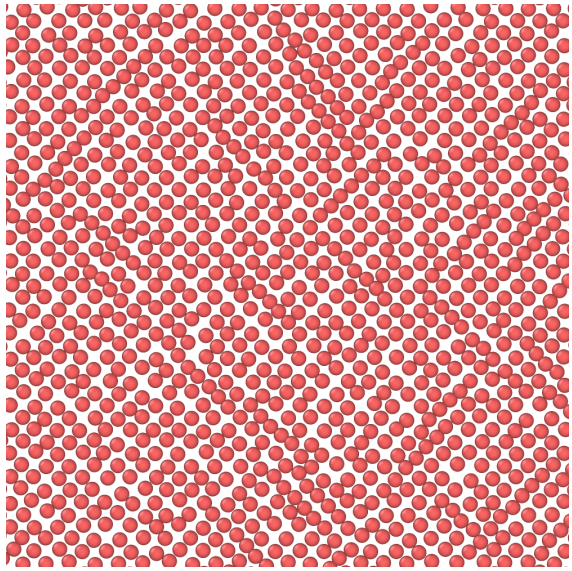

Figure 7: Top down view of fluid particles in isochoric conditions which has formed a hexagonal monolayer at height $h = 2^{2/3}\sigma \approx 1.59\sigma$. The solid particles are not shown. The mean normal pressure is $\langle P \rangle = (9.4 \pm 0.1)\varepsilon/\sigma^3$, specific internal energy $\langle u \rangle = (-4.39 \pm 0.03)\varepsilon/m$, difference in the specific entropy $\langle \Delta s \rangle = -9.7 k_B/m$, and difference in specific Helmholtz energy is $\langle \Delta f \rangle = 11.4\varepsilon/m$ [25].

4.2 A small system phase transition.

Figs. 3 to 6 showed a family of curves that represent the small system in a transition region for small values of h. This transition is special for a small thermodynamic system, it disappears when surface number density increases. How can we understand better the behavior of the particles in this region?

For the system to change from a fluid to a close-packing structure (face-centered cubic or hexagonal close-packed) without defects, the surface number density Γ must be

$$\Gamma = \frac{k}{r^2}, \tag{20}$$

where k is the number of layers (for a monolayer $k = 1$) and r is the distance between the fluid particles. The total potential energy is at a minimum at the distance $r = 2^{1/6}\sigma \approx 1.12\sigma$, which is where the Lennard-Jones/spline interaction potential is at a minimum. The interaction potential is short-ranged, it is zero for distances larger than the cut-off at $r_c \approx 1.74\sigma$. The surface number density for

a monolayer ($k = 1$) is $\Gamma \approx 0.79$, and for a double layer ($k = 2$) it is $\Gamma \approx 1.59$. An odd number of layers can complete the face-centered cubic lattice of walls without faults, while an even number of layers must have an odd number of stacking faults.

In the extreme case of a monolayer, we assume that the fluid is packed in such a way that each fluid particle lies on average at a distance $r_0 = 2^{1/6}\sigma$ away from eight solid particles and four fluid particles. In addition, there are two solid particle neighbours and four fluid particle neighbours each at a distance $r_a = 2^{2/3}\sigma$. All other particles lie beyond the cutoff distance r_c and do not contribute to the potential energy.

The minimum specific potential energy of a monolayer is then

$$e_{p,0} = 10u^{\mathrm{LJ/s}}(r_0) + 4u^{\mathrm{LJ/s}}(r_a) \approx -10.39\varepsilon/m, \qquad (21)$$

where m is the particle mass. Taking into account thermal fluctuations, it is

$$\langle e_p \rangle = e_{p,0} + a\langle r^2 \rangle \qquad (22)$$

where a is a constant. Assuming no defects, the average deviation from the average position can be set to zero. The quadratic term represents the lowest order correction to the mean specific potential energy due to thermal fluctuations making the fluid particle spend on average more time away from the average position. By the equipartition theorem, we then obtain the mean potential energy of a fluid particle

$$\langle e_p \rangle = e_{p,0} + \frac{3}{2}k_{\mathrm{B}}T \approx -7.39\varepsilon/m. \qquad (23)$$

The expected minimum mean specific internal energy is the sum of the mean specific potential and kinetic energies

$$\langle u \rangle_{\min} = \langle e_p \rangle + \langle e_k \rangle \approx -4.39\varepsilon/m \qquad (24)$$

where we have used that the mean specific kinetic energy is $\langle e_k \rangle = 3k_{\mathrm{B}}T/(2m) = 3\varepsilon/m$ at a temperature $T = 2\varepsilon/k_{\mathrm{B}}$.

The observed minimum of the specific internal energy for $\Gamma = 0.79$ is indeed $\langle u \rangle = (-4.39 \pm 0.03)\varepsilon/m$ at $h = 2^{2/3}\sigma \approx 1.59\sigma$, see Fig. 4. The simulated structure is visualised in Fig. 7. The figure shows that the fluid particles have formed a hexagonal monolayer layer. The mean normal pressure is $\langle P \rangle = (9.4 \pm 0.1)\varepsilon/\sigma^3$, difference in the specific entropy $\langle \Delta s \rangle = -9.7k_{\mathrm{B}}/m$, and difference in specific Helmholtz energy is $\langle \Delta f \rangle = 11.4\varepsilon/m$. The specific internal energy is at a minimum at this height, however, the Helmholtz energy is not.

A transition from a fluid to a close-packed structure under stress does not imply a first-order phase transition, a continuous transition from a fluid to a close-packed structure packing may occur. In other words, the free energy can be smooth and continuous during the transition.

Consider for comparison the familiar pressure-volume isotherms of cubic equations of state, for example, the van der Waals equation, for temperatures below the critical point. The Helmholtz energy is a non-convex function of volume. The binodal curve intersects the pressure-volume isotherms at two points $a = (p_{\mathrm{eq}}, V_{\mathrm{l}})$ and $b = (p_{\mathrm{eq}}, V_{\mathrm{g}})$ for $T < T_c$. The part of the isotherm between point a and b is known as the van der Waals loop. The Helmholtz energy is a non-convex function in this region. The line between the points a and b corresponds to the Maxwell construction of equal areas. See equation 14. The double Legendre-Fenchel transform of the specific Helmholtz energy f gives its convex envelope f^{**}, which corresponds to the Maxwell construction of equal areas. The spinodal curve intersects the isotherm at the local minimum and maximum, the spinodal region is a subset of the binodal region. The binodal region is metastable, while the spinodal region is unstable. Experimentally it is observed that fluids do not necessarily follow the van der Waals loop, but rather the straight line connecting points a and b. This is a first-order phase transition, as the pressure is non-smooth at the points a and b. The system is free to decompose in the binodal and spinodal region, which is energetically more favorable. During liquid-vapor phase decomposition the pressure is constant and equal to P_{eq}. The constant pressure corresponds to the double tangent line in the free energy. This double tangent line is the largest convex curve that satisfies $f^{**} \leq f$, which is exactly its convex envelope.

The states in the binodal and spinodal regions can be stable due to the restrictions that the confinement imposes on the system. The coexistence of fluid and close-packed structures is not possible in these simulations, as this would imply that there would be regions with differing heights. This could be possible if the walls were free to rotate or deform, however, the system is restricted such that the height is everywhere the same. In isochoric conditions, there is a smooth transition from a fluid to a close-packed structure. In isobaric conditions, the system is less restricted, and the system undergoes a first-order phase transition when it enters the spinodal region, see Figs. 8 (center). This is because the spinodal region is unstable. The set of control variables provide different stable states with their different restrictions on the system.

4.3 Response functions.

In the isobaric conditions, it is useful to consider the response function

$$K_{N,T} = -A\left(\frac{\partial h}{\partial P}\right)_{N,T} = -\left(\frac{\partial^2 G}{\partial P^2}\right)_{N,T} \geq 0, \qquad (25)$$

where $K_{N,T}/Ah$ is the isothermal compressibility [27]. As the states with negative $K_{N,T}$ cannot be stable under height fluctuations, $K_{N,T}$ is restricted to be non-negative. This can be seen in Fig. 8, where the states with negative $K_{N,T}$ in isochoric conditions are not available in isobaric conditions. The region with negative compressibility (positive slope) corresponds to the spinodal region, which is the region between the local minimum and maximum. In the isochoric ensemble, the height is a control variable, and states

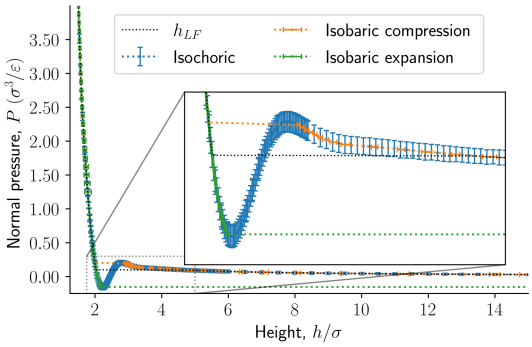

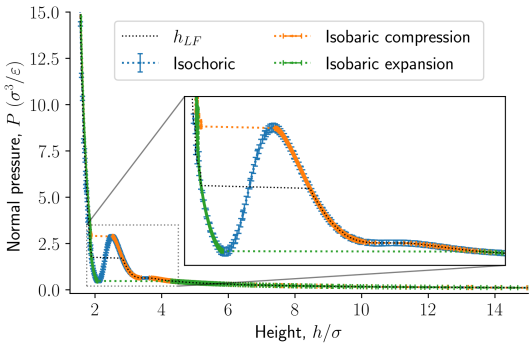

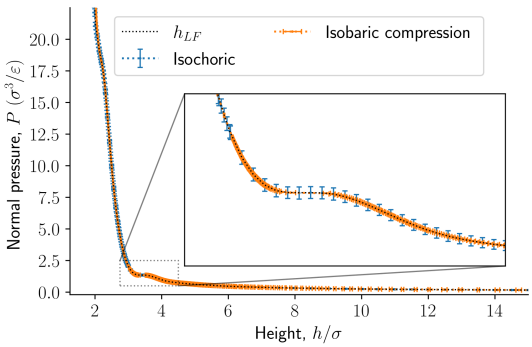

Figure 8: Normal pressure as a function of the height for isochoric and for isobaric conditions. The surface number density in each figure is $\Gamma = 0.22$, $\Gamma = 0.81$, and $\Gamma = 1.18$ from top to bottom. The top and middle figures shows the isobaric expansion and compression curves.

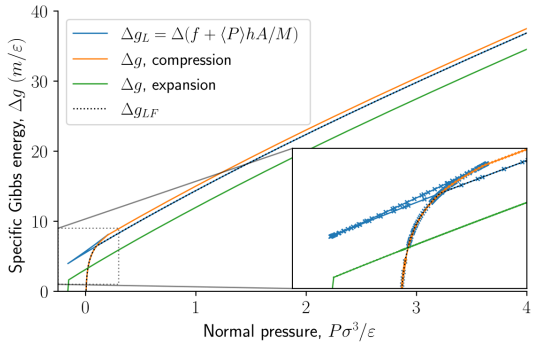

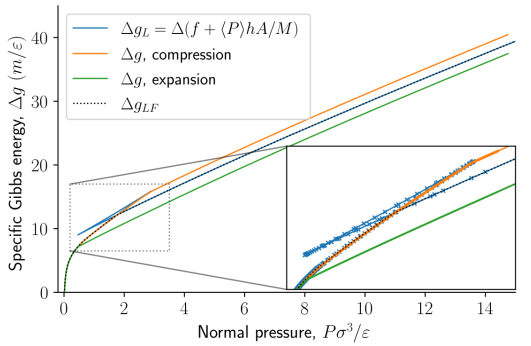

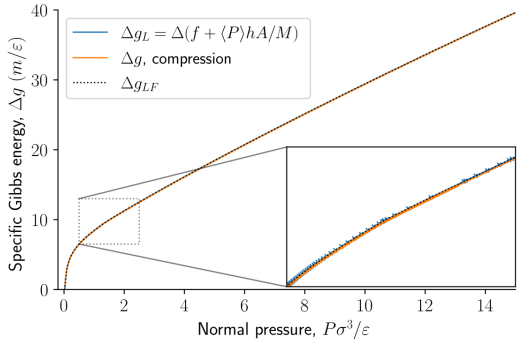

Figure 9: Specific Gibbs energy as a function of normal pressure. The surface number densities from top to bottom are $\Gamma = 0.22$, $\Gamma = 0.81$, and $\Gamma = 1.18$, respectively.

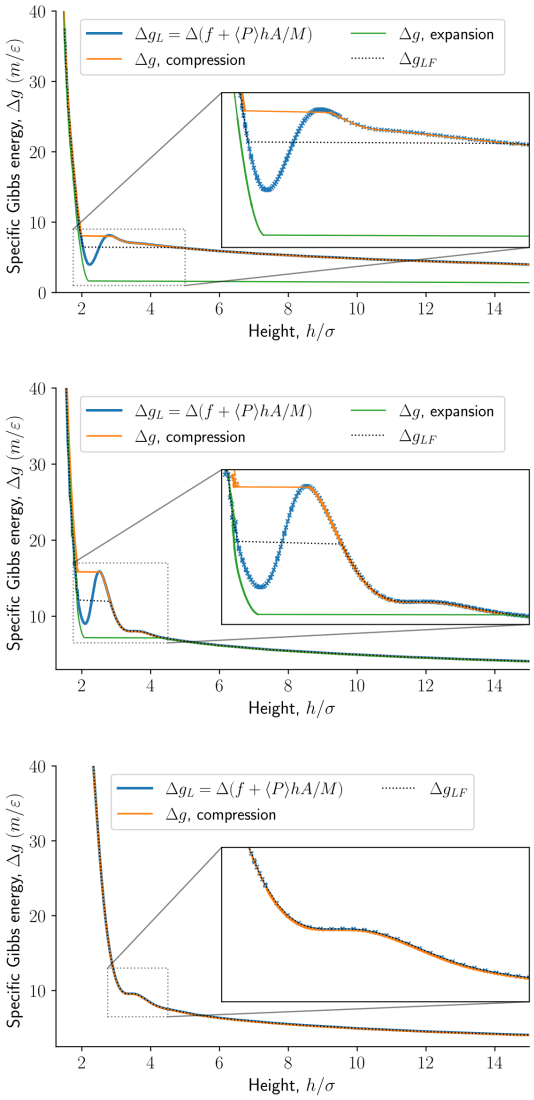

Figure 10: Specific Gibbs energy as a function of height. The surface number density in the figures from top to bottom are $\Gamma = 0.22$, $\Gamma = 0.81$, and $\Gamma = 1.18$, respectively.

with negative isothermal compressibility can be realized. In other words, the response function

$$\frac{1}{K_{N,T}} = -\frac{1}{A}\left(\frac{\partial P}{\partial h}\right)_{N,T} = \frac{1}{A^2}\left(\frac{\partial^2 F}{\partial h^2}\right)_{N,T} \tag{26}$$

can be negative. This can be seen in Fig. 8.

The function $g_{\mathrm{LF}}(N, P, T)$ presents two non-smooth points, indicating a first-order phase transition. The isothermal compressibility in isochoric conditions is negative, and is well defined in all available states. In isobaric conditions, the isothermal compressibility is undefined when the free energy is non-smooth. It is well defined and non-negative for all other states. The reason for this is that the normal pressure is increased by applying a directed force that seeks to compress the system. If the system was to increase its volume in response to this compression force, the fluid center of mass would have to move in the direction opposite to the applied force, thus violating conservation of linear momentum.

4.4 The specific Gibbs energy as a function of normal pressure. Legendre-Fenchel transforms.

Figs. 8 presents the normal pressure-height relationships for isochoric and isobaric conditions. The states available for the system to follow in isochoric conditions are blue, while isobaric conditions provide states given by the orange and green curves. The orange curve is for isobaric compression and the green curve is for isobaric expansion. Once the maximum in a curve is reached during isobaric compression, the system will switch to a smaller height. Alternatively, by isobaric expansion all points near the minimum become accessible. The dotted line is the height computed from the derivative of the Legendre-Fenchel transform g_{LF} with respect to the normal pressure P, see equation 3. This curve gives the Maxwell construction of equal areas, or in other words the straight line across the van der Waals loop or the binodal region. For isobaric conditions, the system is metastable in the binodal region and unstable in the spinodal region.

The specific Gibbs energy is presented in Figs. 9 and 10 as a function of normal pressure and height, respectively. For the large thermodynamic system, i.e. the bottom panels where $\Gamma = 1.18$, the specific Gibbs energy of compression (orange curve) coincides with the Legendre transform (blue curve), and the Legendre-Fenchel transform (black dotted curve) of the specific Helmholtz energy. This is the expected behavior of large systems.

At lower surface number densities, the Legendre transform ceases to apply. But we can still understand the system in terms of its thermodynamic properties. The normal pressure-height curves form a van der Waals loop for isochoric conditions. The specific Gibbs energy from compression differs from that of expansion for isobaric conditions. The Legendre-Fenchel transform (dotted curve) follows the Legendre transform (blue curve), except in the van

der Waals loop, which is cut out by the Legendre-Fenchel transform.

The underlying distribution of normal pressures in the isochoric conditions is highly peaked, implying that the conditions for the saddlepoint approximation, necessary for the Legendre-Fenchel transform, are obeyed. The small error bar in the normal pressure, which is the standard deviation, testifies to this, see Fig. 8. The mean relative standard deviation is 1.1%, 0.4%, 0.09% for $\Gamma = 0.22$, $\Gamma = 0.81$, and $\Gamma = 1.18$, respectively.

The results of the slit pore simulations show that structural changes are more restricted when in isochoric conditions than in isobaric conditions. The findings are similar to observations of polymer stretching [16]. Also here a transition was found between states. But then the different regimes referred to the type of degrees of freedom of the molecule (active or frozen rotational or stretching degrees of freedom) [16, 17]. We have seen that the Legendre-Fenchel transforms apply to two widely different cases, so we may pose the question: Does the transform apply in general to energy conversion in small systems? From the mathematics point of view, this seems likely [28, 29]. More data is needed before we may conclude, but this study brings out an interesting perspective. If the answer is yes, we may have a new tool for energy conversion in small systems.

When the Helmholtz energy is non-convex in the isochoric ensemble the system exhibits hysteresis in the isobaric ensemble. Hysteresis means that the state of the system depends on the system's history. The specific Gibbs energy depends on whether the system comes from a compressed or expanded state. In the isobaric ensemble, available states can be explored by first compressing and then expanding the system. One of the two available states at the same controlled normal pressure in the compression and expansion curves are metastable, the other state is stable. The Legendre-Fenchel transform gives the stable states. Since the piston cannot deform the energy barrier to go from a metastable state to a stable state is high, which is the reason for the pronounced hysteresis in this system. The loop created in the specific Gibbs energy profile in isobaric conditions is interesting. The existence of a loop means in principle, that work can be extracted from the loop by only two steps, namely compression, and expansion. The slit pore may serve as a very first model for deformable porous media in this context.

5 Conclusions

The normal pressure varies with the height. The excess normal pressure, the normal pressure minus the bulk pressure, is often called the disjoining or solvation pressure [19, 3]. The disjoining pressure is typically defined in the grand canonical ensemble (an open system). The disjoining pressure oscillates with a period equal to the fluid particle diameter because of the fluid packing between the walls. The mechanism of the excess normal pressure is the same here as for an open system, but the behaviour of the normal pressure observed in the closed system is different than for an open system. The observation of disjoining pressure is not new, see for example the work by Israelachvili [19]. It has been observed in simulations as well as experimentally. However, Israelachvili does not apply thermodynamics and the machinery that follows it. In this work, we have expanded upon the work by Israelachvili and others by giving a thermodynamic description. As a result, we get additional relations that can be used, for example, Maxwell relations.

In isochoric conditions, there is a smooth transition from a fluid to a close-packed structure. The Helmholtz energy of this smooth transition is non-convex for small surface number densities. The system is restricted in such a way that there must be a smooth transition. It is not possible for the system to have coexistence of a fluid and a close-packed structure because that would imply that the system could have two different heights at the same time. A possible future generalization could be to allow the solid walls to deform in a less restricted manner such that it would be possible for the system to have varying heights. In this way the system would allow for coexistence of a fluid and a close-packed structure. We hypothesize that the hysteresis in such a system will be less pronounced. Vapor-liquid coexistence is not restricted in this way, the vapor and liquid can have two different volumes. Since the height is controlled, the system is also restricted to that height. However, the normal pressure is controlled in isobaric conditions. As a result, there is a first-order phase transition from a fluid to a close-packed structure for small surface number densities. There is no coexistence of fluid and close-packed structure for the same reason as for isochoric conditions. The Legendre transform does not apply to non-convex free energies, and we have shown the Legendre-Fenchel transform must be applied.

Small systems in Hill's sense are not extensive. They are characterized by giving different responses to their ensemble of control. In the present case, we have studied and compared two small systems, i.e. isochoric and isobaric fluids confined to slit pores. Despite their smallness, we have found that they are perfectly well describable by thermodynamics when the theory is adjusted to deal with smallness. One such adjustment means to use Legendre-Fenchel transforms, rather than Legendre transforms. Doing that, we have shown that the specific Helmholtz energy can be transformed into the specific Gibbs energy. The findings are general, and support the systematic approach of Hill for descriptions of other small systems.

Author Contributions

O.G. contributed to formal analysis, investigation, methodology, software, and visualisation. D.B. and S.K contributed to supervision. All authors contributed to conceptualization, writing original drafts, reviewing, and editing. All authors have read and agreed to the published version of the

manuscript.

Conflicts of interest

There are no conflicts to declare.

Acknowledgements

The simulations were performed on resources provided by UNINETT Sigma2 - the National Infrastructure for High Performance Computing and Data Storage in Norway. We thank the Research Council of Norway through its Centres of Excellence funding scheme, project number 262644, PoreLab.

References

[1] JK Brennan and W Dong. Phase transitions of one-component fluids adsorbed in random porous media: Monte Carlo simulations. *The Journal of chemical physics*, 116(20):8948–8958, 2002.

[2] John K Brennan and Wei Dong. Molecular simulation of the vapor-liquid phase behavior of Lennard-Jones mixtures in porous solids. *Physical review E*, 67(3):031503, 2003.

[3] Olav Galteland, Dick Bedeaux, and Signe Kjelstrup. Nanothermodynamic description and molecular simulation of a single-phase fluid in a slit pore. *Nanomaterials*, 11(1):165, 2021.

[4] Bjørn A Strøm, Jianying He, Dick Bedeaux, and Signe Kjelstrup. When thermodynamic properties of adsorbed films depend on size: Fundamental theory and case study. *Nanomaterials*, 10(9):1691, 2020.

[5] Bjørn A Strøm, Dick Bedeaux, and Sondre K Schnell. Adsorption of an Ideal Gas on a Small Spherical Adsorbent. *Nanomaterials*, 11(2):431, 2021.

[6] Øivind Wilhelmsen, Dick Bedeaux, and David Reguera. Tolman length and rigidity constants of the Lennard-Jones fluid. *The Journal of chemical physics*, 142(6):064706, 2015.

[7] Terrell L Hill. *Thermodynamics of small systems, part 1*. Benjamin, 1963.

[8] Terrell L Hill. *Thermodynamics of small systems, part 2*. Benjamin, 1964.

[9] W. Dong. Thermodynamics of interfaces extended to nanoscales by introducing integral and differential surface tensions. *Proceedings of the National Academy of Sciences*, 118(3), 2021.

[10] Signe Kjelstrup, Dick Bedeaux, Alex Hansen, Bjørn Hafskjold, and Olav Galteland. Non-isothermal transport of multi-phase fluids in porous media. the entropy production. *Frontiers in Physics*, 6:126, 2018.

[11] Signe Kjelstrup, Dick Bedeaux, Alex Hansen, Bjørn Hafskjold, and Olav Galteland. Non-isothermal transport of multi-phase fluids in porous media. Constitutive equations. *Frontiers in Physics*, 6:150, 2019.

[12] Dick Bedeaux, Signe Kjelstrup, and Sondre K Schnell. *Nanothermodynamics. General theory*. NTNU, Trondheim, Norway, 2020.

[13] Olav Galteland, Dick Bedeaux, Bjørn Hafskjold, and Signe Kjelstrup. Pressures inside a nano-porous medium. The case of a single phase fluid. *Frontiers in Physics*, 7:60, 2019.

[14] Máté Erdős, Olav Galteland, Dick Bedeaux, Signe Kjelstrup, Othonas A Moultos, and Thijs JH Vlugt. Gibbs ensemble Monte Carlo simulation of fluids in confinement: Relation between the differential and integral pressures. *Nanomaterials*, 10(2):293, 2020.

[15] Michael T Rauter, Olav Galteland, Máté Erdős, Othonas A Moultos, Thijs JH Vlugt, Sondre K Schnell, Dick Bedeaux, and Signe Kjelstrup. Two-phase equilibrium conditions in nanopores. *Nanomaterials*, 10(4):608, 2020.

[16] Eivind Bering, Signe Kjelstrup, Dick Bedeaux, J Miguel Rubi, and Astrid S de Wijn. Entropy production beyond the thermodynamic limit from single-molecule stretching simulations. *The Journal of Physical Chemistry B*, 124(40):8909–8917, 2020.

[17] Eivind Bering, Dick Bedeaux, Signe Kjelstrup, Astrid S de Wijn, Ivan Latella, and J Miguel Rubi. A Legendre–Fenchel Transform for Molecular Stretching Energies. *Nanomaterials*, 10(12):2355, 2020.

[18] Olav Galteland, Fernando Bresme, and Bjørn Hafskjold. Solvent-Mediated Forces between Ellipsoidal Nanoparticles Adsorbed at Liquid–Vapor Interfaces. *Langmuir*, 36(48):14530–14538, 2020.

[19] Jacob N Israelachvili. *Intermolecular and surface forces*. Academic press, 2015.

[20] Hugo Touchette. Legendre-Fenchel transforms in a nutshell, 2005. available at: `https://appliedmaths.sun.ac.za/~htouchette/archive/notes/lfth2.pdf` (Nov. 2021).

[21] Ralph Tyrell Rockafellar. *Convex analysis*. Princeton university press, 2015.

[22] Steve Plimpton. Fast parallel algorithms for short-range molecular dynamics. *Journal of computational physics*, 117(1):1–19, 1995.

[23] Aidan P Thompson, H Metin Aktulga, Richard Berger, Dan S Bolintineanu, W Michael Brown, Paul S Crozier, Pieter J in't Veld, Axel Kohlmeyer, Stan G Moore, Trung Dac Nguyen, et al. LAMMPS-A flexible simulation tool for particle-based materials modeling at the atomic, meso, and continuum scales. *Computer Physics Communications*, page 108171, 2021.

[24] Bjørn Hafskjold, Karl Patrick Travis, Amanda Bailey Hass, Morten Hammer, Ailo Aasen, and Øivind Wilhelmsen. Thermodynamic properties of the 3D Lennard-Jones/spline model. *Molecular Physics*, 117(23-24):3754–3769, 2019.

[25] Alexander Stukowski. Visualization and analysis of atomistic simulation data with OVITO–the Open Visualization Tool. *Modelling and Simulation in Materials Science and Engineering*, 18(1):015012, 2009.

[26] Kim R. Kristiansen. Transport Properties of the Simple Lennard-Jones/Spline Fluid I: Binary Scattering and High-Accuracy Low-Density Transport Coefficients. *Frontiers in Physics*, 8:271, 2020.

[27] Alessandro Campa, Lapo Casetti, Ivan Latella, Agustín Pérez-Madrid, and Stefano Ruffo. Concavity, response functions and replica energy. *Entropy*, 20(12):907, 2018.

[28] Jeffrey Commons, Ying-Jen Yang, and Hong Qian. Duality Symmetry, Two Entropy Functions, and an Eigenvalue Problem in Gibbs' Theory. *arXiv preprint arXiv:2108.08948*, 2021.

[29] Hong Qian. Thermodynamic Behavior of Statistical Event Counting in Time: Independent and Correlated Measurements. *arXiv preprint arXiv:2109.12806*, 2021.

Article VIII

Olav Galteland, Michael T. Rauter, Kevin K. Varughese, Dick Bedeaux, Signe Kjelstrup

Defining the Pressures of a Fluid in a Nanoporous, Heterogeneous Medium

Submitted 2022
DOI: 10.48550/arXiv:2201.13060

Article VIII

Article VIII

Defining the pressures of a fluid in a nanoporous, heterogeneous medium

Olav Galteland[a,*], Michael T. Rauter[a], Kevin K. Varughese[a], Dick Bedeaux[a], and Signe Kjelstrup[a]

[a]PoreLab, Department of Chemistry, Norwegian University of Science and Technology
[*]Corresponding author: olav.galteland@ntnu.no

February 1, 2022

Abstract

We describe the thermodynamic state of a single-phase fluid confined to a porous medium with Hill's thermodynamics of small systems, also known as nanothermodynamics. This way of defining small system thermodynamics, with a separate set of control variables, may be useful for the study of transport in non-deformable porous media, where presently no consensus exists on pressure computations. For a confined fluid, we observe that there are two pressures, the integral and the differential pressures. We use molecular simulations to investigate and confirm the nanothermodynamic relations for a representative elementary volume (REV). For a model system of a single-phase fluid in a face-centered cubic lattice of solid spheres of varying porosity, we calculate the fluid density, fluid-solid surface tension, replica energy, integral pressure, entropy, and internal energy.

Keywords: nanothermodynamics, Hill's thermodynamics of small systems, porous media, molecular simulations, integral pressure, representative elementary volume, heterogeneous media

1 Introduction

Transport in porous media takes place in a vast range of systems, natural as well as man-made. It is thus important to have a deep understanding of the relevant driving forces and their coupling, for instance to describe production of clean water [1, 2, 3], CO_2 sequestration [4, 5, 6], transport of oxygen, hydrogen, and water in fuel cell catalytic layers [7, 8], and transport in lithium-ion battery electrodes and separators [9, 10, 11].

The long-range aim of this work is to obtain a general thermodynamic theory of transport of immiscible fluids in porous media on the macroscale [12, 13, 14]. This theory must first describe the thermodynamic state of the fluids in the porous media. To do this we employ a bottom-up approach, a procedure that includes all details of the system on the nanoscale in the construction of a representative elementary volume (REV) [15, 16, 17]. The procedure gives a coarse-grained description of the REV on the macroscale, or what is called the Darcy level [15, 12, 16, 13, 14]. A central issue is to find the pressure of the REV. Figure 1 illustrates the problem for the cases studied in this work. A fluid (blue) occupies the pores in a porous material (grey). The pores are so narrow that interactions between fluid and wall become significant, or in other words, that the fluid-wall surface energy becomes significant. But how can we define and determine the properties of the REV, for instance, the pressure? Can we find a representative elementary volume, for which this is possible? In this work, we aim to find answers to these questions.

In bulk fluids, the hydrostatic pressure is well defined, measurable, and well documented as the driving force of the fluid flow. In porous media, where fluids are confined by the pores, however, there is no consensus of neither the thermodynamic nor the mechanical definitions of the pressures. The microscopic mechanical pressure tensor is inherently ambiguous [18, 19]. In this context, we make an emphasis on the milestone work of Israelachvili [20] who

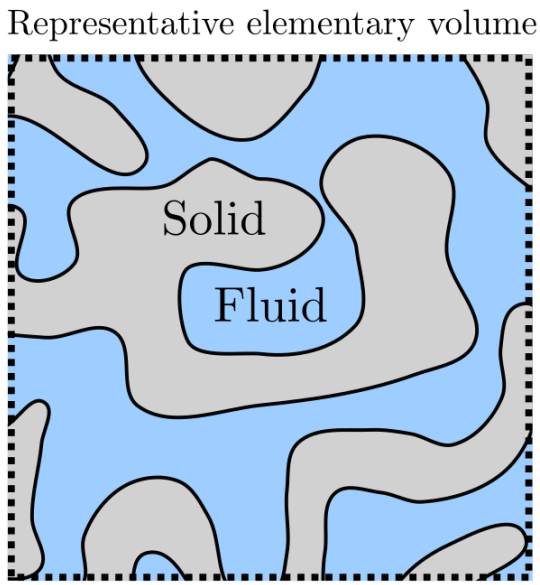

Figure 1: A single-phase and -component fluid in a porous medium. The fluid-solid interfaces can have complex shapes and the volumes can be on the nanoscale.

documented short- and long-range forces on fluid particles exerted by the surroundings, and on the thermodynamic analysis that was pioneered by Derjaguin [21].

We have previously proposed thermodynamic definitions for the pressure of heterogeneous media, applying Hill's idea of thermodynamics for small systems [13, 14, 22, 23, 24]. Hill's definitions have so far only been tested under simple conditions [25, 22, 23, 26]. They have not been studied for a variety of shapes and pore sizes.

In Hill's thermodynamics of small systems or nanothermodynamics (See Bedeaux and Kjelstrup [17]), the REV of the porous medium is considered as an open system, controlled by the temperature, chemical potential, or pressure in the environment. The thermodynamic analysis is thus applied to a grand canonical ensemble of systems and a new variable is introduced, the replica energy, i.e. the energy needed to create one more small system in the ensemble. An adjusted Gibbs-Duhem equation (the Hill-Gibbs-Duhem's equation) appears. This opens up a new route to determine the REV pressure.

Using this as a starting point in section 2, we shall find expressions for the so-called integral and differential pressures of the REV, from the system's replica energy. We present a new route to the pressure via the chemical potential of the reservoir in equilibrium with the REV. Molecular dynamics simulations, described in section 3, will be used to illustrate and verify the theoretical steps.

2 Theory

The systematic procedure of Hill consists of the three steps [17], which we repeat to give an overview of the procedure. Concepts will be defined in the text that follows.

1. To start, define the items which make the system small in Hill's sense, by defining the relevant REV. Find the corresponding Hill-Gibbs equation. Next, define the environmental variables that control the system.

2. From an analysis of the ensemble of small systems, find the system's replica energy in terms of its subdivision potential.

3. Derive the corresponding Hill-Gibbs-Duhem equation. This equation can be used to find the REV thermodynamic variables and their interrelations.

2.1 The general Hill-Gibbs equation of an ensemble of open porous media REVs

We shall consider the REV of a porous medium, filled with a single-phase, single-component fluid, see figure 1. The REV volume is $V = V^f + V^s$, where V^f is the volume of the fluid and V^s is the volume of the solid. The porosity is the fraction of the fluid volume to the total volume, $\phi = V^f/V$. These are time-independent properties in the system. The REV is a small system in Hill's sense [27, 17] because the fluid is confined; it does not have bulk-scale properties. The system is open for the supply of fluid particles and energy. The number of solid particles is fixed, however.

The ensemble of $\mathcal{N}$ REVs has a total entropy S_t, total fluid volume V_t^f, total number of fluid particles N_t^f, total number of solid particles N_t^s (with total volume V_t^s), and total fluid-solid surface area A_t. The total differential of the total internal energy of the ensemble of REVs is then

$$\mathrm{d}U_t = T\mathrm{d}S_t - p^f\mathrm{d}V_t^f - p^s\mathrm{d}V_t^s + \mu^f\mathrm{d}N_t^f + \mu^s\mathrm{d}N_t^s + \gamma\mathrm{d}A_t + \varepsilon\mathrm{d}\mathcal{N}. \tag{1}$$

This equation has been called the Hill-Gibbs equation [17, 23]. The temperature, fluid pressure, and solid pressures, chemical potentials, and surface tension are defined from the variables involved as

$$\begin{aligned}
T &\equiv \left(\frac{\partial U_t}{\partial S_t}\right)_{V_t^f,V_t^s,N_t^f,N_t^s,A_t,\mathcal{N}}, & p^f &\equiv \left(\frac{\partial U_t}{\partial V_t^f}\right)_{S_t,V_t^s,N_t^f,N_t^s,A_t,\mathcal{N}},\\
p^s &\equiv \left(\frac{\partial U_t}{\partial V_t^s}\right)_{S_t,V_t^f,N_t^f,N_t^s,A_t,\mathcal{N}}, & \mu^f &\equiv \left(\frac{\partial U_t}{\partial N_t^f}\right)_{S_t,V_t^f,V_t^s,N_t^s,A_t,\mathcal{N}},\\
\mu^s &\equiv \left(\frac{\partial U_t}{\partial N_t^s}\right)_{S_t,V_t^f,V_t^s,N_t^f,A_t,\mathcal{N}}, & \gamma &\equiv \left(\frac{\partial U_t}{\partial A_t}\right)_{S_t,V_t^f,V_t^s,N_t^f,N_t^s,\mathcal{N}}.
\end{aligned} \tag{2}$$

The subdivision potential ε is the property that deals with system smallness in particular. It is introduced with its conjugate variable, the number of REVs, $\mathcal{N}$. The subdivision potential is the internal energy required to add one more REV to the ensemble under the specified conditions,

$$\varepsilon \equiv \left(\frac{\partial U_t}{\partial \mathcal{N}}\right)_{S_t,V_t^f,V_t^s,N_t^f,N_t^s,A_t}. \tag{3}$$

When the subdivision potential differs from zero the system is small. This property will, as we shall see below, adjust the common variables like the pressure, and turn them into effective new variables. In the case of the pressure, the adjustment leads to the integral pressure, central for porous media.

2.2 The replica energy

To find the properties of one system, we need to describe the thermodynamic state of a single-phase, single-component fluid in the REV. The fluid is free to move (the system is open), while the solid is not. The system exchanges fluid particles with the surroundings, but not solid particles. The variables that are controlled by contact with the environment are the temperature and the fluid chemical potential. Apart from these, as stated above, the fluid volume, solid volume, surface area, and the number of solid particles are control variables too. The type of ensemble

constituted by this set of variables is particularly suited for the transport of fluids through a porous medium.

In order to change the set of variables in the general expression equation 1, into the above preferred set of control variables, we express the additive variables in the original set of total variables by their controlled value times the number of replicas. This provides also the single system properties that we are after. The controlled fluid and solid volumes, and surface area per REV are $V_t^f = V^f\mathcal{N}$, $V_t^s = V^s\mathcal{N}$, and $A_t = A\mathcal{N}$, respectively. In addition we introduce the controlled number of solid particles per REV, $N_t^s = N^s\mathcal{N}$. By introducing these control variables into the Hill-Gibbs equation for the ensemble, we obtain

$$\mathrm{d}U_t = T\mathrm{d}S_t - p^f\mathcal{N}\mathrm{d}V^f - p^s\mathcal{N}\mathrm{d}V^s + \mu^f\mathrm{d}N_t^f + \mu^s\mathcal{N}\mathrm{d}N^s + \gamma\mathcal{N}\mathrm{d}A + X\mathrm{d}\mathcal{N}, \tag{4}$$

where the last term is the replica energy of one small system

$$X = \varepsilon - p^fV^f - p^sV^s + \gamma A + \mu^sN^s. \tag{5}$$

The replica energy [27, 28] expresses in a simpler way, the energy required to add one more small system to the ensemble of systems under the conditions controlled. The combination of terms can define the integral pressure minus the integral solid chemical potential times number of solid particles [23],

$$-\hat{p}V + \hat{\mu}^sN^s \equiv X, \tag{6}$$

however, we need an additional equation to determine both $\hat{p}$ and $\hat{\mu}^s$ separately. Through the introduction of an ensemble of the systems, we have achieved that the internal energy, here U_t, is an Euler homogeneous of the first order in the number of REVs. This gave Hill the motivation for the use of an ensemble, and to define the conjugate variables ε and $\mathcal{N}$.

2.3 The Hill-Gibbs equation for a single small system

We are now in a position to integrate the total differential of the total internal energy, see equation 4, at constant T, V^f, V^s, μ^f, N^s, and A. This gives,

$$U_t = TS_t + \mu^fN_t^f + X\mathcal{N}. \tag{7}$$

By introducing the REV average properties, we obtain the internal energy of one REV,

$$U = TS + \mu^fN^f + X. \tag{8}$$

The total differential of the internal energy of one REV is

$$\mathrm{d}U = T\mathrm{d}S - p^f\mathrm{d}V^f - p^s\mathrm{d}V^s + \mu^f\mathrm{d}N^f + \mu^s\mathrm{d}N^s + \gamma\mathrm{d}A. \tag{9}$$

By differentiating the internal energy of the REV and using its total differential, we obtain the total differential of the replica energy

$$\mathrm{d}X = \mathrm{d}(-\hat{p}V + \hat{\mu}^sN^s) = -S\mathrm{d}T - p^f\mathrm{d}V^f - p^s\mathrm{d}V^s - N^f\mathrm{d}\mu^f + \mu^s\mathrm{d}N^s + \gamma\mathrm{d}A. \tag{10}$$

The equation is the outcome of step 2 in Hill's procedure presented in the introduction to this section. The equation can be seen as an extension of Gibbs-Duhem's equation, so we have called it Hill-Gibbs-Duhem's equation [17]. Applications can now be specified.

The partial derivatives of the replica energy follow

$$\begin{aligned} S &= -\left(\frac{\partial X}{\partial T}\right)_{V^f,V^s,\mu^f,N^s,A}, \qquad p^f = -\left(\frac{\partial X}{\partial V^f}\right)_{T,V^s,\mu^f,N^s,A}, \\ p^s &= -\left(\frac{\partial X}{\partial V^s}\right)_{T,V^f,\mu^f,N^s,A}, \qquad N^f = -\left(\frac{\partial X}{\partial \mu^f}\right)_{T,V^f,V^s,N^s,A}, \\ \mu^s &= \left(\frac{\partial X}{\partial N^s}\right)_{T,V^f,V^s,N^f,A}, \qquad \gamma = \left(\frac{\partial X}{\partial A}\right)_{T,V^f,V^s,N^f,\mu^s}. \end{aligned} \tag{11}$$

With this set of equations we can calculate all the necessary REV properties of a porous medium. We shall concentrate on the integral fluid pressure and the route to this quantity via the chemical potential.

2.4 The integral pressure and the chemical potential of the solid in the REV

We apply here the conditions of constant temperature, fluid volume, solid volume, number of solid particles, and surface area. The Hill-Gibbs-Duhem's equation reduces to

$$\mathrm{d}X = \mathrm{d}(-\hat{p}V + \hat{\mu}^s N^s) = -N^f \mathrm{d}\mu^f \tag{12}$$

or, after dividing by V, the volume of the REV,

$$\mathrm{d}x = \mathrm{d}(-\hat{p} + \hat{\mu}^s \rho^s) = -\rho^f \mathrm{d}\mu^f \tag{13}$$

Where the density of the fluid in the REV is $\rho^f = N^f/V$ and the density of the solid is $\rho^s = N^s/V$. These densities are of the total REV volume V, and not the fluid volume V^f or solid volume V^s. The difference of the replica energy density can be calculated from

$$x - x_\infty = -\int_{-\infty}^{\mu^f} \rho^f \mathrm{d}\mu'^f, \tag{14}$$

The replica energy density is zero as the fluid chemical potential approaches minus infinity. The replica energy density depends on two unknown variables, $\hat{p}$ and $\hat{\mu}^s$. To proceed we need to know more about these variables.

2.4.1 Constant integral pressure across boundary

The integral pressure of the REV can be obtained from equation 13

$$\mathrm{d}\hat{p} = \rho^f \mathrm{d}\mu^f + \rho^s \mathrm{d}\hat{\mu}^s. \tag{15}$$

The fluid in the porous medium is in equilibrium with its environment, here the bulk phase fluid that surrounds the system (denoted b). The environment has the same temperature. The integral pressure was observed to be constant across the phase boundary inside a pore [25]. We shall therefore make the assumption that also in this case;

$$\hat{p} = p^b \tag{16}$$

where p^b is the bulk pressure of a fluid in equilibrium with the porous medium. For an ideal gas in a cubic confinement it has been shown that the integral pressure is equal to the bulk pressure [29]. If this applies for this system, we also have

$$\hat{p} = \int_{-\infty}^{\mu^f} \rho^b \mathrm{d}\mu'^f, \tag{17}$$

where ρ^b is the fluid number density in the bulk phase. The integral pressure is zero as the fluid chemical potential approaches minus infinity. As a consequence, the integral pressure depends only on the fluid chemical potential and temperature. The integral chemical potential of the solid in the REV is then

$$\hat{\mu}^s = \frac{1}{\rho^s}\int_{-\infty}^{\mu^f}(\rho^b - \rho^f)\mathrm{d}\mu'^f. \tag{18}$$

The solid chemical potential is zero at minus infinite fluid chemical potential. The entropy density of the REV is

$$s = \frac{S}{V} = \frac{1}{T}(u - \mu^f\rho^f - x) \tag{19}$$

where we used equation 8 and introduced the replica energy density, x.

2.5 Pressures and surface tension

There are three pressures; the integral, fluid and solid pressures. The latter two are differential pressures. The integral pressure is a combination of the differential pressures and the (differential) surface tension,

$$\hat{p} = p^f\phi + p^s(1-\phi) - \gamma A/V = p^b. \tag{20}$$

We assume the integral pressure to be equal everywhere in equilibrium and also equal to the bulk pressure of a bulk fluid in equilibrium with the porous medium. If we also assume the distances between solid surfaces to be large and their curvature to be small, we can approximate the fluid pressure to be equal to the bulk pressure [23]. In that case, the solid pressure is equal to

$$p^s = p^b + \frac{\gamma A}{V^s}. \tag{21}$$

3 Simulation details

Systems of fluid and solid particles were investigated with molecular dynamics simulations using LAMMPS [30, 31]. The three different systems have been simulated: A bulk fluid, a single solid particle surrounded by fluid particles, and a face-centered cubic (fcc) lattice of solid particles filled with fluid particles in the pore space. The two latter systems are illustrated in figure 2. The systems were simulated in the grand canonical ensemble and had periodic boundary conditions in all directions. The bulk fluid was simulated to calculate the bulk pressure as a function of the fluid chemical potential. The single solid particle surrounded by fluid particles will be considered as if the lattice constant of the fcc lattice is large. This system was simulated to calculate the fluid-solid surface tension when the solid particles are far apart. The thermodynamic properties of the fluid in the fcc lattice were calculated as a function of the fluid chemical potential.

The temperature was controlled by using a Nosé-Hoover thermostat [33, 34] adapted by Shinoda *et. al.* [35]. The fluid chemical potential was controlled by using grand canonical Monte Carlo insertions and deletions of fluid particles [36]. A particle is inserted at random position in the simulation box with a probability

$$\mathrm{acc}(N^f \to N^f + 1) = \min\left\{1, \quad \frac{V}{\Lambda^3(N^f+1)}\exp[\beta(\mu - E_p(N^f+1) + E_p(N^f)]\right\}. \tag{22}$$

A random particle is removed from the simulation box with a probability

$$\mathrm{acc}(N^f \to N^f - 1) = \min\left\{1, \quad \frac{\Lambda^3(N^f+1)}{V}\exp[-\beta(\mu + E_p(N^f-1) - E_p(N^f)]\right\}. \tag{23}$$

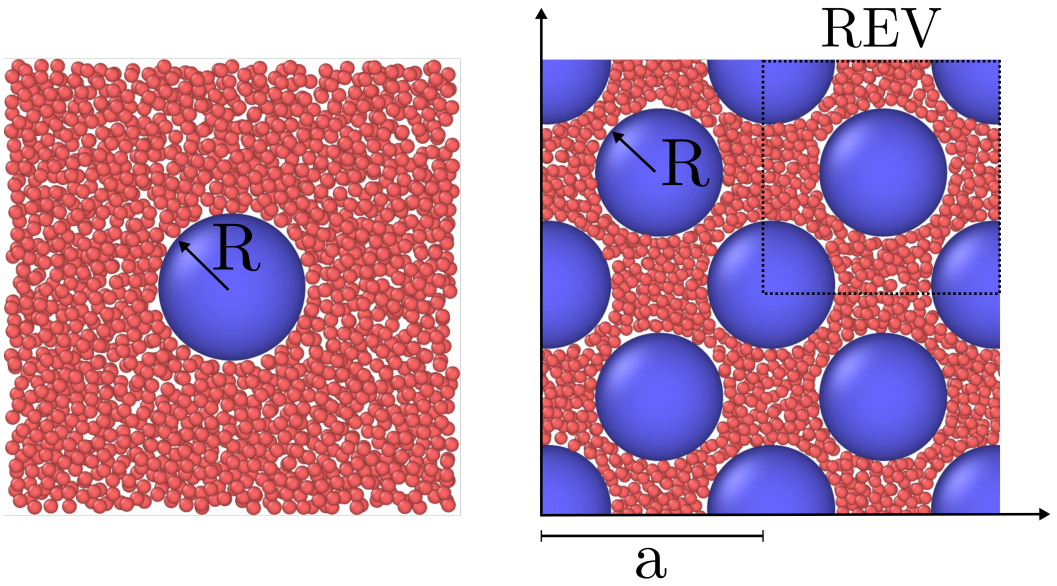

Figure 2: Visualization of a two of the simulated systems. Fluid particles (red) and solid particles (blue) are visualised with OVITO [32]. Only the particles in a slab centered on the solid particles of thickness 2.5σ is shown. The fluid chemical potential is $\mu^f = \zeta$ and the radius of the solid particles is $R = 5\sigma$. Left: Single solid particle. Right: An fcc lattice with lattice constant $a = 17.5\sigma$ and porosity $\phi = 0.61$.

Where $\Lambda = \sqrt{h^2/(2\pi m k_\mathrm{B} T)}$ is the de Broglie thermal wavelength, h is the Planck constant, E_p is the potential energy and $\beta = 1/(k_\mathrm{B}T)$ where k_B is Boltzmanns constant.

3.1 Simulation procedure

In the bulk system, the fluid chemical potential was varied in the range $\mu^f \in [-7, 1]$, in which the fluid density varied from a dilute gas to a dense liquid. The system was initialized with an empty cubic simulation box of volume $V = (40\sigma)^3$, and the grand canonical Monte Carlo technique was used to insert particles. The simulation was run until the average number of fluid particles was no longer increasing. The bulk fluid number density $\rho^b = N^f/V$ and pressure $p = (P_{xx} + P_{yy} + P_{zz})/3$ were calculated as a function of the fluid chemical potential for 10^7 steps. The calculation of the mechanical pressure tensor $P_{\alpha\beta}$ is described below in subsection 3.4.

The system of the single solid particle was simulated by first placing the solid particle in the center of the cubic simulation box of volume $V = (30\sigma)^3$. The radius of the solid particle was $R = 5\sigma$, where σ is the diameter of the fluid particle. The fluid chemical potential was varied in the range $\mu \in [-7, 1]\zeta$, where ζ is the minimum of the pair-wise interaction. The system was initialized by placing the fluid particles in an fcc lattice with a fluid number density approximately equal to the bulk fluid number density around the solid particle at a given fluid chemical potential. This was done to reduce the computational time. The simulation was run until the average number of fluid particles no longer increased, after which it was run for an additional 10^7 steps to calculate the surface tension as a function of the fluid chemical potential. The calculation of the surface is described below in section 3.4.

The fcc lattice of solid particles was fixed in space with lattice constant in the range $a \in [15, 30]\sigma$, the radius of the solid particles was $R = 5\sigma$. The simulation box lengths were $L = 2a$, total volume $V = 8a^3$, number of solid particles $N^s = 32$, and solid volume $V^s = 128\pi R^3/3$. We have previously found that the smallest REV of such a system is a quarter unit cell [22]. The fluid particles were inserted in the pore space in between the solid particles.

The porosity of the system was

$$\phi = \frac{V^f}{V} = 1 - \frac{16\pi R^3}{3a^3}, \tag{24}$$

where the radius of the solid particles was $R = 5\sigma$ given that the lattice constant is $a \geq 2\sqrt{2}R \approx 14\sigma$. For lower values of a the solid particles overlap, however, we do not look at such systems. The porosity varied from approximately 0.38 to 0.92. The fluid chemical potential, number of solid particles, temperature, and volume were controlled.

The system was initialized by placing the solid particles in an fcc lattice with lattice constant a and fluid particles also in an fcc lattice with a number density approximately equal to $\rho^b(\mu^f)$ around the solid particles. The simulation was run until the number of fluid particles was constant, after which the simulation was run for an additional 10^7 timesteps to calculate thermodynamic properties.

3.2 The Lennard-Jones/spline potential

The particles interacted with the Lennard-Jones/spline (LJ/s) potential [37], which is equal to the Lennard-Jones potential up to the inflection point r_s shifted by a hard-core diameter d. At r_s a third degree polynomial is fitted for the potential to be zero at the cut-off r_c and the force and potential to be continuous at the inflection point r_s and cut-off r_c. See the works by Hafskjold *et al.* [37] and Kristiansen [38] for details on the properties of the LJ/s potential. The LJ/s potential is,

$$\nu^{\mathrm{LJ/s}}(r) = \begin{cases} 4\zeta\left[\left(\frac{\sigma}{r-d}\right)^{12} - \left(\frac{\sigma}{r-d}\right)^{6}\right] & \text{if } r < r_s, \\ a(r-r_c)^2 + b(r-r_c)^3 & \text{if } r_s < r < r_c, \\ 0 & \text{else} \end{cases} \tag{25}$$

where ζ is the minimum of the interaction potential. This symbol is used to avoid confusion with the subdivision potential ε. The soft-core diameter is σ, d is the hard-core diameter, $r = |\boldsymbol{r}_j - \boldsymbol{r}_i|$ is the distance between particle i and j. The distance $r = \sigma + d$ is the smallest distance where the potential is zero. The Lennard-Jones/spline interaction potential was equal for all particle pairs, but was shifted with hard-core diameter d. There were three particle pair interactions, fluid-fluid, fluid-solid, and solid-solid, and only the hard-core diameter varied between them. The solid-solid interaction we set to zero. The hard-core diameter was $d_{\mathrm{ff}} = 0$, $d_{\mathrm{fs}} = 4.5\sigma$, and $d_{\mathrm{ss}} = 9\sigma$ for the fluid-fluid, fluid-solid, and solid-solid interactions, respectively. The solid particle radius was defined as $R \equiv (d_{\mathrm{ss}} + \sigma)/2 = 5\sigma$. Other definitions of the radii are possible, for example based on Gibbs dividing surface or the surface of tension. The parameters a, b, r_s and r_c were determined such that the potential and the force were continuous at $r = r_s$ and $r = r_c$. The masses of fluid particles were m, and the solid particles were considered to have infinite mass as they were fixed in space.

3.3 Internal energy density

The internal energy density was calculated as the sum of the kinetic and potential energy densities,

$$u = \frac{1}{V}\left(\sum_{i=1}^{N}\sum_{j>i}^{N} u^{\mathrm{LJ/s}}(r_{ij}) + \frac{1}{2}\sum_{i=1}^{N} m_i(\boldsymbol{v}_i \cdot \boldsymbol{v}_i)\right) \tag{26}$$

where V is the total volume, N is the total number of particles, and $\boldsymbol{v}_i$ is the velocity of particle i. The solid particles did not contribute to the kinetic energy, as their velocities were controlled to be zero. The internal energy density was used to calculate the entropy density, see equation 19.

3.4 The mechanical pressure tensor

The mechanical pressure tensor was calculated in spherical and Cartesian coordinates, see Ikeshoji *et.al.* for details [39]. It was calculated in spherical coordinates for the single solid particle surrounded by fluid, and in Cartesian coordinates for the bulk fluid and the fcc lattice of solid particles with inserted fluid particles. For the bulk fluid and fcc lattice, the pressure was calculated for the whole simulation box, with sides $L \in [30, 60]\sigma$ and interaction cut-off $r_c \approx 1.74\sigma$. While for the single solid particle it was calculated in spherical shell subvolumes with the origin at the center of the solid particle. This was done to calculate the surface tension.

To avoid confusion between the thermodynamic and mechanical pressures, we will use lower case p for all thermodynamic pressures and upper case P for mechanical pressures. We make this distinction because there is no consensus on how, if possible, to connect the two for heterogeneous media [40, 41, 42, 23].

The mechanical pressure tensor can be written as the sum of the ideal gas contribution and a virial contribution,

$$P_{\alpha\beta} = \rho k_{\mathrm{B}} T \delta_{\alpha\beta} + P^{v}_{\alpha\beta}, \tag{27}$$

where $\delta_{\alpha\beta}$ is the Kronecker delta and the subscripts give the components of the tensor. The virial contribution is due to particle pair interaction, and is calculated as a sum over all particle pairs. For a subvolume V_k the virial contribution is

$$P^{v}_{\alpha\beta} = -\frac{1}{V_k} \sum_{i=1}^{N} \sum_{j>i}^{N} f_{ij,\alpha} \int_{C_{ij} \in V_k} \mathrm{d}l_{\beta}. \tag{28}$$

Where N is the total number of particles and $f_{ij,\alpha}$ is the α-component of force acting on particle i due to particle j. The line integral is along the part of the curve C_{ij} that is contained in the subvolume V_k. The virial contribution is inherently ambiguous as any continuous curve that starts at the center particle i and ends at the center particle j is permitted [18, 43, 19]. In this work, we have used the Irving-Kirkwood curve, which is the straight line from the center of particle i to the center of particle j.

The Cartesian mechanical pressure tensor was calculated for the whole simulation box. The line integral in the virial contribution reduces it to

$$P^{v}_{\alpha\beta} = -\frac{1}{V_k} \sum_{i=1}^{N} \sum_{j>i}^{N} f_{ij,\alpha} r_{ij,\beta}. \tag{29}$$

where r_{ij} is the line for the center of particle i to the center of particle j.

The pressure is calculated as the mean of the diagonal components of the Cartesian mechanical pressure tensor. The bulk pressure is

$$p^{b} = \frac{1}{3}(P_{xx} + P_{zz} + P_{yy}). \tag{30}$$

This was also calculated for the fluid in the fcc lattice of solid spheres. However, we have not equated it to a thermodynamic property.

The fluid-solid surface tension was calculated for the single-sphere simulation case from the spherical mechanical pressure tensor,

$$\gamma = \frac{1}{R^2} \int_{R}^{r_0} (P_N - P_T) r^2 \mathrm{d}r. \tag{31}$$

Where $R = 5\sigma$ is the solid particle radius, and $r_0 = 14\sigma$ is a position in the fluid far away from the fluid-solid surface. The normal component is $P_N = P_{rr}$ and the tangential component is $P_T = (P_{\phi\phi} + P_{\theta\theta})/2$. This is the fluid-solid surface tension of the porous medium given that the surfaces are sufficiently far apart. This will be used to calculate the solid pressure, see equation 21.

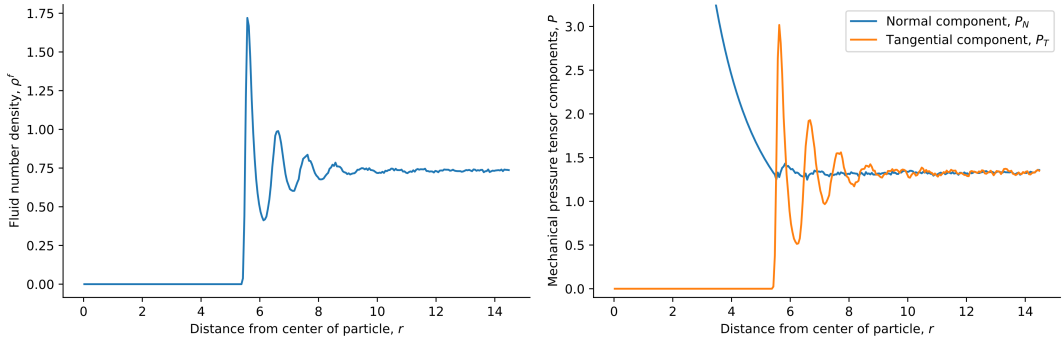

Figure 3: Local fluid number density (left) and normal and tangential pressure tensor components (right) in spherical shells as a function of the distance from the center of the spherical particle in the single-sphere simulation case. The fluid chemical potential is fixed to $\mu^f = 1\zeta$ and the particle radius is $R = 5\sigma$.

4 Results and discussion

4.1 Single solid particle surrounded by fluid

For the single solid sphere, we show the local fluid number density and mechanical pressure tensor components of the surrounding fluids in figure 3. The fluid chemical potential is fixed at the minimum of the pair-wise interaction potential, ζ, giving $\mu^f = 1\zeta$. At this fluid chemical potential, the bulk density is $\rho^b = 0.8\sigma^{-3}$. The fluid particles pack in layers close to the surface of the solid particle of radius $R = 5\sigma$, as reflected in the density variations in figure 3. The tangential component of the mechanical pressure tensor, shown in orange to the right in the figure, has the same variation. The normal and tangential components were used to calculate the surface tension, shown in figure 4 (see below). In this calculation, we do not equate the solid pressure to the mechanical pressure in any way. Inside the solid particle, the tangential component is zero. This is because the cut-off of the fluid-fluid interaction is relatively short, meaning that no fluid-fluid interaction contributes to the pressure inside the solid sphere. It is only the fluid-solid interactions that contribute to the pressure inside, and these contribute only to the normal component. The normal component is proportional to r^{-2} as a consequence, see Fig.3. This follows from mechanical equilibrium in spherical coordinates,

$$P_T(r) = P_N(r) + \frac{r}{2}\frac{\partial P_N}{\partial r}. \tag{32}$$

We used mechanical equilibrium and found that the mechanical pressure calculation in spherical coordinates is consistent with this.

The surface tension was calculated for a single solid sphere surrounded by fluid particles, as a function of the fluid chemical potential. This is presented in figure 4. It was calculated from the components of the mechanical pressure tensor, see equation 31. Fluid particles have reduced contact with each other and with the solid in the lower chemical potential-regime ($\mu^f \in [-7, -3]\zeta$), which is characterized by low densities. The surface tension is accordingly very small. The surface tension between fluid and solid increases sharply at a chemical potential of around $\mu^f = -2.3\zeta$. The increase indicates increasing interactions between particles (fluid-fluid and fluid-solid). For a chemical potential below $\approx 2.3\zeta$, the fluid is more vapor-like, while above this value, it is more liquid-like.

In figure 5 the corresponding solid pressure is shown as a function of fluid chemical potential for a single-sphere surrounded by fluid particles. It is calculated from the surface tension and bulk pressure, see equation 21. The bulk pressure monotonically increases with the fluid chemical potential.

So far, the variations are all expected from mechanical equilibrium and standard thermodynamics as given by

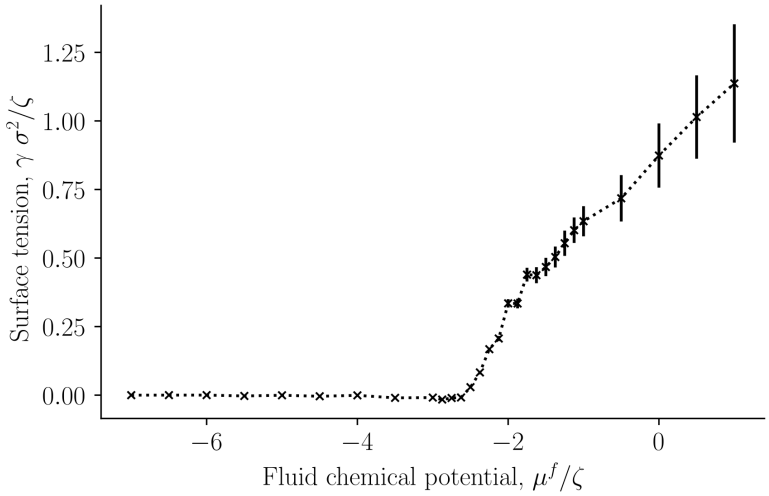

Figure 4: Surface tension for the single-sphere case γ as a function of fluid chemical potential μ^f.

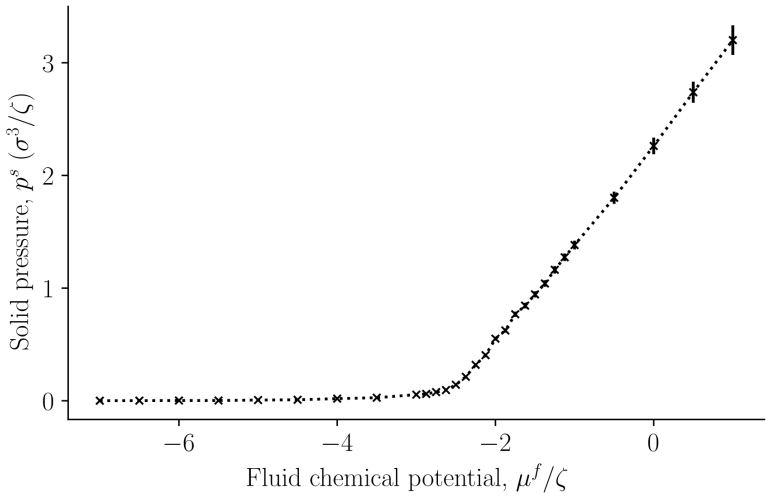

Figure 5: The solid pressure, p^s, in a single sphere, calculated from equation 21 as a function of the fluid chemical potential μ^f of the surrounding fluid.

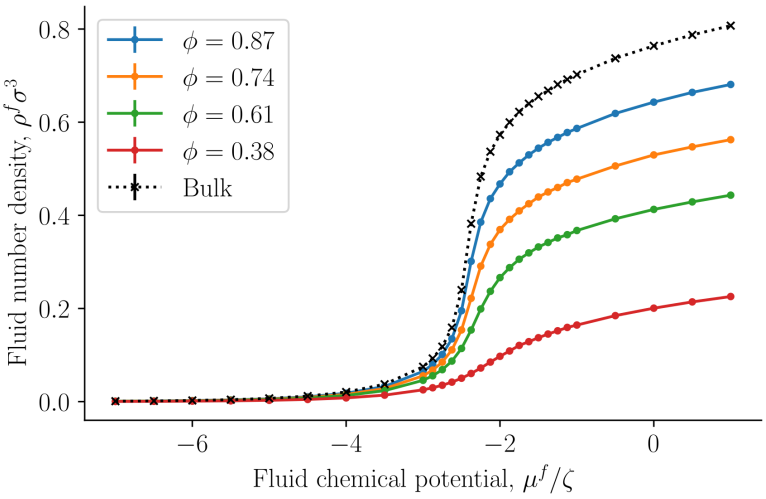

Figure 6: Fluid number density $\rho^f = N^f/V$ as a function of fluid chemical potential μ^f at varying porosity $\phi = V^f/V$.

the Young-Laplace equation. It is reasonable that the pressure of the solid increases monotonously, following the variation in the surface tension.

4.2 The fluid number density and the replica energy density

Figure 6 presents the fluid number density $\rho^f = N^f/V$, where V is the total REV volume, as a function of the controlled fluid chemical potential μ^f for various porosities ϕ of the fcc lattice. Results shown as black crosses represent bulk fluid or the limit where the porosity approaches unity. The fluid number density starts at approximately zero density for small fluid chemical potentials (a dilute gas-like phase) and converges to a density of a dense liquid-like phase. The fluid number density decreases with decreasing porosity, which is mainly because of decreased fluid volume compared to total volume. The fluid particles form layers on the solid surface, as was seen in figure 3.

The replica energy density is a characteristic property of the small system. It is shown for the first time for a regular fcc-lattice in figure 7. The property was obtained as the integral over the fluid density, of the fluid chemical potential, see equation 14. The replica energy density approaches the bulk fluid value (black crosses) in the thermodynamic limit of increasing porosity, as expected. We see a similar development in the replica energy density, as seen in the curve for the pressure of the solid around the single sphere. The replica energy is negative and increases with decreasing porosity. When compared with other thermodynamic properties like the internal energy (see below), the value is sizable. The system is small in the sense that it has non-negligible replica energy.

The integral solid chemical potential was next calculated from the fluid number density of the REV and the bulk, see equation 18. It is presented in figure 8 as a function of the fluid chemical potential. The integral solid chemical potential is much larger than the fluid chemical potential because each solid particle has a radius ten times larger than a fluid particle. This implies that each solid particle interacts with more particles than each fluid particle. The energy required to add one more solid particle is very large compared to adding one more fluid particle. Interestingly, the integral solid chemical potential is independent of the porosity, it is a function of fluid number density and fluid chemical potential. We interpret this to mean that the solid particle are sufficiently far away from each other, such that the integral solid chemical potential is unaffected by the porosity.

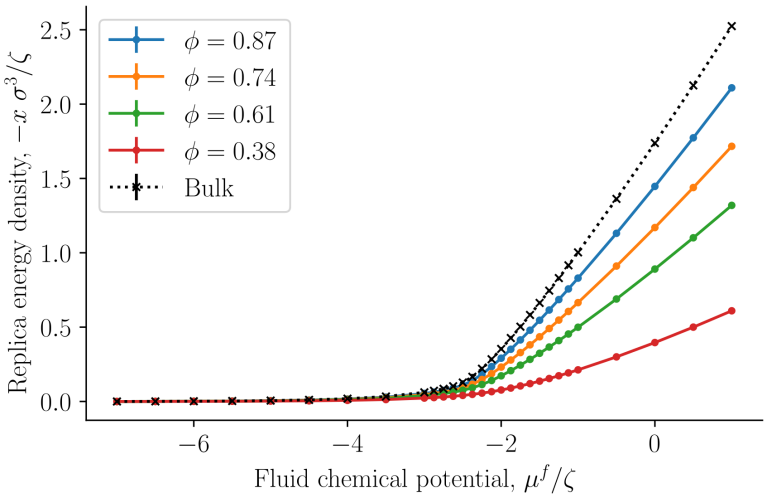

Figure 7: The negative replica energy density $-x = -X/V$ as a function of the fluid chemical potential μ^f at varying porosities $\phi = V^f/V$.

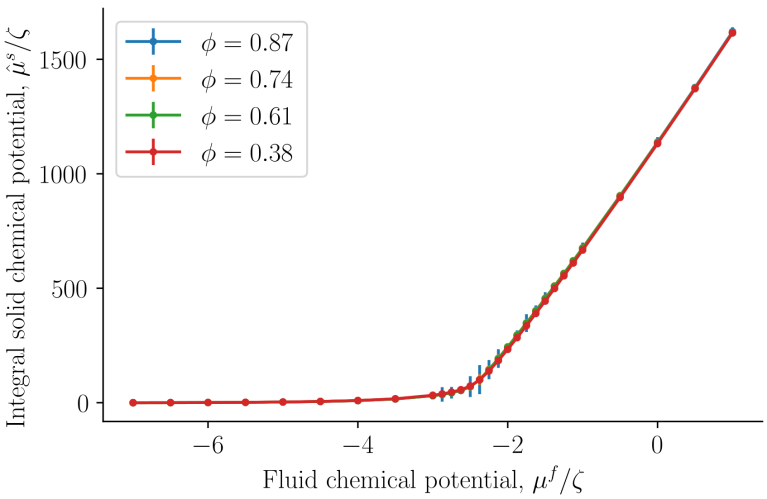

Figure 8: Integral solid chemical potential as a function of the fluid chemical potential μ^f at varying porosities $\phi = V^f/V$.

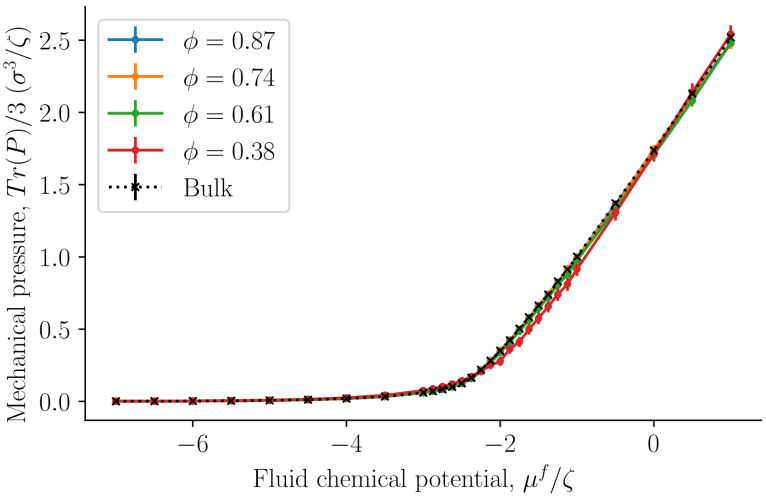

Figure 9: Trace of the mechanical pressure divided by three as a function of the fluid chemical potential μ^f for varying porosities $\phi = V^f/V$.

Figure 9 compares the average of the diagonal components of the mechanical pressure for the bulk fluid (black crosses) and the fcc lattice of spheres filled with fluid particles. The mechanical pressure was calculated in Cartesian coordinates for the whole simulation box, as described by equation 29. The bulk value was now equated to the thermodynamic bulk pressure, which was assumed to be equal to the integral pressure. Note that we did not equate the trace of the mechanical pressure tensor in the heterogeneous porous medium to any thermodynamic property. Figure 9 serves purely for a comparison. However, even though the geometry inside the porous medium is more complex than what can be captured by the Cartesian mechanical pressure tensor, the values fall almost on the same line. This could suggest that the mean of the diagonal components of the Cartesian mechanical pressure tensor gives the integral pressure. An exception is seen for the data obtained with the smallest porosity, $\phi = 0.38$, when fluid chemical potentials vary between approximately $\mu = -2\zeta$ and $\mu = -\zeta$. The given porosity is near the closest packing possible for spheres. While this is interesting, it may only hold for the present case, with a relatively simple structure.

4.2.1 Internal energy and entropy densities

The internal energy and entropy densities as a function of the fluid chemical potential are presented in figure 10 and 11, respectively. The internal energy and entropy are divided by the REV volume V to give the respective densities. The variation in the internal energy and entropy densities as a function of the fluid chemical potential, is similar to that shown by fluids above the critical point, when they are described by cubic equations of state, for example, the van der Waals equations of state. It is therefore reasonable that the maxima of the internal energy and entropy densities are a consequence of a structural transition that takes place at the chemical potential in question. This will explain why all maxima are located at the same chemical potential (-2.3 ζ). This location is close to the value of the chemical potential, where the fluid-solid surface tension starts to increase and also where the replica energy density begins to deviate stronger from its bulk value (see figures 4 and 7). The maxima locations remain at the same chemical potential, as the porosity decreases and are given by the location in the bulk fluid. It may therefore be possible to estimate this position using the equation of state for the bulk fluid. Thus, one can determine for

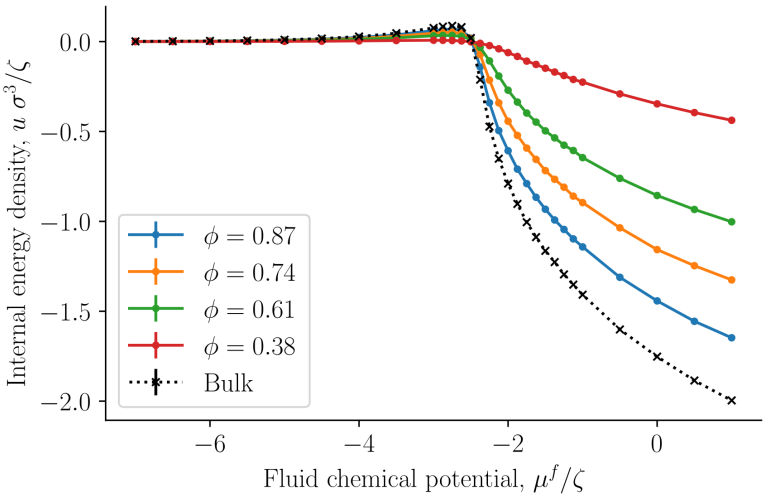

Figure 10: Internal energy density $u = U/V$ as a function of the fluid chemical potential μ^f for varying porosities $\phi = V^f/V$.

which fluid states it is particularly important to take the system size into account.

The absolute value of the internal energy density decreased with the porosity, reflecting the fact that the fluid number density decreased with the porosity. The entropy density became larger as we approached the bulk value. This observation is typical for phase transitions in small systems, it becomes less clear cut first order, and has less of a discontinuity in the phase variables [28].

4.3 Small system effects

A system is small when we need to take into account the subdivision potential to accurately describe the system. The smallness of a system can also be measured by the replica energy (for the present system, see equation 5). The replica energy depends in general on the set of control variables, and has accordingly an equivalent bulk variable [17]. It changes proportional to the subdivision potential. The value of the subdivision potential is included in the deviation of the replica energy from the corresponding value of a bulk fluid, see equation 5. This deviation can be seen in figure 7; it increases with decreasing porosity. While a change in replica energy is expected with additional contributions of the solid, the application of the replica energy as a variable allow us to quantify the smallness of the system, the smallness that originate from the subdivision potential. For evaluation of the state of smallness, the single contributions given in equation 5 must be computed independent of one another. We were not able to compute the subdivision potential here, but the replica energy density may still be used to assess whether small system effects can be neglected or not. This can be done by evaluating the total replica energy difference together with the entropy density. Consider for the purpose of such an evaluation the left-hand side of the peak in entropy density. Due to the small replica energy differences between the fluid bulk value and the corresponding values of the nanoporous medium for small chemical potentials, it may be speculated that the subdivision potential is negligible for vapor-like densities. On the right hand side of the peak, the difference is sizeable which is why the subdivision potential cannot be assumed to be negligible a priori. It must therefore be included in the thermodynamic analysis to ensure first-order Euler homogeneity in the total internal energy.

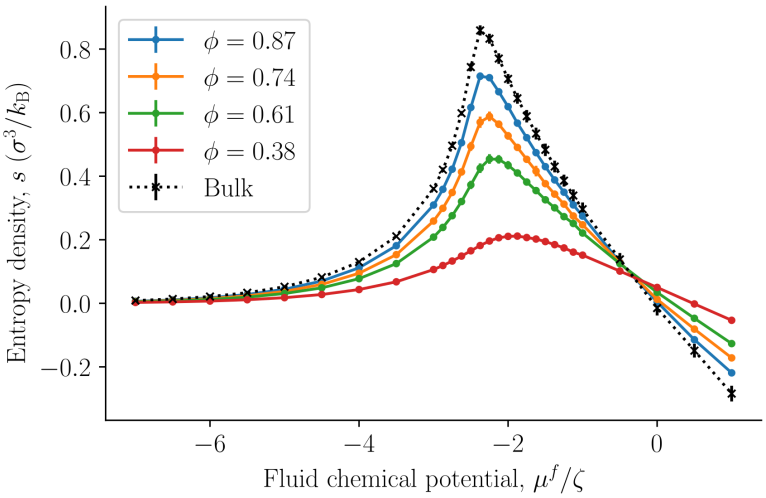

Figure 11: The entropy density $s = S/V$ as a function of the fluid chemical potential μ^f for varying porosities $\phi = V^f/V$. The integral pressure is assumed to be equal to the bulk pressure.

4.4 The pressure of a REV in a porous medium

We are now in a position to discuss, if not answer completely, the questions posed upfront; what is the pressure of a representative elementary volume (REV)?

In the present case, the structure of the porous system was regular fcc, and all different microstates are represented by a small REV, a unit cell for all practical purposes. A system with irregular structure has probably a larger REV. All thermodynamic properties defined, refer to the actual REV.

Equations 15,16 and 20 most central in the description. These relations were derived using Hill's systematic procedure for porous media with nanoscale pores. The effective pressure $\hat{p}$ of the REV was given in equation 15. We see that the expression is consistent with Young-Laplace equation. Not only a set of system variables is central in the theory; also the set of control variables need be specified. When this is done, we can arrive, in the present case, at the expression linking $\hat{p}$ to two unknown system variables.

In order to proceed, we have next taken the bold assumption stated in equation 16, that the integral pressure $\hat{p}$, which clearly differ from the differential pressure p, is constant across the medium at equilibrium. It is then not far from the next possible step; to construct the driving force for mass transport using $\hat{p}$.

The mean of the diagonal components of the Cartesian mechanical pressure tensor, presented in figure 9, gives a good approximation of the integral pressure for the largest porosities. This can give an alternative route to obtain the integral pressure when the porosity is large. However, for small porosities it deviates from the bulk pressure and the integral pressure.

5 Conclusion

The thermodynamic method of Hill for nanoscale systems was used to describe the thermodynamic state of a single-phase fluid confined to a porous medium. The size and shape of the porous media were restricted, such that the description can be said to be general for any porous media.

The system was open for fluid to be exchanged with the environment, while the solid was not allowed to be

exchanged with the environment. In addition, the temperature was controlled by the environment, and the fluid and solid volumes, surface area, and number of solid particles were controlled.

Nanothermodynamics introduces two new conjugate variables, the subdivision potential and the number of replicas. The subdivision potential was incorporated into the definition of the integral pressure and integral solid chemical potential. A fundamental assumption used in this work is that the integral pressure is constant everywhere in equilibrium. We have shown in previous works that this holds for simple porous media such as the slit pore [25, 23].

We have used this framework to demonstrate how to compute the fluid number density, replica energy density, integral solid chemical potential, internal energy density, and entropy density of a fluid confined to a face-centered cubic lattice of solid particles. The radius of the solid particles was ten times larger than the fluid particles, and the porosity varied from $\phi = 0.38$ to $\phi = 0.87$. These porosities range from almost closest packing to rather open structures. We have used this system as a relatively simple model of porous media, computing all its thermodynamic properties, in particular its integral and differential pressures, liquid-solid surface tension, and solid pressure of a single solid particle surrounded by fluid particles.

This way of defining the small system thermodynamic properties, for a given set of control variables, may be useful for the study of transport in non-deformable porous media.

Conflict of Interest Statement

The authors declare that the research was conducted in the absence of any commercial or financial relationships that could be construed as a potential conflict of interest.

Author Contributions

O.G. contributed to formal analysis, investigation, methodology, software, and visualization. D.B. and S.K contributed to supervision. All authors contributed to conceptualization, writing original drafts, reviewing, and editing. All authors have read and agreed to the published version of the manuscript.

Funding

This work was funded by the Research Council of Norway through its Centres of the Excellence funding scheme, project number 262644, PoreLab.

Acknowledgments

The simulations were performed on resources provided by UNINETT Sigma2 - the National Infrastructure for High-Performance Computing and Data Storage in Norway. We thank the Research Council of Norway.

References

[1] M. T. Rauter, S. K. Schnell, and S. Kjelstrup, "Cassie–Baxter and Wenzel States and the Effect of Interfaces on Transport Properties across Membranes," *J. Phys. Chem. B*, 2021.

[2] M. T. Rauter, S. K. Schnell, B. Hafskjold, and S. Kjelstrup, "Thermo-osmotic pressure and resistance to mass transport in a vapor-gap membrane," *Phys. Chem. Chem. Phys.*, 2021.

[3] M. Qasim, M. Badrelzaman, N. N. Darwish, N. A. Darwish, and N. Hilal, "Reverse osmosis desalination: A state-of-the-art review," *Desalination*, vol. 459, pp. 59–104, 2019.

[4] H. Li, J. P. Jakobsen, Ø. Wilhelmsen, and J. Yan, "PVTxy properties of CO2 mixtures relevant for CO2 capture, transport and storage: Review of available experimental data and theoretical models," *Appl. Energy*, vol. 88, no. 11, pp. 3567–3579, 2011.

[5] M. Ramdin, T. W. de Loos, and T. J. Vlugt, "State-of-the-art of CO2 capture with ionic liquids," *Ind. Eng. Chem. Res*, vol. 51, no. 24, pp. 8149–8177, 2012.

[6] M. E. Boot-Handford, J. C. Abanades, E. J. Anthony, M. J. Blunt, S. Brandani, N. Mac Dowell, J. R. Fernández, M.-C. Ferrari, R. Gross, J. P. Hallett, *et al.*, "Carbon capture and storage update," *Energy Environ. Sci.*, vol. 7, no. 1, pp. 130–189, 2014.

[7] M. Sauermoser, N. Kizilova, B. G. Pollet, and S. Kjelstrup, "Flow field patterns for proton exchange membrane fuel cells," *Front. Energy Res.*, vol. 8, p. 13, 2020.

[8] J. Wang, "Theory and practice of flow field designs for fuel cell scaling-up: a critical review," *Appl. Energy*, vol. 157, pp. 640–663, 2015.

[9] L. Spitthoff, A. F. Gunnarshaug, D. Bedeaux, O. Burheim, and S. Kjelstrup, "Peltier effects in lithium-ion battery modeling," *J. Chem. Phys*, vol. 154, no. 11, p. 114705, 2021.

[10] A. F. Gunnarshaug, S. Kjelstrup, D. Bedeaux, F. Richter, and O. S. Burheim, "The reversible heat effects at lithium iron phosphate-and graphite electrodes," *Electrochim. Acta*, vol. 337, p. 135567, 2020.

[11] Y. Zhao, P. Stein, Y. Bai, M. Al-Siraj, Y. Yang, and B.-X. Xu, "A review on modeling of electro-chemo-mechanics in lithium-ion batteries," *J. Power Sources*, vol. 413, pp. 259–283, 2019.

[12] S. M. Hassanizadeh and W. G. Gray, "Mechanics and thermodynamics of multiphase flow in porous media including interphase boundaries," *Adv. Water Resour.*, vol. 13, no. 4, pp. 169–186, 1990.

[13] S. Kjelstrup, D. Bedeaux, A. Hansen, B. Hafskjold, and O. Galteland, "Non-isothermal transport of multi-phase fluids in porous media. the entropy production," *Front. Phys.*, vol. 6, p. 126, 2018.

[14] S. Kjelstrup, D. Bedeaux, A. Hansen, B. Hafskjold, and O. Galteland, "Non-isothermal transport of multi-phase fluids in porous media. Constitutive equations," *Front. Phys.*, vol. 6, p. 150, 2019.

[15] J. Bear, *Dynamics of fluids in porous media*. Courier Corporation, 1988.

[16] M. J. Blunt, *Multiphase flow in permeable media: A pore-scale perspective*. Cambridge University Press, 2017.

[17] D. Bedeaux, S. Kjelstrup, and S. K. Schnell, *Nanothermodynamics. General theory*. NTNU, Trondheim, Norway, 2020.

[18] J. Irving and J. G. Kirkwood, "The statistical mechanical theory of transport processes. IV. The equations of hydrodynamics," *J. Chem. Phys.*, vol. 18, no. 6, pp. 817–829, 1950.

[19] P. Schofield and J. R. Henderson, "Statistical mechanics of inhomogeneous fluids," *Proc. R. Soc. Lon. Ser.-A*, vol. 379, no. 1776, pp. 231–246, 1982.

[20] J. N. Israelachvili, *Intermolecular and surface forces*. Academic press, 2015.

[21] B. Derjaguin, "Untersuchungen über die Reibung und Adhäsion, IV," *Kolloid Z.*, vol. 69, no. 2, pp. 155–164, 1934.

[22] O. Galteland, D. Bedeaux, B. Hafskjold, and S. Kjelstrup, "Pressures inside a nano-porous medium. The case of a single phase fluid," *Front. Phys.*, vol. 7, p. 60, 2019.

[23] O. Galteland, D. Bedeaux, and S. Kjelstrup, "Nanothermodynamic description and molecular simulation of a single-phase fluid in a slit pore," *Nanomaterials*, vol. 11, no. 1, p. 165, 2021.

[24] O. Galteland, E. Bering, K. Kristiansen, D. Bedeaux, and S. Kjelstrup, "Legendre-Fenchel transforms capture layering transitions in porous media," *arXiv preprint arXiv:2111.15253*, 2021.

[25] M. T. Rauter, O. Galteland, M. Erdős, O. A. Moultos, T. J. Vlugt, S. K. Schnell, D. Bedeaux, and S. Kjelstrup, "Two-Phase Equilibrium Conditions in Nanopores," *Nanomaterials*, vol. 10, no. 4, p. 608, 2020.

[26] M. Erdős, O. Galteland, D. Bedeaux, S. Kjelstrup, O. A. Moultos, and T. J. Vlugt, "Gibbs Ensemble Monte Carlo Simulation of Fluids in Confinement: Relation between the Differential and Integral Pressures," *Nanomaterials*, vol. 10, no. 2, p. 293, 2020.

[27] T. L. Hill, *Thermodynamics of small systems, part 1.* Benjamin, 1963.

[28] T. L. Hill, *Thermodynamics of small systems, part 2.* Benjamin, 1964.

[29] V. Bråten, D. Bedeaux, Ø. Wilhelmsen, and S. K. Schnell, "Small size effects in open and closed systems: What can we learn from ideal gases about systems with interacting particles?," *J. Chem. Phys.*, vol. 155, no. 24, p. 244504, 2021.

[30] S. Plimpton, "Fast parallel algorithms for short-range molecular dynamics," *J. Comput. Phys.*, vol. 117, no. 1, pp. 1–19, 1995.

[31] A. P. Thompson, H. M. Aktulga, R. Berger, D. S. Bolintineanu, W. M. Brown, P. S. Crozier, P. J. in't Veld, A. Kohlmeyer, S. G. Moore, T. D. Nguyen, *et al.*, "LAMMPS-A flexible simulation tool for particle-based materials modeling at the atomic, meso, and continuum scales," *Comput. Phys. Commun.*, p. 108171, 2021.

[32] A. Stukowski, "Visualization and analysis of atomistic simulation data with OVITO–the Open Visualization Tool," *Model. Simul. Mater. Sc.*, vol. 18, no. 1, p. 015012, 2009.

[33] S. Nosé, "A unified formulation of the constant temperature molecular dynamics methods," *J. Chem. Phys.*, vol. 81, no. 1, pp. 511–519, 1984.

[34] W. G. Hoover, "Canonical dynamics: Equilibrium phase-space distributions," *Phys. Rev. A*, vol. 31, no. 3, p. 1695, 1985.

[35] W. Shinoda, M. Shiga, and M. Mikami, "Rapid estimation of elastic constants by molecular dynamics simulation under constant stress," *Phys. Rev. B*, vol. 69, no. 13, p. 134103, 2004.

[36] D. Frenkel and B. Smit, *Understanding Molecular Simulation: From Algorithms to Applications*, vol. 1. Elsevier, 2001.

[37] B. Hafskjold, K. P. Travis, A. B. Hass, M. Hammer, A. Aasen, and Ø. Wilhelmsen, "Thermodynamic properties of the 3D Lennard-Jones/spline model," *Mol. Phys.*, vol. 117, no. 23-24, pp. 3754–3769, 2019.

[38] K. R. Kristiansen, "Transport Properties of the Simple Lennard-Jones/Spline Fluid I: Binary Scattering and High-Accuracy Low-Density Transport Coefficients," *Front. Phys.*, vol. 8, p. 271, 2020.

[39] T. Ikeshoji, B. Hafskjold, and H. Furuholt, "Molecular-level calculation scheme for pressure in inhomogeneous systems of flat and spherical layers," *Mol. Simulat.*, vol. 29, no. 2, pp. 101–109, 2003.

[40] Y. Long, J. C. Palmer, B. Coasne, M. Śliwinska-Bartkowiak, and K. E. Gubbins, "Pressure enhancement in carbon nanopores: a major confinement effect," *Phys. Chem. Chem. Phys.*, vol. 13, no. 38, pp. 17163–17170, 2011.

[41] D. van Dijk, "Comment on "Pressure enhancement in carbon nanopores: a major confinement effect" by Y. Long, J. C. Palmer, B. Coasne, M. Sliwinska-Bartkowiak and K. E. Gubbins, Phys. Chem. Chem. Phys., 2011, 13, 17163," *Phys. Chem. Chem. Phys.*, vol. 22, no. 17, pp. 9824–9825, 2020.

[42] Y. Long, J. C. Palmer, B. Coasne, K. Shi, M. Śliwińska-Bartkowiak, and K. E. Gubbins, "Reply to the 'Comment on "Pressure enhancement in carbon nanopores: a major confinement effect"' by D. van Dijk, Phys. Chem. Chem. Phys., 2020, 22," *Phys. Chem. Chem. Phys.*, vol. 22, no. 17, pp. 9826–9830, 2020.

[43] A. Harasima, "Molecular theory of surface tension," *Adv. Chem. Phys*, vol. 1, pp. 203–237, 1958.

Article IX

Olav Galteland, Michael T. Rauter, Mina Bratvold, Thuat Trinh, Dick Bedeaux, Signe Kjelstrup

Local Thermodynamic Description of Isothermal Single-Phase Flow in Porous Media

Submitted 2022
DOI: 10.48550/arXiv:2203.02334

Article IX

Article IX

Local thermodynamic description of isothermal single-phase flow in porous media

Olav Galteland[a,*], Michael T. Rauter[a], Mina S. Bratvold[a], Thuat T. Trinh[a], Dick Bedeaux[a], and Signe Kjelstrup[a]

[a]PoreLab, Department of Chemistry, Norwegian University of Science and Technology
[*]Corresponding author: olav.galteland@ntnu.no

March 7, 2022

Abstract

Darcy's law for porous media transport is given a new local thermodynamic basis in terms of the grand potential of confined fluids. The local effective pressure gradient is determined using non-equilibrium molecular dynamics, and the hydraulic conductivity and permeability are investigated. The transport coefficients are determined for single-phase flow in face-centered cubic lattices of solid spheres. The porosity changed from that in the closest packing of spheres to near unity in a pure fluid, while the fluid mass density varied from that of a dilute gas to a dense liquid. The permeability varied between $5.7 \times 10^{-20}\,\mathrm{m}^2$ and $5.5 \times 10^{-17}\,\mathrm{m}^2$, showing a porosity-dependent Klinkenberg effect. Both transport coefficients depended on the average fluid mass density and porosity but in different ways. These results set the stage for a non-equilibrium thermodynamic investigation of coupled transport of multi-phase fluids in complex media.

Keywords: nanothermodynamics, Hill's thermodynamics of small systems, non-equilibrium thermodynamics, non-equilibrium molecular dynamics, nanoporous media, compressible flow, representative elementary volume

1 Introduction

Porous media are everywhere in nature and technology, and transport through them is important. To take some widely different examples; we need to describe the transport of nanoparticles across cell layers with medicine to cancerous tissue [1]. We also need to describe the selective transport across the porous separators in batteries and fuel cells [2]. We are aiming for a description that reflects the underlying properties of the single pores.

Much of the fundamental work on flow in porous media has been done for the pore-scale, see Helmig for a pedagogical presentation [3]. Recent developments in imaging techniques and computer capabilities have improved our understanding of the physics at pore-scale considerably [4]. But there is no consensus on how to upscale from the pore-scale to the Darcy scale. On the Darcy scale, transport is described as taking place between representative elementary volumes (REVs).

The REV in this work is defined to be large enough to be statistically representative of the system. From a statistical mechanics point of view, the REV includes all available microstates of the system. In this work, we are investigating a compressible single-phase fluid in a porous structure made up of solid particles in a face-centered cubic (fcc) lattice. The system is illustrated in Fig. 1. The blue large spheres represent solid, while the red particles

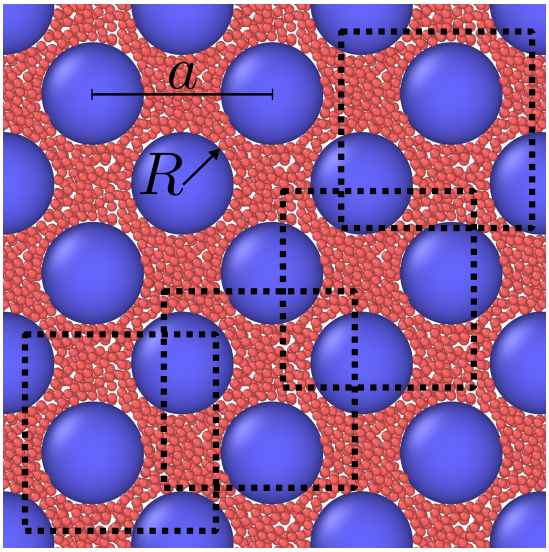

Figure 1: The representative elementary volume (REV) for a single-phase fluid in a face-centered cubic lattice of solid spheres is the same size as the unit cell of the lattice. The radius of the solid particles is R and the lattice constant is a. The squares with dashed lines mark the magnitude of the REV. All regions have the same thermodynamic properties.

represent the fluid. We shall use additive variables to define the REV, similar to Whitaker [5]. This definition of the REV differs from the one suggested by Nordahl and Ringrose [6] who used a constant permeability as criterion. Because of the fcc symmetry, a unit cell is here a proper choice of REV. Around any point in the porous medium, we can choose a unit cell with this point at its center. In this way, we can obtain a continuous path between unit cells on the REV scale. We first determine the pressures of the REV at equilibrium, as a function of the temperature, fluid mass density, and porosity, $\hat{p}(T, \rho_f, \phi)$. This can be regarded as finding the equation of state of the REV. Up to this point, we have used REV densities much like Whitaker [5].

Thermodynamic theories for transport in porous media are little developed. In confinement, fluid thermodynamic properties will deviate from their corresponding bulk phase values. In an attempt to find a continuous description on the Darcy scale, we need to reflect on properties of the pore scale or sub-pore scale, including the nanometer scale. Hence, we need descriptions of fluxes and forces for the REV of the porous medium. Is it possible to find a description that does not explode in complexity, but still brings forward the characteristic properties of the smaller scale, such as wetting and adsorption? Pore-scale descriptions of REVs have contained up to 27 variables [7]. We have claimed that we can reduce the number of variables to a more practical number, and describe here the first steps in the direction to apply this relatively new thermodynamic procedure for coarse-graining [8, 9, 10].

In our search for a thermodynamic coarse-graining procedure to be applied to transport in porous media, we have chosen to define effective thermodynamic variables by sets that combine in an additive manner [11, 12, 10]. We have derived the Gibbs equation for the REV, and in the analysis of transport, we have assumed validity of Gibbs equation. This gives the entropy production for the REV and a thermodynamic basis for Darcy's law in isothermal system. Our proposal to find the equation of state and the Gibbs equation is new. Here, we apply the method to isothermal, compressible, single-phase flow. This entails obtaining the REV grand potential as the sum of contributions from all phases and surfaces. A theory of transport on the Darcy scale follows in a way which is

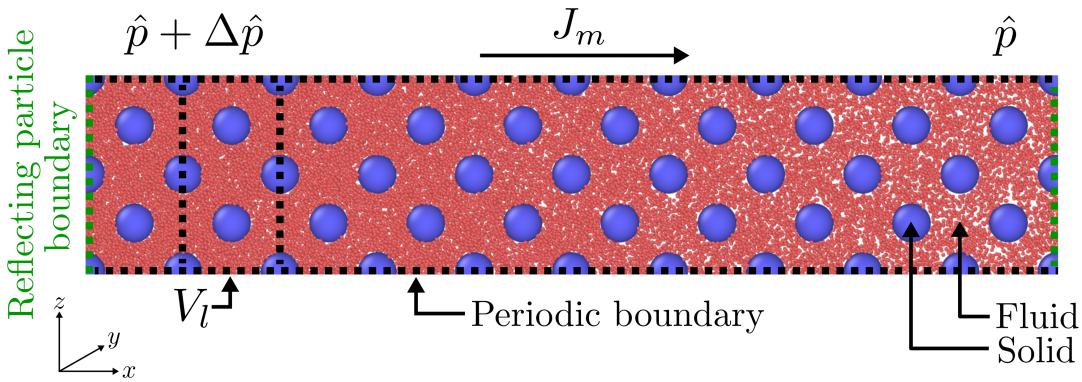

Figure 2: A visualization of a simulation, with porosity $\phi \approx 0.87$ and average bulk fluid mass density $\rho_b = (237 \pm 1)\,\mathrm{kg/m^3}$. The blue particles represent the solid particles of a fcc lattice, while the red particles represent the fluid particles. There is an integral pressure difference $\Delta\hat{p}$, which drives a mass flux J_m from left to right. The slab of volume V_l was used as REV. The simulation box had periodic boundaries in all directions (black dashed line), apart from particles crossing the x-boundary from left to right. Here the reflecting particle method was applied, see section 3 for details of this boundary condition [25]. The simulated system was visualized with OVITO [26].

standard in non-equilibrium thermodynamics.

An excellent tool to analyze transport in porous media is non-equilibrium molecular dynamics (NEMD) [13]. This tool allows us to simulate molecular properties (like velocities and forces), yet upscale to fluid properties (like pressure) on the Darcy scale. In NEMD, we solve Newton equations for particles, so the outcome can also be used to assess assumptions made in the thermodynamic theory. In this sense the tool supplements lattice Boltzmann simulations and numerical solutions to the Navier-Stokes equation. A downside is that the length and time scale becomes limited as NEMD is a computationally expensive technique. Here, we will use NEMD to simulate the flow of methane-like molecules in a face-centered cubic (fcc) lattice made up of spherical solid particles, see Fig. 2. We will investigate a vast range of fluid densities, which varies from highly compressible to nearly incompressible. NEMD has been used to simulate many transport processes in heterogeneous media, as documented by, for example, Ikeshoji and Hafskjold [14, 15, 16].

We use our coarse-graining procedure to obtain the effective pressure of the REV. Its negative gradient is the driving force for fluid flow. The effective pressure of a REV, $\hat{p}$, is called the integral pressure. It is in general a combination of pressures, surface tensions, and line tensions. This approach originates from nanothermodynamics, as described by Hill [17]. We believe, however, that this procedure for other porous media and other fluids. We have shown that the method can replace the use of Young or Young-Laplace's law [9]. For a recent formulation of nanothermodynamics, see Bedeaux, Kjelstrup, and Schnell [18].

It is our long-range aim to obtain a procedure that provides equations of transport in porous media in general. Not only for isothermal transport of one fluid but also coupled transport due to other driving forces, for example, thermal driving forces [19, 20]. We start with a single-phase flow, to document the use of new concepts on porous media pressure in a simple way. We have reported equilibrium studies with this coarse-graining procedure previously [8, 21, 9, 22, 23, 24]. We expand these results to non-equilibrium conditions in this work.

This work aims to analyze this simple transport problem and compare its results to expressions that are common in the literature, most importantly Darcy's law in the presence of the Klinkenberg effect [3], but also the Kozeny-Carman equation [27, 28, 29, 30].

Fig. 2 illustrates the chosen system, a fcc lattice of solid particles (blue), all with radius R, and a lattice constant

a. The porosity ϕ is varied by varying a. The lattice is periodic in all directions. The REV is the size of the lattice unit cell [8], but here we chose to integrate to a slab of volume V_l. The volume V_l contains four unit cells and is practical for the purpose. A pressure difference arises using a reflecting particle boundary, which forces a mass flux J_m through the cross-sectional area. This boundary-driven method gives minimal disturbance of fluid particles away from the boundary.

In Section 2, we recapitulate the necessary thermodynamic equilibrium relations of the pertinent REV, followed by a description of transport, and a procedure to find pressure profiles away from equilibrium. The equilibrium and non-equilibrium simulation procedures that are applied, are described in Section 3. The results are discussed in Section 4. We give the results needed to determine the local driving force inside the porous medium. The equation of state of the porous medium is central here. The hydraulic conductivity and the permeability are however strong functions of porosity and average fluid mass density. We shall also see that the Klinkenberg correction, as described by Helmig [3], applies to the fluid permeability.

2 The thermodynamic variables of the REV

2.1 The grand potential and the pressure

We have chosen to describe the state of a porous medium using a basis set of thermodynamic variables that are additive in the sense that each coarse-grained variable in the REV is a sum of contributions from all bulk phases, surfaces, and possible contact lines [11, 12, 10]. The REV variables are controlled by the environment [18]. In the present case, the control variables are temperature, volume, and fluid chemical potential. The REV of interest belongs therefore to a grand canonical ensemble. We recapitulate the thermodynamic description of a REV of this kind at equilibrium before we define the situation in the presence of flow.

In nanothermodynamic theory, the grand potential Υ of the REV is given by minus the so-called *integral* pressure of the REV times the volume. The adjective "integral" was coined by Hill [17] to reflect the fact that it is an integrated property. Conversely, the normal pressure was called the differential pressure. We can regard the integral pressure as the *effective* pressure of the REV. The grand potential is,

$$\Upsilon = -\hat{p}V. \tag{1}$$

In this expression, $\hat{p}$ and V are the integral pressure and the volume of the REV, respectively. It can be understood as the defining equation for $\hat{p}$. The grand potential has its basis in statistical mechanics

$$\Upsilon = -k_{\mathrm{B}}T \ln \Xi, \tag{2}$$

where Ξ is the grand canonical partition function, k_{B} is Boltzmann's constant, and T is the temperature. This basis explains why Υ has additive contributions. Weakly coupled sub-systems will add to Υ, and result in a product of partition functions. This expression explains also why the REV needs to include all possible micro-states of the system.

A more colloquial name of the grand potential is the compressional energy, since it is a product of pressure and volume, which is related to work. In the present case, the grand potential has several additive contributions. We obtain

$$\hat{p}V = \hat{p}_f V_f + \hat{p}_s V_s - \hat{\gamma}A \tag{3}$$

The contributions are from the fluid and solid phases, and the fluid-solid surface. The symbols $\hat{p}_f$, $\hat{p}_s$ are the integral pressure of the fluid and solid, respectively, and $\hat{\gamma}$ is the integral fluid-solid surface tension. The surface energies are

more significant because of the fluid confinement. For large fluid volumes, the surface energy may be neglected. However, when Young-Laplace's and Young's equations are significant for multi-phase flow the surface energies in this equation are too. The volume of the fluid and solid are V_f and V_s, respectively, and A is the surface area between the solid and the fluid. The sum of the fluid and solid volumes is equal to the REV volume $V = V_f + V_s$, and the porosity is $\phi = V_f/V$. It follows that the fluid mass density of the REV is

$$\rho_f = \frac{M_f}{V_f + V_s} \tag{4}$$

where M_f is the mass of the fluid in the REV. This fluid mass density follows the coarse-graining procedure. This density is not the internal density given by M_f/V_f. The individual contributions to the integral pressure are not needed, we only need the total sum. The integral pressure is obtained by calculating an equation of state in equilibrium conditions, which is applied to non-equilibrium conditions. The equation of state for the porous medium must as all equations of state be found from experiments or simulations. In the present work, the last method gives the equation of state for the present medium

$$\hat{p} = \hat{p}(T, \rho_f, \phi). \tag{5}$$

The functional dependence of $\hat{p}$ on the variables (ρ_f, ϕ) will here be investigated by simulations at isothermal conditions. The value of $\hat{p}$ shall also be found by dividing both sides of Eq. 3 by the REV volume. This gives

$$\hat{p} = \hat{p}_f \phi + \hat{p}_s(1 - \phi) - \hat{\gamma} A/V. \tag{6}$$

In earlier work we determined $\hat{p}_s$ from known values of A, V and ϕ [8]. Here we shall use Eq. 6 to compute $\hat{p}$ and compare the result to the result from Eq. 5. Both procedures are completely general. In Eq. 6 we apply an independent computation of the single parameters. The two expressions will be shown here to give the same result.

The general relation between the differential and integral pressures is given by

$$p = \left[\frac{\partial(\hat{p}V)}{\partial V}\right]_{T,\mu} = \hat{p} + V\left(\frac{\partial \hat{p}}{\partial V}\right)_{T,\mu} \tag{7}$$

This shows that p or $\hat{p}$ can enter the equation of state for the porous medium, see Eq. 5. The fcc lattice used in the present model poses a special condition on the two pressures. Because of the lattice symmetry, the integral pressure will not depend on the REV volume, giving the special condition $p = \hat{p}$ for the REV. Any block of adjacent unit cells will therefore also give the same value of $\hat{p}$, see Fig. 1. It follows that the integral pressure in this lattice is independent of the size of the REV. As a consequence, the differential pressure of the REV is identical to the integral pressure, $p = \hat{p}$ for the REV. This is only the case for this special system, and not in general. To be general, we will keep the integral pressure $\hat{p}$.

Such an equality does *not* apply for $\hat{p}_f$, $\hat{p}_s$ and $\hat{\gamma}$, which in general differ from p_f, p_s and γ. Only if the spheres are far apart, $\hat{p}_f = p_f$, and if the spheres are large enough, also $\hat{\gamma} = \gamma$. This was the special case considered before [8]. In that work, we required that the fluid volume was so large that the fluid pressure was equal to the bulk pressure and that the fluid-solid curvature was so small that the surface tension did not depend on it. By using such requirements, we cannot take into account any disjoining pressure [31] or Tolman length [32]. The procedure in this work is more general and can describe such effects and other capillary effects.

The presence of additional fluid phases would contribute by similar terms to Eq. 6. The saturation will appear as a variable, and there are contributions from three-phase contact lines. Eq. 6 is an alternative definition of the integral pressure of the REV. When there is equilibrium at the boundary between the porous medium and the bulk

phase surrounding the porous medium, we have the condition

$$\hat{p} = p_b. \tag{8}$$

This condition was recently used to determine the solid integral pressure $\hat{p}_s$ [22]. We shall here use the relation 8 to determine the REV integral pressure in the equation of state (Eq. 5). The equation of state is next applied to non-equilibrium conditions assuming local equilibrium. This procedure is possible for any geometry.

2.2 The effective pressure gradient

The Gibbs equation can be written in terms of coarse-grained variables of the REV, as described in the previous section. By introducing the entropy, mass, and energy balance equations, we can then obtain the entropy production of the REV. In the present isothermal single-phase case, the entropy production has only one flux-force product. The flux conjugate to the negative pressure gradient is the volume flux, J_V

$$J_V = -l\frac{\partial \hat{p}}{\partial x}. \tag{9}$$

This expression gives a *thermodynamic* basis for Darcy's law; which is a locally linear relationship between the volume flux and the driving force valid for the porous medium. According to non-equilibrium thermodynamics, this equation does not assume laminar flow conditions. The only assumption is that there is local equilibrium and that the fluxes are linear combinations of the forces. These assumptions have been shown to hold for coupled heat and mass transport through liquid-vapor interfaces [33] and membranes [34]. The conductivity coefficient (the hydraulic conductivity), l, is a function of state variables. The driving force is not necessarily constant along the medium. We need the local value of $\partial\hat{p}/\partial x$ and J_V to find l.

When the porous medium is in contact with bulk fluids at both ends, the boundary condition will always give $\Delta\hat{p} = \Delta p_b$. In the experimental situation, the gradient is the pressure difference divided by the length L of the medium and the conductivity coefficient is the coefficient l obtained from

$$J_V = -l\frac{\Delta\hat{p}}{L} = -l\frac{\Delta p_b}{L}. \tag{10}$$

The permeability k enters Darcy's law on the form

$$J_V = -\frac{k}{\eta_b}\frac{\Delta\hat{p}}{L} = -\frac{k}{\eta_b}\frac{\Delta p_b}{L}, \tag{11}$$

where η_b is the shear viscosity of the bulk fluid, and

$$l = \frac{k}{\eta_b} \tag{12}$$

The volume flux is related to the mass flux by the fluid mass density, $J_V = J_m/\rho_f$. While J_V varies, J_m is constant in the steady state,

$$J_m = J_V\rho_f = -\rho_f\frac{k}{\eta_b}\frac{\partial\hat{p}}{\partial x}. \tag{13}$$

We shall determine the coefficients l and k from the last two equations, with information of the mass flux J_m, fluid mass density of the REV, ρ_f, and integral pressure gradient $\partial\hat{p}/\partial x$. Their dependence on the fluid mass density ρ_f and the porosity ϕ is of interest.

The original form of Darcy's law was obtained experimentally for the laminar flow of a single-phase fluid through

a porous medium. It has also been given a mechanical basis [3]. The Reynolds number, used to characterize flow patterns, is here calculated from $\mathrm{Re} = 2RJ_m/\eta_b$, where J_m is the mass flux, and $2R$ the diameter of the solid particles. For Reynolds numbers considered in this work, the flow is laminar [3].

A question of general interest is how the permeability of a porous medium, as used in Darcy's law, can be related to the properties of the porous medium. A well-known approach for a bed of granular solids is given by the Kozeny-Carman equation. As the name suggests, it was first derived by Kozeny [27], assuming that the fluid in the porous medium could be described as contained in a set of non-interfering parallel channels with the same internal surface and pore volume, as the medium itself. The solid phase was a packed bed. The general equation was written as [27, 28, 29, 30]

$$J_V = -\frac{\tau^2 V^2 \phi^3}{c_0 A^2} \frac{1}{\eta_b} \frac{\Delta p}{L} \tag{14}$$

where ϕ is the porosity, c_0 denotes the Kozeny constant, τ is the tortuosity, and A/V is the surface-to-volume ratio. The tortuosity is the average length a particle travels across the medium divided by the medium length L. For monodisperse spheres of diameter d the permeability simplifies to

$$k = \frac{\tau^2 d^2}{c_0} \frac{\phi^3}{(1-\phi)^2}. \tag{15}$$

Klinkenberg gave a correction for low-density compressible fluids with basis in fluid slippage at the wall [35]. When this correction is included, the effective permeability, k, is written as

$$k = k_0 \left(1 + \frac{b}{p}\right) \tag{16}$$

where k_0 is the absolute permeability and b is the Klinkenberg constant [3]. The correction was found to be relevant for permeabilities k¡ 10 $^{-13}$ m^2 [36].

3 Molecular simulations

3.1 The porous medium

Systems of a single-phase and single-component fluid were simulated in a porous structure using molecular dynamics simulations with LAMMPS [37]. The porous solid structure was composed of solid spherical particles in a face-centered cubic (fcc) lattice. The fluid particles were free to move, while the solid particles were immovable. As a consequence, the porous medium was non-deformable. The mass of the fluid particles was m, while the mass of the solid particle was not defined since they were immovable. The radius of the solid particles was R and the lattice constant was a.

The particles interacted with the Lennard-Jones/spline potential, which is a pair-wise interaction potential that models non-bonded neutral atom interactions. It is for example an accurate model for noble gasses and methane [38, 39, 40, 41]. See Hafskjold *et al.* [42] and Kristiansen [43] for details on the thermodynamic and transport properties for this potential. The potential is

$$u(r) = \begin{cases} \infty & \text{if } r \le d, \\ 4\epsilon \left[\left(\frac{\sigma}{r-d}\right)^{12} - \left(\frac{\sigma}{r-d}\right)^{6} \right] & \text{if } d < r \le r_s, \\ a(r-r_c)^2 + b(r-r_c)^3 & \text{if } r_s < r \le r_c, \\ 0 & \text{if } r > r_c. \end{cases} \tag{17}$$

Where $r = \|\boldsymbol{r}_j - \boldsymbol{r}_i\|$ was the distance between particle i and j. The interaction strength was characterized by the depth of the interaction potential ϵ, and the particle diameter was characterized by the distance σ. The hard-core diameter of the particles was d. The parameters a, b, r_s and r_c were set such that the potential and its derivative were continuous at r_s and r_c.

The simulation data were related to SI units by using parameters ϵ, σ, and the fluid particle mass m for methane [38, 39]. The aim of this is not to give accurate data for methane transport, but rather to present more identifiable values. The parameters were in terms of SI units

$$\epsilon/k_\mathrm{B} = 148.1\,\mathrm{K}, \quad \sigma = 0.381\,\mathrm{nm}, \quad \text{and} \quad m = 2.661 \times 10^{-26}\,\mathrm{kg}. \tag{18}$$

The parameters $\epsilon_\mathrm{ff} = \epsilon_\mathrm{fs} = \epsilon$ and $\sigma_\mathrm{ff} = \sigma_\mathrm{fs} = \sigma$ were equal for the fluid-fluid and solid-fluid interactions, while the hard-core diameter was zero for the fluid-fluid interactions $d_\mathrm{ff} = 0$ and $d_\mathrm{fs} = 4.5\sigma \approx 1.7\,\mathrm{nm}$ for the fluid-solid interactions. The solid did not interact with other solid particles. The radius of the solid was constant and defined to be $R := d_\mathrm{fs} + \sigma_\mathrm{fs}/2 = 5\sigma \approx 1.9\,\mathrm{nm}$, at which point the potential energy of the fluid-solid interaction is zero. The fluid-solid slip conditions were not precisely defined, but depended on the shape of the fluid-solid surface and fluid-solid interactions. The fluid-solid surface was completely smooth.

The lattice constant was varied from $a = 2\sqrt{2}R \approx 5.4\,\mathrm{nm}$ to $a = 40\sigma \approx 15.2\,\mathrm{nm}$, where the lower limit is where the surface of the solid particles are in contact. The porosity and surface-to-volume ratio of the porous structure were

$$\phi = 1 - \frac{16\pi R^3}{3a^3} \quad \text{and} \quad A/V = \frac{16\pi R^2}{a^3}. \tag{19}$$

Consequently, the porosity varied from 0.26 to 0.97 and the surface-to-volume ratio varied between approximately $0.05\,\mathrm{nm}^{-1}$ and $1.17\,\mathrm{nm}^{-1}$. The fcc lattice has four octahedral and eight tetrahedral voids. The octahedral voids are the largest and can accommodate a sphere of radius $a/2 - R$, which varies from 0.8 nm to 5.7 nm in the cases studied here.

3.2 Shear viscosity

The shear viscosity of the bulk fluid was calculated with the OCTP plugin [44] from the time-integral of the auto-correlation function of the off-diagonal components of the Cartesian mechanical pressure tensor,

$$\eta_{\alpha\beta} = \lim_{t\to\infty} \frac{1}{2t} \frac{V}{k_B T} \left\langle \left(\int_0^t P_{\alpha\beta}\left(t'\right) \mathrm{d}t' \right)^2 \right\rangle. \tag{20}$$

The system consisted of 32000 fluid particles and was initialized at temperature $T = 296.2\,\mathrm{K}$ and bulk mass density in the range 4.8 to $385\,\mathrm{kg/m^3}$. The system was equilibrated with an NVT-ensemble for 2×10^6 steps. After that, an additional 2×10^6 steps were run in the NVE ensemble to collect data and compute the shear viscosity. The time step was $\delta t = 1.375\,\mathrm{fs}$. The statistics were improved by running 30 independent simulations. The shear viscosity is shown as a function of the fluid mass density in Fig. 3.

3.3 Simulation procedure

3.3.1 Equilibrium conditions

The systems were initialized by creating a fcc unit cell of solid particles with varying lattice constant a in a cubic simulation box of side lengths a. In addition, a bulk fluid without solid particles was simulated. The boundaries of the simulation box were periodic. The temperature of the fluid was controlled with a Nosé-Hoover type thermostat

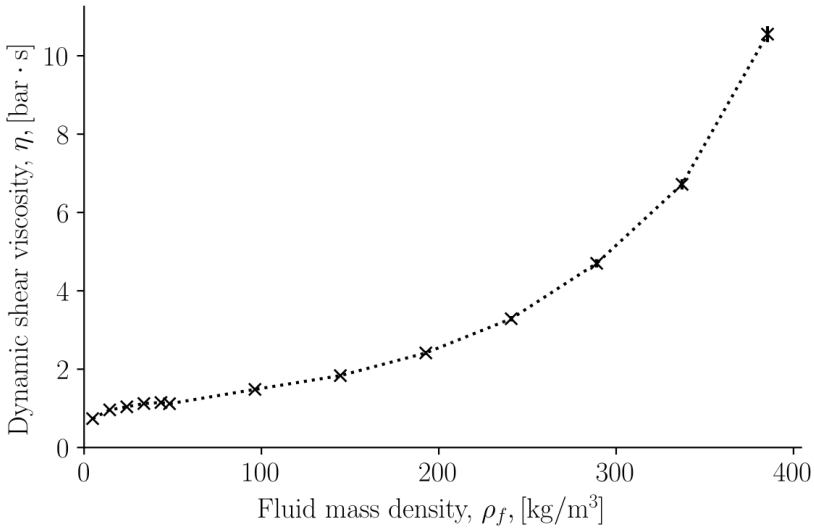

Figure 3: Shear viscosity as a function of fluid mass density.

to be constant and equal to $T = 2\epsilon/k_\mathrm{B} = 296.2\,\mathrm{K}$ [45], which is in the supercritical region ($T_c = 0.885\epsilon/k_\mathrm{B} \approx 131\,\mathrm{K}$ [42]). A supercritical fluid was investigated to avoid phase separation.

Fluid particles were inserted and removed from the porous structure using the grand canonical Monte Carlo [46]. This was done to generate initial configurations with varying lattice constants that were in equilibrium with each other. Fluid particles were inserted into the pores with an acceptance probability

$$\mathrm{acc}(N_f \to N_f + 1) = \min\left\{1, \quad \frac{V}{\Lambda^3(N_f+1)} \exp[\beta(\mu_f - \Delta E_p]\right\} \tag{21}$$

and a random fluid particle was removed from the simulation box with an acceptance probability

$$\mathrm{acc}(N_f \to N_f - 1) = \min\left\{1, \quad \frac{\Lambda^3(N_f+1)}{V} \exp[-\beta(\mu_f + \Delta E_p]\right\}. \tag{22}$$

Where $\beta = 1/k_\mathrm{B}T$ is the thermodynamic beta, $\Lambda = \sqrt{h^2/(2\pi m k_\mathrm{B} T)}$ is the de Broglie thermal wavelength, h is the Planck constant, N_f the number of fluid particles, and ΔE_p is the potential energy difference of the system, when inserting or removing a fluid particle. The fluid chemical potential varied in the interval $\mu_f \in [-10, 10]\epsilon$, which resulted in a bulk fluid mass density variation from $\rho_b = (3.3 \pm 0.2)\,\mathrm{kg/m^3}$ to $(409.9 \pm 0.5)\,\mathrm{kg/m^3}$. The simulations were run until the average number of fluid particles reached a constant value. For the largest porosities and chemical potentials, this took up to 9×10^6 steps. The time step was $\delta t = 2.75\,\mathrm{fs}$.

Fig. 4 illustrates nine visualizations of the equilibrium simulations for three porosities and three chemical potentials. The figure provides a visual impression of the range of conditions studied, from closest packing of spheres and porosity $\phi \approx 0.26$ (bottom row) to an open fcc lattice with porosity $\phi \approx 0.97$ (top row). The three chemical potentials used in the snapshots correspond to bulk mass densities $\rho_b = [(39.9 \pm 0.8), (236 \pm 1), (350.9 \pm 0.8)]\mathrm{kg/m^3}$ from left to right. The figure parts are scaled such that the figure sizes become the same. In the simulations, the

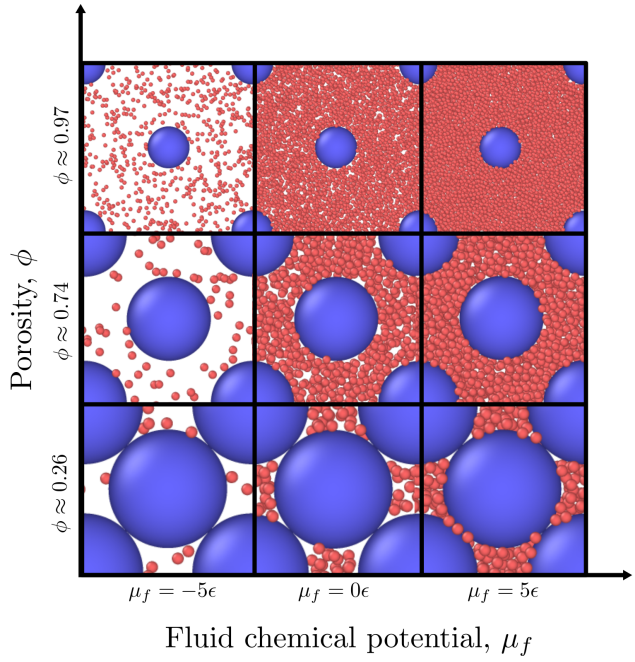

Figure 4: Nine initialized simulations in equilibrium conditions of varying fluid chemical potential and porosity. The three chemical potentials used in the snapshots correspond to bulk mass densities $\rho_b = [(39.9 \pm 0.8), (236.0 \pm 1.1), (350.9 \pm 0.8)]\text{kg/m}^3$ from left to right. Each illustration is scaled such that the figure sizes become the same. In the simulations, the radius of the blue solid particles was constant in all simulations. The simulated system was visualized with OVITO [26].

radius of all blue solid particles was the same.

3.3.2 Non-equilibrium conditions

The unit cells were replicated twice in the y- and z-directions and ten times in the x-direction in these studies. The final side lengths of the simulation box in non-equilibrium conditions were $(10, 2, 2)a$, where a is the lattice constant. The grand canonical Monte Carlo fluid particle insertions and removals from the porous medium were stopped, while the temperature was controlled with a Nosé-Hoover type thermostat [45]. However, the temperature was also controlled separately in each REV (volume V_l) to ensure that there was no temperature gradient.

The reflecting particle method (RPM) [25] was applied to the x-boundary of the simulation box to induce an integral pressure gradient. The RPM allowed particles to cross the periodic x-boundary from right to left with a probability $1 - q$ and be reflected with a probability $q \in [0, 1]$. A value $q = 0$ entailed that no fluid particles were reflected, while a value $q = 1$ entailed that all fluid particles were reflected when attempting to cross the x-boundary from right to left. The fluid particles were never reflected when crossing the x-boundary from left to right. The pressure gradient was controlled by varying the probability q. This is a boundary-driven non-equilibrium molecular dynamics method to induce a pressure gradient that has minimal disturbance on the fluid particles away from the boundary. The simulations were run until they had reached steady-state, where the mass flux was constant along the x-axis. For the longest simulations, this took up to 8×10^6 steps. The time step was $\delta t = 2.75\,\text{fs}$.

The mass fluxes and integral pressures were calculated in layers l of volume V_l along the x-axis. The volume of

each layer was equal to the lattice constant a and spanned the simulation box in the y- and z-directions. The side lengths of the layers were $(a, 2a, 2a)$ in the x-, y- and z-directions, respectively. The volume of each layer (the REV) was consequently $V_l = 4a^3$. Each layer contains four unit cells. The mass flux through layer l was calculated as

$$J_{l,m} = \frac{1}{V_l} \sum_{i \in V_l} m_i v_{i,x} = \rho_{f,l} \langle v_{i,x} \rangle \tag{23}$$

where m_i is the mass of fluid particle i, $v_{i,x}$ is the velocity of fluid particle i in the x-direction, and $\langle v_{i,x} \rangle$ is the average particle velocity in the x-direction. The sum is over all particles in the layer V_l. The integral pressure of each layer was calculated by relating the fluid mass density $\rho_{f,l}$ to the integral pressure calculated in equilibrium.

With this procedure, we were able to determine the transport coefficients l and k. The procedure has been used earlier by us to establish the same gradient in integral pressure [24], however, the permeability calculations are done for the first time here.

4 Results and discussion

The results of this work are shown in Figs. 5 - 14. The results are presented and discussed with reference to the simulation procedure (Section 3.3) and to the Theory (Section 2).

4.1 Equilibrium conditions. The equation of state

The fluid mass density in the REV is shown as a function of fluid chemical potential in Fig. 5. The chemical potential was set by the environment. The fluid mass density is shown for a varying porosity. We see that the fluid mass density in the REV increases monotonically with the chemical potential, approaching the value of the adjacent bulk phase (shown by black crosses in the figure). This approach is as expected.

The fluid mass density of the REV differs from the mass density outside the porous medium. But, the fluid mass density of the REV, corrected by the porosity will also differ from the outside value (not shown in the figure). This indicates that thermodynamic properties change upon fluid confinement. In the low porosity case, the effect is large. For a fluid chemical potential near 0 J, the density ρ_f changes by a factor of 50, as the porosity changes from densest packing of spheres to bulk fluid. Every single curve deviates from the bulk vapor mass density when the fluid chemical potential is around -10^{20} J, where the adsorption of fluid into the pores starts to seriously increase. The numbers refer to the chosen model; methane.

The dependence of the integral pressure on the fluid mass density for the various porosities is presented in Fig. 6. The rise in the integral pressure from a few bars to (3184 ± 27) bar is shown for all porosities. The slope of the curves increases with decreasing porosity. The bulk isotherm is again indicated by black crosses and gives the lower limit of the variation. Again, the curves approach the bulk value as the porosity increases, as expected. The curves apply for a temperature $T = 2.0\epsilon/k_{\mathrm{B}} = 296.2\,\mathrm{K}$.

The mean free path of the bulk vapor densities can be estimated with the kinetic theory of gases with the equation $\ell = (\sqrt{2}\pi\sigma^2 n_b)^{-1}$, where n_b is the number density of fluid particles in the bulk phase. For the lowest bulk mass density, $\rho_b = (3.3 \pm 0.2)\,\mathrm{kg\,m^{-1}}$ the mean free path is estimated to be $\ell = (12.7 \pm 0.9)\,\mathrm{nm}$. The octahedral voids in the fcc lattice can accommodate spheres with diameter 1.6 nm to 11.4 nm for the varying porosities, in which case the system is in the Knudsen flow regime. For a bulk mass density $\rho_b = (24.2 \pm 0.6)\,\mathrm{kg\,m^{-1}}$, the mean free path is estimated to be $\ell = (1.71 \pm 0.05)\,\mathrm{nm}$. The system will be in the Knudsen flow regime for the lowest densities.

The curves obtained for the equilibrium condition Eq. 6, can be regarded as an equation of state relating the temperature, porosity, and fluid mass density of the REV to the integral pressure, see equation Eq. 5. we shall

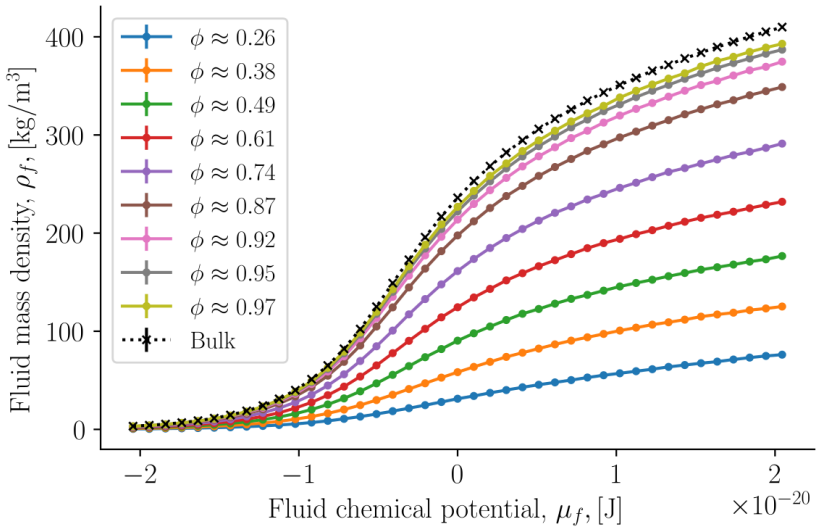

Figure 5: Fluid mass density as a function of fluid chemical potential for varying porosities. Bulk fluid values are indicated by black crosses at the top.

use the sets of relations in the same manner as an equation of state. Once we know the fluid mass density of the REV, we know also the chemical potential that controls it from Fig. 5, and therefore also the corresponding integral pressure from Fig. 6.

4.2 Non-equilibrium conditions

By applying the reflective boundary method we generated a mass flux, a fluid mass density difference, and a difference in integral pressure difference across the porous medium. By increasing the reflecting probability q we increased the gradients. In this manner, we varied the integral pressure gradient between approximately $\Delta\hat{p}/L = -7\,\mathrm{bar\,\mu m^{-1}}$ and $20\,000\,\mathrm{bar\,\mu m^{-1}}$. The corresponding Reynolds numbers varied from approximately zero up to $\mathrm{Re} = 3.54 \pm 0.08$. Gradients that are generated in non-equilibrium molecular dynamics can be very large because the length of the simulation box is relatively short and the method can apply strong forces.

The fluid mass density profiles across the porous medium are shown in Fig. 7 for a porosity $\phi \approx 0.87$, and an average fluid mass density of the REV $\rho_f = (351.3 \pm 0.7)\,\mathrm{kg/m^3}$. The Reynolds numbers varied from $\mathrm{Re} = 0.02 \pm 0.01$ to $\mathrm{Re} = 0.67 \pm 0.02$. From the fluid mass density profiles, we obtained the integral pressure profiles. Examples are shown in Fig. 8. The integral pressure gradients were calculated from the integral pressure profiles. The gradient in integral pressure was in good approximation constant. This was not expected and is also not needed in the data reduction procedures. Because the mass flux is constant at a steady state (mass conservation), and the driving force is approximately constant, it follows that $\rho_f l$ and $\rho_f k/\eta$ were constant across the porous medium. The conductivity and the permeability are not necessarily constant in a porous medium of varying porosity.

There is not yet much experience with the integral pressure of porous media reported in the literature. It is therefore appealing to examine the contributions to the integral pressure from the bulk phases and surface, and test our way to compute $\hat{p}$ from the equation of state, Eq. 5. By assuming $\hat{p}_f = p_f$, $\hat{p} = p_f$ and $\hat{\gamma} = \gamma$, the individual

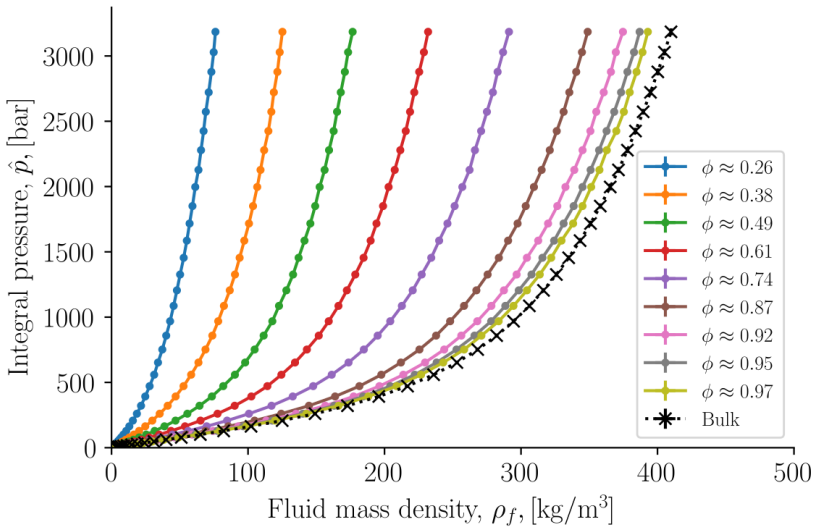

Figure 6: Integral pressure as a function of fluid mass density for varying porosities, or equation of state for the porous medium. Bulk fluid values are shown by black crosses at the bottom.

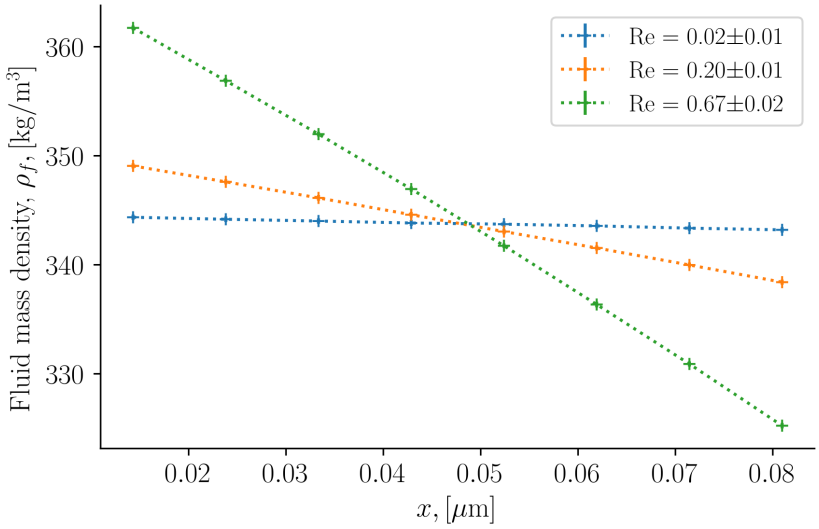

Figure 7: Fluid mass density as a function of the x-coordinate for porosity $\phi \approx 0.87$, average fluid mass density $\rho_b = (351.3 \pm 0.7)\,\mathrm{kg/m^3}$, and varying Reynolds numbers.

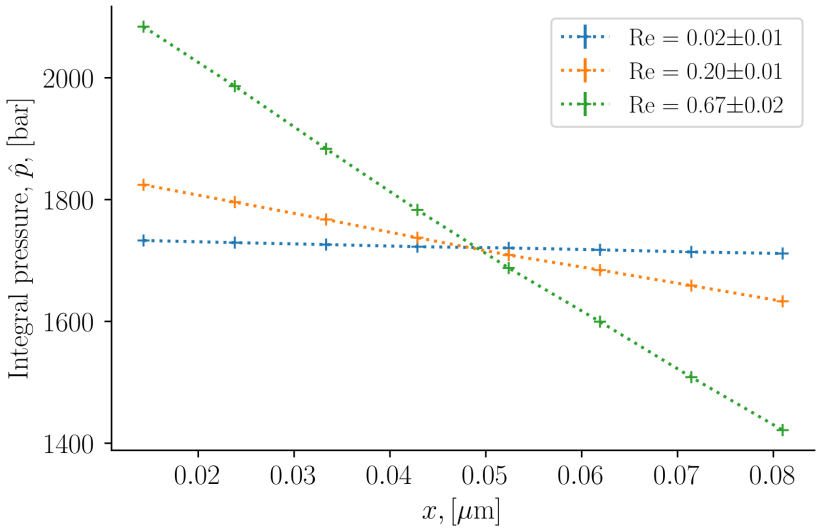

Figure 8: Integral pressure as a function of the x-coordinate for porosity $\phi \approx 0.87$, average fluid mass density $\rho_b = (351.3 \pm 0.7)\,\mathrm{kg/m^3}$, and varying Reynolds numbers.

contributions can be calculated. The outcome is illustrated in Fig. 9, again for a porosity $\phi \approx 0.87$, average fluid mass density $\rho_b = (351.3 \pm 0.7)\,\mathrm{kg/m^3}$. The Reynolds number was now $\mathrm{Re} = 0.67 \pm 0.02$. The assumptions hold for large porosities when the disjoining pressure is zero, and when the surface tension is independent of the fluid-solid surface curvature. These assumptions are not necessary for the continued analysis of this work, they are just chosen to illustrate a case with individual contributions. The surface tension γ was calculated from the spherical mechanical pressure tensor. The value increases monotonically with increasing density between $(0.079 \pm 0.009)\,\mathrm{mN\,m^{-1}}$ and $(34 \pm 1)\,\mathrm{mN\,m^{-1}}$. See the supplementary information for more details on the surface tension.

The integral solid pressure was calculated from the integral pressure and surface tension

$$\hat{p}_s = p_f + \gamma A / V_s \tag{24}$$

where A is the fluid-solid surface area and V_s is the volume of the solid phase, see Eq. 3. In Fig. 9, we see the local contributions from the gradient in fluid pressure $\phi \nabla p_f = (-8629 \pm 106)\,\mathrm{bar\,\mu m^{-1}}$, in integral solid pressure $(1-\phi)\nabla \hat{p}_s = (-9965 \pm 215)\,\mathrm{bar\,\mu m^{-1}}$, and in surface tension $(A/V)\Delta\gamma = (370 \pm 214)\,\mathrm{bar\,\mu m^{-1}}$. The single parts sum to the total value shown in the figure. This value of $\hat{p}$ was also determined from the equation of state, Eq. 5. Within the accuracy of the calculation, we confirmed our hypothesis that the two routes give the same result.

A control of isothermal conditions was carried out. We know that a pressure difference may generate a temperature difference, or vice versa [19]. Constant temperature is therefore a condition for the single flux-force product of the entropy production, and consequently for Darcy's law's applicability. We, therefore, confirmed that the temperature was constant across the system.

Figure 10 shows plots that are used to determine the conductivity and permeability in Darcy's law. Rather than using the volume flux, we have used the mass flux on the ordinate axis, as this flux, but not the volume flux is constant across the porous media in a steady state. The figure illustrates varying porosities $\phi \approx [0.26, 0.61]$ and the

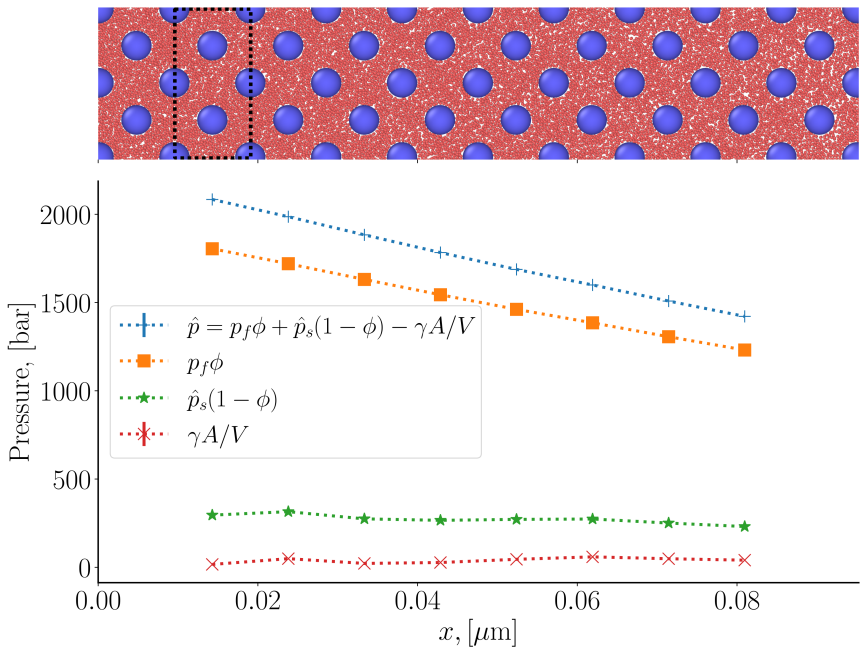

Figure 9: Profile of porosity $\phi \approx 0.87$, average fluid mass density $\rho_b = (351.3 \pm 0.7)\,\mathrm{kg/m^3}$ and Reynolds number $\mathrm{Re} = 0.67 \pm 0.02$. **Top:** Visualization of the simulation box. The border of a layer of volume V_l is marked with a dashed line. **Bottom:** Contributions from the bulk phases and the surface to the integral pressure as function of the x-coordinate. The x-axis of the visualization correspond to the graph. The points in the graph gives the x-position of the center of the REV (the volume V_l).

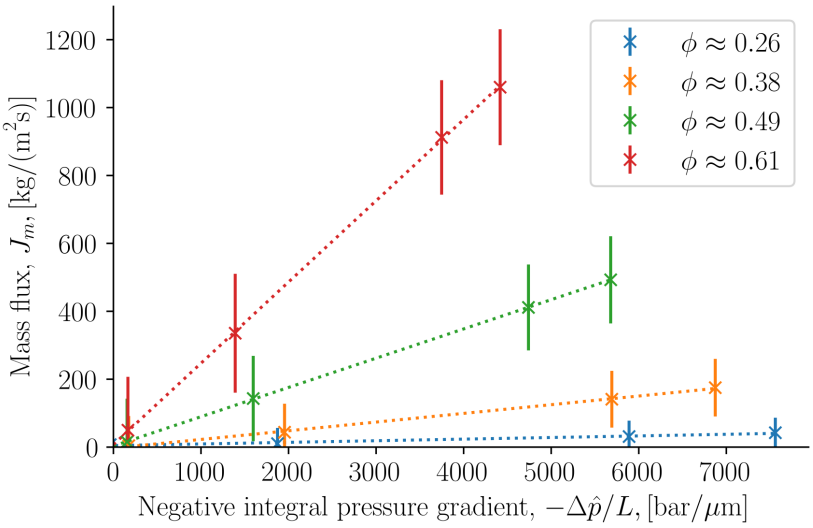

Figure 10: The mass flux as a function of the negative integral pressure gradient for porosities $\phi \approx [0.26, 0.61]$ and average bulk fluid mass density $\rho_b = (108 \pm 1)\,\mathrm{kg/m^3}$. The dashed lines are linear fits to the points.

average bulk fluid mass density was $\rho_b = (108 \pm 1)\,\mathrm{kg/m^3}$ in these plots.

We see that the mass fluxes in all cases can be regarded as linear functions of the negative integral pressure gradient; the dashed lines are linear fits to the calculated mass fluxes. Also observed is that the fluxes intersect the origin of the axes. This behavior is compatible with a linear theory like NET. There is no threshold for transport at low-pressure gradients.

4.3 Conductivity and permeability

Fig. 8 gave the integral pressure gradient inside the porous medium. The integral pressure gradient from this figure together with the constant mass flux was used to determine the conductivity of the porous medium. The conductivity was plotted in Fig. 11 as a function of the factor $\phi^3/(1-\phi)^2$ in the Kozeny-Carman equation. There was no convincing relationship between the variables.

It is more interesting to consider the permeability k. Its value was computed from the conductivity l and the shear viscosity η_b, and the results are shown as a function of the inverse average integral pressure (which here happens to be the same as the inverse differential pressure) in Fig. 12. We see that the permeability increases with a constant slope for large values of the inverse average integral pressure (low densities), where the fluid is highly compressible. For small values (high densities), the slope decreases as the fluid become less compressible. This behavior is expected from the Klinkenberg correction [35, 36]. The results at the low pressure were therefore fitted to a straight line and extrapolated to the high-pressure end to obtain the absolute permeability, k_0.

The dependence of the permeability on other lattice parameters is shown in the log-plot of the permeability as a function of the porosity in Fig. 13. A systematic variation is demonstrated over a change in four orders of magnitude of k. The absolute permeability was calculated using the Klinkenberg correction formula (in the range where this correction applies), by plotting the permeability vs $1/p$ and extrapolating to very large pressures. The

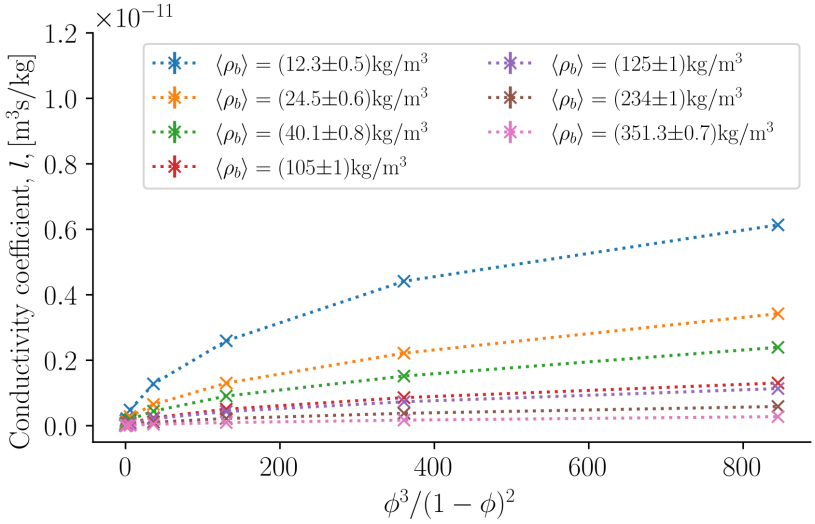

Figure 11: Conductivity coefficient as a function of the porosity factor $\phi^3/(1-\phi)^3$ for various average fluid mass densities.

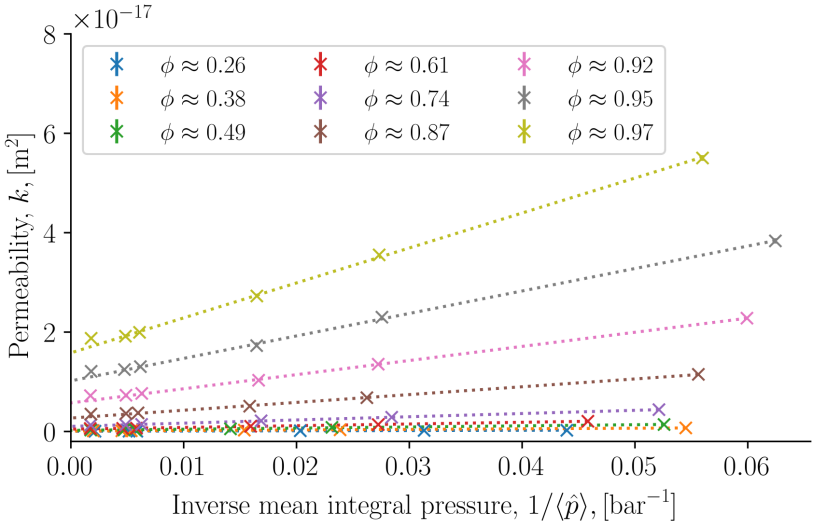

Figure 12: Permeability as a function of inverse average pressure pressure.

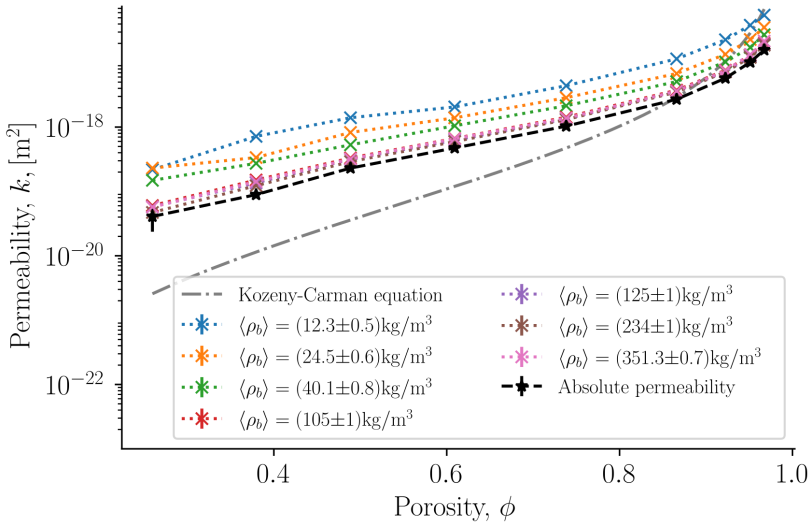

Figure 13: Permeability in logarithmic scale as a function of the porosity ϕ for varying average bulk fluid mass density. The Kozeny-Carman equation is shown as a black dashed curve for a tortuosity $\tau = 1$.

absolute permeability is shown as a black dashed line. We see that the absolute permeabilities form a lower limit for the family of calculated permeabilities. On the other hand, the Kozeny-Carman equation with tortuosity $\tau = 1$, shown as a grey dash-dotted line, does not bring out any new physical insight.

Fig. 14 shows the Klinkenberg coefficient b as a function of porosity ϕ. The coefficient is porosity dependent and significant for the whole range of porosities. To a good approximation, the dependence is linear for porosities below 0.6. The coefficient can be understood from the lack of interaction between solid spheres and fluid particles on the particle level, which here is consistent with slippage.

5 Conclusion and Perspectives

We have demonstrated a new thermodynamic procedure to find the local effective pressure gradient that drives the mass flow through a porous medium. The REV was constructed from additive thermodynamic variables, such that the Gibbs equation and in turn the entropy production and flux-force equations could be derived. The method was applied to single-phase fluid flow in an isothermal medium of varying porosity and fluid mass density under laminar flow conditions. The hydraulic conductivity as well as the permeability were shown to vary with porosity and fluid mass density, and give values that are typical in the literature. The systems studied in this work were in steady-state. This does not pose any limitation on the method. The procedure can be used to describe transients. It is interesting that the system supported the behavior behind the Klinkenberg effect, and that we obtained variables of a size compatible with this effect, *e.g.* $k < 10^{-13}\text{m}^2$.

The procedure has its thermodynamic basis in standard non-equilibrium thermodynamics as combined with Hill's method of nanothermodynamics to describe the confined fluid. This method should now be tested with a two-phase flow, to help solve problems stated in the literature on the upscaling problem; i.e. on how we can properly describe the porous medium microstates, that is the origin of Darcy scale behavior. For instance, we can define the

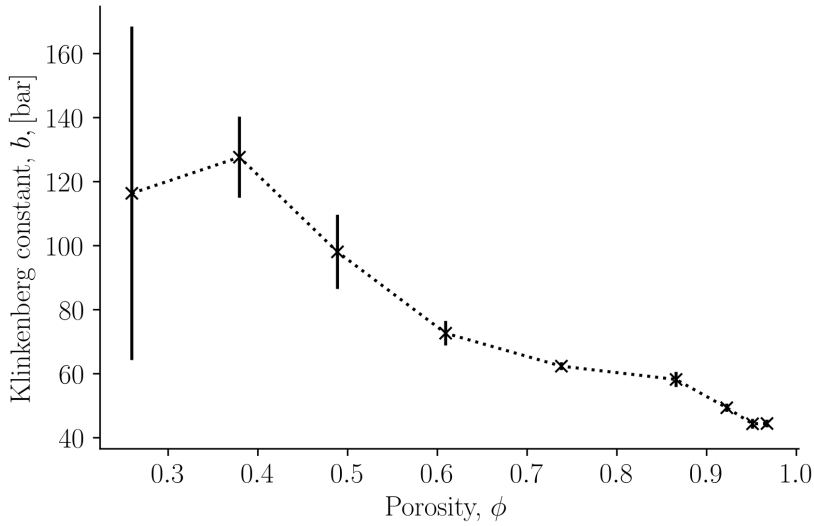

Figure 14: Klinkenberg constant b as a function of porosity ϕ.

effective pressure without consideration of the capillary pressure. For two-phase flow, the REV will be larger than a unit cell to include the statistical variation of the two-phases.

A particular symmetric lattice was chosen to illustrate the derivations. This should also not be regarded as a limitation. The method could be accommodated to deal with pore distributions. It can be applied to highly confined systems, where the disjoining pressure is significant. The central point is the proper construction of the grand potential.

Competing Interests The authors have no relevant financial or non-financial interests to disclose.

Author Contributions O.G. contributed to formal analysis, investigation, methodology, software, visualization, conceptualization, writing original drafts, reviewing, and editing. S.K. and D.B. contributed to formal analysis, investigation, methodology, conceptualization, supervision, writing original drafts, reviewing, and editing. T.T.T. computed viscosities and contributed to reviewing and editing. M.S.B. and M.T.R. contributed to early versions of software, visualization, methodology, conceptualization, reviewing, and editing. All authors have read and agreed to the published version of the manuscript.

Funding This work was funded by the Research Council of Norway through its Centres of Excellence funding scheme, project number 262644, PoreLab.

Acknowledgments The authors acknowledge valuable comments to the last version of the manuscript from Steffen Berg and Hamidreza Erfani Gahrooei. The simulations were performed on resources provided by UNINETT Sigma2 - the National Infrastructure for High-Performance Computing and Data Storage in Norway with project numbers nn9229k and nn8022k. We thank the Research Council of Norway for its Centres of Excellence funding scheme, project number 262644, PoreLab.

Supplementary information to "Local thermodynamic description of isothermal single-phase flow in porous media"

Olav Galteland, Michael T. Rauter, Mina S. Bratvold, Thuat T. Trinh, Dick Bedeaux and Signe Kjelstrup

PoreLab, Department of Chemistry, Norwegian University of Science and Technology

March 4 2022

1 Surface tension

The fluid-solid surface tension was calculated from the spherical mechanical pressure tensor of a single solid sphere surrounded by a fluid of varying mass density. This was considered as the surface tension of a lattice with a large lattice constant, such that the solid surfaces were far apart. The mechanical pressure tensor can be written as a sum of an ideal gas contribution and a virial contribution. The diagonal components of the mechanical pressure tensor were calculated in spherical shells with origin at the center of the solid sphere

$$P_{\alpha\beta}(r) = \rho(r) k_{\mathrm{B}} T \delta_{\alpha\beta} + P^{v}_{\alpha\beta}(r), \tag{25}$$

where r is the distance to the origin, $\rho(r)$ is the fluid mass density of the spherical shell, $\delta_{\alpha\beta}$ is the Kroenecker delta and $P^{s,v}_{\alpha\beta}$ is the virial contribution. The subscripts α and β refer to the spherical coordinates, (r, θ, ϕ). The virial contribution is

$$P^{v}_{\alpha\beta}(r) = -\frac{1}{V(r)} \sum_{i=1}^{N} \sum_{j>i}^{N} f_{ij,\alpha} \int_{C_{ij} \in V(r)} \mathrm{d}l_{\beta}. \tag{26}$$

where $V(r)$ is the volume of the spherical shell, $f_{ij,\alpha}$ is the α-component of the force acting on particle i due to particle j. The line integral is along the Irving-Kirkwood contour C_{ij} [**?**, **?**, **?**], which is the straight line between particle i and j. The line integral gives the length of the β-component of the contour C_{ij} that is contained in the spherical shell $V(r)$. The surface tension is calculated from the pressure tensor

$$\gamma = \frac{1}{R^2} \int_{R}^{r_0} (P_N - P_T) r^2 \mathrm{d}r, \tag{27}$$

where $P_N = P_{rr}$ is the normal to the fluid-solid surface and $P_T = (P_{\theta\theta} + P_{\phi\phi})/2$ is tangential to it. The integral limit r_0 is a position in the fluid far away from the fluid-solid surface such that $P_N = P_T$. The surface tension is shown as a function of fluid mass density in Fig. 15.

References

[1] T. Stylianopoulos, L. Munn, and R. Jain, "Reengineering the physical microenvironment of tumors to improve drug delivery and efficacy: From mathematical modeling to bench to bedside," *Trends in cancer*, vol. 4, p. 292, 2018.

[2] A. Zlotorowicz, K. Jayasayee, P. Dahl, M. Thomassen, and S. Kjelstrup, "Tailored porosities of the cathode layer for improved polymer electrolyte fuel cell performance," *J. Power Sources*, vol. 287, pp. 472–477, 2015.

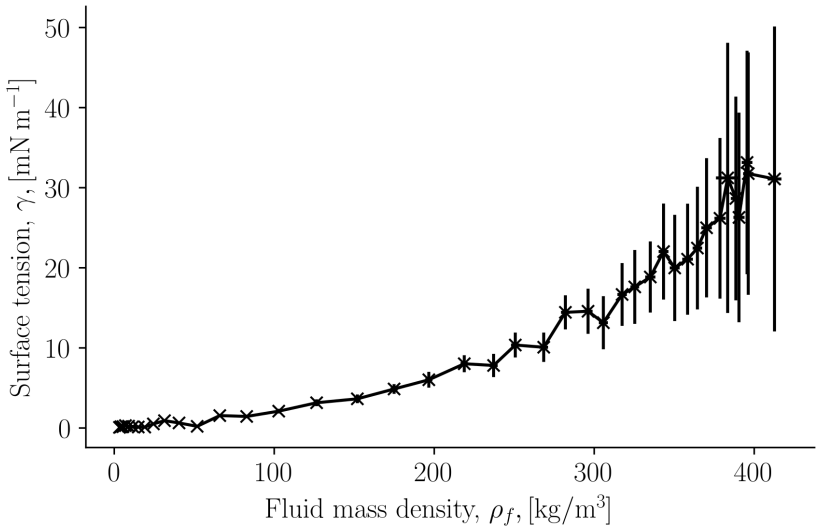

Figure 15: Solid-fluid surface tension as a function of fluid mass density for a single solid sphere surrounded by a fluid.

[3] R. Helmig, *Multiphase Flow and Transport Processes in the Subsurface*. Berlin: Springer, 1997.

[4] M. J. Blunt, *Multiphase flow in permeable media: A pore-scale perspective*. Cambridge: Cambridge University Press, 2017.

[5] S. Whitaker, "Flow in porous media I: A theoretical derivation of Darcy's law," *Transport in porous media*, vol. 1, no. 1, pp. 3–25, 1986.

[6] K. Nordahl and P. S. Ringrose, "Identifying the representative elementary volume for permeability in heterolithic deposits using numerical rock models," *Mathematical geosciences*, vol. 40, no. 7, pp. 753–771, 2008.

[7] W. Gray and M. Hassanizadeh, "Macroscale continuum mechanics for multiphase porous media flow including interface boundaries," *Adv. Water Resource*, vol. 21, pp. 261–281, 1998.

[8] O. Galteland, D. Bedeaux, B. Hafskjold, and S. Kjelstrup, "Pressures inside a nano-porous medium. The case of a single phase fluid," *Front. Phys.*, vol. 7, p. 60, 2019.

[9] M. T. Rauter, O. Galteland, M. Erdős, O. A. Moultos, T. J. Vlugt, S. K. Schnell, D. Bedeaux, and S. Kjelstrup, "Two-Phase Equilibrium Conditions in Nanopores," *Nanomaterials*, vol. 10, no. 4, p. 608, 2020.

[10] D. Bedeaux and S. Kjelstrup, "Fluctuation-dissipation theorems for flow in porous media," *Entropy*, vol. 24, p. 46, 2021.

[11] S. Kjelstrup, D. Bedeaux, A. Hansen, B. Hafskjold, and O. Galteland, "Non-isothermal transport of multi-phase fluids in porous media. The entropy production," *Front. Phys.*, vol. 6, p. 126, 2018.

[12] S. Kjelstrup, D. Bedeaux, A. Hansen, B. Hafskjold, and O. Galteland, "Non-isothermal transport of multi-phase fluids in porous media. Constitutive equations," *Front. Phys.*, vol. 6, p. 150, 2019.

[13] B. D. Todd and P. J. Daivis, *Nonequilibrium molecular dynamics: theory, algorithms and applications*. Cambridge: Cambridge University Press, 2017.

[14] B. Hafskjold, T. Ikeshoji, and S. K. Ratkje, "On the molecular mechanism of thermal diffusion in liquids," *Mol. Phys.*, vol. 80, no. 6, pp. 1389–1412, 1993.

[15] T. Ikeshoji and B. Hafskjold, "Non-equilibrium molecular dynamics calculation of heat conduction in liquid and through liquid-gas interface," *Mol. Phys.*, vol. 81, no. 2, pp. 251–261, 1994.

[16] B. Hafskjold and T. Ikeshoji, "Non equilibrium molecular dynamics simulation of coupled heat-and mass transport across a liquid/vapor interface," *Mol. Sim.*, vol. 16, no. 1-3, pp. 139–150, 1996.

[17] T. L. Hill, *Thermodynamics of small systems, Parts I & II*. New York: Dover Publications, 1994.

[18] D. Bedeaux, S. Kjelstrup, and S. K. Schnell, *Nanothermodynamics. General theory*. Trondheim: PoreLab, Norwegian University of Science and Technology, 2020.

[19] M. T. Rauter, S. K. Schnell, B. Hafskjold, and S. Kjelstrup, "Thermo-osmotic pressure and resistance to mass transport in a vapor-gap membrane," *Phys. Chem. Chem. Phys.*, 2021.

[20] M. T. Rauter, S. K. Schnell, and S. Kjelstrup, "Cassie–Baxter and Wenzel States and the Effect of Interfaces on Transport Properties across Membranes," *J. Phys. Chem. B*, 2021.

[21] M. Erdős, O. Galteland, D. Bedeaux, S. Kjelstrup, O. A. Moultos, and T. J. Vlugt, "Gibbs Ensemble Monte Carlo Simulation of Fluids in Confinement: Relation between the Differential and Integral Pressures," *Nanomaterials*, vol. 10, no. 2, p. 293, 2020.

[22] O. Galteland, D. Bedeaux, and S. Kjelstrup, "Nanothermodynamic description and molecular simulation of a single-phase fluid in a slit pore," *Nanomaterials*, vol. 11, no. 1, p. 165, 2021.

[23] O. Galteland, E. Bering, K. Kristiansen, D. Bedeaux, and S. Kjelstrup, "Legendre-Fenchel transforms capture layering transitions in porous media," *arXiv preprint arXiv:2111.15253*, 2021.

[24] O. Galteland, M. T. Rauter, M. Bratvold, D. Bedeaux, and S. Kjelstrup, "Defining the pressures of a fluid in a nanoporous, heterogeneous medium," *arXiv preprint arXiv:2201.13060*, 2022.

[25] J. Li, D. Liao, and S. Yip, "Coupling continuum to molecular-dynamics simulation: Reflecting particle method and the field estimator," *Physical Review E*, vol. 57, no. 6, p. 7259, 1998.

[26] A. Stukowski, "Visualization and analysis of atomistic simulation data with OVITO–the Open Visualization Tool," *Model. Simul. Mater. Sc.*, vol. 18, no. 1, p. 015012, 2009.

[27] J. Kozeny, "Uber kapillare leitung der wasser in boden," *Sitzungsber. Akad. Wiss.*, vol. 136, pp. 271–306, 1927.

[28] P. C. Carman, "Fluid flow through granular beds," *T. I. Chem. Eng.-Lond.*, vol. 15, pp. 150–166, 1937.

[29] P. C. Carman, *Flow of gases through porous media*. New York: Academic Press, 1956.

[30] C. F. Berg, "Permeability description by characteristic length, tortuosity, constriction and porosity," *Transport in porous media*, vol. 103, no. 3, pp. 381–400, 2014.

[31] J. N. Israelachvili, *Intermolecular and surface forces*. New York: Academic Press, 2015.

[32] R. C. Tolman, "The effect of droplet size on surface tension," *The journal of chemical physics*, vol. 17, no. 3, pp. 333–337, 1949.

[33] A. Røsjorde, D. Fossmo, D. Bedeaux, S. Kjelstrup, and B. Hafskjold, "Nonequilibrium molecular dynamics simulations of steady-state heat and mass transport in condensation: I. local equilibrium," *Journal of colloid and interface science*, vol. 232, no. 1, pp. 178–185, 2000.

[34] I. Inzoli, S. Kjelstrup, D. Bedeaux, and J.-M. Simon, "Transport coefficients of n-butane into and through the surface of silicalite-1 from non-equilibrium molecular dynamics study," *Microporous and Mesoporous materials*, vol. 125, no. 1-2, pp. 112–125, 2009.

[35] L. Klinkenberg, "The permeability of porous media to liquids and gases," *American Petroleum Institute*, pp. 200–213, 1941.

[36] A. Baehr and M. Hult, "Evaluation of unsaturated zone air permeability through pneumatic tests," *water Resources Research*, vol. 27, no. 1, pp. 2605–2627, 1991.

[37] A. P. Thompson, H. M. Aktulga, R. Berger, D. S. Bolintineanu, W. M. Brown, P. S. Crozier, P. J. in't Veld, A. Kohlmeyer, S. G. Moore, T. D. Nguyen, *et al.*, "LAMMPS-A flexible simulation tool for particle-based materials modeling at the atomic, meso, and continuum scales," *Comput. Phys. Commun.*, p. 108171, 2021.

[38] W. A. Steele, *The interaction of gases with solid surfaces*. Oxford: Pergamon Press, 1974.

[39] M. Miyahara and K. E. Gubbins, "Freezing/melting phenomena for Lennard-Jones methane in slit pores: a Monte Carlo study," *J. Chem. Phys.*, vol. 106, no. 7, pp. 2865–2880, 1997.

[40] A. McGaughey and M. Kaviany, "Thermal conductivity decomposition and analysis using molecular dynamics simulations. Part I. Lennard-Jones argon," *Int. J. Heat Mass Tran.*, vol. 47, no. 8-9, pp. 1783–1798, 2004.

[41] G. Rutkai, M. Thol, R. Span, and J. Vrabec, "How well does the Lennard-Jones potential represent the thermodynamic properties of noble gases?," *Mol. Phys.*, vol. 115, no. 9-12, pp. 1104–1121, 2017.

[42] B. Hafskjold, K. P. Travis, A. B. Hass, M. Hammer, A. Aasen, and Ø. Wilhelmsen, "Thermodynamic properties of the 3D Lennard-Jones/spline model," *Mol. Phys.*, vol. 117, no. 23-24, pp. 3754–3769, 2019.

[43] K. R. Kristiansen, "Transport Properties of the Simple Lennard-Jones/Spline Fluid I: Binary Scattering and High-Accuracy Low-Density Transport Coefficients," *Front. Phys.*, vol. 8, p. 271, 2020.

[44] S. H. Jamali, L. Wolf, T. M. Becker, M. de Groen, M. Ramdin, R. Hartkamp, A. Bardow, T. J. H. Vlugt, and O. A. Moultos, "Octp: A tool for on-the-fly calculation of transport properties of fluids with the order-n algorithm in lammps," *J. Chem. Inf. Model.*, vol. 59, pp. 1290–1294, 2019.

[45] W. Shinoda, M. Shiga, and M. Mikami, "Rapid estimation of elastic constants by molecular dynamics simulation under constant stress," *Phys. Rev. B*, vol. 69, no. 13, p. 134103, 2004.

[46] D. Frenkel and B. Smit, *Computational science series: Understanding molecular simulation: from algorithms to applications*. San Diego: Academic press, 2002.

Appendix A

Corrections to articles

The corrections to the known misprints in the articles printed in this thesis are as follows.

1. **Article III, page 5, and line 13:**

   $R \equiv (\sigma_{ff} + \sigma_{rr}) = 5.5\sigma_0$ should be $R \equiv (R_{ff} + R_{rr}) = 5\sigma_0$

2. **Article VI, page 8, and line 15:**

   $\hat{p}_\perp(h) \equiv \frac{1}{h}\int_0^h P_\perp(h)x = P_\perp(h)$ should be $\hat{p}_\perp(h) \equiv \frac{1}{h}\int_0^h P_\perp(h)\mathrm{d}x = P_\perp(h)$

3. **Article VI, page 8, and line 21:**

   $P_\perp(h) = \int_0^h f_{fs}(x)\rho(x,h)x$ should be $P_\perp(h)\int_0^h f_{fs}(x)\rho(x,h)\mathrm{d}x$

4. **Article VI, page 14, and line 4:**

   $\hat{p}(h) = \frac{1}{h}\int_{h_0}^h \hat{p}_\perp h' = \int_{h_0}^h \frac{2\hat{\gamma}}{h'^2}h'$ should be $\hat{p}(h) = \frac{1}{h}\int_{h_0}^h \hat{p}_\perp \mathrm{d}h' = \int_{h_0}^h \frac{2\hat{\gamma}}{h'^2}\mathrm{d}h'$

Bibliography

[1] Hugo Touchette. Legendre-Fenchel Transforms in a Nutshell, 2005. available at: `https://appliedmaths.sun.ac.za/~htouchette/archive/notes/lfth2.pdf` (Nov. 2021).

[2] Ralph Tyrell Rockafellar. *Convex Analysis*. Princeton university press, 2015.

[3] Eivind Bering, Dick Bedeaux, Signe Kjelstrup, Astrid S de Wijn, Ivan Latella, and J Miguel Rubi. A Legendre-Fenchel Transform for Molecular Stretching Energies. *Nanomaterials*, 10(12):2355, 2020.

[4] Olav Galteland, Fernando Bresme, and Bjørn Hafskjold. Solvent-Mediated Forces Between Ellipsoidal Nanoparticles Adsorbed at Liquid-Vapor Interfaces. *Langmuir*, 36(48):14530–14538, 2020.

[5] Olav Galteland. A Molecular Dynamics Study of Prolate Ellipsoidal Nanoparticles Adsorbed at Liquid-Vapour Interfaces. Master's thesis, NTNU, 2017.

[6] Aidan P Thompson, H Metin Aktulga, Richard Berger, Dan S Bolintineanu, W Michael Brown, Paul S Crozier, Pieter J in 't Veld, Axel Kohlmeyer, Stan G Moore, Trung Dac Nguyen, et al. Lammps A Flexible Simulation Tool for Particle-Based Materials Modeling at the Atomic, Meso, And Continuum Scales. *Comput. Phys. Commun.*, page 108171, 2021.

[7] Marco Sauermoser, Natalya Kizilova, Bruno G Pollet, and Signe Kjelstrup. Flow Field Patterns for Proton Exchange Membrane Fuel Cells. *Front. Energy Res.*, 8:13, 2020.

[8] Junye Wang. Theory and Practice of Flow Field Designs for Fuel Cell Scaling-up: A Critical Review. *Appl. Energy*, 157:640–663, 2015.

[9] Deanna M D'Alessandro, Berend Smit, and Jeffrey R Long. Carbon Dioxide Capture: Prospects for New Materials. *Angew. Chem. Int. Ed.*, 49(35):6058–6082, 2010.

[10] Hailong Li, Jana P Jakobsen, Øivind Wilhelmsen, and Jinyue Yan. Pvtxy Properties of CO2 Mixtures Relevant for CO2 Capture, Transport and Storage: Review of Available Experimental Data and Theoretical Models. *Appl. Energy*, 88(11):3567–3579, 2011.

[11] Mahinder Ramdin, Theo W de Loos, and Thijs JH Vlugt. State-of-the-art of CO2 Capture With Ionic Liquids. *Ind. Eng. Chem. Res*, 51(24):8149–8177, 2012.

[12] Matthew E Boot-Handford, Juan C Abanades, Edward J Anthony, Martin J Blunt, Stefano Brandani, Niall Mac Dowell, José R Fernández, Maria-Chiara Ferrari, Robert Gross, Jason P Hallett, et al. Carbon Capture and Storage Update. *Energy Environ. Sci.*, 7(1):130–189, 2014.

[13] Thomas M McDonald, Jarad A Mason, Xueqian Kong, Eric D Bloch, David Gygi, Alessandro Dani, Valentina Crocella, Filippo Giordanino, Samuel O Odoh, Walter S Drisdell, et al. Cooperative Insertion of CO2 in Diamine-Appended Metal-Organic Frameworks. *Nature*, 519(7543):303–308, 2015.

[14] Mai Bui, Claire S Adjiman, André Bardow, Edward J Anthony, Andy Boston, Solomon Brown, Paul S Fennell, Sabine Fuss, Amparo Galindo, Leigh A Hackett, et al. Carbon Capture and Storage (CCS): The way Forward. *Energy Environ. Sci.*, 11(5):1062–1176, 2018.

[15] Michael T Rauter, Sondre K Schnell, and Signe Kjelstrup. Cassie-Baxter and Wenzel States and the Effect of Interfaces on Transport Properties Across Membranes. *J. Phys. Chem. B*, 2021.

[16] Michael T Rauter, Sondre K Schnell, Bjørn Hafskjold, and Signe Kjelstrup. Thermo-osmotic Pressure and Resistance to Mass Transport in a Vapor-gap Membrane. *Phys. Chem. Chem. Phys.*, 2021.

[17] Muhammad Qasim, Mohamed Badrelzaman, Noora N Darwish, Naif A Darwish, and Nidal Hilal. Reverse Osmosis Desalination: A State-of-the-art Review. *Desalination*, 459:59–104, 2019.

[18] Norbert Kuipers, Jan Henk Hanemaaijer, Hans Brouwer, Jolanda van Medevoort, Albert Jansen, Frank Altena, Peter van der Vleuten, and Henk Bak. Simultaneous Production of High-Quality Water and Electrical Power From Aqueous Feedstock's and Waste Heat by High-Pressure Membrane Distillation. *Desalination Water Treat.*, 55(10):2766–2776, 2015.

[19] L Keulen, LV Van Der Ham, NJM Kuipers, JH Hanemaaijer, TJH Vlugt, and S Kjelstrup. Membrane Distillation Against a Pressure Difference. *J. Membr. Sci.*, 524:151–162, 2017.

[20] Lena Spitthoff, Astrid Fagertun Gunnarshaug, Dick Bedeaux, Odne Burheim, and Signe Kjelstrup. Peltier Effects in Lithium-ion Battery Modeling. *J. Chem. Phys*, 154(11):114705, 2021.

[21] Astrid Fagertun Gunnarshaug, Signe Kjelstrup, Dick Bedeaux, Frank Richter, and Odne Stokke Burheim. The Reversible Heat Effects at Lithium Iron Phosphate-and Graphite Electrodes. *Electrochim. Acta*, 337:135567, 2020.

[22] Ying Zhao, Peter Stein, Yang Bai, Mamun Al-Siraj, Yangyiwei Yang, and Bai-Xiang Xu. A Review on Modeling of Electro-Chemo-Mechanics in Lithium-ion Batteries. *J. Power Sources*, 413:259–283, 2019.

[23] Xi Yin, Ling Lin, Hoon T Chung, Siddharth Komini Babu, Ulises Martinez, Geraldine M Purdy, and Piotr Zelenay. Effects of MEA Fabrication and Ionomer Composition on Fuel Cell Performance of PGM-Free ORR Catalyst. *ECS Trans.*, 77(11):1273, 2017.

[24] Dick Bedeaux, Signe Kjelstrup, and Sondre K Schnell. *Nanothermodynamics. General Theory.* PoreLab, Trondheim, Norway, 2020.

[25] Lars Onsager. Reciprocal Relations in Irreversible Processes. I. *Phys. Rev.*, 37(4):405, 1931.

[26] Lars Onsager. Reciprocal Relations in Irreversible Processes. II. *Phys. Rev.*, 38(12):2265, 1931.

[27] Sybren Ruurds De Groot and Peter Mazur. *Non-equilibrium Thermodynamics.* Courier Corporation, 2013.

[28] Signe Kjelstrup and Dick Bedeaux. *Non-equilibrium Thermodynamics of Heterogeneous Systems.* World Scientific, 2008.

[29] Kjetil Nordahl and Philip S Ringrose. Identifying the Representative Elementary Volume for Permeability in Heterolithic Deposits Using Numerical Rock Models. *Math, Geosci.*, 40(7):753–771, 2008.

[30] Stephen Whitaker. Flow in Porous Media I: A Theoretical Derivation of Darcy's law. *Transp. Porous Media*, 1(1):3–25, 1986.

[31] Billy D Todd and Peter J Daivis. *Nonequilibrium Molecular Dynamics: Theory, Algorithms and Applications*. Cambridge University Press, 2017.

[32] Thomas Ramstad, Alex Hansen, and Pål-Eric Øren. Flux-Dependent Percolation Transition in Immiscible two-Phase Flows in Porous Media. *Phys. Rev. E*, 79(3):036310, 2009.

[33] Stig Bakke and Pål-Eric Øren. 3-D Pore-Scale Modelling of Sandstones and Flow Simulations in the Pore Networks. *SPE J.*, 2(02):136–149, 1997.

[34] Glenn Tørå, Pål-Eric Øren, and Alex Hansen. A Dynamic Network Model for two-Phase Flow in Porous Media. *Transp. Porous Media*, 92(1):145–164, 2012.

[35] Tom Bultreys, Kamaljit Singh, Ali Q Raeini, Leonardo C Ruspini, Pål-Eric Øren, Steffen Berg, Maja Rücker, Branko Bijeljic, and Martin J Blunt. Verifying Pore Network Models of Imbibition in Rocks Using Time-Resolved Synchrotron Imaging. *Water Resour. Res.*, 56(6):e2019WR026587, 2020.

[36] Thomas Ramstad, Pål-Eric Øren, and Stig Bakke. Simulation of two-Phase Flow in Reservoir Rocks Using a Lattice Boltzmann Method. *SPE J.*, 15(04):917–927, 2010.

[37] Thomas Ramstad, Nasiru Idowu, Cyril Nardi, and Pål-Eric Øren. Relative Permeability Calculations From two-Phase Flow Simulations Directly on Digital Images of Porous Rocks. *Transp. Porous Media*, 94(2):487–504, 2012.

[38] Yun Long, Jeremy C Palmer, Benoit Coasne, Malgorzata Śliwinska-Bartkowiak, and Keith E Gubbins. Pressure Enhancement in Carbon Nanopores: A Major Confinement Effect. *Phys. Chem. Chem. Phys.*, 13(38):17163–17170, 2011.

[39] David van Dijk. Comment on "Pressure Enhancement in Carbon Nanopores: A Major Confinement Effect" by Y. Long, JC Palmer, B. Coasne, M.

Śliwinska-Bartkowiak and KE Gubbins, Phys. Chem. Chem. Phys., 2011, 13, 17163. *Phys. Chem. Chem. Phys.*, 22(17):9824–9825, 2020.

[40] Yun Long, Jeremy C Palmer, Benoit Coasne, Kaihang Shi, Malgorzata Śliwińska-Bartkowiak, and Keith E Gubbins. Reply to the 'Comment on "Pressure Enhancement in Carbon Nanopores: A Major Confinement Effect"'by D. Van Dijk, Phys. Chem. Chem. Phys., 2020, 22. *Phys. Chem. Chem. Phys.*, 22(17):9826–9830, 2020.

[41] JH Irving and John G Kirkwood. The Statistical Mechanical Theory of Transport Processes. IV. The Equations of Hydrodynamics. *J. Chem. Phys.*, 18(6):817–829, 1950.

[42] P Schofield and James R Henderson. Statistical Mechanics of Inhomogeneous Fluids. *Proc. R. Soc. Lond. A Math. Phys. Sci.*, 379(1776):231–246, 1982.

[43] Henry Darcy. *Les Fontaines Publiques de la Ville de Dijon*. Victor Dalmont, 1856.

[44] A. Zlotorowicz, K. Jayasayee, P.I. Dahl, M.S. Thomassen, and S. Kjelstrup. Tailored Porosities of the Cathode Layer for Improved Polymer .

[45] Máté Erdős, Olav Galteland, Dick Bedeaux, Signe Kjelstrup, Othonas A Moultos, and Thijs JH Vlugt. Gibbs Ensemble Monte Carlo Simulation of Fluids in Confinement: Relation Between the Differential and Integral Pressures. *Nanomaterials*, 10(2):293, 2020.

[46] Michael T Rauter, Olav Galteland, Máté Erdős, Othonas A Moultos, Thijs JH Vlugt, Sondre K Schnell, Dick Bedeaux, and Signe Kjelstrup. Two-phase Equilibrium Conditions in Nanopores. *Nanomaterials*, 10(4):608, 2020.

[47] Olav Galteland, Dick Bedeaux, and Signe Kjelstrup. Nanothermodynamic Description and Molecular Simulation of a Single-Phase Fluid in a Slit Pore. *Nanomaterials*, 11(1):165, 2021.

[48] Olav Galteland, Dick Bedeaux, Bjørn Hafskjold, and Signe Kjelstrup. Pressures Inside a Nano-Porous Medium. The Case of a Single Phase Fluid. *Front. Phys.*, 7:60, 2019.

[49] Olav Galteland, Michael T Rauter, Kevin K Varughese, Dick Bedeaux, and Signe Kjelstrup. Defining the Pressures of a Fluid in a Nanoporous, Heterogeneous Medium. *arXiv:2201.13060*, 2022.

[50] Olav Galteland, Michael T Rauter, Mina S Bratvold, Thuat T Trinh, Dick Bedeaux, and Signe Kjelstrup. A Local Thermodynamic Description of Isothermal Single-Phase Flow in Nanoporous Media. *arXiv:2203.02334*, 2022.

[51] P Peter Atkins and J De Paula. *Atkins' Physical Chemistry*. Oxford University Press, Oxford, 2014.

[52] A. D. McNaught and A. Wilkinson. *IUPAC. Compendium of Chemical Terminology, 2nd ed.* Blackwell Scientific Publications, Oxford, 1997.

[53] Olav Galteland, Eivind Bering, Kim Kristiansen, Dick Bedeaux, and Signe Kjelstrup. Legendre-Fenchel Transforms Capture Layering Transitions in Porous Media. *arXiv:2111.15253*, 2021.

[54] F Bresme and M Oettel. Nanoparticles at Fluid Interfaces. *J. Phys. Condens. Matter*, 19(41):413101, 2007.

[55] Fernando Bresme, Hartwig Lehle, and Martin Oettel. Solvent-Mediated Interactions Between Nanoparticles at Fluid Interfaces. *J. Chem. Phys.*, 130(21):214711, 2009.

[56] Terrell L Hill. *Thermodynamics of Small Systems Two Volumes Bound as One*. Dover, 1964.

[57] Terrell L Hill. Perspective: Nanothermodynamics. *Nano Lett*, 2001.

[58] Terrell L Hill. A Different Approach to Nanothermodynamics. *Nano Lett.*, 1(5):273–275, 2001.

[59] Terrell L Hill. Extension of Nanothermodynamics to Include a one-Dimensional Surface Excess. *Nano Lett.*, 1(3):159–160, 2001.

[60] Terrell L Hill and Ralph V Chamberlin. Fluctuations in Energy in Completely Open Small Systems. *Nano Lett.*, 2(6):609–613, 2002.

[61] Boris Derjaguin. Untersuchungen Über die Reibung und Adhäsion, IV. *Kolloid Z.*, 69(2):155–164, 1934.

[62] Jacob N Israelachvili. *Intermolecular and Surface Forces*. Academic press, 2015.

[63] Bjørn A Strøm, Jianying He, Dick Bedeaux, and Signe Kjelstrup. When Thermodynamic Properties of Adsorbed Films Depend on Size: Fundamental Theory and Case Study. *Nanomaterials*, 10(9):1691, 2020.

[64] Bjørn A Strøm, Dick Bedeaux, and Sondre K Schnell. Adsorption of an Ideal gas on a Small Spherical Adsorbent. *Nanomaterials*, 11(2):431, 2021.

[65] Signe Kjelstrup and Dick Bedeaux. *Non-equilibrium Thermodynamics of Heterogeneous Systems*. World Scientific, second edition, 2020.

[66] Jing Xu, Signe Kjelstrup, and Dick Bedeaux. Molecular Dynamics Simulations of a Chemical Reaction; Conditions for Local Equilibrium in a Temperature Gradient. *Phys. Chem. Chem. Phys.*, 8(17):2017–2027, 2006.

[67] Thierry Savin, Kirill S Glavatskiy, Signe Kjelstrup, Hans Christian Öttinger, and Dick Bedeaux. Local Equilibrium of the Gibbs Interface in two-Phase Systems. *EPL*, 97(4):40002, 2012.

[68] A Røsjorde, DW Fossmo, D Bedeaux, S Kjelstrup, and B Hafskjold. Nonequilibrium Molecular Dynamics Simulations of Steady-State Heat and Mass Transport in Condensation: I. Local Equilibrium. *J. Colloid Interace Sci.*, 232(1):178–185, 2000.

[69] Bjørn Hafskjold, Dick Bedeaux, Signe Kjelstrup, and Øivind Wilhelmsen. Nonequilibrium Thermodynamics of Surfaces Captures the Energy Conversions in a Shock Wave. *Chem. Phys. Lett.*, 738:100054, 2020.

[70] Bjørn Hafskjold, Dick Bedeaux, Signe Kjelstrup, and Øivind Wilhelmsen. Theory and Simulation of Shock Waves: Entropy Production and Energy Conversion. *Phys. Rev. E*, 104(1):014131, 2021.

[71] Michael Schaefer, Christian Bartels, and Martin Karplus. Solution Conformations and Thermodynamics of Structured Peptides: Molecular Dynamics Simulation With an Implicit Solvation Model. *J. Mol. Biol.*, 284(3):835–848, 1998.

[72] Bruno Rizzuti and Valerie Daggett. Using Simulations to Provide the Framework for Experimental Protein Folding Studies. *Arch. Biochem. Biophys.*, 531(1-2):128–135, 2013.

[73] Richard Lavery, Anne Lebrun, Jean-François Allemand, David Bensimon, and Vincent Croquette. Structure and Mechanics of Single Biomolecules: Experiment and Simulation. *J. Phys. Condens. Matter*, 14(14):R383, 2002.

[74] Gregory A Voth. *Coarse-Graining of Condensed Phase and Biomolecular Systems*. CRC press, 2008.

[75] Peter L Freddolino, Anton S Arkhipov, Steven B Larson, Alexander McPherson, and Klaus Schulten. Molecular Dynamics Simulations of the Complete Satellite Tobacco Mosaic Virus. *Structure*, 14(3):437–449, 2006.

[76] Anton Arkhipov, Peter L Freddolino, and Klaus Schulten. Stability and Dynamics of Virus Capsids Described by Coarse-Grained Modeling. *Structure*, 14(12):1767–1777, 2006.

[77] Xue Wang, Fengting Xu, Jiasen Liu, Bingquan Gao, Yanxin Liu, Yujia Zhai, Jun Ma, Kai Zhang, Timothy S Baker, Klaus Schulten, et al. Atomic Model of Rabbit Hemorrhagic Disease Virus by Cryo-Electron Microscopy and Crystallography. *PLOS Pathog.*, 9(1):e1003132, 2013.

[78] Yasushi Shibuta, Shinji Sakane, Eisuke Miyoshi, Shin Okita, Tomohiro Takaki, and Munekazu Ohno. Heterogeneity in Homogeneous Nucleation From Billion-Atom Molecular Dynamics Simulation of Solidification of Pure Metal. *Nat. Commun.*, 8(1):1–9, 2017.

[79] Sridhar Kumar Kannam, BD Todd, Jesper Schmidt Hansen, and Peter J Daivis. How Fast Does Water Flow in Carbon Nanotubes? *J. Chem. Phys.*, 138(9):094701, 2013.

[80] Daan Frenkel and Berend Smit. *Understanding Molecular Simulation: From Algorithms to Applications*, volume 1. Elsevier, 2001.

[81] Michael P Allen and Dominic J Tildesley. *Computer Simulation of Liquids*. Oxford university press, 2017.

[82] John Edward Jones. On the Determination of Molecular Fields. —II. From the Equation of State of a gas. *P. R. Soc. Lond. A-Conta.*, 106(738):463–477, 1924.

[83] William C Swope, Hans C Andersen, Peter H Berens, and Kent R Wilson. A Computer Simulation Method for the Calculation of Equilibrium Constants

for the Formation of Physical Clusters of Molecules: Application to Small Water Clusters. *J. Chem. Phys.*, 76(1):637–649, 1982.

[84] Loup Verlet. Computer "Experiments" on Classical Fluids. I. Thermodynamical Properties of Lennard-Jones Molecules. *Phys. Rev.*, 159(1):98, 1967.

[85] Nicholas Metropolis, Arianna W Rosenbluth, Marshall N Rosenbluth, Augusta H Teller, and Edward Teller. Equation of State Calculations by Fast Computing Machines. *J. Chem. Phys.*, 21(6):1087–1092, 1953.

[86] Bjørn Hafskjold, Karl Patrick Travis, Amanda Bailey Hass, Morten Hammer, Ailo Aasen, and Øivind Wilhelmsen. Thermodynamic Properties of the 3D Lennard-Jones/Spline Model. *Mol. Phys.*, 117(23-24):3754–3769, 2019.

[87] Kim R. Kristiansen. Transport Properties of the Simple Lennard-Jones/Spline Fluid I: Binary Scattering and High-Accuracy Low-Density Transport Coefficients. *Front. Phys.*, 8:271, 2020.

[88] Jesper Schmidt Hansen, BD Todd, and Peter J Daivis. Prediction of Fluid Velocity Slip at Solid Surfaces. *Phys. Rev. E*, 84(1):016313, 2011.

[89] Sridhar Kumar Kannam, BD Todd, Jesper Schmidt Hansen, and Peter J Daivis. Slip Flow in Graphene Nanochannels. *J. Chem. Phys.*, 135(14):016313, 2011.

[90] Sridhar Kumar Kannam, BD Todd, Jesper Schmidt Hansen, and Peter J Daivis. Slip Length of Water on Graphene: Limitations of non-Equilibrium Molecular Dynamics Simulations. *J. Chem. Phys.*, 136(2):024705, 2012.

[91] Shuichi Nosé. A Unified Formulation of the Constant Temperature Molecular Dynamics Methods. *J. Chem. Phys.*, 81(1):511–519, 1984.

[92] William G Hoover. Canonical Dynamics: Equilibrium Phase-Space Distributions. *Phys. Rev. A*, 31(3):1695, 1985.

[93] Wataru Shinoda, Motoyuki Shiga, and Masuhiro Mikami. Rapid Estimation of Elastic Constants by Molecular Dynamics Simulation Under Constant Stress. *Phys. Rev. B*, 69(13):134103, 2004.

[94] Peter J Daivis and Denis J Evans. Comparison of Constant Pressure and Constant Volume Nonequilibrium Simulations of Sheared Model Decane. *J. Chem. Phys.*, 100(1):541–547, 1994.

[95] Berk Hess. Determining the Shear Viscosity of Model Liquids From Molecular Dynamics Simulations. *J. Chem. Phys.*, 116(1):209–217, 2002.

[96] Peter J Daivis and BD Todd. A Simple, Direct Derivation and Proof of the Validity of the SLLOD Equations of Motion for Generalized Homogeneous Flows. *J. Chem. Phys.*, 124(19):194103, 2006.

[97] A Harasima. Molecular Theory of Surface Tension. *Adv. Chem. Phys*, 1:203–237, 1958.

[98] Bjørn Hafskjold and Tamio Ikeshoji. Microscopic Pressure Tensor for Hard-Sphere Fluids. *Phys. Rev. E*, 66(1):011203, 2002.

[99] Edgar M Blokhuis and Dick Bedeaux. Pressure Tensor of a Spherical Interface. *J. Chem. Phys.*, 97(5):3576–3586, 1992.

[100] Ju Li, Dongyi Liao, and Sidney Yip. Coupling Continuum to Molecular-Dynamics Simulation: Reflecting Particle Method and the Field Estimator. *Phys. Rev. E*, 57(6):7259, 1998.